Sapienza University of Rome

CIVIL AND INDUSTRIAL ENGINEERING
Ph.D. Course in Energy and Environment

RADON IN INDOOR AIR AND WATER: DESIGN AND DEVELOPMENT OF EXPERIMENTAL APPARATUSES AND MEASUREMENT PROTOCOLS

Design, realization and commissioning of an experimental apparatus to in-situ measure the radon exhalation rate from vertical surfaces and of a radon chamber for radon continuous monitors testing and calibration in controlled atmospheres. Development and testing of a quality assurance program to measure the radon concentration in water through the emanometry test method.

Candidate:
Christian Di Carlo
1545299

Thesis advisor:
Prof. Romolo Remetti

Research supervisors:
Dr. Francesco Bochicchio
Dr. Gennaro Venoso

Thesis submitted in October 2020

Contents

List of Figures

List of Tables

Acknowledgements

Grazie, a chi mi ha chiesto "cosa studi?".
Grazie, a chi l'ha capito, e a chi ha fatto finta di esserci riuscito.

Grazie, a chi mi ha chiesto "come va?".
Grazie, a chi è stato ad ascoltare la risposta.

Grazie, a chi mi ha chiesto "ma tu, al dottorato, ci hai mai pensato?".
Grazie, a chi, tre anni fa, mi ha voluto.
Grazie, a chi in tre anni ci ha creduto.
Grazie, a chi, tre anni dopo, non si è pentito.

Grazie mamma e grazie papà.

Grazie amici miei.

Grazie.

Abstract

Exposure to the decay products of radon (used in brief to refer to the isotope 222 of Rn) and thoron (used to refer to the isotope 220 of Rn) represents, on average, approximately half of the overall effective dose from natural sources suffered per year by the global population, i.e. 2.4 mSv year^{-1} (United Nations Scientific Committee on the Effects of Atomic Radiation, 2008). In particular, the UNSCEAR Report from 2008 reports effective doses due to radon and thoron inhalation of 1.15 mSv year^{-1} and 0.1 mSv year^{-1}, respectively.

Due to the relatively low outdoor concentration[1], most of the exposure to radon occurs indoor where a wide variability exists in radon daughters concentration (Nero and Nazaroff, 1984). Both temporal (e.g. Tokonami et al., 2003; Iimoto, 2000; Hopke et al., 1995) and spatial (e.g. Prasad et al., 2016; Tokonami et al., 2003; Ramachandran and Ramu, 1994) variability of the equilibrium factors [2] surely reflects on radon progeny variability, but the latter is mainly caused by the difference in indoor radon concentration over time and from an indoor place to another.

According to the World Health Organization (2010), indoor radon concentration depends on two main factors: typology of building construction and ventilation specifications and habits. Both of them affect the indoor radon concentration by influencing the relative contributions of the various radon sources. Several authors (e.g. Nazaroff and Nero, 1988) suggest that radon can enter building interiors:

i) directly from soil due to radium-containing rocks still in the crust;

ii) via radon-carriers utilities such as water and, in principle, natural gas;

iii) indirectly from crustal materials no longer incorporated in crust but contained into building structure in the form of concrete, brick and the like.

[1] In 1982, UNSCEAR reported the mean annual value of radon concentration in outdoor air at ground level varies between 0.1 and 10 becquerel per cubic metre, with a typical value in populated areas of 3 Bq m^{-3} (United Nations Scientific Committee on the Effects of Atomic Radiation, 1982). UNSCEAR 1993 (United Nations Scientific Committee on the Effects of Atomic Radiation, 1993) reported 10 Bq m^3 as typical outdoor ^{222}Rn and ^{220}Rn concentrations. Past and recent results of radon measurements outdoors (Iida et al., 1996; Oikawa et al., 2003) have confirmed such estimates.

[2] In the following, values of 0.4 (United Nations Scientific Committee on the Effects of Atomic Radiation, 2000, 1993, 1988) and 0.7 (mean value between 0.6 from (United Nations Scientific Committee on the Effects of Atomic Radiation, 2006, 2000) and 0.8 from (United Nations Scientific Committee on the Effects of Atomic Radiation, 1993, 1988)), will be assumed as "typical" for equilibrium factors in indoor and outdoor conditions respectively.

The relative contribution of each of these entry patterns obviously depends on specific circumstances, i.e. building characteristics (including building materials, construction typology and floor level), morphology and composition of the underlying soil, ventilation features, occupancy patterns and living habits of occupants.

Council Directive 2013/59/EURATOM requires Member States to *consider* any source of radon ingress, whether from soil, building materials or water (European Commission, 2014). This is required when preparing the national action plan to address long-term risks from radon exposure. In particular, regarding building materials, Member States are explicitly required to identify (and/or develop) strategy, including methods and tools, to identify building materials with significant radon exhalation rate.

Pertaining to building materials, several measurements of radon exhalation rate have been reported on literature through the years (e.g. Avramović et al., 2019; Leonardi et al., 2018) (more references are available in the text). However, as firstly highlighted by Sahoo et al. (2011), the difference between radon exhalation from samples and that from walls has not been investigated enough. As a result of this lack of knowledge, measurements of radon exhalation from building materials samples have been commonly used to assess the effective dose attributable to radon exhaled from walls in indoor environment (Feng and Lu, 2016; Gupta et al., 2013; Mahur et al., 2008; Ujić et al., 2010) even though different geometries and boundary conditions characterize the two scenarios. In fact, if the one dimensional (1-D) geometry better describes the radon flux from masonry surfaces, mainly walls, it is not suitable to the radon exhalation from a sample of building material, the latter better modelled as a three dimensional (3-D) phenomenon.

Currently, two main possibilities exist to provide reliable values of radon exhalation rate from a wall. The first is estimating the radon surface exhalation rate from a wall as related to that from a building material sample. This approach has been proposed by Sahoo et al. (2011) and recalled by Orabi (2018). It relies on the comparison between the 3-D model of the radon flux from the building material sample and the 1-D model used to assess flux from a wall made up by the same material. The 1-D model solution proposed by the authors – firstly reported by Jonassen and McLaughlin (1980) and later recalled by Nazaroff and Nero (1988) – is obtained under three main conditions: *i*) the diffusion is the only mechanism governing the radon transport, *ii*) the radon concentration inside the wall is an even function, symmetric with respect to the wall half thickness and *iii*) the room inner volume is much higher than the void wall volume. In other words, the solution is valid only when advective contribution is negligible and both wall surfaces are free to exhale into a radon-free space. As a matter of fact, the boundary conditions adopted by Sahoo et al. (2011) and Orabi (2018), despite being far from commonly verified, are not even declared at all. The resulting formulations can so lead to misleading predictions of radon surface flux from an existing wall.

The issue just described is an evidence of the need to provide a systematic review of the differential equations describing the radon migration, as well as the corresponding solutions for any reasonable boundary conditions sets. This task has been accomplished by the Chapter 2 of this work. The aim is to provide the readers with a comprehensive description of how typical scenarios for radon transport are mathematically modelled as well as to clarify the assumptions

underlying the solutions. In particular, the review has addressed either diffusive, advective and diffusive plus advective transport of radon through a slab, the latter containing radium sources or not, in different scenarios.

The second possibility to provide reliable values of radon exhalation rate from a wall is in-situ measuring radon exhalation rate directly from the wall surface, i.e. through the so-called accumulation method described by ISO 11665-7 (International Organization for Standardization, 2012a). To the author knowledge, no published study exists of in-situ applications of the ISO method to vertical surfaces. This is mainly due to the several issues affecting the measuring apparatuses available on the market. Firstly, they are not specifically designed for vertical surfaces so they are not self-standing and equipped with a frame supporting the accumulation can. Secondly, they are not provided with sealing systems of any kind and the air exchanges between inside and outside the accumulation container, other than not being prevented, are not traceable at all. Besides, they are sold by the continuous radon monitor manufacturers, so the compatibility is assured only with a specific model of a specific detector. Furthermore, the analysis of the radon concentration registered to obtain exhalation rate value is a quite slow, multi-step and not automatized process completely up to the operator.

Chapter 3 of this work deals with design, commissioning and realization of the first custom apparatus specifically conceived to in-situ measure the radon exhalation rate directly from walls vertical surfaces. The prototype, fully developed at the Laboratory of Radioactivity of the Italian National Institute of Health, is intended to solve such critical issues that have prevented similar apparatuses from being adopted by the radon experts: mechanically sustaining the accumulation can during the measurement without interfering with the measurements itself (*i*) and assuring the sealing of the chamber relative to the radon detector (*ii*) and the wall under investigation (*iii*). The prototype also aims to avoid the interfering effect of the chamber pressurization during the measurement and to reduce the effect of the back-diffusion on the accumulation process. The apparatus presented has been already successfully used in some surveys in large buildings to reconstruct the likely radon migration path through some surface flux measurements at different locations in different rooms.

The apparatus has been designed for a specific continuous radon monitor model but the configuration can be adapted, with very few modifications, to other radon detectors. The choice comprehends the large number of low-cost detectors that entered, and are still entering, the market in the last few years. This quite recent and sudden entry into the market of a large number of different detectors for both professional and "domestic" purpose has turn a spotlight on the need of increasing the number of testing facilities and calibration apparatuses. These facilities should always rely on radon chambers that are designed to produce reference atmospheres whose radon activity concentration depends on the radium source employed and on the chamber volume. According to the current state of the art, radon chambers are characterized by significant costs as design, construction, commissioning, and maintenance are concerned. In particular, critical issues are *i*) materials used for the structure and the sealing, *ii*) fan system for concentration homogenization, *iii*) source-chamber interface circuit and *iv*) control instrumentation. Furthermore, industries, agencies or institutions managing a radon chamber need as many radium sources as the radon concentrations required by the different calibration protocols. Holding

more than one source complicates the licensing requirements concerned with radioactive materials possession established by the national transpositions of the Council Directive 2013/59/Euratom (European Commission, 2014).

Chapter 4 of this work describes an innovative 0.1 m^3 radon chamber fully designed, built and tested at the laboratory of Radiation Protection of Sapienza – University of Rome. It has been conceived as and easy-to-assemble, cheap and small facility dedicated to research on radon and calibrations services. The main innovation stands in the way radon activity concentration is varied and controlled within the chamber atmosphere: the system, in fact, may allow to establish a wide range of ^{222}Rn concentrations through a single ^{226}Ra source placed outside the control volume and by means of two air circulation circuits controlled by specific electric pumps remotely controlled and actuated. On view of this, the apparatus is intended to be suitable for several applications, such as: *i*) calibrating both passive and active radon detectors at different radon concentrations, *ii*) checking the response linearity of both passive and active radon detectors and *iii*) studying the dynamic response of the continuous radon monitors to sudden changes in radon concentration.

Pertaining to the water as an indoor exposure source to radon, the Council Directive 2013/51 (European Commission, 2013) introduced several requirements to Member States about radon concentration in water, including: *i*) to adopt a parametric value (equal to 100 $Bq\,L^{-1}$) above which the risk has to be evaluated and remedial actions have to be considered, and *ii*) to carry out representative surveys in order to identify water sources whose radon content might exceed such a parametric value. The implementation of the Council Directive has led to a considerable increase of radon concentration measurements in drinking waters. The Directive indicates for the method of analysis a minimum limit of detection (or detection limit, DL) of 10 $Bq\,L^{-1}$, i.e. 10% of the parametric value. Test methods satisfying such a limit are, mainly, gamma-ray spectrometry, liquid scintillation counting, and emanometry, whose achievable lowest detection limit are 10, 0.05 and 0.04 $Bq\,L^{-1}$, respectively (Jobbágy et al., 2017). Findings from previous studies showed no statistically significant differences between results from the three different measuring techniques (Pujol and Pérez-Zabaleta, 2017). The test method using emanometry, regulated by the international standard ISO 13164-3 (International Standard Organization, 2013), has been used in several surveys thanks to its advantages: mainly, the possibility to use different detectors with low-to-moderate costs (i.e. 1-20 k€), the low achievable uncertainty (i.e. up to 5%) (Jobbágy et al., 2017), the suitability for in-situ measurements and the very short turnaround time (International Organization for Standardization, 2014).

Chapter 5 of this work deals with the development of a specific quality assurance (QA) protocol for measurements of radon in water contemporary performed with different measuring chains by emanometry technique. This protocol is intended to allow increasing the number of measurements performed, i.e. samples analysed per day, considering that, for the emanometry test method, the water samples have to be analysed one at a time. The effectiveness of such a protocol has been evaluated by studying the results reproducibility and participating to an international proficiency test organized by the European Commission Joint Research Centre (JRC). The quality assurance protocol has been so adopted, with excellent results, during the first survey addressing the radon concentration in self-bottled mineral spring waters.

Chapter 1

Sources of Indoor Radon

Exposure to the decay products of radon (in the following frequently referred to as ^{222}Rn or simply Rn) and thoron (hereafter often ^{220}Rn) represents approximately half of the worldwide average overall effective dose, i.e. 2.4 mSv year^{-1} (United Nations Scientific Committee on the Effects of Atomic Radiation, 2008), suffered per year by the global population from naturally occurring radionuclides. In particular, UNSCEAR 2008 Report refers values for effective dose due to inhalation of radon and thoron of 1.15 mSv year^{-1} and 0.1 mSv year^{-1} respectively.

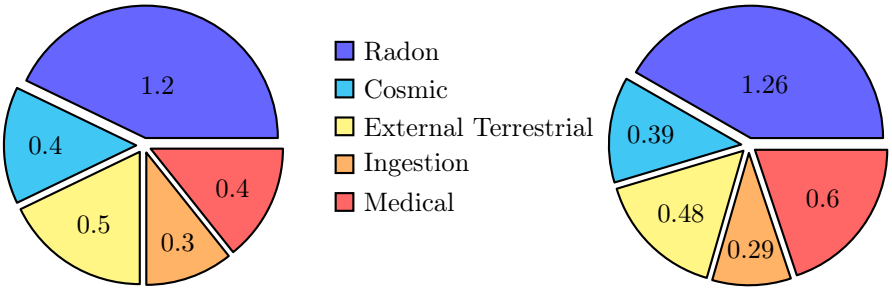

Figure 1.1: UNSCEAR estimates of worldwide average exposures (in mSv y^{-1}) of the public from 2000 and 2008 reports, respectively. According to UNSCEAR classification, "radon" in legend groups together all natural radioactive sources giving dose to individuals through inhalation (i.e. radon, thoron, other than these radionuclides from uranium and thorium series.)

Due to the relatively low outdoor radon concentration[1], most of the expo-

[1] In 1982, UNSCEAR reported the mean annual value of radon concentration in outdoor air at ground level varies between 0.1 and 10 becquerel per cubic metre, with a typical value in populated areas of 3 Bq m^{-3} (United Nations Scientific Committee on the Effects of Atomic Radiation, 1982). UNSCEAR 1993 (United Nations Scientific Committee on the Effects of Atomic Radiation, 1993) reported 10 Bq m^3 as typical outdoor ^{222}Rn and ^{220}Rn concentrations. Past and recent results of radon measurements outdoors (Iida et al., 1996; Oikawa et al., 2003) have confirmed such estimates.

sure to radon progeny occurs indoor, the latter environment being characterized by a wide variability in daughters concentration (Nero and Nazaroff, 1984). This variability arises partly from different equilibrium factors[2] (several studies dealt with equilibrium factor temporal (e.g. Tokonami et al., 2003; Iimoto, 2000; Hopke et al., 1995) and spatial (e.g. Prasad et al., 2016; Tokonami et al., 2003; Ramachandran and Ramu, 1994) variability, but is caused mainly by the difference in indoor radon concentration from one building to another.

According to World Health Organization (2010), indoor radon concentration varies with two main factors: typology of building construction and ventilation characteristics/habits. Although the indoor radon concentration is affected by ventilation rate (in the recent past, several works addressed such a correlation with a systematic approach, e.g. Chao et al., 1997), the major source of the variability in radon concentration from one building to another has been observed to be the different entry rates from its various sources.

Several authors (e.g. Nazaroff and Nero, 1988) suggest that radon can enter building interiors:

i) directly from soil due to radium-containing rocks still in the crust;

ii) via radon-carriers utilities such as water and, in principle, natural gas;

iii) indirectly from crustal materials, no longer incorporated in crust but contained into building structure in the form of concrete, brick and the like.

The relative contribution of each of these entry patterns obviously depends on specific circumstances, i.e. not listed in order of importance, building characteristics (including building materials, construction typology, floor levels, etcetera), morphology and composition of the underlying soil, ventilation features, occupancy patterns and living habits of occupants. Through the years it has become clearer and clearer that the direct ingress from soil ordinarily dominates the indoor radon concentration (Nazaroff and Nero, 1988).

UNSCEAR, in quantifying the different contributions, discusses three distinct actual models: a wooden and a masonry house modeled by Arvela (1995) and a third masonry house model described and addressed by the United Nations Scientific Committee on the Effects of Atomic Radiation (1988, 1993). For the first one ($C_{\mathrm{Rn}} = 140\,\mathrm{Bq\,m^{-3}}$, air exchange rate $0.5\,\mathrm{h^{-1}}$), characterized by an overall Rn entry rate of $70\,\mathrm{Bq\,m^{-3}\,h^{-1}}$, the main contribution to indoor radon concentration obviously arises from the underlying earth (86% advection and 6% diffusion[3]), with less significant entries due to outdoor air (4%), walls (diffusion, 3%) and water supply (1%). For the second one ($C_{\mathrm{Rn}} = 180\,\mathrm{Bq\,m^{-3}}$, air

[2] In the following, values of 0.4 (United Nations Scientific Committee on the Effects of Atomic Radiation, 2000, 1993, 1988) and 0.7 (mean value between 0.6 from (United Nations Scientific Committee on the Effects of Atomic Radiation, 2006, 2000) and 0.8 from (United Nations Scientific Committee on the Effects of Atomic Radiation, 1993, 1988)), will be assumed as "typical" for equilibrium factors in indoor and outdoor conditions respectively.

[3] Radon diffusion from the soil through the concrete slab has been frequently ignored; however, some measurements show that radon diffusion through foundation slabs can be a significant mechanism for radon entry into dwellings.

Nevertheless, the advective entry through the gap between the floor slab and the foundation walls keep on being recognised as the most important route for radon-bearing soil air.

The increased advective flow through the gaps of the floor slab also decreases the relative contribution of diffusion, even lower than that through the slab.

exchange rate $0.5\,h^{-1}$), the overall entry increases to $90\,Bq\,m^{-3}\,h^{-1}$: the contributions from soil, both advective[4] and diffusive, as well as those from outdoor air and water supply, keep almost constant in absolute terms but significantly decrease in relative ones (73% advection and 4% diffusion) due to the contemporary much more relevant role played by the radon diffusing through the building walls (18%). Results for the UNSCEAR model are finally reported in Table 1.1.

Table 1.1: Summary of relative contributions to indoor radon accumulation coming from all the sources. Results refer to a model masonry building with a volume of $250\,m^3$, a surface area of $450\,m^2$, and an air exchange rate of $1\,h^{-1}$ (United Nations Scientific Committee on the Effects of Atomic Radiation, 2000).

Sources of radon		*Contribution to radon entry*
Building Materials	Diffusion, walls and ceiling	17%
	Diffusion, floor slab	2%
Subjacent soil	Diffusion through the slab	17%
	Diffusion through gaps	7%
	Advection	36%
Outdoor air	Infiltration	17%
Water	Degassing	2%
Natural gas	Consumption	$< 1\%$
Total		100%

Some other works confirm these findings about contributions coming from the outdoor air, [2–9] $Bq\,m^{-3}\,h^{-1}$ (Gesell, 1983) and the soil beneath the building, [5–80] $Bq\,m^{-3}\,h^{-1}$ (Wilkening et al., 1972). Referring to domestic water, the corresponding entry rate strongly depends on radon concentration in it, and the same applies to building materials walls and floor slabs, whose contribution is mainly affected by composition and laying procedure.

Recent studies, further discussed hereafter, demonstrate how under some circumstances (i.e. tunnels or cavities in building structure getting in communication rooms walls with foundations and soil beneath the building), the advective contribution, often neglected when dealing with walls, can be significant too and even predominant.

1.1 Soil beneath the building

When speaking about soil as a source of indoor radon, the literature refers to the portion of radon produced (by radioactive decay of radium-226) in the earthen materials underlying the structure that moves directly through the building boundaries into the indoor atmosphere.

The key parameters in *building* the contribution of soil into indoor air concentration could be summarized as follows:

i) **Radon availability**

- The concentrations of elements in the ^{238}U and ^{232}Th series, all varying within wide ranges, represent the starting point in evaluating the

[4] In the following, as in literature, "advection" and "convection" are used equivalently with regard to radon migration. The same applies to "advective" and "convective"

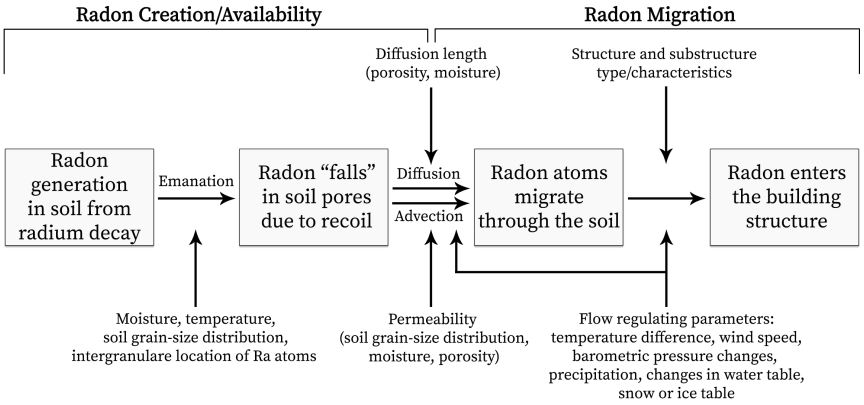

Figure 1.2: Schematic representation (modified on that from Nazaroff and Nero, 1988) of the different steps taking radon from the radioactive "creation" to the ingrowth into indoor atmosphere. The horizontal arrows reports the physical phenomena that allow radon to start its migration moving from solid matrix. Chemical and physical parameters affecting the migration phenomena are placed close to vertical arrows.

soil *strength* as ^{222}Rn and ^{220}Rn (the later discussion focuses only on 222-isotope), source. The more recent estimates (collecting data from both independent surveys and the UNSCEAR Global Survey on Exposures to Natural Radiation Sources from the United Nations Scientific Committee on the Effects of Atomic Radiation, 2008) of average concentrations in soil reports activities per unit mass of 33 Bq kg^{-1} for ^{238}U. The Joint Research Centre (JRC) has recently made available the European map of uranium concentration in soil (Joint Research Center, 2017a), created using approximately 5000 data from topsoil samples (collected at 0-20 cm depth) belonging to, other than national databases (Belgium, Czech Republic and Estony), two European databases: *i*) the Geochemical Atlas of Europe and *ii*) the Geochemical Mapping of Agricultural and Grazing Land soil in Europe.

– The radon-222 atoms so-created have a certain probability of falling into soil pores. This probability mainly depends on porosity, density, temperature, moisture and grain-size of soil as well as on the distribution and location of Ra atoms in solid matrix with respect to pore surfaces.

ii) **Radon migration**

– Radon atoms start migrating in soil by both by molecular diffusion (governed by the Fick's law) and advective transport (governed by the Darcy's law). Diffusion is mainly affected by soil porosity and moisture, whereas advection strongly depends on permeability, in turn function of soil grain-size distribution, moisture and porosity. The latter mechanism is governed by flow-regulating parameters such as temperature differences, wind speed, barometric pressure changes and water-related phenomena.

– The survived (i.e. not decayed and not migrated into outdoor air) Rn atoms now start migrating through building boundaries, i.e. diffusion through foundation slabs or advection through the existing gap near the foundation walls.

In the following, the soil parameters influencing creation and migration phenomena, as well as the physical formulations governing how and how much radon moves from soil to enter the indoor atmosphere, will be discussed in brief. Such a short review is not intended to be systematic: thanks to the strong similarity between soil and building materials behaviours, this section is aimed to make the readers aware of radon governing mechanism and properties in general.

As universally acknowledged, the contribution to indoor radon coming from the soil strongly depends on some physical parameters of the soil itself, being some of these strictly linked with "nuclear processes" and some others not.

1.1.1 Grain-size distribution, porosity and moisture content

The soil volume is generally distinguished in two main portions: *i*) the **solid** fraction, consisting mainly of mineral grains of different sizes and, in lesser percentage, of a small amount of organic matter; *ii*) the **void** fraction, which can be filled with liquid, generally water, and gas, usually having a composition strongly similar to the air one.

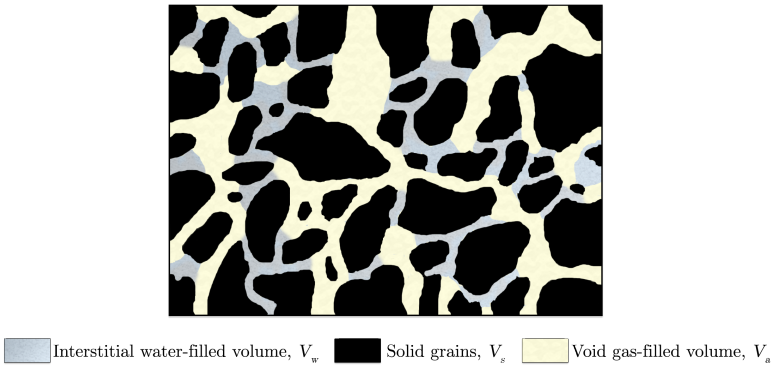

Figure 1.3: Structure of typical soil partitioning into three volumes: solid, water-filled and gas-filled.

Moving from this general concept, the **porosity** is defined as the ratio of the volume of voids to the total volume (this and the following definition are taken from Soil Science Glossary Terms Committee, 2008).

$$\epsilon = \frac{V_v}{V} \tag{1.1}$$

$$V_v = V_w + V_a \tag{1.2}$$

$$V = V_w + V_a + V_s \tag{1.3}$$

where V_v stands for the volume of the void fraction (water, V_w, and air, V_a) and V for the total volume (made of void, V_v, and solid grains, V_s).

The **moisture** content is defined as the ratio of void volume filled with water to the total volume:

$$m = \frac{V_w}{V} \tag{1.4}$$

According to the latter formulation, being $V_w \leq V_v$, the moisture content can not exceed the porosity. When $V_w = V_v$, the **degree of saturation**[5] is 100% that means the entire pore volume is filled with water.

1.1.2 Permeability

Soil **permeability** can be defined as the ease with which fluids (gases or liquids) penetrate or pass through a bulk mass of soil or a layer of soil (Sparks, 2003). The role played by permeability in the radon transport through advection will be discussed later on by introducing the Darcy's law.

The permeability is universally recognized to be a strong function of soil grain size distribution (Nazaroff, 1992) as well as the geometrical characteristics of grains and pores and the relative connections. Generally, size, shape and connectivity patterns of pores determine how easily the air (containing radon) flows through the soil. Typically, large pores and good connectivity lead to high permeability, whereas the same pores with a worse degree of connectivity would have lower permeability. Moreover, soil with grain size distribution shifted to higher diameters have generally higher permeability due to lower frictional resistance encountered.

The permeability of soil strongly depends on the degree of saturation, S (1.5) (Nazaroff, 1992). Generally, it is observed to be roughly constant for saturation of pores up to 0.4 (Rogers and Nielson, 1991). When exceeding the latter value, the air permeability start diminishing to 0 for $S = 1$.

Many other parameters, hereafter not discussed in details, influence soil air permeability: *i*) fissures, cracks, and other structural pore space; *ii*) the anisotropy of soil permeability, being far from rare (e.g. sedimentary beds deposited in layers); *iii*) the presence of biopores, i.e. penetration in the soil due to animals or plants activity.

The Joint Research Centre (JRC) of the European Commission have recently made available online, in the framework of the European Atlas of natural radiation project (Cinelli et al., 2019), a European map of soil permeability (Joint Research Center, 2017b).

1.1.3 Diffusivity

Similarly to the role played by permeability in regulating the magnitude of convective transport, the molecular diffusivity (or **diffusion coefficient**) is for sure the key parameter of the diffusion process. It can be interpreted as the tendency of a substance to migrate down its concentration gradient in a material. This tendency will be discussed in details later on when introducing and debating on the first Fick's law which relates a concentration gradient to a flux.

[5]
$$S = \frac{V_w}{V_v} = \frac{V_w}{V_a + V_w} \tag{1.5}$$
.

But for now, let us just focus on the different ways (at least four, despite in the following only the two most used are presented) the diffusion coefficient can be written and so referred to, depending on whether one uses bulk or pore volume at denominator of radon concentration, C ($\mathrm{Bq\,m^{-3}}$) and bulk or pore area at the denominator of the flux density, J^d_{Rn} ($\mathrm{Bq\,m^{-2}\,s^{-1}}$).

In general (no standardization currently exists in literature when dealing with terminology and symbols of diffusion coefficients), the **bulk** diffusion coefficient, in the following referred to as D (but frequently denoted k_e, e.g. in Culot et al., 1976), relates the interstitial concentration of the diffusing species (Rn activity concentration in void volume, V_v, of porous material, in our case) to the flux density across the geometrical cross sectional area, A. The **effective**

Figure 1.4: Reference areas used for the definition of both bulk and effective diffusion coefficient. The representation is rearranged from Culot et al. (1976).

diffusion coefficient, in the following denoted D_e (frequently mentioned as k^*_e, e.g. in Culot et al., 1976), relates the same interstitial concentration of D to the flux density across the *pore* area, A^*. By considering the equations 1.1, 1.2 and 1.3

$$D_e = D\,\frac{A}{A^*} \tag{1.6}$$

The eq. 1.6 opens the way to an assumption commonly adopted when dealing with molecular diffusion of radon in porous media: the equality between the fraction of open pore area in a unit cross-section and porosity (Eq. 1.1), ϵ, with the aim to avoid the addition of a further parameter correlating A and A^*.

$$\frac{A^*}{A} \approx \frac{V_v}{V} = \epsilon \tag{1.7}$$

$$D_e = D\,\frac{A}{A^*} = D\,\frac{V}{V_v} = \frac{D}{\epsilon} \tag{1.8}$$

Obviously, the effective diffusion coefficient is always higher than the bulk one being the porosity of a porous medium the ratio of the void volume to total volume.

Several and different methods are available to measure the radon diffusion coefficient in soil and novel techniques, both based on *theoretical* approaches

(e.g. Monte Carlo simulations, Feng et al., 2019) and on experimental protocols (Ryzhakova, 2014; Hosoda et al., 2009), are still being proposed, updated and improved. The purpose of the current publication is not to provide readers with results of recent measurements or systematic summary of findings from the present and past: it is sufficient to recall the upper bound of radon diffusion coefficient in sol given, as expected, by that of radon in open air, $D_0 = 1.2 \cdot 10^{-5}\,\mathrm{m^2\,s^{-1}}$ (Hirst and Harrison, 1939). In all porous media, such as soil, the rate of radon movement or flux through a soil may be slower than the diffusion in a homogeneous medium, such as pure air, for two main reasons: *i*) a smaller volume is available for diffusion, i.e. the porosity is much lower than unity, *ii*) the path travelled by the diffusing flow is tortuous, so longer, around particles, i.e. tortuosity factor[6] is higher than unity for porous material.

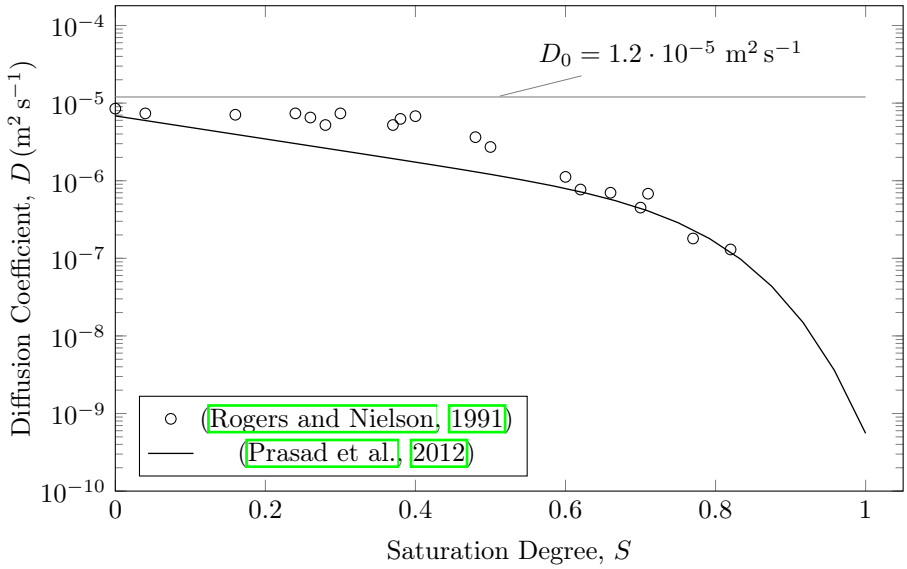

Figure 1.5: Comparison between experimentally measured values by Prasad et al. (2012) and those computed by the equation proposed by Rogers and Nielson (1991). Porosity assumed in the equation equals the one found for measured samples, $\epsilon = 57\%$.

A quite large database collecting data for diffusion coefficient in different soils is given by Nazaroff (1992) and references therein. A typical value of radon effective diffusion coefficient in low moisture content (up to 50%) soil is $10^{-6}\,\mathrm{m^2\,s^{-1}}$, the latter results confirmed by recent measurements (Prasad et al., 2012).

The most influencing parameters when evaluating radon diffusion coefficient in porous media are **porosity** and **saturation degree**. Both affect D_e by operating on the air volume available to radon for migration. In particular: *i*) with decreasing porosity, the void volume inside the medium proportionally gets lower; *ii*) with increasing saturation degree, the fraction of void volume not water-filled decreases (Figure 1.4). Rogers and Nielson (1991) proposed a well-fitting correlation that can be used to easy evaluate radon diffusion coefficient

[6] The diffusive tortuosity, τ_d, is computed as the squared ratio of the average length of a chemical's diffusive pathway, L_d, to the straight-line length, L_s (Epstein, 1989).

as a function of porosity, ϵ, and saturation degree, S:

$$D_e = D_0 \epsilon \exp(-6S\epsilon - 6S^{14\epsilon}) \tag{1.9}$$

1.1.4 Emanation coefficient

The **emanation fraction** can be interpreted as the ratio of radon produced by radioactive decay in solid grains that leaves the solid matrix to enter the void volume – both water and air-filled – of the soil.

Several experimental measurements, aiming both to be systematic or not, of the emanation coefficient have been carried out through the years. A summary of results from measurements performed until the very last years of the eighties are reported by Nazaroff and Nero (1988). Such coefficient resulted to range between 0.05 and 0.7 with a typical value being 0.2 (Nazaroff, 1992).

The radioactive decay of radium-226 [7] is the starting point in the radon emanation process.

$$^{226}_{88}\mathrm{Ra} \xrightarrow{\alpha\ decay} {}^{222}_{88}\mathrm{Rn} + {}^{4}_{2}\mathrm{He}^{++} + Q_{value} \tag{1.13}$$

$$Q_{value} = 4870.62\,\mathrm{keV} \tag{1.14}$$

$$E_{^{222}_{88}\mathrm{Rn}} = 86.21\,\mathrm{keV} \tag{1.15}$$

Moving from the energy of radon atoms produced by radioactive decay, the distance travelled by them can be computed accordingly. Such a length is obviously depending on the density and composition of the material. Tanner (1980) reported the range of ^{222}Rn ranging between 0.02 and 0.07 μm for *common materials*, and being 0.1 μm for water and 63 μm for air. In the lower value of ^{222}Rn range in water than in air should be found the explanation of the large impact of moisture content in increasing the emanation coefficient. In other words, water stops heavy nuclei better than air so enhancing the probability that a Rn atom is stopped during its recoil while passing through a water-filled void. Strong and Levins (1982), in the framework of the first systematic study addressing the influence of moisture content on emanation coefficient, reported an increase of about 370% when the moisture content was increased from 0.2 to 5.7 % (weight percentage).

Temperature has a great influence on radon emanation coefficient, although this effect is of minor importance over the common temperature range experienced by the soil in the environment. Zhang et al. (2019) reported a systematic review (Figure 1.6) of findings concerning emanation coefficient behavior vs. temperature of the soil sample.

[7] The nuclear data for radioactive decay are taken from Chisté and Bé (2007) and Martin (2013).

$$m_{0,^{226}_{88}\mathrm{Ra}} = 226.025406\,u \tag{1.10}$$

$$m_{0,^{222}_{86}\mathrm{Rn}} = 222.017574\,u \tag{1.11}$$

$$m_{0,^{4}_{2}\mathrm{He}} = 4.002603\,u \tag{1.12}$$

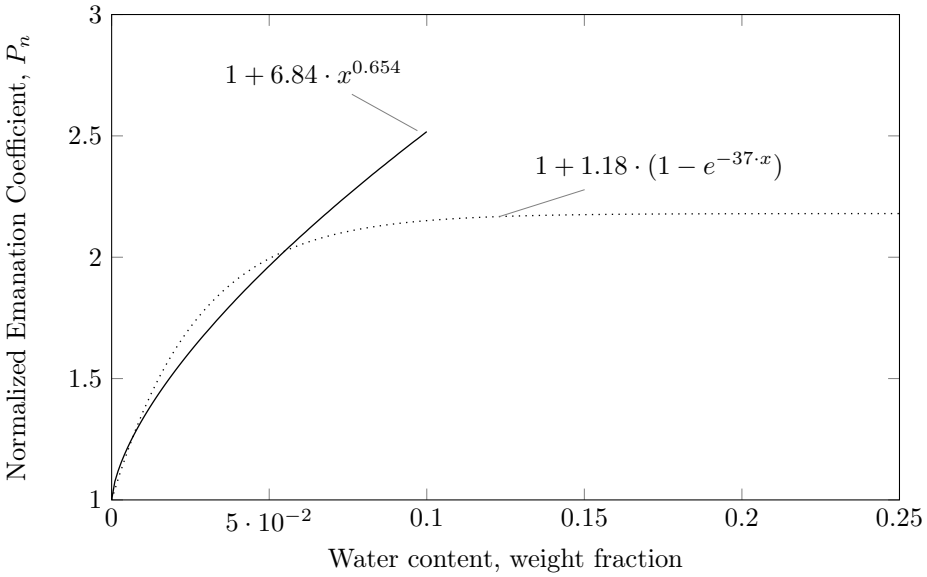

Figure 1.6: Relative emanation coefficient as a function of the water content of soil. Values are normalized to the emanation power with no water. The fitting functions are determined by Bossew (2003) for soil samples. For small water contents (<10%) a different function (plain line) describes the dependency better than the one (dotted line) for the whole range of humidity (0–30%).

The size and shape of particles obviously affect the amount of radium that is close enough to the grain surface to allow the radon escape towards pores. If radium atoms were uniformly distributed throughout a grain, the emanation coefficient would approach an inverse proportion to the particle diameter when the latter exceeds 0.1 μm (Ishimori et al., 2013; Ziegler and Biersack, 1985). On the contrary, if radium atoms were mainly distributed on the grain surface, the emanation coefficient would be constant regardless of the particle diameter.

Two other factors significantly affecting the emanated Rn fraction are the presence of pores and their specific areas. Increasing the first or the second (or both) would result in the emanation coefficient getting greater: an almost perfect linear relationship has been found by Jobbágy et al. (2009).

1.2 Building materials

Contribution from building materials to indoor radon concentration has been already discussed in section 1.1. Referring to the masonry house model introduced and employed in evaluating different contributions to radon entry by the United Nations Scientific Committee on the Effects of Atomic Radiation (2000), diffusion from walls and ceiling has been reported to contribute for the 17% to the overall radon entry into indoor environment. The advective radon entry is not even mentioned and considered by the discussed room model. However, under some circumstances, for example in the presence of tunnels or cavities in building structures getting in communication rooms walls with foundations and soil beneath the building, this contribution can become significant too and even

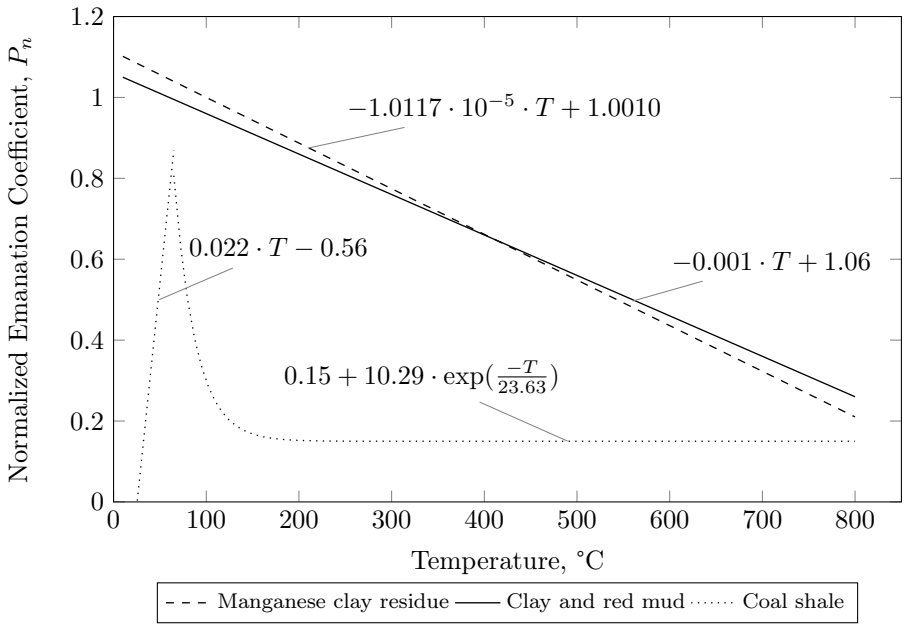

Figure 1.7: Comparison of emanation coefficient behaviour for three different types of soil. The fitting functions have been collected by Zhang et al. (2019). The normalization is different for the three functions: the first is normalized to the value at 100 °C (≈ 25%), the second to 200 °C(≈ 18% for clay and ≈ 7% for red mud) or 400 °C (26% for red mud) depending on the specific soil type, and the third to 65 °C (≈ 30%). The different shapes are due to the temperature gradient that gets established inside the sample: relatively large for manganese clay and lower for coal shale.

predominant (Carpentieri et al., 2019).

Generally, both diffusive and convective transport from and through the building materials could gain importance when dealing with sources of radon indoor at floor levels other than the ground floor. This scenario is far from uncommon especially in large buildings with a significant vertical development.

Analogously to what previously introduced for the soil (Figure 1.2), the starting point in assessing the diffusive contribution to indoor radon concentration is the evaluation of the building material source strength, i.e. the radon availability, in terms of concentration of radon precursor, ^{226}Ra[8].

A database of activity concentration measurements of natural radionuclides (definitely including ^{226}Ra) in European building materials has been realized in 2017 by Nuccetelli et al. (2018) by collecting data of about 23000 samples of **bulk materials** from 26 of 28 European Member States and 4 non EU Countries (Turkey, Macedonia, Switzerland and Norway) [9]:

[8]Data are sometimes expressed directly in terms of ^{238}U concentration. Considering the half-lives of ^{226}Ra (i.e. 1600 y) and ^{238}U (i.e. $4.68 \cdot 10^9$ y), under undisturbed physical condition and on the geological scale, a secular equilibrium is well established between these two elements. **Considering so, in the following ^{238}U and ^{226}Ra activity concentrations will be treated as equivalent to each other.**

[9]Please note that for each of the following categories, the number of Member States data are available from significantly vary. For tuff, as example, only Germany and Italy *contribute* to the database. Pozzolana is the only material considered for which all data (29) come from

i) brick: national averages of ^{226}Ra specific activity range from 7 Bq kg^{-1} to 84 Bq kg^{-1} with a mean value of 51 Bq kg^{-1} ($CV = 41\%$) (these values and the following ones for all the other categories are taken from Trevisi et al., 2018);

ii) concrete: national averages of ^{226}Ra specific activity range from 14 Bq kg^{-1} to 272 Bq kg^{-1} with a mean value of 59 Bq kg^{-1} ($CV = 103\%$);

iii) cement: national averages of ^{226}Ra specific activity range from 25 Bq kg^{-1} to 87 Bq kg^{-1} with a mean value of 50 Bq kg^{-1} ($CV = 36\%$);

iv) aggregates: national averages of ^{226}Ra specific activity range from 4 Bq kg^{-1} to 69 Bq kg^{-1} with a mean value of 23 Bq kg^{-1} ($CV = 76\%$);

v) tiles;

vi) natural raw materials distinguished in:

- clay: 56 (18–94)[10] Bq kg^{-1};
- chalk (i.e. $CaCO_3$): (9–23) Bq kg^{-1}[11];
- gypsum (i.e. $CaSO_4 \cdot 2\,H_2O$): 18 (4–60) Bq kg^{-1};
- lime (i.e. CaO): 19 (11–30) Bq kg^{-1};
- limestone (i.e. $CaCO_3$): 14 (5–31) Bq kg^{-1};
- bulk stone: 39 (11–90) Bq kg^{-1};
- tuff: samples from Germany have a mean specific activity of 74 (47–100) Bq kg^{-1}, whereas the Italian ones reach 157 (12–316) Bq kg^{-1}.

vii) natural stones used as superficial material: national averages of ^{226}Ra specific activity range from 4 Bq kg^{-1} to 202 Bq kg^{-1} with a mean value of 63 Bq kg^{-1} ($CV = 76\%$);

viii) *ashes (fly and bottom)*: national averages [in brackets values for bottom ashes] of ^{226}Ra specific activity range from 75 [68] Bq kg^{-1} to 815 [1391] Bq kg^{-1} with a mean value of 91 [345] Bq kg^{-1} ($CV = 90\%$ [125%]);

ix) *bauxite residues/red mud*: national averages of ^{226}Ra specific activity range from 97 Bq kg^{-1} to 301 Bq kg^{-1} with a mean value of 205 Bq kg^{-1} ($CV = 38\%$);

x) *by-product gypsum*: national averages of ^{226}Ra specific activity range from 22 Bq kg^{-1} to 668 Bq kg^{-1} with a mean value of 318 Bq kg^{-1} ($CV = 62\%$);

xi) *metallurgical slag*: national averages of ^{226}Ra specific activity range from 15 Bq kg^{-1} to 336 Bq kg^{-1} with a mean value of 139 Bq kg^{-1} ($CV = 57\%$).

The last four items, written in italic, are generally referred to as generally NORM (Naturally Occurring Radioactive Material). These materials are all residues from different industries that since the late eighties have been used in order to move towards an economy based on re-use and recycling (Leonardi et al., 2018).

the same Country (Italy).

[10] Mean of national averages (min–max).

[11] The mean is not reported because data have been collected from only three Countries.

1.2.1 Emanation coefficient

Many of parameters introduced when dealing with migration of radon through the soil can be transferred to the discussion of radon being generated and transported through building materials. As previously seen, the emanation fraction can be interpreted as the ratio of radon produced by radioactive decay in solid grains that leaves the solid matrix to enter the void volume – both water- and air-filled – of the soil.

Table 1.2: Emanation coefficient of ^{222}Rn in building materials: comparison between values from Nazaroff and Nero (1988) and those from the database built by Nuccetelli et al. (2018). In italic NOR materials. Even if the values from Nuccetelli et al. (2018) have been recently updated by extendind the dataset to 13 EU and 4 non EU countries (Nuccetelli et al., 2020), such updates are not considered because the results are grouped for categories of building materials.

Building Materials	Emanation Coefficient		
	(Nazaroff and Nero, 1988)	(Nuccetelli et al., 2018)	
	Range	AM	Range
Concrete	0.1–0.4	0.24	0.01–0.85
Brick	0.02–0.1	0.12	0.002–0.67
Gypsum	0.03–0.2	0.13	0.03–0.24
Cement	0.02–0.05	0.12	0.007–0.56
Fly Ash	0.002–0.02	0.01	0.005–0.02
Coal Ash	–	0.005	0.004–0.009
Gypsum[a]	–	0.13	0.03–0.21

[a] Gypsum provided as industrial by-product.

As regards bricks, if Nazaroff and Nero (1988) – the authors collect values from literature of seventies and eighties – report emanation coefficients ranging from 2 to 10%, more recent findings – collecting data from 13 EU Member States and 4 non EU Countries – report a range of 0.2–67% with an arithmetic mean of 12% (Nuccetelli et al., 2018).

Concerning concrete, the emanation coefficient range by Nazaroff and Nero (1988) is 10–40%, whereas it becomes larger, i.e. 1–85% with a mean value of 24%, for Nuccetelli et al. (2018).

Besides bricks and concrete, Table 1.2 collects emanation fractions for the most used building materials including industrial by-products. Data are split in two in order to make it easier to compare findings of the past (results of measurements performed until the late eighties) to the most recent ones (results of measurements, available on literature, until 2018). Being the tendency of moving towards re-use and recycling mainly modern, by-products like coal ash and gypsum have not been included in the collection of data by Nazaroff and Nero (1988).

An interesting discussion is offered by the comparison between gypsum conceived as raw material and gypsum resulting from industrial processes (mainly from the production of phosphoric acid from the phosphoric mineral, the so-called fosforite). Looking at Table 1.2, no difference emerges between the emanation fractions of the raw material and the by-product material: this means that, $CaSO_4H_2O$ usually referred to as *phosphogypsum* to better get distin-

guished from the raw gypsum, although enriched in ^{226}Ra[12], does not significantly differs regarding the percentage of radon atoms being produced by decay in solid matrix that pass to the void volume.

As previously introduced when dealing with the emanation coefficient of soil, the emanated fraction strongly depends on radium distribution and grain size (and shape). Regarding building materials, the uniform distribution within grains is often a characteristic of primary minerals (Garver and Baskaran, 2004), including some process residues such as fly ash (Kalkwarf et al., 1985). This kind of distribution leads to a radon emanation coefficient being inversely proportional to grain size (when diameter exceeds 0.1 μm). On the contrary, a uniform distribution over the surface is a characteristic of secondary minerals such as sedimentary deposits and residues such as sand filters (Sakoda et al., 2010a,b). In this second case, the emanation coefficient keeps almost constant not depending on the grain size.

Moisture content is well known to have a huge effect on the emanation coefficient of building materials analogously to what previously observed for soil. This is caused by the drop experienced by typical recoil ranges when radon atoms loss energy in water. Some works specificly addressed the emanation coefficient for building materials, including industry by-products (e.g. Barton and Ziemer, 1986). The results were about the same previously seen for soil: the emanated fraction increases as a function of moisture content up to a certain value ranging around 10% (weight percentage) of water content.

1.2.1.1 How to measure emanation coefficient

Several methods are available to measure the emanation coefficient. They could be grouped in two: *i*) test methods involving separate measurements of radium content in solid matrix and radon released in an accumulation volume, *ii*) gamma spectrometry under some specific conditions.

In the former, the sample material is enclosed in a cylindrical container where it is held for more than 4 weeks (necessary to establish the radioactive equilibrium between ^{222}Rn and ^{226}Ra). Then, the radon activity released into the air from the sample material is measured. The circulation *circuit* can be either closed or open: in the first case (Figure 1.8 (*a*)), air circulates in a closed loop which comprehends the vessel, the pump and the radon detector, in the second one (Figure 1.8 (*b*)), the air is taken from the outside and it flows through the vessel, the pump and the radon detector before being released outwards.

Radon concentration is measured by the detector placed inside the measuring apparatus. The total activity of radium in the sample material can be measured by various methods such as alpha spectrometry, gamma spectrometry and liquid scintillation spectrometry.

The emanation coefficient is obtained by the following formulas (Ishimori et al., 2013): Eq. 1.16 for the loop configuration, Eq. 1.17 for the flow-through configuration.

[12] The by-product gypsum enrichment in ^{226}Ra results from the acid attack by H_2SO_4 leading to the production of phosphoric acid. During such a phase, almost 90% of ^{226}Ra contained in the starting mineral (fosforite) has been observed to move to the solid phase, i.e. the resulting phosphogypsum (Agenzia Nazionale per la Protezione dell'Ambiente (ANPA), 2000).

$$P = \frac{C_{\mathrm{Rn}}\, V}{C_{\mathrm{Ra}}\, m} \tag{1.16}$$

$$P = \frac{C_{\mathrm{Rn}}\, (\Gamma + \lambda\, V)}{C_{\mathrm{Ra}}\, m\, \lambda} \tag{1.17}$$

where:

C_{Rn} is the radon-222 activity concentration ($\mathrm{Bq\,m^{-3}}$)
C_{Ra} is the radium-226 specific activity ($\mathrm{Bq\,kg^{-1}}$)
Γ is the air flow rate ($\mathrm{m^3\,s^{-1}}$)
λ is the radon-222 decay constant ($\mathrm{s^{-1}}$)
V is the net volume of the system, i.e. vessel, tubes and detector sensitive volume ($\mathrm{m^3}$)
m is the mass of the sample (kg)

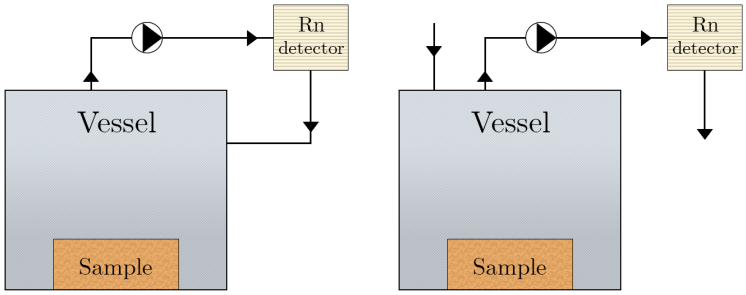

(a) *Loop configuration* (b) *Flow-through configuration*

Figure 1.8: Schematic diagram of the two test methods for emanation coefficient measurement.

A further non-destructive method is based only on gamma spectrometry. The procedure starts by removing radon from sample pores and from grain surfaces: the sample is left in direct contact with the outdoor air for several hours. Than, a first measurements is performed: the sample is placed in a closed radon proof container and gamma spectrometry is performed with the aim to determine counts, N_0, of ^{214}Pb (294 keV and 352 keV) and ^{214}Bi (609 keV 1120 keV). If radon is assumed to be in equilibrium with all its progeny the N_0 counts are attributable to the radon atoms contained in the solid matrix. After this first measurement, the spectral analysis is repeated several times: if the ^{214}Pb or ^{214}Bi counts seem to reach equilibrium within a month, the measurement result should be corrected to take into account the leakage from the vessel. The counts registered (and corrected for leakage) in equilibrium condition, N_{eq}, can be assumed as representative of the radon (in equilibrium with its progeny) both in pores and in solid matrix. This amount of radon, being comprehensive of atoms both in solid grains and in voids, can be considered in equilibrium with the radium content of the sample. Thus, $N_{eq} - N_0$ are counts attributable to radon in pores. The emanation coefficient can be so obtained as:

$$P = \frac{N_{eq} - N_0}{N_{eq}} \tag{1.18}$$

1.2.1.2 How to estimate radon emanation coefficient

Due to the complexity lying in methods to measure radon emanation coefficient in building materials, through the years some empirical correlation have been proposed to try to give a first, and maybe rough, estimation of this coefficient, given a certain value measured in some specific condition.

In order to evaluate the emanation coefficient at different saturation degrees, Zhuo et al. (2006) proposed the following empirical equation relating the radon emanation to S, being the latter a well known influencing factor for the emanation fraction.

$$P(S) = P_0 \left[1 + 1.85(1 - e^{-18.8\,S})\right] \tag{1.19}$$

where:

$P(S)$ is the emanation fraction, function of the saturation degree of the building materials
P_0 is the emanation coefficient of the building material in dry condition
S is the saturation degree of the building material.

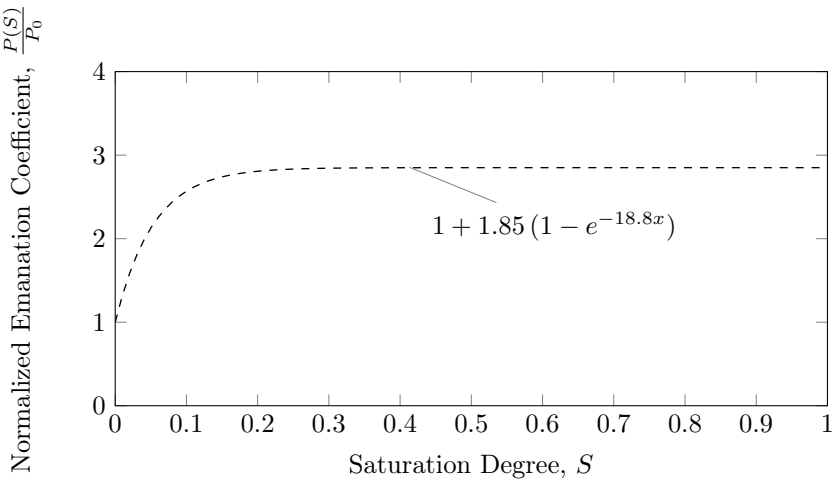

Figure 1.9: Plot of the empirical equation proposed by Zhuo et al. (2006) to estimate radon emanation coefficient in porous media once known the value for dry sample.

1.2.2 Diffusion Length

When dealing with migration of radon through building materials, the capability of a certain medium to allow molecular diffusion through itself is generally expressed in terms of diffusion length, defined as:

$$R = \sqrt{\frac{D_e}{\lambda}} \tag{1.20}$$

Table 1.3: Diffusion length of ^{222}Rn in building materials: comparison between values from Nazaroff and Nero (1988) and those from the most recent studies concerning a wide set of samples for each materials (Keller et al., 2001; Narula et al., 2010). Between brackets the number of samples considered by Keller et al. (2001). Narula et al. (2010) consider 2 samples for each material.

Building Materials	Diffusion Length (10^{-3} m)				
	Nazaroff and Nero		Keller et al.		Narula et al.
	Range	AM	n°	Range	AM
Gypsum	800–1300	1060	(12)	790–1280	1110
Heavy Concrete	–[a]	60	(8)	20–70	–
Aerated Concrete	–[a]	790	(5)	690–980	–
Brick	200–400	410	(8)	220–490	–
Sandstone	–	1020	(3)	930–1110	1090
Limestone	–	400	(5)	310–490	–
Pumice	–	840	(8)	650–1050	–
Granite	–	–		–	170
Cement	–	–		–	760
Wall Putty	–	–		–	69
Fly Ahs	–	–		–	980

[a] Nazaroff and Nero (1988) simply refer to "concrete", $R \in [0.06 - 0.2]$ m.

1.2.2.1 How to measure radon diffusion length

Folkerts et al. (1984) developed a measuring method for the experimental determination of the radon diffusion length in porous media. The sample of building material is fixed with a Rn-tight material (e.g. silicon rubber) to a hemispherically shaped container, denominated by the inventors as “reservoir volume”. Radon is pumped inside this volume from a dry ^{226}Rn source. In order to make negligible the radon production rate from the sample, the concentration established by the source in equilibrium condition should be high enough. The opposite face of the building material sample is fixed to a second hemispherically shaped accumulation container whose volume is referred to as “receiving volume”. Both the volumes are connected to two Rn detectors operating in diffusion mode.

Some time should elapse from the beginning of radon circulation through the source for a steady state condition to be established inside the experimental apparatus. Once reached such a condition, the radon concentration keeps constant in both volumes and, as a consequence, the concentration gradient through the slab. Due to the negligibility of radon production from the sample, the following equation can be assumed as representative of diffusive flow in steady state:

$$D_e \frac{d^2C(x)}{dx^2} - \lambda C(x) = 0 \tag{1.21}$$

where:

D_e is the effective diffusion coefficient ($\mathrm{m^2\,s}$)
$C(x)$ is the radon concentration at x ($\mathrm{Bq\,m^{-3}}$)
λ is the radon decay constant ($\mathrm{s^{-1}}$).

The concentration at $x = 0$ is assumed to be $C(0) = C_{res}$, whereas on the other side of the slab ($x = d$, where d is the thickness of sample) $C(d) = C_c$.

The solution of Eq. 1.21, graphically reported by Figure 1.14, is:

$$C(x) = \frac{1}{2\ \sinh(\frac{d}{R})}[(C_c - C_{res}e^{-\frac{d}{R}})e^{\frac{x}{R}} + (C_{res}e^{\frac{d}{R}} - C_c)e^{-\frac{x}{R}}] \tag{1.22}$$

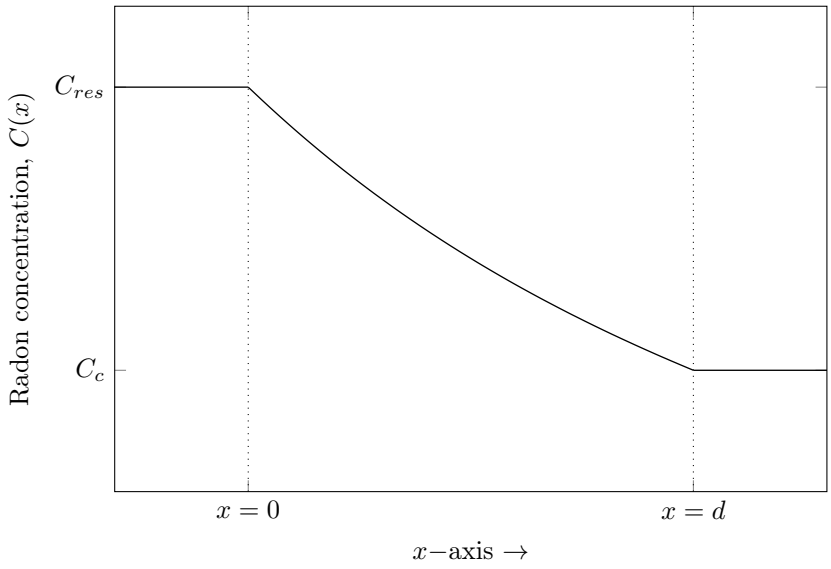

Figure 1.10: Distribution of radon concentration along $x-$axis in steady state condition during the experimental measurements of diffusion length.

Now, the flux rate, φ, can be easily determined through an activity balance in the receiving volume in steady state condition.

$$\varphi\frac{A}{V_c} = \lambda C_c \tag{1.23}$$

where:

A is the interface active surface of the sample (m^2)
V_c is the active volume of the receiving hemisphere (m^3).

By substituting Eq. 1.22 in the first Fick's law, $\varphi = D_e\epsilon\ \frac{dC(x)}{dx}$, the following transcendental equation is obtained:

$$R = \sqrt{\frac{D_e}{\lambda}} = \frac{\varphi\ \sinh(\frac{d}{R})}{\epsilon\lambda\{C_{res} - C_c\ \cosh(\frac{d}{R})\}} \tag{1.24}$$

The diffusion length, R, is so obtained by means of an iteration procedure.

1.2.3 Porosity

The similarity among soil and building materials in the approaches used to deal with generation and transport of radon applies to porosity too. As well as for emanation coefficient and diffusion length, porosity is strongly influenced by several material specifics, e.g. when dealing with concrete, water-cement ratio,

curing age, aggregate type, aggregate proportion in mixture. Unlike the resulting porosity is strictly connected to all the influencing factors, it is still considered useful to report a brief summary of typical values for the most common materials used in constructions (Table 1.4). Such a strong correlation between porosity and material characteristics is the reason why the following table only reports wide ranges and no specific ϵ values.

Table 1.4: Expectable porosity of some building materials: summary of recent literature findings.

Building Materials	Porosity, ϵ	References
Concrete[a]	up to 0.3	(Li et al., 2019)
Brick[c]	0.3–0.4	(Hall and Hamilton, 2015)
Limestone[b]	up to 0.3	(Hall and Hamilton, 2015)
Sandstone[b]	0.1–0.2	(Hall and Hamilton, 2015)
Tuff	up to 0.4[d]	(Wedekind et al., 2013)
Pumice	0.7	(Raviv et al., 1999)

[a] details on aggregates, binder and relative proportions in the reference.
[b] bulk density ranging from 1800 to 2700 $\mathrm{kg\,m^{-3}}$.
[c] data are for fired clay brick.
[d] Raviv et al. (1999) reports 0.6 for yellow tuff.

1.2.4 Permeability

As seen before when dealing with the overall contribution of masonry structures other than floor and ceiling, the building materials source term could become predominant as a consequence of convective transport through vertical boundaries, i.e. walls. This happens, for example, when walls are crossed by tunnels, cavities or structures getting them in direct connection with underground locals or the soil itself. Thus, being the advective transport worth of major concern, the permeability, which regulates the pressure driven migration, could rise to key role in regulating the transport of radon through building materials.

Permeability data are available only for concrete, whose relative proportion among components (i.e. water, cement, aggregates) strongly influences the resulting value. Renken and Rosenberg (1995) discussed measurements for three concrete mix: *i*) a typical concrete for basement slab ($\epsilon = 0.12$), *ii*) a concrete obtained by substituting in the first mix one forth of the Portland cement with fly ash ($\epsilon = 0.20$) and *iii*) a last mix with an increases water to cement ratio ($\epsilon = 0.17$). The authors obtained k values of $1.35 \cdot 10^{-16}$ $\mathrm{m^2}$[13], $4.97 \cdot 10^{-16}$ $\mathrm{m^2}$ and $3.00 \cdot 10^{-16}$ $\mathrm{m^2}$ for the three mixed considered.

Rogers and Nielson (1992) performed measurements, obtaining similar results, with concrete samples of porosity ranging from 0.17 to 0.26.

The permeability is significantly affected by pressure difference. The most recent study addressing such an issue is by Chauhan and Kumar (2015) whose results are graphically reported in Figure 1.7.

[13] The must used unit of permeability is the Darcy (D). A medium with a permeability of 1 darcy permits a flow of $1\,\mathrm{cm^3\,s^{-1}}$ of a fluid with viscosity 1 mPa s under a pressure gradient of $1\,\mathrm{atm\,cm^{-1}}$ acting across an area of $1\,\mathrm{cm^2}$. Converted to SI units, 1 darcy is equivalent to $0.986\,923\,3\,\mu\mathrm{m^2}$. This conversion is usually approximated as $1\,\mu\mathrm{m^2}$ (Society of Petroleum Engineers, 1984).

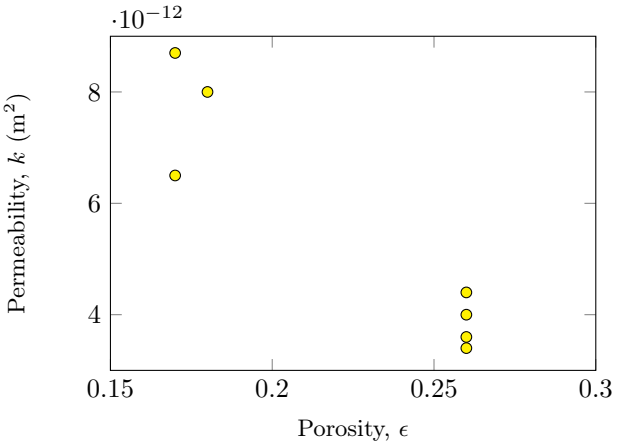

Figure 1.11: Experimental results from Rogers and Nielson (1992) for permeability to radon of concrete samples.

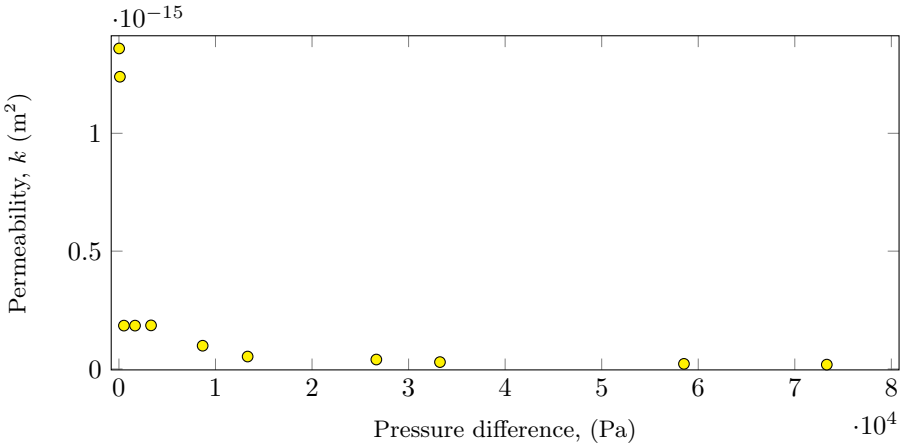

Figure 1.12: Variation of radon permeability with pressure differential.

1.3 Radon in water

Exposure to radon dissolved in drinking waters can derive directly from ingestion of water [14] and indirectly from the inhalation of air containing radon degassed from water.

Water can be radon-enriched in two different ways:

- **Emanation** of radon **into water-filled porous**, or interstitial spaces, of rocks matrices;

[14] Radon contained in drinking water can be ingested giving so dose to the lining of the stomach (World Health Organization, 2017). A definitive correlation between consumption of drinking-water containing radon and an increase of risk of stomach cancer (World Health Organization, 2010) has not been stated yet. Studies carried out until now do not indicate a major effect of ingested natural radon on stomach cancer risk increase (Auvinen et al., 2005; Ye et al., 1998).

- Radioactive decay taking place directly in water considering **uranium and radium** are both soluble **in water**.

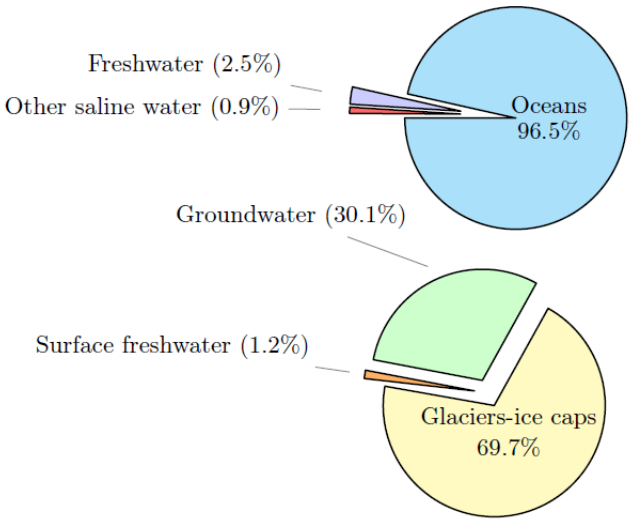

Figure 1.13: Distribution of water on the planet and, focusing on freshwater, the relative distribution of resources among **groundwater**, **surface water** and glaciers/ice caps. (Gleick et al., 1993). Please note that the water contained in the oceans is not considered surface water.

Drinking water sources can be roughly classified in **groundwater** and **surface water**. Groundwater is defined as "water that is found beneath the surface of the Earth in conditions of 100 percent saturation". If the saturation degree is less than 100%, then water is considered soil moisture.

Surface waters can be described as the water that is on the surface of the Earth. This includes different sources, some of them, like the oceans, not giving contribution to the global amount of freshwater. Considering the overall freshwater amount available on the planet, ground ice and permafrost (not available for being directly used for human consumption, irrigation and industrial processes) contribute for the 69.0%, lakes for the 20.9%, rivers for the 0.49% and swamps, water in the atmosphere, soil moisture and others for the remaining part.

Water supply to consumers could be mainly achieved through **private wells**, pumping groundwater from an aquifer to the house, or **water distribution networks**, whose sources could be either surface water or groundwater. In case of water distribution system, a significant percentage of water coming from the source undergoes a purification treatment (in Italy such a percentage is estimated by ISTAT (2017) to reach 33%).

Focusing on water for human consumption (i.e. drinking water), in Europe, groundwater has always played a major part in water supplies (UNESCO et al., 1992) and this is clearly shown by data reported in Table 1.5. In America, just before 40% of public water is supplied from groundwater. In Africa and Asia, the majority of largest cities use mainly surface water, but several millions of people living in the rural areas depend on groundwater. The supply scenario

Table 1.5: The proportion of groundwater in drinking water supplies in some European countries in 1988 (UNEP et al., 1989).

Country	
Denmark	98%
Portugal	94%
Germany	89%
Italy	88%
Switzerland	75%
Belgium	67%
Netherlands	67%
Luxembourg	66%
Sweden	49%
United Kingdom	35%
Spain	20%
Norway	15%

significantly changes in Saharan Africa where, untreated groundwater supplied from protected wells represents the main source for population water supply.

Concerning Italy, most updated data have been provided by the Census of Waters for Civil Usage carried out by the Italian National Institute of Statistics in 2017 (Figure 1.14).

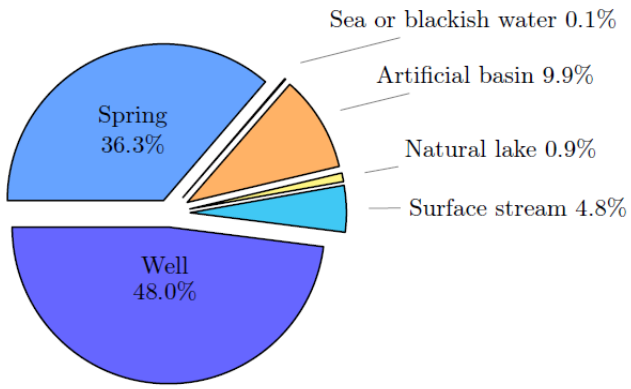

Figure 1.14: Distribution of water intended for human consumption in Italy among the corresponding supply sources (ISTAT, 2017).

The 84.3% of the Italian water yearly withdrawn for human consumption comes from groundwater, in particular 48.0% and 36.3% from wells and springs respectively. The remaining part is surface water taken from both natural and artificial basins or from surface streams.

Groundwater from springs and wells, due to the relatively short time elapsing between water extraction and its use, is more likely to experience an increased radon concentration. Levels of radon in surface waters are *typically* low due to the natural degassing into the outdoor air taking please during natural flow of streams or the resting of basins. However, the concentration of radon in water

may range over several orders of magnitude, generally being the highest in well water, intermediate in spring water and the lowest in all surface water.

Table 1.6: Typical values and upper boundaries for radon concentration in the three main supply sources: well, spring and surface waters (United Nations Scientific Committee on the Effects of Atomic Radiation, 1993).

Type of supply	Radon Concentration ($\mathrm{Bq\,L^{-1}}$)	
	Typical	Up to
Well water	100	80000
Spring water	10	4000
Surface water	1	10

Due to the relatively low solubility of radon in water, better addressed in the following sections, about 90% of the dose attributable to radon in drinking waters comes from inhalation rather than ingestion (United Nations Scientific Committee on the Effects of Atomic Radiation, 1993). For such a reason, domestic water will be considered in the following only as a source of indoor airborne radon without considering the radioactive intake coming from ingestion. This approach is strongly supported, and maybe overstated, by WHO. In particular the World Health Organization believes that, being the dose from radon present in drinking-water normally received from inhalation rather than ingestion, it is more appropriate to measure the radon concentration in air than in drinking-water.

1.3.1 Single-cell model

The following differential equation could be use to model the indoor radon concentration, C_i, resulting from a certain radon in water concentration, C_a.

$$\frac{dC_i}{dt} = S + C_0\,\lambda_v^* - C_i\,\lambda_v^* + \frac{C_w\,W^*\,e^*}{V} \tag{1.25}$$

where:

C_0 is the outdoor radon concentration ($\mathrm{Bq\,m^{-3}}$)
S is the entry rate per unit volume for all other sources ($\mathrm{Bq\,m^{-3}\,s^{-1}}$)
λ_v^* is the instantaneous air exchange rate ($\mathrm{s^{-1}}$)
C_w is the concentration of radon in water ($\mathrm{Bq\,m^{-3}}$)
W^* is the instantaneous water-use rate ($\mathrm{m^3\,s^{-1}}$)
V is the volume of the cell, i.e. dwelling ($\mathrm{m^3}$)
e^* is the instantaneous transfer efficiency, weighted for the different usages, from water to air.

Now, if Eq. 1.25 is integrated over a period long enough to suppress the periodic and aperiodic components leading to variation of indoor radon concentration:

$$\frac{1}{T}\int_0^T dC_i = 0 \tag{1.26}$$

$$\frac{1}{T}\int_0^T C_i\,\lambda_v^*\,dt = \frac{1}{T}\int_0^T (C_0\,\lambda_v^* + S)\,dt + \frac{1}{T}\int_0^T \frac{C_w\,W^*\,e^*}{V}\,dt \tag{1.27}$$

If $C_i = C + C_a^*$, where C is the indoor concentration without the radon in water contribution and C_a^* the instantaneous increase due to water, Eq. 1.27 can be split in two, referring to water absence and presence respectively.

$$\frac{1}{T}\int_0^T C\,\lambda_v^*\,dt = \frac{1}{T}\int_0^T (C_0\,\lambda_v^* + S)\,dt \tag{1.28}$$

$$\frac{1}{T}\int_0^T C_a^*\,\lambda_v^*\,dt = \frac{1}{T}\int_0^T \frac{C_w\,W^*\,e^*}{V}\,dt \tag{1.29}$$

Let introduce a mean air exchange rate, λ_v, weighted with the instantaneous increase in air concentration due to water:

$$\lambda_v = \frac{\int_0^T C_a^*\,\lambda_v^*\,dt}{\int_0^T C_a^*\,dt} \tag{1.30}$$

By including λ_v in Equation 1.24:

$$\frac{1}{T}\int_0^T C_a^*\,dt = \frac{1}{\lambda_v\,T}\int_o^T \frac{C_w\,W^*\,e^*}{V}\,dt \tag{1.31}$$

The following time-average values are defined too:

$$C_a = \frac{1}{T}\int_0^T C_a^*\,dt \tag{1.32}$$

$$W = \frac{1}{T}\int_0^T W^*\,dt \tag{1.33}$$

$$e = \frac{\int_o^T W^*\,e^*\,dt}{\int_o^T W^*} \tag{1.34}$$

$$V = const. \tag{1.35}$$

$$C_w = const. \tag{1.36}$$

In Eq. 1.34, the use-weighted transfer efficiency is further weighted with respect to the use rate. This can be explained by considering, for example, an integration time that can be split into two subsequent period: the first one characterized by activities with significant water usage in terms of m^3 and high transfer efficiency (use-weighted), and the second one during which the consumption is very low as well as the transfer efficiency of radon into the indoor atmosphere. In similar scenario, if e was averaged simply over time, this would result in an underestimation being the higher efficiency associated to higher water-use rate.

The following equation is obtained:

$$C_a = \frac{C_w\,W\,e}{\lambda_v\,V} \tag{1.37}$$

In order to remove the complication introduced by the need of weighting the air exchange rate with the instantaneous variation of indoor radon concentration due to transfer from water, generally λ_v is assumed simply constant over the integration period considered.

All the previous boundary conditions fixed, Eq. 1.37 can be easily used to estimate the increase in radon indoor concentration due to potable water over a long-term period.

1.3.2 Water-use rates

The results from several national and international papers and reports are summarised in Table 1.7. In particular, for each reference analysed and then considered, the per capita domestic water-use rate is listed together with the distribution among the different in-house activities.

A similar critical review had been done by Nazaroff and Nero (1988) by collecting all data available up to 1988 but referring to American studies only. In that case, data resulted to be very well fitted by a lognormal distribution with a geometric mean of 189 $\mathrm{L\,person^{-1}\,d^{-1}}$ and a geometric standard deviation of 1.57 $\mathrm{L\,person^{-1}\,d^{-1}}$.

Table 1.7 focuses the summary on data from the European Countries. The first two rows, reporting data about the United States of America, refer to the "Residential End Uses of Water" Report whose most recent versions have been published in 1999 (Mayer et al., 1999) and 2016 (DeOreo et al., 2016). These reference have to be used as a useful comparison term for the subsequent rows listing water-use rates for European Member States.

Water-use rates are distinguished into eight categories: dishwashing, shower, bath, toilet, laundry, faucet and all the others grouped together. This way of dividing the in-house usages of domestic water are taken directly as they are from the "Residential End Uses of Water" Report. Bendito et al. (2009) refer to the same criteria of classification. Data from Danske Vandværkers Forening and Danmarks Statistik (1997); Statistiska Centralbyrån (2000); Environment Agency/Ofwat (2000); Statistics Norway (1981); Finnish Environment Institute (1999); RIVM (1999) make reference to a different way of grouping domestic water usage. *Shower* and *bath* are not directly mentioned in favour of the expression *personal hygiene* (in Table 1.7 fully attributed to *shower*). This choice is justified by conservative reasons and it will be fully understood in the next section. Furthermore, for these Countries the category *drinking and cooking* appears and the corresponding consumption has been attributed to *faucet* column. As regards the United Kingdom, similar considerations as before applies to *drinking* category that falls into *faucet* column. The leakages, referred to as *other* are excluded because they are not of interest for the purposes here addressed. Referring to Germany (Schleich and Hillenbrand, 2007), *personal hygiene*, *cooking* and *drinking* categories have been all attributed to *faucet* column whereas *bath* and *shower* contributions, similarly to what done for other EU Member States, have entirely gone to *shower*. The same criteria applies to both France (Costa et al.) (*personal hygiene* is not listed) and Italy (ISTAT, 2017).

1.3.3 Transfer efficiency

Solubility of radon in water increases with decreasing temperature. Boyle was the first to measure the solubility coefficient as a function of temperature and he found values of 0.51, 0.25 and 0.16 at 0.0, 20.0 and 39.1°C respectively (Boyle, 1911).

The solubility is now expressed through the Ostwald absorption coefficient, K, which describes the ratio of the radon concentration in water, $C_{\mathrm{Rn},w}$, to the radon concentration in air, $C_{\mathrm{Rn},a}$, at thermodynamic equilibrium. This coefficient can be computed using the following mathematical formula(Battino

Table 1.7: Per capita in-house water-use rates (L person^{-1} day^{-1}). Data source: (Danske Vandværkers Forening and Danmarks Statistik, 1997) Denmark, (Statistiska Centralbyrån, 2000) Sweden, (Environment Agency/Ofwat, 2000) England and Wales, (Statistics Norway, 1981) Norway, (Finnish Environment Institute, 1999) Finland, (RIVM, 1999) The Netherlands, (UK2) United Kinkdom. Water leakages are, where explicitly distinguished, excluded from the use rate.

Reference	Country	Dishwashing	Shower	Bath	Toilet	Laundry	Faucet	Other	Total
(Mayer et al., 1999)	USA	3.8	43.9	4.5	70.0	56.8	41.2	6.0	226
(DeOreo et al., 2016)	USA	2.6	42.0	5.7	53.7	36.3	42.0	9.5	192
(Bendito et al., 2009)	EU Member States	11.4[a]	42.5	11.2	39.9	14.7	13.2	4.3	137
(DK, 1997)	Denmark	14.0	49.0[b]	-[b]	37.0	18.0	10.0	19.0	136
(SW, 1995)	Sweden	38.0	57.0[b]	-[b]	38.0	28.0	9.0	19.0	189
(E&W, 2000)	England&Wales	0.0	32.0[b]	-[b]	53.0	22.0	5.0	48.0	160
(NO, 1981)	Norway	20.0	40.0[b]	-[b]	30.0	25.0	8.0	7.0	130
(FI, 1998)	Finland	18.0	57.0[b]	-[b]	17.0	16.0	4.0	3.0	116
(NE, 1998)	Netherlands	5.7	53.6[b]	-[b]	36.2	23.1	1.7	7.7	128
(UK, 2015)	United Kingdom	12.0[c]	18.0	19.6	45.0	31.5	6.0	10.5[d]	143
(Schleich and Hillenbrand, 2007)	Germany	7.6	37.8[e]	-[e]	40.3	17.6	15.1[f]	7.6[d]	126
(Costa et al.)	France	14.8	57.5[e]	-[e]	29.6	17.8	10.4	17.8[d]	148
(ISTAT, 2017)[g]	Italy	15.4	62.7[e]	-[e]	68.2	24.2	23.1	24.2[d]	220

[a] The value, reported by the reference for an household, is here kept unchanged for a single person.
[b] The Member States communications report values for *personal hygiene* here attributed to *shower*.
[c] Referred to as *washing up* and it probably includes also *personal hygiene*.
[d] It comprehends the *outdoor* usages, i.e. *gardening* and *car washing*.
[f] *Shower* and *bath* are not distinguished in the report and the sum is here attributed to *shower*.
[g] Obtained as the sum of *personal hygiene*, *cleaning* and *cooking/drinking*.
[h] Use rates percentages are taken from ARPAE Emilia Romagna.

and Clever, 1965; Weigel, 1978):

$$\frac{C_{\mathrm{Rn},w}}{C_{\mathrm{Rn},a}} = K = 0.105 + 0.405\, e^{-0.0502\, T} \tag{1.38}$$

where T has to be expressed in Celsius degrees.

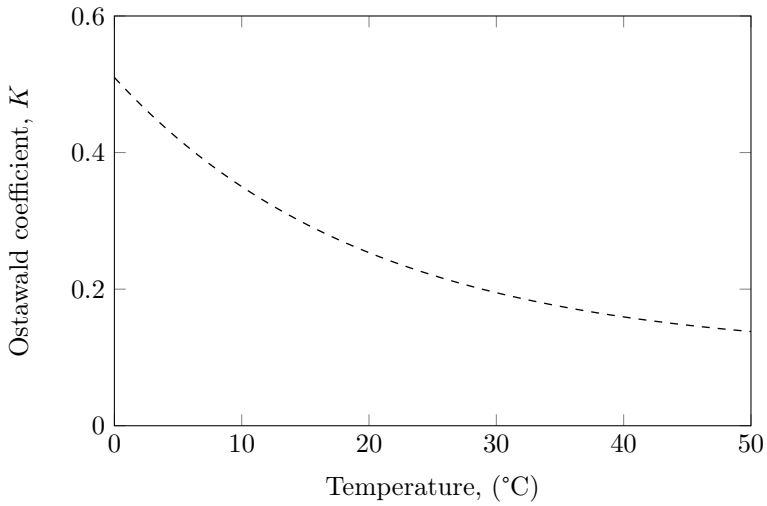

Figure 1.15: Ratio of the radon concentration in water to the radon concentration in air, at thermodynamic equilibrium, as a function of water temperature.

In order to better understand the meaning of the Ostwald coefficient it should be recalled that it stands for the ratio of radon concentration in water to radon concentration in air only if the thermodynamic equilibrium is verified. For this to happen, a period long enough should elapse or some external phenomena should intervene in order to make the process shorter, e.g. artificial degassing provoked by water agitation or bubbling.

In order to practically understand the meaning of K, consider a toilet tank holding $0.02\,\mathrm{m}^3$ (V_w) of water at $20\,^\circ\mathrm{C}$ in a closed bathroom of $15\,\mathrm{m}^3$ (V_a). The Ostwald coefficient computed by the Eq. 1.38 is 0.25. To determine the final concentrations in air and water the two following equations should be considered:

$$K(T_f) = \frac{C_{\mathrm{Rn},w,f}}{C_{\mathrm{Rn},a,f}} \tag{1.39}$$

$$V_w\,(C_{\mathrm{Rn},w,i} - C_{\mathrm{Rn},w,f}) + V_a\,(C_{\mathrm{Rn},a,i} - C_{\mathrm{Rn},a,f}) = 0 \tag{1.40}$$

where the subscript i and f stand for *initial* and *final* respectively. The Eq. 1.40 is obtained by considering the mass conservation equation during the spontaneous degassing process. If the initial radon concentration in water is supposed to be $100\,\mathrm{Bq\,L^{-1}}$, the system of Eqs. 1.39 and 1.40 returns $C_{\mathrm{Rn},w,f} = 0.033\,\mathrm{Bq\,L^{-1}}$ and $C_{\mathrm{Rn},a,f} = 0.133\,\mathrm{Bq\,L^{-1}}$. This means that the 99.97% of radon initially dissolved in water should be passed to the gaseous phase.

However, some measurements carried out through the years have shown that the equilibrium is not attained in real scenario: so, the actual fraction released in residence is generally much smaller. Such an experimental parameter,

in the following referred to as *transfer efficiency*, has to be computed as the ration of radon activity (or activity concentration) in water after a given time period (depending on the specific type of use) to the radon activity (or activity concentration) in the same water at the beginning of the observation period.

Table 1.8: Transfer efficiency for the release of radon from water to air, by domestic use.

Type of use	Transfer Efficiency, e		
	Partridge et al.	Gesell and Prichard	Hess et al.
Dishwashing	0.98[a]	0.90	0.98
Shower	0.71	0.63	0.65
Bath	0.60[b]	0.47	0.30[e]
Toilet	0.29[c]	0.30	0.30[e]
Laundry	0.98[d]	0.90	0.90[e]
Faucet	0.28	0.45	0.30[e]

[a] Arithmetic mean of values for shower with cold and hot water.
[b] Value obtained for bathing with hot water.
[c] 0.24 for bowl and 0.5 for tank.
[d] Value obtained for hot (or warm) wash cycle lasting 18 minutes.
[e] Values estimated in the reference

Values for transfer efficiency found by Partridge et al. (1979) was then recalled by Prichard (1987). Harley et al. (2014) found even an higher value for shower, $e = 0.92$.

The typical way to asses exposure to radon exhaled from water is at the scale of the entire house and over relatively long measurement periods (i.e. days or longer, National Research Council, 1999). Under such conditions, transfer of Rn from water into homes atmosphere is commonly modelled by a transfer coefficient:

$$C_T = \frac{\Delta C_{\mathrm{Rn},a}}{C_{\mathrm{Rn},w}} \tag{1.41}$$

Several surveys showed C_T approximately centred on approximately 10^{-4} within a wide variability range (Vinson et al., 2008; National Research Council, 1999; Nazaroff et al., 1987; Hess et al., 1982).

1.3.4 Radon concentration in water

Radon concentrations in water have been found to range over an extremely wide range, from effectively zero to more than 10^3 Bq L^{-1}. As previously seen, groundwaters are those likely to experience higher radon concentration due to their close contact with the rocks beneath the soil.

Radon activity concentrations are highly variable not only among the different water types but even within the same type. According to Jobbágy et al. (2016), "this can be mainly explained by their origin, lithology of the aquifer host rocks and the different processes on their way to the consumer (e.g. degassing, dilution, decay)". Where the path covered by drinking water from the original source (i.e. aquifer for groundwater and basin or stream for surface water) to the sampling point is *short* (compared to the half-life of ^{222}Rn), the radon content is more likely to reach high levels.

According to surveys carried out on radon activity concentration in water, the large majority of drinking water (coming from both surfaces or aquifers) do not bring elevated radon risk due to their consumption. This is mainly because: *i*) waters usually undergo water treatment (before being sent to consumers' houses) where radon is removed, either deliberately through forced bubbling or unintentionally through spontaneous degassing, from the waters together with other dissolved gases (Jobbágy et al., 2016); *ii*) radon has generally an higher probability to escape towards the air than accumulating into the water, as it usually happens to surface water being in close contact with the air. The situation can be different for groundwaters, since they are not in contact with the outdoor free air but with rocks rich in uranium (or radium). The poorness of free spaces beneath the soil also helps the radon concentration to increase by accumulating between the impermeable layers delimiting the aquifer.

Table 1.9 contains a quite comprehensive summary of findings about radon in water concentration all over the Europe. It does not contain any reference to spring waters: this type of water will be later addressed in a specicly dedicated chapter.

Table 1.9: Summary of recent literature findings about radon in water concentration in different water types.

Water type	$C_{^{222}\mathrm{Rn}}$ (Bq L^{-1})	Country	Geology	References
Drinking water	<3	Serbia (Novi Sad)		(Todorovic et al., 2012)
	0.3–24	Hungary		(Somlai et al., 2007)
	0.3–24	Greece and Cyprus		(Nikolopoulos and Louizi, 2008)
	1.46–644	Austria	Granite bedrock	(Wallner et al., 2008)
	100		Granite bedrock	(Gruber et al., 2009)
	<1.3–1800	Germany		(Beyermann et al., 2010)
	1.9–112.8	Portugal		(Lopes et al., 2004)
	0.2–71.1	UK		(Henshaw et al., 1993)
Surface water	<1	Slovenia		(International Standard Organization, 2013)
Groundwater	1–1000	Spain (La Garrotxa)		(International Standard Organization, 2013)
	0.2–26		Volcanic	(Moreno et al., 2014)
	3043	Poland (Sudety Mountains)	Volcanic	(Przylibski et al., 2014)
	3800	Finland		(Salonen, 1988)
	1220	Germany (East Bavaria)	Granite	(Trautmannsheimer et al., 2002)
	17–3856	Portugal (Nisa)	Granite	(Pereira et al., 2015)
	5.8–36.6	Northern Ireland	Sandstone	(Gibbons and Kalin, 1997)
Well water	10-300	Norway	Granite & Slate	(International Standard Organization, 2013)
	1–40	Hungary (Southern Plain)		(Somlai et al., 2007)
	4–63560	Sweden (Stockholm County)		(Skeppström and Olofsson, 2006)
	47–1600	Belgium (Visé)		(Bourgoignie et al., 1982)
	77000	Finland	Granite bedrock	(Salonen, 1988)
	385–3702	Bosnia & Herzegovina (Tuzla)	Limestone	(Kasić et al., 2016)
	1.5–10	Italy (Pesaro-Urbino)	Sedimentary rocks	(Desideri et al., 2005)

Chapter 2

Radon migration through building boundaries: a systematic review

Council Directive 2013/59/EURATOM requires Member States to *consider* any source of radon ingress, whether from soil, building materials or water (European Commission, 2014). This is demanded when preparing the national action plan to address long-term risks from radon exposure. In particular, regarding building material, Member States are explicitly required to identify (and/or develop) strategies, including methods and tools to identify building materials with significant radon exhalation rate.

Knowing the radon exhalation rate from building boundaries (this expression will be used in the following when referring to all indoor masonry structures, mainly walls and floors) is also crucial when choosing the best remedial strategies to reduce indoor radon concentration.

The rate at which radon is exhaled from building materials strongly depends on:

i) the exhalation-influencing properties of the materials itself (or mixture of materials), mainly radium content, diffusivity, emanation coefficient and permeability;

ii) those elements referred to as installation conditions, mainly width and geometry of the slab, how units are laid in and bound together, binding elements and covering layers;

iii) the environmental parameters affecting either the inner characteristics of the building materials or the phenomena leading to radon migration. As an example, the air exchange rate of locals strongly influences the indoor radon concentration (Vasilyev et al., 2015), and in turn, the concentration gradient regulating the diffusive transport. Analogously, the emanation coefficient strongly depends on temperature (Zhang et al., 2019)). The pressure gradient inside and outside the slab both affect directly the advective transport and the permeability of the slab (Chauhan and Kumar, 2015).

Several measurements of radon exhalation rate from building materials samples have been reported on literature through the years (Avramović et al., 2019; Al-Azmi et al., 2018; Leonardi et al., 2018; Jagadeesha and Narayana, 2017; Kovács et al., 2017; Campos et al., 2017; Sharma et al., 2016; Saad et al., 2014; Bavarnegin et al., 2013; Hassan et al., 2011; Chen et al., 2010; Ujić et al., 2010; Shweikani and Raja, 2009; Mahur et al., 2008; Sahoo et al., 2007; Rahman et al., 2007; Righi and Bruzzi, 2006; Maged and Ashraf, 2005; Stoulos et al., 2003; Petropoulos et al., 2001). However, as firstly highlighted by Sahoo et al. (2011), the difference, or the existing relationship, between radon exhalation from samples and that from walls has not been considered enough. Results from measurements of radon exhalation from building materials samples have been currently used to asses the effective dose attributable to radon exposure in indoor environment (Feng and Lu, 2016; Gupta et al., 2013; Mahur et al., 2008; Ujić et al., 2010). The one dimensional (1-D) geometry, considered when modelling the radon flux from masonry surfaces (mainly walls) is not applicable at all to the radon exhalation from a block of building material, the latter much better described by a three dimensional (3-D) model. This leads to different radon exhalation per unit surface area of the matrix and per unit time, in the two scenarios.

Given the above, two main possibilities are capable of providing reasonable values of radon exhalation rate from a wall: *i*) in-situ measuring radon exhalation rate directly from the wall surface, i.e. through the so-called accumulation methods described by International Organization for Standardization (2012a) and *ii*) estimating the radon surface exhalation rate from a wall as related to that from its building material sample. When dealing with measurements of the (*i*)-kind, several issues could affect the results: an innovative specific apparatus has been conceived by the author and its design, construction and commissioning will be introduced and discussed later on. The approach (*ii*) has been instead proposed by Sahoo et al. (2011) and recalled by Orabi (2018).

The approach proposed by Sahoo et al. (2011) relies on the comparison between the 3-D modelling of the radon flux from building material sample with that 1-D used to assess flux from a wall made up by the same materials. The 1-D model solution proposed by the authors – firstly reported by Jonassen and McLaughlin (1980) and later recalled by Nazaroff and Nero (1988) – is obtained under three main conditions: *i*) the diffusion is the only mechanism governing the radon transport, *ii*) the radon concentration inside the wall is an even function, symmetric with respect to the wall half thickness and *iii*) the room inner volume is much higher than the void wall volume. In other words, the solution is valid only when advective contribution is negligible and both wall surfaces are free to exhale into a radon-free space.

Orabi (2018), although he differently evaluated the ratios of 1-D to 3-D models' outputs, moved from the same solution of the one dimensional equation of radon migrations through the wall.

The boundary conditions implicitly adopted by Sahoo et al. (2011) and Orabi (2018), despite being far from commonly verified, are not declared at all by the authors. The resulting formulations can so lead to misleading predictions of radon surface flux from an existing wall.

The issue just described is an evidence of the need to provide a systematic review of the differential equations describing the radon migration, as well as the corresponding solutions for any reasonable boundary conditions. This work

has the aim to provide the readers with a such a comprehensive description of how typical scenarios for radon transport are mathematically modelled as well as to clarify the assumptions underlying the solutions.

2.1 Radon migration mechanisms and related quantities

2.1.1 Diffusive Transport - Fick's Law

The diffusive transport refers to the tendency of a molecular species to migrate down its concentration gradient through a material (Nazaroff and Nero, 1988). Such a molecular motion is governed by the Fick's Law that expresses the species flux as a function of the species concentration gradient. The coefficient influencing the magnitude of this correlation is termed the **diffusion coefficient** or the molecular diffusivity.

The diffusion coefficient in open air (D_0) needs to be adjusted in any porous media in order to account for two different phenomena: i) the presence of solid particles causes the diffusion paths of species to deviate from straight lines, so the diffusion coefficient must be corrected for the tortuosity τ, in turn defined as the ratio of the actual distance travelled by the species (l) per unit length of the medium (x), $\tau = \frac{\Delta l}{\Delta x}$ (Shen and Chen, 2007) (according to Dullien (1979), $\tau = \frac{(\Delta l)^2}{(\Delta x)^2}$); ii) the cross-sectional area through which diffusion occurs is reduced by a fraction equal to the ratio of the open pore area, A^*, to the total cross-section, A, i.e. the areal porosity (Nimmo, 2004).

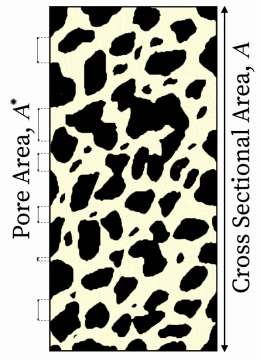

Figure 2.1: Open pore area at a given cross-section of a porous material: rearrangement from Culot et al. (1976).

The **bulk coefficient**, in the following referred to as D, relates the gradient of interstitial concentration of diffusing radon (Bq per m^3 of pore volume) to the flux density over the cross-sectional area (Bq per m^2 of the cross-section). Hence, it accounts for both the lengthening of the path travelled (i) and the reductions in cross-sectional area (ii). According to (Shen and Chen, 2007):

$$D = D_0 \tau^2 \tag{2.1}$$

As an example, in case of high porous media, τ is well approximated by the

porosity ϵ, so $\tau^2 \approx \epsilon^2$ (Ullman and Aller, 1982) and:

$$D = D_0 \epsilon^2 \tag{2.2}$$

firstly proposed by (Buckingham, 1904). Different correlations have been proposed depending on the relationship best fitting the function $\tau(\epsilon)$ (Matyka et al., 2008; Shen and Chen, 2007).

The **effective coefficient**, in the following referred to as D_e, relates the gradient of interstitial concentration of diffusing radon (Bq per m^3 of pore volume) to the flux density over the cross-sectional pore area (Bq per m^2 of the pore area). The effective coefficient can be equivalently defined as that relating the gradient of the radon bulk concentration (Bq per m^3 of total volume) to the flux density over a cross-sectional pore area (Bq per m^2 of the effective cross-sectional area). D_e is related to D by the following relationship:

$$D_e = D \frac{A}{A^*} \approx D \frac{V}{V_v} = \frac{D}{\epsilon} \tag{2.3}$$

where:

- V_v is the void volume of the porous material, both water- and gas-filled (m^3)
- V is the overall volume of the porous material (m^3)
- ϵ is the porous material porosity defined as the fraction of the total material volume that is taken up by the pore space (Nimmo, 2004) .

As mentioned by Culot et al. (1976), correlating D and D_e through the porosity ϵ means assuming the equality between the areal porosity (i.e. the fraction of open pore area in a unit cross-section) and the volume porosity, i.e. $\frac{A^*}{A} \approx \frac{V^v}{V} = \epsilon$. This assumption is legit in case of porous media with random structure (Dullien, 1979).

No standardization exists in literature about the symbolism of the diffusion coefficients: k_e (Culot et al., 1976; Nero and Nazaroff, 1984), K_e (Jonassen and McLaughlin, 1980), D_B (Porstendörfer, 1994; López-Coto et al., 2014) have been used to denote the bulk coefficient as well as k_e^* (Culot et al., 1976; Nero and Nazaroff, 1984), K_e^* (Jonassen and McLaughlin, 1980), D' (Antonopoulos-Dornis et al., 1998), D (Rogers et al., 1995) and D_c (Rogers and Nielson, 1991) to refer to the effective coefficient.

The diffusion of radon in porous media is generally modelled through the first Fick's law:

$$\boldsymbol{J}^d_{\mathrm{Rn}} = -\boldsymbol{D}_e \nabla C_{\mathrm{Rn}} \tag{2.4}$$

where:

- $\boldsymbol{J}^d_{\mathrm{Rn}}$ is the diffusive flux density of radon activity per unit pore area of the material ($\mathrm{Bq\,m^{-2}\,s^{-1}}$)
- $\boldsymbol{D}_e$ is the effective diffusion-dispersion tensor (Shen and Chen, 2007) ($\mathrm{m^2\,s^{-1}}$)
- C_{Rn} is the activity concentration of radon per unit volume of interstitial space ($\mathrm{Bq\,m^{-3}}$).

If the radon flux is only due to the gradient activity concentration, i.e. no advection (i), the material is isotropic (ii) and homogeneous (iii), the diffusion-dispersion tensor reduces to:

$$\boldsymbol{D}_e = D_e \boldsymbol{I} = \begin{bmatrix} D_e & 0 & 0 \\ 0 & D_e & 0 \\ 0 & 0 & D_e \end{bmatrix} \tag{2.5}$$

Formulating the diffusion mechanism of radon through Eq. 2.4 is based on two further assumptions. First, all the kinetic interactions of radon atoms happen as in the open air, i.e. with other gas molecules and not with the solid boundaries of grains (Nazaroff and Nero, 1988). The reasonability of this assumption depends on the range of radon atoms relative to the dimension of open pores. According to Tanner (1980), the recoil range of ^{222}Rn varies from 0.02 to 0.07 µm for common materials, being 63 nm for the air. Similar values have been later found by Nazaroff and Nero (1988), 65 nm, and (Wilkening, 1990), 60 nm. The pore size distribution of porous materials, either building materials or soils, have been studied by various authours: some results are reported in Table 2.1.

Table 2.1: Typical pore sizes of building materials and *soils*. The full pore size distribution is generally reported in the corresponding reference.

Building Materials	Pore Diameter (µm)	References
Basalt	0.03[a]	(Yan et al., 2015)
Clay Brick	0.01–80	(Straube, 1998)
Clay	up to 2	(Marshall et al., 1996)
Concrete[b]	0.002–0.3	(Straube, 1998)
Concrete[c]	0.008–5	(Winslow, 1968)
Concrete[d]	0.008–0.4	(Winslow, 1968)
Granite	0.48[e]	(Yan et al., 2015)
Mudstone	0.02[f]	(Yan et al., 2015)
Limestone[g]	up to 10[h]	(Ordóñez et al., 1997)
Coarse-grained Sandstone	0.4–8	(Kashif et al., 2019)
Fine-grained Sandstone	0.002–3.2	(Kashif et al., 2019)
Sand	60–2000	(Marshall et al., 1996)
Silt	2–60	(Marshall et al., 1996)
Siltstone	0.04[i]	(Yan et al., 2015)

[a] Average pore diameter. The dominant pores concentrate between 5–50 nm, whose volume accounts for about 50% of the total.
[b] Water to cement ration $w/c = 0.7$.
[c] Water to cement ration $w/c = 0.4$, age 320 days.
[d] Water to cement ration $w/c = 0.6$, age 318 days.
[e] Average pore diameter. The dominant pore size concentrates in the range of 303–2119 nm, whose volume accounts for more than 40% of the total.
[f] Average pore diameter. The dominant pore size concentrates in the range of 9.1–90.7 nm, whose volume accounts for more than 50% of the total.
[g] Five different limestones are considered by the authors.
[h] $> 95\%$ of open pores have a diameter lower than 10 µm.
[i] Average pore diameter. The pore distribution is concentrated in the range of 22.7–90.7 nm, whose volume accounts for over 70% of the total.

This assumption, generally good for soils except for those mainly made of clay, can becomes too *strong* for building materials (see Table 2.1). When pore diameters are mostly lower than the recoil range of radon, as it happens for most building materials, the gaseous atoms collide with the wall rather than colliding with other atoms. As a consequence, the diffusion coefficient of radon in open air, D_0, needs to be substituted by the Knudsen diffusivity to account for the diameter of pores (Knudsen, 1909). The flux density would keep on being proportional to the concentration gradient but the diffusivity would become a strong function of position within the pore (Youngquist, 1970; Nazaroff and Nero, 1988).

The issue gets particularly relevant considering that boundary walls and soils are generally made of concrete whose pore size distribution, regardless of the age and the water to cement ratio of the aggregate (Figure 2.2 shows the cumulative pore volume distribution for a $w/c = 0.4$ cement paste 267 days-aged), has mesopores ($2\,\text{nm} < d < 50\,\text{nm}$) reveals micropores ($d < 2\,\text{nm}$) strongly prevailing on macropores ($d > 50\,\text{nm}$).

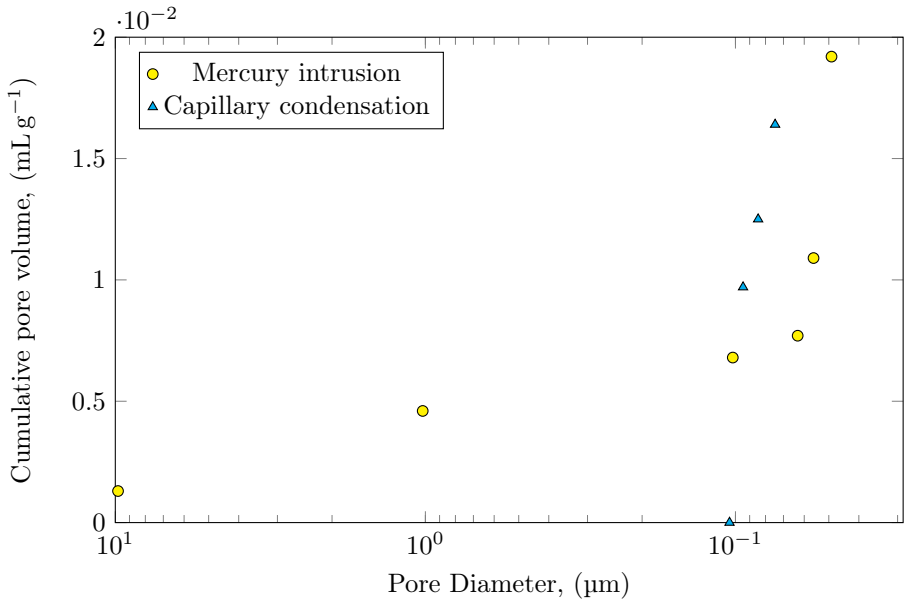

Figure 2.2: Cumulative pore volume distribution for $w/c = 0.4$ cement paste (age 267 days) (Winslow, 1968). Results obtained by two different measuring methods are reported: mercury intrusion (circle-marked) and capillary condensation (triangle-marked).

The second approximation is that all radon in the soil exists in one of the two states: in the air filling the voids or in the solid matrix (Nazaroff and Nero, 1988). In order to fulfil this condition, three simplifications need to be accepted. First, the pores size distribution is assumed to be unimodal, despite, for example, the bimodal fitting curves have been found to better match with the concrete pore size distributions than the other curves (Chung et al., 2020). Second, the fraction of radon contained in water-filled pores is assumed to be negligible. The solubility or radon in water, increasing with decreasing temperature, is expressed through the Ostwald absorption coefficient, K, computed as the ratio of the radon concentration in water, $C_{\text{Rn},\,w}$, to the radon concentration in air, $C_{\text{Rn},\,w}$, at thermodynamic equilibrium (Battino and Clever, 1965; Weigel, 1978). The ratio of the radon activity in water phase, $A_{\text{Rn},w}$, to the radon activity in gaseous phase, $A_{\text{Rn},g}$, decreases with increasing temperature, saturation degree fixed, and increases with increasing saturation degree S[1], temperature fixed (Figure 2.3). As a consequence, the second assumption is good at higher temperature and lower saturation degrees: e.g. at the temperature of 20 °C, the radon in

[1]The saturation degree is computed as the ratio of water-filled pores volume to the total pores volume, e.g. $S = 1$ means that all pores are water-filled.

gas-filled pores is 10 times that in water-filled ones if the saturation degree is 0.3 whereas, the saturation degree fixed, if the temperature decreases to 5 °C, the same ratio is halved.

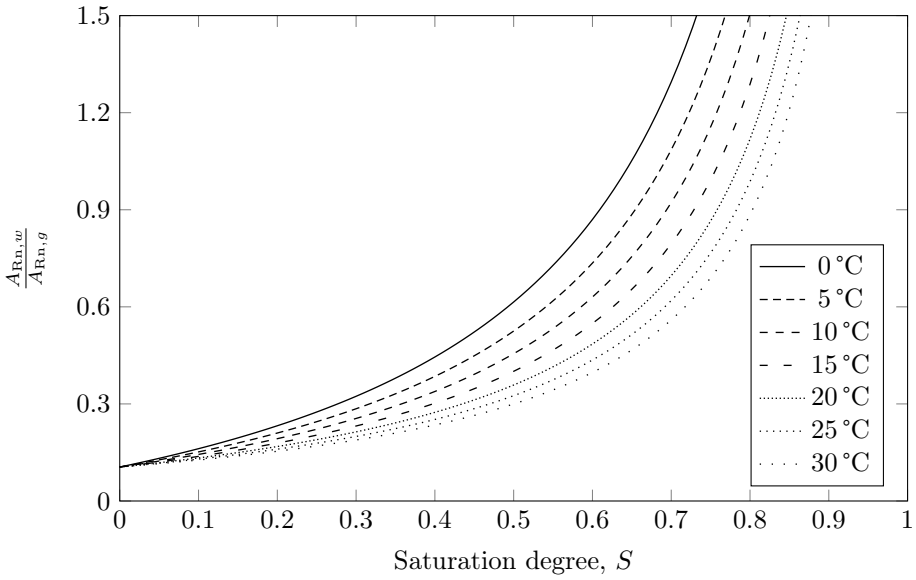

Figure 2.3: Ratio of the radon activity in water phase, $A_{\mathrm{Rn},w}$, to the radon activity in gaseous phase, $A_{\mathrm{Rn},g}$, at thermodynamic equilibrium, as a function of saturation degree S and for different temperature.

Finally, the third underlying assumption requires that no appreciable adsorption of radon atoms happens on the surface of solid grains. This seemed a good assumption to (Nazaroff and Nero, 1988) because radon, being a noble gas, is inert and its condensation temperature is much lower than the environmental temperature. Baretto (1973) observed a strong radon adsorption at temperatures below −20 °C. A temperature rise has been later confirmed to determine an increase in the physical adsorption of radon gas on soil solid grains (Iskandar et al., 2004; Lee et al., 2010) but results have been extended to porous materials in general (Sahu et al., 2016).

2.1.2 Convective Transport - Darcy's Law

Advection describes the fluid transport of a certain molecular species via bulk motion, the latter being determined by a difference of fluid's head between two sections. Advection requires the fluid to be in motion, so cannot happen in not porous materials. It does not include transport of substances by molecular diffusion. Because the effects of gravity are generally neglected, the advective transport usually refers to the migration of a species down a pressure gradient and so it is in the case of radon transport through a porous material. The governing equation of advection is the so-called Darcy's law (Whitaker, 1986; Darcy, 1856):

$$\boldsymbol{v} = -\frac{k}{\mu}\nabla P \tag{2.6}$$

where:

- $\boldsymbol{v}$ is the flow velocity, or superficial velocity in the speaking of Nazaroff and Nero (1988), i.e. the volumetric fluid flow rate ($\mathrm{cm^3\,s^{-1}}$) per unit geometrical area ($\mathrm{cm^2}$) defined over a region large relative to individual pores but small relative to the overall dimensions of the material ($\mathrm{m\,s^{-1}}$)
- ∇P is the pressure gradient ($\mathrm{Pa\,m^{-1}}$)
- k is the permeability of the porous material ($\mathrm{m^2}$)
- μ is the carrying fluid dynamic viscosity ($\mathrm{Pa\,s}$).

The Eq. 2.6 is valid in the hypotheses of neglecting the effects of gravity (i), i.e. the motion is governed only by the pressure gradient, low Reynolds number (ii), such to treat the flow through porous material as a viscous flow through a pipe, and isotropic permeability (iii).

In case of anisotropic porous media, the permeability should be substituted by the 3x3 permeability tensor (Guin et al., 1971; Rice et al., 1970), $\boldsymbol{K}$, and Darcy's law becomes (Scheidegger, 1974):

$$\boldsymbol{v} = -\frac{1}{\mu}\boldsymbol{K}\cdot\nabla P \tag{2.7}$$

Given the flow velocity, the advective transport of radon in porous media is modelled as follow:

$$\boldsymbol{J}^{a}_{\mathrm{Rn}} = \frac{C_{\mathrm{Rn}}\boldsymbol{v}}{\epsilon} = -C_{\mathrm{Rn}}\frac{1}{\mu}\frac{\boldsymbol{K}}{\epsilon}\cdot\nabla P \tag{2.8}$$

where:

- $\boldsymbol{J}^{a}_{\mathrm{Rn}}$ is the advective flux density of radon activity per unit pore area of the material ($\mathrm{Bq\,m^{-2}\,s^{-1}}$)
- C_{Rn} is the activity concentration of radon per unit volume of interstitial space ($\mathrm{Bq\,m^{-3}}$).
- ϵ is the porous material porosity.

The Darcy's law has been extensively used in applications at Reynolds number[2] values of up to 1 (Chaudhary et al., 2011) and a general consensus exists about Darcy's law applicability for an upper limit of Re value between 1–10 for average grain size and velocity (Bear, 1975). Flows below this limit are fully dominated by viscous force and Darcy's law applies. For higher Re numbers, due to emerging importance of inertial forces, deviations of fluid flow from Darcy's law have been observed even if the flow keeps laminar (Muskat, 1907; Forchheimer, 1901; Dupuit, 1863). The critical Re values for non-Darcy flows have been observed to vary according to media. Critical values of 0.01–0.1 resulted

[2]Other than distinguishing the laminar and non-laminar flow, Reynolds number, Re, is used to predict the region of applicability of the Darcy's law (Wang et al., 2019):

$$Re = \frac{d_0 v}{\nu} \tag{2.9}$$

where:

- v is the average flow velocity ($\mathrm{cm\,s^{-1}}$)
- d_0 is the mean grain diameter (cm)
- ν is is the kinematic viscosity coefficient of the fluid in motion ($\mathrm{cm^2\,s^{-1}}$)

for disordered porous media (Andrade et al., 1999), 0.4–3 for loosely consolidated sandstones and 10–1000 for unconsolidated sands (Fancher and Lewis, 1933). For flows in porous media with Reynolds numbers greater than about 1 to 10, an inertial term, known as Forchheimer term (Forchheimer, 1901), should be added to the Darcy's equation.

According to (Nazaroff and Nero, 1988), as in the case of applying Fick's law to porous media, also in the development of Darcy's law the pores need to be large relative to the mean free path of the gas. If not, the particle-wall interactions get more probable, giving rise to additional wall friction known as Knudsen friction. Knudsen developed a semi-empirical model considering both viscous (i.e. transition region) and Knudsen friction (i.e. small capillarities) (Carrigy et al., 2013).

2.2 Radon only diffusive transport through a slab without sources

Generally, radon sources can be neglected inside a porous medium when at least one among *i*) ^{226}Ra (in the following, often referred to simply as "radium") concentration, *ii*) emanation fraction has been found (or it assumed) to be low enough. Rogers et al. (1995) assumed negligible the radon generated in a concrete sample due to a radium concentration in solid matrix lower than $90\,\mathrm{Bq\,kg^{-1}}$. Additionally, if no significant pressure difference exists between its two sides, advection is negligible so the radon flux through the medium is fully described by Eq. 2.4.

Referring to Figure 2.4, if $\frac{dC_{\mathrm{Rn}}}{dy} \approx 0$ and $\frac{dC_{\mathrm{Rn}}}{dz} \approx 0$ the radon flux through the wall is one dimensional (1-D). Alternatively, if it is assumed that the thickness of the slab is much smaller than the height or width, thus the effective radon exhaling areas are orthogonal to x-axis. Once the steady state is reached, i.e. $\frac{dC_{\mathrm{Rn}}}{dt} = 0$, the process may be modelled as follows:

$$D_e \frac{d^2 C_{\mathrm{Rn}}(x)}{dx^2} - \lambda_{\mathrm{Rn}} C_{\mathrm{Rn}}(x) = 0 \tag{2.10}$$

where:

- D_e is the effective diffusivity of porous medium along the x-axis, i.e. $\frac{D}{\epsilon}$ ($\mathrm{m^2\,s^{-1}}$)
- C_{Rn} is the activity concentration of radon per unit volume of interstitial space ($\mathrm{Bq\,m^{-3}}$).
- λ_{Rn} is the radon decay constant ($\mathrm{s^{-1}}$)

The differential equation 2.10 is homogeneous and the corresponding solution is:

$$\begin{aligned} C_{\mathrm{Rn}} &= Ae^{-\sqrt{\frac{\lambda_{\mathrm{Rn}}\epsilon}{D}}x} + Be^{\sqrt{\frac{\lambda_{\mathrm{Rn}}\epsilon}{D}}x} = \\ &= Ae^{-\frac{x}{R}} + Be^{\frac{x}{R}} = \\ &= Ae^{-xr} + Be^{xr} \end{aligned} \tag{2.11}$$

where R is the diffusion length (Jonassen and McLaughlin, 1980):

$$R = \sqrt{\frac{D_e}{\lambda_{\mathrm{Rn}}}} \tag{2.12}$$

$$r = \frac{1}{R} = \sqrt{\frac{\lambda_{\mathrm{Rn}}}{D_e}} \tag{2.13}$$

The only meaningful boundary conditions to be considered in case of diffusing walls without sources are fixed concentrations on both sides.

2.2.1 Fixed radon concentration on both sides of a finite slab

Such a scenario is pretty common when measuring diffusivity of porous medium (e.g. Culot et al., 1976; Hsu et al., 1994; Keller et al., 2001). The computation of D_e, in fact, generally uses the radon concentration recorded on the side coupled with a source or a reservoir chamber, and an average value the concentration recorded in a receiving (or measuring) container. In such experiments, great care is taken in preventing pressure difference over the slab since the migration of radon should occur only by a concentration gradient over the material (Hsu et al., 1994). If the radon sources inside the medium are assumed to be negligible, solutions of Eq. 2.11 need to be provided for diffusivity computation.

Referring to Figure 2.4, the boundary conditions can be written as follows:

$$\begin{cases} C_{\mathrm{Rn}}(x=0) = C_l & \text{(2.14a)} \\ C_{\mathrm{Rn}}(x=T) = C_r & \text{(2.14b)} \end{cases}$$

From the boundary conditions:

$$\begin{aligned} A &= C_l - \frac{C_r - C_l e^{-rT}}{2\sinh(rT)} = \\ &= \frac{C_l(e^{rT} - e^{-rT}) - C_r + C_l e^{-rT}}{2\sinh(rT)} = \\ &= \frac{C_l e^{rT} - C_r}{2\sinh(rT)} \end{aligned} \tag{2.15}$$

$$B = \frac{C_r - C_l e^{-rT}}{2\sinh(rT)} \tag{2.16}$$

The solution can thus be written as:

$$\begin{aligned} C_{\mathrm{Rn}}(x) &= \frac{C_l e^{rT} - C_r}{2\sinh(rT)} e^{-rx} + \frac{C_r - C_l e^{-rT}}{2\sinh(rT)} e^{rx} = \\ &= \frac{1}{2\sinh(rT)} \left[(C_l e^{rT} - C_r) e^{-rx} + (C_r - C_l e^{-rT}) e^{rx} \right] \end{aligned} \tag{2.17}$$

The influence of diffusion length on $C_{\mathrm{Rn}}(x)$ shape is shown in Figure 2.5.

The corresponding exhalation rate, E ($\mathrm{Bq\,m^{-2}\,s^{-1}}$), on the right side of the

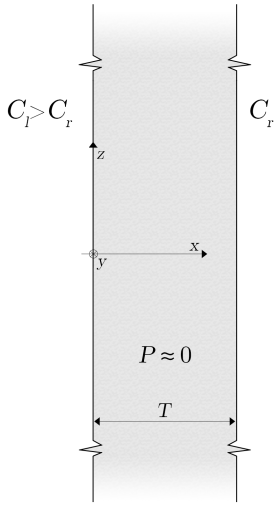

Figure 2.4: Schematic representation of a porous slab with no radon sources inside, i.e. $P \approx 0$, where P is the radon production rate per unit total volume of porous medium. The radon concentration on both sides of the wall is constant if steady state is reached: C_l on the left and C_r on the right. Slab dimensions along y and z axes are much greater than along x-axis.

slab can be computed as (Jonassen and McLaughlin, 1980):

$$\begin{aligned} E(T) &= -D\frac{dC_{\mathrm{Rn}}(x)}{dx}\bigg|_{x=T} = \\ &= -\frac{D}{2\sinh(rT)}\left[r(C_r - C_l e^{-rT})e^{rx} - r(C_l e^{rT} - C_r)e^{-rx}\right] = \\ &= \frac{Dr}{\sinh(rT)}\left[C_l - C_r\cosh(rT)\right] \end{aligned} \tag{2.18}$$

The radon concentration function (Eq. 2.17), and the corresponding exhalation rate (Eq. 2.18) may be also applied in case of radon diffusion through outer walls if inner radon sources are such to neglect P. On the contrary, the negligibility of the pressure gradient needs to be assessed case by case: in naturally ventilated buildings, the pressure differences between indoors and outdoors have been found to be generally lower than 5 Pa, whereas the average pressure differences after renovation in buildings with mechanical exhaust are generally higher, ≈ 19.1 Pa (Leivo et al., 2015). Such values have been found to further increase according to the magnitude of stack and wind effect (Čechák et al., 2004). Considering the very low (although ranging from approximately 1 to more than 100 $\mathrm{Bq\,m^{-3}}$ (United Nations Scientific Committee on the Effects of Atomic Radiation, 2000)) outdoor radon concentration, i.e. 10 $\mathrm{Bq\,m^{-3}}$ (United Nations Scientific Committee on the Effects of Atomic Radiation, 1993), in such a scenario a net radon flux always occurs from indoor to outdoor ($C_r \approx 0\,\mathrm{Bq\,m^{-3}}$).

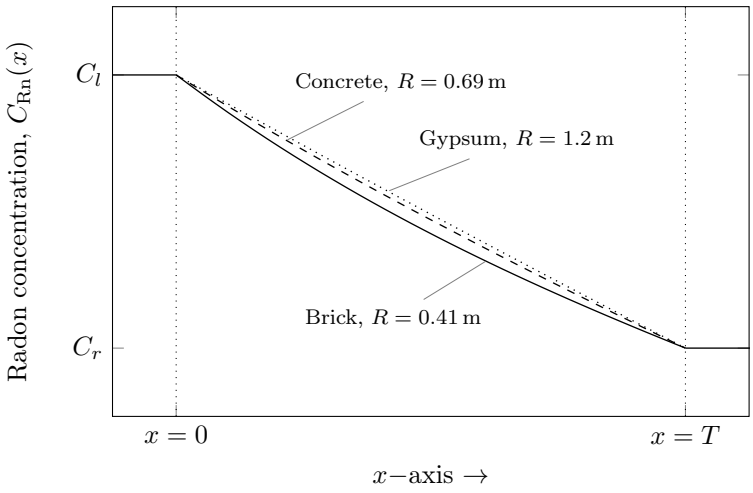

Figure 2.5: Shape of radon concentration along $x-$axis in steady state condition for walls made of three different materials if $P \approx 0$. Radon diffusion length of brick, aerated concrete and gypsum are taken from Keller et al. (2001).

This leads to:

$$C_{\mathrm{Rn}}(x) = \frac{C_l}{2\sinh rT}(e^{rT}e^{-rx} - e^{-rT}e^{rx}) \tag{2.19}$$

$$E(T) = -D\frac{dC_{\mathrm{Rn}}(x)}{dx}\bigg|_{x=T} = \frac{DC_l r}{\sinh rT} \tag{2.20}$$

2.3 Radon only diffusive transport through a slab with inner sources

When building materials with high radium concentration are used, the concentration obeys the diffusion equation with decay and production terms (Nero and Nazaroff, 1984). If the the steady state is reached, i.e. $\frac{dC_{\mathrm{Rn}}}{dt} = 0$, and the same geometrical hypotheses formulated in section 2.2 still apply, the diffusion of radon inside the material along the x-axis is governed by the equation:

$$D_e\frac{d^2C_{\mathrm{Rn}}(x)}{dx^2} - \lambda_{\mathrm{Rn}}C_{\mathrm{Rn}}(x) + G_v = 0 \tag{2.21}$$

where:

- D_e is the effective diffusivity of porous medium along the x-axis, i.e. $\frac{D}{\epsilon}$ ($\mathrm{m^2\,s^{-1}}$)
- C_{Rn} is the activity concentration of radon per unit volume of interstitial space ($\mathrm{Bq\,m^{-3}}$).
- λ_{Rn} is the radon decay constant ($\mathrm{s^{-1}}$)
- G_v is the radon emanation rate, or alternatively the radon production rate, per unit pore volume ($\mathrm{Bq\,m^{-3}}$). Some authors (e.g. Culot et al., 1976) express this term as $G_v = \frac{P}{\epsilon}$, being P the radon emanation rate per unit total volume and ϵ the porosity.

The linear differential equation is not homogeneous and the solution has to be built as the sum of the homogeneous and the particular solution. The homogeneous solution is the same previously seen for the no-source case, so:

$$C_{\mathrm{Rn},h}(x) = Ae^{-xr} + Be^{xr} \tag{2.22}$$

The particular solution has the form $C_{\mathrm{Rn}}(x) = e^{\lambda x}Q(x)$ with $\lambda = 0$ and $Q(x)$ polynomial of the same degree of G_v, i.e. 0.

$$C_{\mathrm{Rn},p}(x) = Cx^0 = C \tag{2.23}$$

By substituting $C_{\mathrm{Rn},p}$ and $\frac{d^2C_{\mathrm{Rn},p}(x)}{dx^2} = 0$ into Eq. 2.21:

$$\begin{aligned} D_e 0 - \lambda_{\mathrm{Rn}} C + G_v &= 0 \\ C_{\mathrm{Rn},p}(x) = C &= \frac{G_v}{\lambda_{\mathrm{Rn}}} \end{aligned} \tag{2.24}$$

The general solution can so be written as:

$$\begin{aligned} C_{\mathrm{Rn}}(x) &= C_{\mathrm{Rn},h}(x) + C_{\mathrm{Rn},p}(x) = \\ &= Ae^{-xr} + Be^{xr} + \frac{G_v}{\lambda_{\mathrm{Rn}}} \end{aligned} \tag{2.25}$$

The scenario described by Eq. 2.25 is common to all those situation with negligible advective transport. This reflects on three different boundary conditions sets to be considered: fixed concentrations on both sides of a finite slab (i), infinite slab with fixed concentration at $x \to +\infty$ (ii) and finite slab inside a vessel with unknown radon concentration (iii).

2.3.1 Fixed concentrations on both sides of a finite slab

Such a scenario applies to inner and outer walls of buildings if the radon production rate is not negligible and different radon concentrations exist on the wall sides. The negligibility of the advective transport in case of outer walls should be discussed case by case following the distinctions made in §2.2.1. For walls dividing two rooms of the same building, the assumption is generally good for workplaces and dwellings with no forced air circulation systems. Referring to Figure 2.6, the boundary conditions can be written as:

$$\begin{cases} C_{\mathrm{Rn}}(x = 0) = C_l & \text{(2.26a)} \\ C_{\mathrm{Rn}}(x = T) = C_r & \text{(2.26b)} \end{cases}$$

C_l^* and C_r^* are than defined as follow:

$$C_l^* = C_l - \frac{G_v}{\lambda_{\mathrm{Rn}}} \tag{2.27}$$

$$C_r^* = C_r - \frac{G_v}{\lambda_{\mathrm{Rn}}} \tag{2.28}$$

The boundary conditions lead to:

$$A = C_l^* - \frac{C_r^* - C_l^* e^{-rT}}{2\sinh(rT)} = \\ = \frac{C_l^*(e^{rT} - e^{-rT}) - C_r^* + C_l^* e^{-rT}}{2\sinh(rT)} = \\ = \frac{C_l^* e^{rT} - C_r^*}{2\sinh(rT)} \tag{2.29}$$

$$B = \frac{C_r^* - C_l^* e^{-rT}}{2\sinh(rT)} \tag{2.30}$$

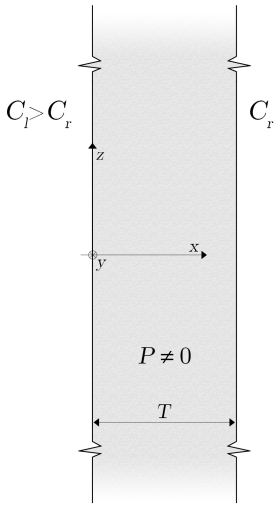

Figure 2.6: Schematic representation of a porous slab with inner radon sources. Except for $G_v = \frac{P}{\epsilon} \neq 0$, this scenario is exactly the same as §2.2.1 (Fig. 2.4).

By sobstituting Eq.s 2.29 and 2.30 in Eq. 2.25:

$$C_{\mathrm{Rn}}(x) = \frac{C_l^* e^{rT} - C_r^*}{2\sinh(rT)} e^{-rx} + \frac{C_r^* - C_l^* e^{-rT}}{2\sinh(rT)} e^{rx} + \frac{G_v}{\lambda_{\mathrm{Rn}}} = \tag{2.31}$$

$$= \frac{1}{2\sinh(rT)}\left[(C_l^* e^{rT} - C_r^*)e^{-rx} + (C_r^* - C_l^* e^{-rT})e^{rx}\right] + \frac{G_v}{\lambda_{\mathrm{Rn}}} = \\ = \frac{1}{2\sinh(rT)}\Big\{(C_l e^{rT} - C_r)e^{-rx} + (C_r - C_l e^{-rT})e^{rx} \\ + 2\frac{G_v}{\lambda_{\mathrm{Rn}}}\left[\sinh(r(x-T)) - \sinh(rx) + \sinh(rT)\right]\Big\} \tag{2.32}$$

The exhalation rate, E ($\mathrm{Bq\,m^{-2}\,s^{-1}}$), on the right side of the slab ($x = T$)

can be so computed as:

$$\begin{aligned} E(T) &= -D\frac{dC_{\mathrm{Rn}}(x)}{dx}\bigg|_{x=T} = \\ &= \frac{Dr}{\sinh(rT)}\left[C_l^* - C_r^*\cosh(rT)\right] \\ &= \frac{Dr}{\sinh(rT)}\left[C_l - C_r\cosh(rT) - \frac{G_v}{\lambda_{\mathrm{Rn}}}(1-\cosh(rT))\right] \end{aligned} \tag{2.33}$$

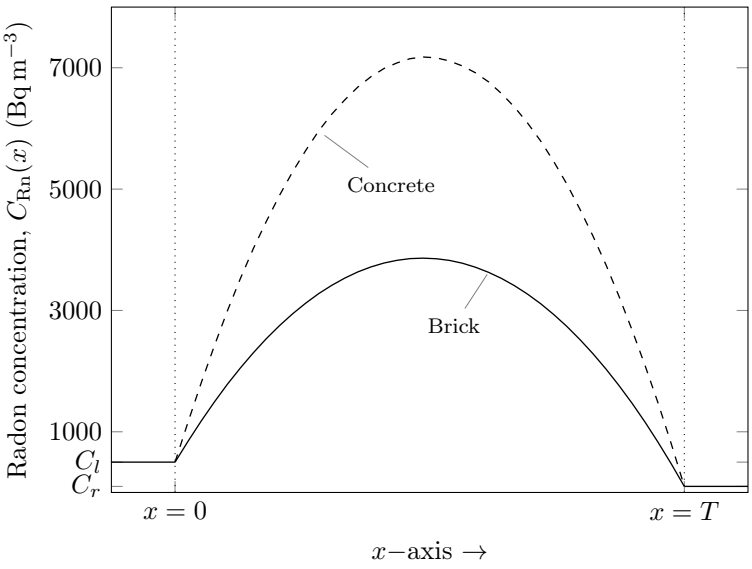

Figure 2.7: Shape of radon concentration along $x-$axis in steady state condition for walls made of bricks and concrete. The following values have been assumed for concrete (i) and brick(ii), respectively: $i)$ $f = 0.24$ (Nuccetelli et al., 2018), $R = 0.69\,\mathrm{m}$ (Keller et al., 2001), $\epsilon = 0.2$ (Li et al., 2019), $C_{^{226}\mathrm{Ra}} = 59\,\mathrm{Bq\,kg^{-1}}$ (Trevisi et al., 2018), $\rho = 2.4\,\mathrm{g\,cm^{-3}}$(Dorf, 2004); $ii)$ $f = 0.12$ (Nuccetelli et al., 2018), $R = 0.41\,\mathrm{m}$ (Keller et al., 2001), $\epsilon = 0.35$ (Hall and Hamilton, 2015), $C_{^{226}\mathrm{Ra}} = 51\,\mathrm{Bq\,kg^{-1}}$ (Trevisi et al., 2018), $\rho = 1.9\,\mathrm{g\,cm^{-3}}$ (Dorf, 2004).

2.3.2 Fixed concentration on a side of an infinite slab

This scenario has been commonly adopted for the radon exhalation rate from the soil (Nero and Nazaroff, 1984) although some examples exist of radon production rate assumed negligible (Suaro, 2014). The reason for this lies in the pressure difference sustained between the pore space and the atmosphere, that is usually small enough to make negligible the pressure induced flux as compared to the diffusion driven one (Chitra et al., 2019; Speelman et al., 2004). For the steady state condition, if soil properties and ^{226}Ra concentration are assumed to be homogeneously distributed, the radon concentration inside the slab satisfies Eq. 2.25. The boundary conditions are:

$$\begin{cases} C_{\mathrm{Rn}}(x=0) = C_0 & \text{(2.34a)} \\ C_{\mathrm{Rn}}(x\to\infty) = C_{max} & \text{(2.34b)} \end{cases}$$

where, C_0, the radon concentration at the surface, is generally close to zero.

Given the reference system in Figure 2.8, from the boundary conditions:

$$B = 0 \tag{2.35}$$

$$A = C_0 - B - \frac{G_v}{\lambda_{^{222}\mathrm{Rn}}}$$

$$A = C_0 - \frac{G_v}{\lambda_{^{222}\mathrm{Rn}}} \tag{2.36}$$

where $B = 0$ because the radon concentration should be finite at $x \to \infty$. The asymptotic radon concentration deep inside the porous material, i.e. C_{max}, resulted to be:

$$C_{max} = \frac{G_v}{\lambda_{\mathrm{Rn}}} \tag{2.37}$$

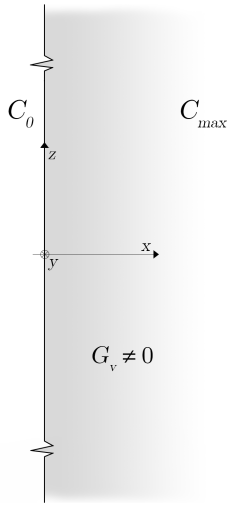

Figure 2.8: Schematic representation of a porous infinite slab with inner radon sources (i.e. $G_v = \frac{P}{\epsilon} \neq 0$), whose right side surface is free to exhale. The free surface is at $x = 0$ and the abscissa grows towards the porous medium.

Based on Eq. 2.25, the boundary conditions lead to:

$$C_{\mathrm{Rn}}(x) = C_0 e^{-rx} + C_{max}(1 - e^{-rx})$$

$$C_{\mathrm{Rn}}(x) = C_0 e^{-rx} + \frac{G_v}{\lambda_{\mathrm{Rn}}}(1 - e^{-rx}) \tag{2.38}$$

The radon concentration function inside the slab is plotted in Figure 2.9 for the same soil with different saturation degrees. The lower the moisture content, the higher the radon diffusion length inside the soil which reflects on a less steep rise to the asymptotic value C_{max}.

The exhalation rate, E ($\mathrm{Bq\,m^{-2}\,s^{-1}}$), is meaningful to be computed only at $x = 0$. In doing this, attention should be paid to the opposite versus of the

x-axis relative to the exhalation process at the free surface: this reflects on the minus before dx.

$$\begin{aligned} E(0) &= -D\frac{dC_{\mathrm{Rn}}(x)}{-\,dx}\bigg|_{x=0} = \\ &= D\left(\frac{G_v}{\lambda_{\mathrm{Rn}}}r - C_0 r\right) = \\ &= \frac{D}{r}\left(\frac{G_v}{\lambda_{\mathrm{Rn}}}\frac{\lambda_{\mathrm{Rn}}}{D_e} - C_0\frac{\lambda_{\mathrm{Rn}}}{D_e}\right) = \\ &= \frac{D}{D_e}\frac{\lambda_{\mathrm{Rn}}}{r}\left(\frac{G_v}{\lambda_{\mathrm{Rn}}} - C_0\right) = \\ &= \frac{\epsilon\lambda_{\mathrm{Rn}}}{r}\left(\frac{G_v}{\lambda_{\mathrm{Rn}}} - C_0\right) \end{aligned} \tag{2.39}$$

If the radon concentration at the surface is assumed to be approximately zero, Eq. 2.39 turned into the one proposed by (Nero and Nazaroff, 1984):

$$E(0) = \epsilon R G_v \tag{2.40}$$

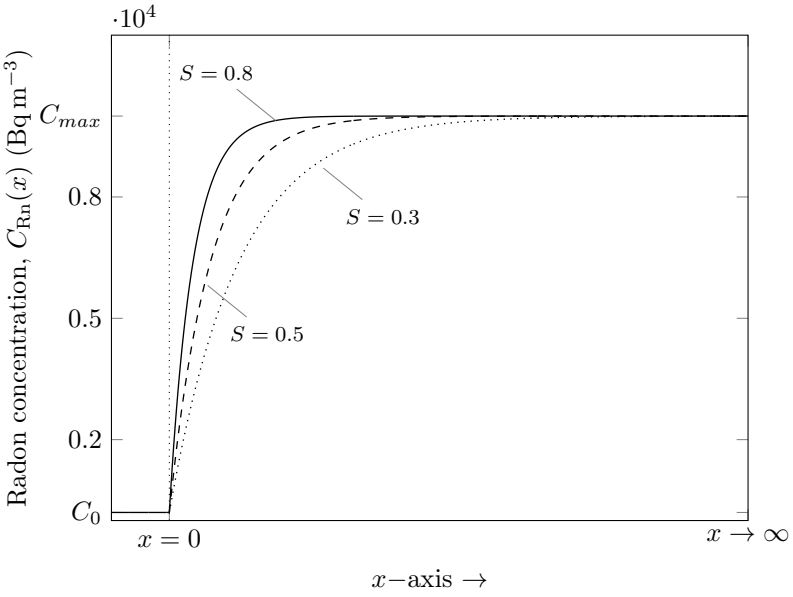

Figure 2.9: Shape of radon concentration along $x-$axis in steady state condition for soils with different saturation degrees, S. As expected, the diffusion length decreases as S increases: $R = 1.2\,\mathrm{m}$ if $S = 0.3$, $R = 0.71\,\mathrm{m}$ if $S = 0.5$ and $R = 0.41\,\mathrm{m}$ if $S = 0.8$ (Abd Ali et al., 2019). The values of the diffusion length are well fitted by the correlation proposed by Rogers and Nielson (1992).

2.3.3 Finite slab inside a vessel with unknown radon concentration inside

The last scenario has been proposed by Jonassen and McLaughlin (1980) to examine the radon exhalation rate from a sample enclosed in a vessel. Given

a slab thickness much smaller than height and width, the radon diffusion is supposed to happen only along the x-axis and, consequently, the exhalation takes place from the surface orthogonal to the diffusion direction (Figure 2.10). The radon concentration established at steady state inside the vessel is unknown.

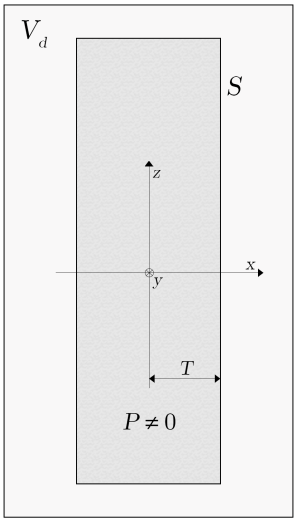

Figure 2.10: Schematic representation of a radon-exhaling sample of porous material in a closed container. The radon production rate inside the material is not neglected (i.e. $G_v = \frac{P}{\epsilon} \neq 0$). The thickness of the slab is assumed to be much smaller than the height or width. The exhaling surface is $2S$. The radon concentration inside the void volume (V_d) is homogeneous at steady state but it is unknown.

The radon concentration function inside the material is assumed to be symmetrical with respect to the y-z plane at $x = 0$, so $C_{\mathrm{Rn}}(x)$ is an even function. When the steady state is reached, the radon concentration is constant and homogeneous inside the vessel, i.e. $C_{\mathrm{Rn}}(|x| \geq T) = C_T$, and the exhalation equals the decay. The boundary conditions can be formalised as follows:

$$\begin{cases} C_{\mathrm{Rn}}(x) = C_{\mathrm{Rn}}(-x) & \text{for } -T < x < T \quad (2.41a) \\ E(T)2S = C_(T)V_d\lambda_{\mathrm{Rn}} & (2.41b) \end{cases}$$

Because of the symmetry about $x = 0$, the formulation of Eq. 2.25 leads to $A = B$. The resulting function is:

$$\begin{aligned} C_{\mathrm{Rn}}(x) &= A(e^{-rx} + e^{rx}) + \frac{G_v}{\lambda_{\mathrm{Rn}}} = \\ &= 2A\cosh(rx) + \frac{G_v}{\lambda_{\mathrm{Rn}}} \end{aligned} \quad (2.42)$$

From the second boundary condition:

$$C_{\mathrm{Rn}}(T) = \frac{E(T)2S}{V_d\lambda_{\mathrm{Rn}}} = \tag{2.43}$$

$$= -\epsilon D_e \frac{dC_{\mathrm{Rn}}(x)}{dx}\bigg|_{x=T} \frac{2S}{V_d\lambda_{\mathrm{Rn}}} =$$

$$= -\frac{\epsilon D_e 2ST}{V_d\lambda_{\mathrm{Rn}}T}(2Ar\sinh(rT)) =$$

$$= -\frac{2}{\alpha}\frac{1}{rT}(A\sinh(rT)) =$$

$$= -\frac{2}{\alpha\beta}(A\sinh(\beta)) \tag{2.44}$$

where:

$V_s = S2T$ is the volume of the slab (m^3)
$\alpha = \frac{V_d}{V_s\epsilon}$ is the ratio of the vessel volume to the void volume of the porous material
$\beta = rT$ is the ratio of the slab half-thicknes to the material diffusion length, i.e. $R = \frac{1}{r}$.

$C_{\mathrm{Rn}}(T)$ can be easily computed from Eq. 2.42 and so substituted in Eq. 2.44:

$$2A\cosh\beta + \frac{G_v}{\lambda_{chRn}} = -\frac{2}{\alpha\beta}(A\sinh(\beta)) \tag{2.45}$$

$$A = -\frac{G_v}{2\lambda_{\mathrm{Rn}}\cosh(\beta)}\left(1 + \frac{1}{\alpha\beta}\tanh(\beta)\right)^{-1} \tag{2.46}$$

Eq.2.42 can be so written as:

$$C_{\mathrm{Rn}}(x) = \frac{G_v}{\lambda_{\mathrm{Rn}}}\left[1 - \frac{\cosh(rx)}{\cosh(\beta) + 1/(\alpha\beta)(\sinh(\beta)}\right] \tag{2.47}$$

If $V \gg V_b$, i.e. the vessel void volume is much higher than the slab pore one, $\alpha \to \infty$ and, consequently, the radon concentration function gets the following formulation:

$$C_{\mathrm{Rn}}(x) = \frac{G_v}{\lambda_{\mathrm{Rn}}}\left[1 - \frac{\cosh(rx)}{\cosh(\beta)}\right] \tag{2.48}$$

The exhalation rate, E ($\mathrm{Bq\,m^{-2}\,s^{-1}}$), has to be computed at the two interfaces with the open air, i.e. $x = T$ and $x = -T$.

$$E(T) = -\epsilon D_e \frac{dC_{\mathrm{Rn}}(x)}{dx}\bigg|_{x=T} = E(-T) = -\epsilon D_e \frac{dC_{\mathrm{Rn}}(x)}{-\,dx}\bigg|_{x=-T} =$$

$$= \epsilon r \frac{D_e}{\lambda_{\mathrm{Rn}}}\tanh\beta =$$

$$= \epsilon R G_v \tanh\beta \tag{2.49}$$

The exhalation rate is the same at the two interfaces, as expected for the actual scenario modelled. According to Jonassen and McLaughlin (1980), this is the value one should expect when the porous material is used as building material for a room which is not completely sealed. The approximation gets better

when the room volume increases, with the ratio of the slab to the indoor air volume approximating zero. This could explain why Eq. 2.49 is commonly adopted by the authors when dealing with the mathematical formulation of the exhalation rate from a wall: Orabi (2018) and Sahoo et al. (2011) have recently taken the expression from Nazaroff and Nero (1988). Due to the lack, in all these works, of a clear identification and reporting of the boundary conditions underlying Eq.2.49, the latter, to the authors knowledge, is applied regardless the negligibility of the advective contribution, the radon concentration on the wall sides and the room dimension.

If the condition $V_s \gg V_b$ is not satisfied, the "net" (as it is defined by Jonassen and McLaughlin (1980)) exhalation rate gets:

$$E'(T) = E'(-T) = \epsilon R G_v \frac{\tanh \beta}{1 + \frac{\tanh \beta}{\alpha \beta}} \tag{2.50}$$

$$= \frac{E}{1 + \frac{\tanh \beta}{\alpha \beta}} \tag{2.51}$$

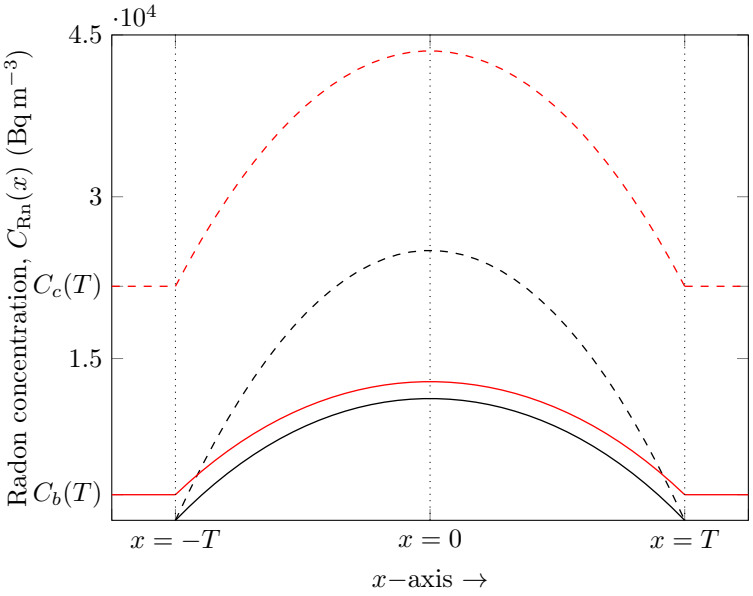

Figure 2.11: Shape of radon concentration along $x-$axis in steady state condition for walls made of bricks (full line) and concrete (dashed line) in case of $V \gg V_b$ (black) and not (red). The following values have been assumed for concrete (i) and brick(ii), respectively: i) $f = 0.24$ (Nuccetelli et al., 2018), $R = 0.69\,\mathrm{m}$ (Keller et al., 2001), $\epsilon = 0.2$ (Li et al., 2019), $C_{^{226}\mathrm{Ra}} = 59\,\mathrm{Bq\,kg^{-1}}$ (Trevisi et al., 2018), $\rho = 2.4\,\mathrm{g\,cm^{-3}}$(Dorf, 2004); ii) $f = 0.12$ (Nuccetelli et al., 2018), $R = 0.41\,\mathrm{m}$ (Keller et al., 2001), $\epsilon = 0.35$ (Hall and Hamilton, 2015), $C_{^{226}\mathrm{Ra}} = 51\,\mathrm{Bq\,kg^{-1}}$ (Trevisi et al., 2018), $\rho = 1.9\,\mathrm{g\,cm^{-3}}$ (Dorf, 2004).

Radon concentration functions of Eqs. 2.47 and 2.48 are plotted in Figure 2.11 in case of walls fully made of concrete or bricks. If the room volume is much higher than the void volume of the slab, the radon concentration in the surrounding space equals zero due to the full dilution inside the open air. When

the volume of the slab gets not negligible, the radon concentration increases both in the vessel and inside the slab.

2.4 Radon diffusive and advective transport through a slab without sources

In many circumstances, the measured radon concentration resulted to be much higher than expected by considering only the diffusion as mechanism governing the radon transport (Minkin, 2002). Basement cracks, holes and other penetrations are well recognized to be responsible of high radon entry rates into structures (Font and Baixeras, 2003). The relative importance of advection increases with increasing pressure gradient: the latter, generally of the order of $5 - 10\,\mathrm{Pa}$, rises to 15 Pa during the heating season (Chauhan and Kumar, 2015). In general under normal room condition, i.e. $\Delta p < 20\,\mathrm{Pa}$, advection is far from being negligible contributing for about 20% to the indoor radon concentration (Kendrick and Langner, 1991; United Nations Scientific Committee on the Effects of Atomic Radiation, 2000; Chauhan and Kumar, 2015).

Under the same hypotheses of §2.2, at steady state, i.e. $\frac{dC_{\mathrm{Rn}}}{dt} = 0$, the radon transport can be modelled as:

$$D_e \frac{d^2 C_{\mathrm{Rn}}(x)}{dx^2} - \lambda_{\mathrm{Rn}} C_{\mathrm{Rn}}(x) \pm \frac{k}{\mu} \frac{\nabla p}{\epsilon} \frac{dC_{\mathrm{Rn}}(x)}{dx} = 0 \tag{2.52}$$

where:

D_e is the effective diffusivity of porous medium along the x-axis, i.e. $\frac{D}{\epsilon}$ ($\mathrm{m^2\,s^{-1}}$)
ϵ is the medium porosity
C_{Rn} is the activity concentration of radon per unit volume of interstitial space ($\mathrm{Bq\,m^{-3}}$)
λ_{Rn} is the radon decay constant ($\mathrm{s^{-1}}$)
∇p is the pressure gradient ($\mathrm{Pa\,m^{-1}}$)
k is the permeability of the porous material ($\mathrm{m^2}$)
μ is the carrying fluid dynamic viscosity ($\mathrm{Pa\,s}$).

The sign of the advective term is positive if the concentration and the pressure gradient are equally oriented and negative otherwise.

The differential equation 2.10 is homogeneous and the corresponding solution is:

$$\begin{aligned} C_{\mathrm{Rn}} &= A e^{\mp \frac{k}{\mu}\frac{\nabla p}{2D} x + \sqrt{\frac{k^2(\nabla p)^2}{\mu^2 4D^2} + \frac{\lambda_{\mathrm{Rn}}\epsilon}{D}}\, x} + B e^{\mp \frac{k}{\mu}\frac{\nabla p}{2D} x - \sqrt{\frac{k^2(\nabla p)^2}{\mu^2 4D^2} + \frac{\lambda_{\mathrm{Rn}}\epsilon}{D}}\, x} = \\ &= A e^{\mp Mx} e^{Nx} + B e^{\mp Mx} e^{-Nx} = \\ &= e^{\mp Mx}\left(A e^{Nx} + B e^{-Nx}\right) \end{aligned} \tag{2.53}$$

where $M = \frac{k}{\mu}\frac{\nabla p}{2D}$ and $N = \sqrt{\frac{k^2(\nabla p)^2}{\mu^2 4D^2} + \frac{\lambda_{\mathrm{Rn}}\epsilon}{D}}$.

2.4.1 Fixed radon concentration on both wall sides of a finite slab

The advective transport has been considered together with the diffusive one for a slab with negligible radon sources by Chauhan and Kumar (2015) to model the exhalation of a concrete slab into a specially designed experimental diffusion chamber. In such a scenario, a concrete slab was exposed to a high radon concentration on a side and ventilated at the other side under an almost fixed pressure gradient ∇P. Looking at the equations from Chauhan and Kumar (2015), in that case the pressure gradient is considered to be opposite to the concentration gradient, although this condition is never made explicit. Differing from that solution, Eq. 2.53 is hereafter applied considering the same direction for both diffusive and advective contributions and arbitrary concentrations on the two sides of the slab.

From a geometrical point of view, the situation is exactly the same previously introduced by 2.4. The only difference lies in the not negligible pressure gradient existing between the two areas divided by the slab:

$$\begin{cases} C_{\mathrm{Rn}}(x=0) = C_l & \text{(2.54a)} \\ C_{\mathrm{Rn}}(x=T) = C_r & \text{(2.54b)} \end{cases}$$

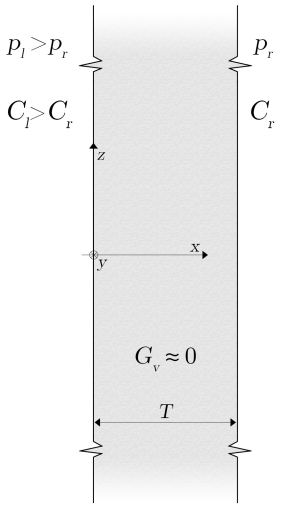

Figure 2.12: Schematic representation of a porous slab with no radon sources inside, i.e. $G_v \approx 0$, in case of not negligible pressure gradient between the slab sides. The radon concentration on both sides of the wall is constant if steady state is reached: C_l on the left and C_r on the right. Wall dimensions along y and z axes are much greater than the one along x.

From the boundary conditions:

$$A = \frac{1}{2\sinh(NT)}\left(\frac{C_r}{e^{-MT}} - C_l e^{-NT}\right) \tag{2.55}$$

$$\begin{aligned} B &= C_l - \frac{1}{2\sinh(NT)}\left(\frac{C_r}{e^{-MT}} - C_l e^{-NT}\right) = \\ &= \frac{C_l e^{NT}}{2\sinh(NT)} - \frac{C_r}{2e^{-MT}\sinh(NT)} = \\ &= \frac{1}{2\sinh(NT)}\left(C_l e^{NT} - \frac{C_r}{e^{-MT}}\right) \end{aligned} \tag{2.56}$$

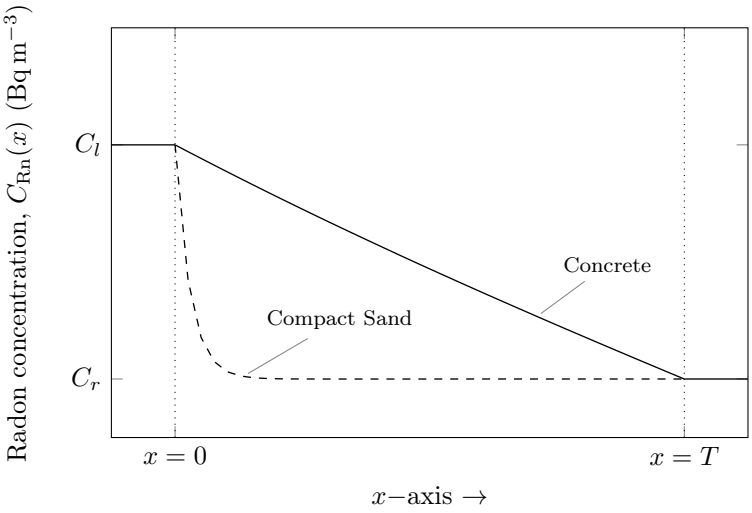

Figure 2.13: Shape of radon concentration along $x-$axis in steady state condition in case of not negligible pressure gradient between the wall sides. The following values have been assumed for concrete (i) and compact sand (ii), respectively: $i)$ $R = 0.69\,\mathrm{m}$ (Keller et al., 2001), $\epsilon = 0.2$ (Li et al., 2019), $k = 10^{-16}$ m^2 (Renken and Rosenberg, 1995; Rogers and Nielson, 1992); $ii)$ $R = 0.41\,\mathrm{m}$ (Keller et al., 2001), $\epsilon = 0.15$ (Hall and Hamilton, 2015), $k = 10^{-10}$ m^2 (Turtiainen). Additionally, for both functions the following values have been assumed for dynamic viscosity and pressure gradient: $\mu = 1.81 \cdot 10^{-5}$ Pa s (Dixon, 2007) and $\nabla P = 5\,\mathrm{Pa}$

The resulting radon concentration function, plotted in Figure 2.12 for heavy concrete and compacted sand, is obtained by substituting Eqs. 2.55 and 2.56 in Eq. 2.53:

$$\begin{aligned} C_{\mathrm{Rn}}(x) &= \frac{e^{-Mx}}{2\sinh(NT)}\left[\left(\frac{C_r}{e^{-MT}} - C_l e^{-NT}\right)e^{Nx} + \left(C_l e^{NT} - \frac{C_r}{e^{-MT}}\right)e^{-Nx}\right] = \\ &= \frac{e^{-Mx}}{2\sinh(NT)}\left[\frac{C_r}{e^{-MT}}e^{Nx} - \frac{C_r}{e^{-MT}}e^{-Nx} + C_l e^{N(T-x)} - C_l e^{-N(T-x)}\right] = \\ &= \frac{e^{-Mx}}{\sinh(NT)}\left[\frac{C_r}{e^{-MT}}\sinh(Nx) + C_l \sinh(N(T-x))\right] \end{aligned} \tag{2.57}$$

The exhalation rate, E ($\mathrm{Bq\,m^{-2}\,s^{-1}}$), computed on the right side of the wall is:

$$\begin{aligned} E(T) &= -D\frac{dC_{\mathrm{Rn}}(x)}{dx}\bigg|_{x=T} = \\ &= -D\left(-\frac{Me^{-MT}C_r}{e^{-MT}} + \frac{e^{-MT}NC_r}{e^{-MT}}\coth(NT) + 0 - \frac{NC_l e^{-MT}}{\sinh(NT)}\cosh 0\right) \\ &= D\left(\frac{NC_l e^{-MT}}{\sinh(NT)} + MC_r - NC_r\coth(NT)\right) \end{aligned} \tag{2.58}$$

2.5 Radon diffusive and advective transport through a slab with inner radon sources

In §2.3 the radon transport has been modelled by considering the diffusive contribution only: in other words the advective transport has been previously neglected similarly to many authors. However, some works exist that consider the pressure gradient, other than the concentration gradient, as causing radon migration inside porous matrix (López-Coto et al., 2014, 2013). Under all the assumptions listed in §2.1 and §2.2, if the steady state is reached, the radon concentration along the x-axis inside a porous material follows the equation:

$$D_e\frac{d^2C_{\mathrm{Rn}}(x)}{dx^2} - \lambda_{\mathrm{Rn}}C_{\mathrm{Rn}}(x) \pm \frac{k}{\mu}\frac{\nabla p}{\epsilon}\frac{dC_{\mathrm{Rn}}(x)}{dx} + G_v = 0 \tag{2.59}$$

where:

- D_e is the effective diffusivity of porous medium along the x-axis, i.e. $\frac{D}{\epsilon}$ ($\mathrm{m^2\,s^{-1}}$)
- ϵ is the medium porosity
- C_{Rn} is the activity concentration of radon per unit volume of interstitial space ($\mathrm{Bq\,m^{-3}}$)
- G_v is the radon emanation rate, or alternatively the radon production rate, per unit pore volume ($\mathrm{Bq\,m^{-3}}$)
- λ_{Rn} is the radon decay constant ($\mathrm{s^{-1}}$)
- ∇p is the pressure gradient ($\mathrm{Pa\,m^{-1}}$)
- k is the permeability of the porous material ($\mathrm{m^2}$)
- μ is the carrying fluid dynamic viscosity (Pa s).

The sign of the advective term is positive if the concentration and the pressure gradient are equally oriented and negative otherwise.

The solution of Eq. 2.59 is the sum of the homogeneous and the particular solution. The homogeneous solution is the same previously seen for the no-source case:

$$C_{\mathrm{Rn},h}(x) = e^{\mp Mx}\left(Ae^{Nx} + Be^{-Nx}\right) \tag{2.60}$$

with $M = \frac{k}{\mu}\frac{\nabla p}{2D}$ and $N = \sqrt{\frac{k^2(\nabla p)^2}{\mu^2 4D^2} + \frac{\lambda_{\mathrm{Rn}}\epsilon}{D}}$.

The particular solution has the form $C_{\mathrm{Rn}}(x) = e^{\lambda x}Q(x)$ with $\lambda = 0$ and $Q(x)$ polynomial of the same degree of G_v, i.e. 0.

$$C_{\mathrm{Rn},p}(x) = Cx^0 = C \tag{2.61}$$

By substituting $C_{\mathrm{Rn},p}$, $\frac{dC_{\mathrm{Rn},p}(x)}{dx} = 0$ and $\frac{d^2C_{\mathrm{Rn},p}(x)}{dx^2} = 0$ into Eq. 2.60:

$$D_e 0 - \lambda_{\mathrm{Rn}} C \pm \frac{k}{\mu}\frac{\nabla p}{\epsilon} 0 + G_v = 0$$

$$C_{\mathrm{Rn},p}(x) = C = \frac{G_v}{\lambda_{\mathrm{Rn}}} \tag{2.62}$$

The general solution can so be written as:

$$C_{\mathrm{Rn}}(x) = C_{\mathrm{Rn},h}(x) + C_{\mathrm{Rn},p}(x) = \\ = e^{\mp Mx}\left(Ae^{Nx} + Be^{-Nx}\right) + \frac{G_v}{\lambda_{\mathrm{Rn}}} \tag{2.63}$$

2.5.1 Fixed radon concentration on both wall sides of a finite slab

When both the pressure gradient and the radon production rate cannot be considered negligible, the radon concentration inside a finite slab dividing two volumes with fixed radon concentration, should be determine from Eq. 2.63 by following the same procedure used in §2.3.1. This scenario commonly applies to outer walls due to the pressure difference generally existing between indoor and outdoor environments mainly due to ventilation and chimney effect. In case of inner walls of workplaces and dwellings, the formulation proposed in §2.3.1 should be abounded in case of forced air circulation systems which are capable of producing significant pressure gradients between adjacent rooms.

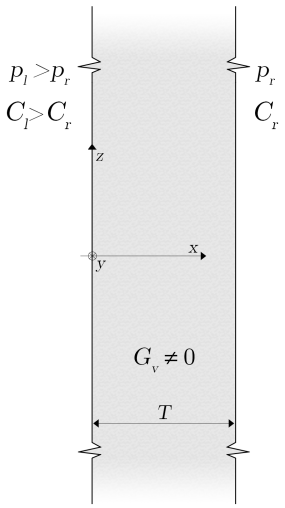

Figure 2.14: Schematic representation of a porous slab with not negligible radon production rate, i.e. $G_v \approx 0$, in case of existing pressure gradient between the slab sides. The radon concentration on both sides of the wall is constant if steady state is reached: C_l on the left and C_r on the right. Wall dimensions along y and z axes are much greater than the one along x.

Referring to Figure 2.14 and pertaining to the boundary conditions, C_l^* and C_r^* can be defined as in §2.3.1.

From the boundary conditions:

$$A = \frac{\frac{C_r^*}{e^{-MT}} - C_l^* e^{-NT}}{2\sinh(NT)} \tag{2.64}$$

$$B = C_l^* - A = \\ = C_l^* - \frac{\frac{C_r^*}{e^{-MT}} - C_l e^{-NT}}{2\sinh(NT)} = \tag{2.65}$$

$$= \frac{C_l^* e^{NT} - C_l^* e^{-NT} - C_r^* e^{MT} + C_l^* e^{-NT}}{2\sinh(NT)} = \\ = \frac{C_l^* e^{NT} - C_r^* e^{MT}}{2\sinh(NT)} \tag{2.66}$$

Moving from Eqs. 2.64 and 2.66, the radon concentration function results to be:

$$C_{\mathrm{Rn}}(x) = \frac{e^{-Mx}}{2\sinh(NT)}\left[\left(C_r^* e^{MT} - C_l^* e^{-NT}\right)e^{Nx} \right. \\ \left. + \left(C_l^* e^{NT} - C_r^* e^{MT}\right)e^{-Nx}\right] + \frac{G_v}{\lambda_{\mathrm{Rn}}} = \\ = \frac{e^{-Mx}}{\sinh(NT)}\left\{\frac{C_r - G_v/\lambda_{\mathrm{Rn}}}{e^{-MT}}\sinh(Nx) \right. \\ \left. - (C_l - G_v/\lambda_{\mathrm{Rn}})\sinh[N(x-T)]\right\} + \frac{G_v}{\lambda_{\mathrm{Rn}}} \tag{2.67}$$

On the right side of the slab, the exhalation rate, E ($\mathrm{Bq\,m^{-2}\,s^{-1}}$), is computed from Eq.2.67:

$$E(T) = -D\left.\frac{dC_{\mathrm{Rn}}(x)}{dx}\right|_{x=T} = \\ = -\frac{DMe^{MT}C_l^*}{\sinh(NT)}\sinh 0 + \frac{De^{MT}C_l^*}{\sinh(NT)}N\cosh 0 + \\ + \frac{DMe^{MT}C_r^*}{\sinh(NT)e^{MT}}\sinh(NT) - \frac{De^{MT}C_r^*}{\sinh(NT)e^{MT}}N\cosh(NT) = \\ = \frac{DNe^{MT}C_l^*}{\sinh(NT)} + DMC_r^* - DNC_r^*\coth(NT) \tag{2.68}$$

2.5.2 Fixed concentration on a side of an infinite slab

In order to take into account also the effect of the pressure gradient on the radon exhalation rate from the soil, moving from the same geometrical assumptions and boundary conditions of §2.3.2 (Eqs. 2.34), the radon concentration profile is described by the solution of the Eq. 2.53.

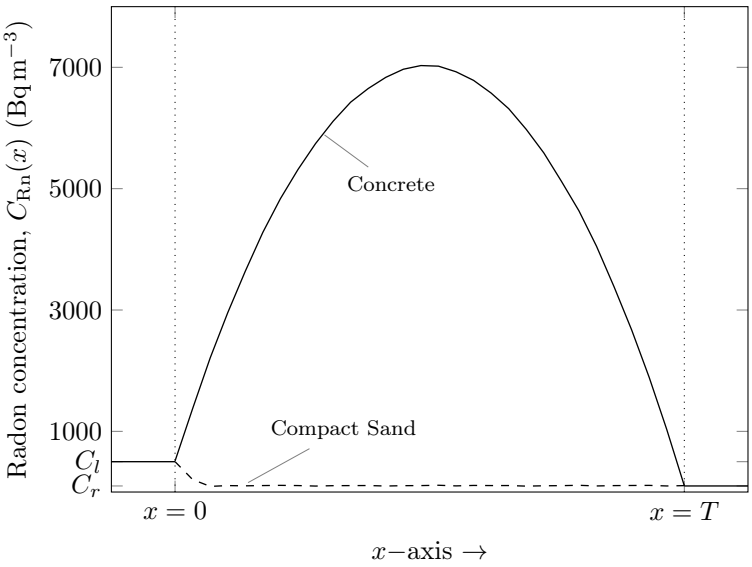

Figure 2.15: Shape of radon concentration along $x-$axis in steady state condition in case both pressure gradient and inner radon production rate are not negligible. The following values have been assumed for concrete (i) and compact sand (ii), respectively: i) $f = 0.24$ (Nuccetelli et al., 2018), $R = 0.69\,\mathrm{m}$ (Keller et al., 2001), $\epsilon = 0.2$ (Li et al., 2019), $C_{^{226}\mathrm{Ra}} = 59\,\mathrm{Bq\,kg^{-1}}$ (Trevisi et al., 2018), $\rho = 2.4\,\mathrm{g\,cm^{-3}}$(Dorf, 2004), $k = 10^{-16}$ m^2 (Renken and Rosenberg, 1995; Rogers and Nielson, 1992); ii) $f = 0.24$ (Seco et al., 2020), $R = 0.41\,\mathrm{m}$ (Keller et al., 2001), $\epsilon = 0.15$ (Hall and Hamilton, 2015), $C_{^{226}\mathrm{Ra}} = 71\,\mathrm{Bq\,kg^{-1}}$ (Seco et al., 2020), $\rho = 2.45\,\mathrm{g\,cm^{-3}}$(Manger, 1963), $k = 10^{-10}$ m^2 (Turtiainen). Additionally, for both functions the following values have been assumed for dynamic viscosity and pressure gradient: $\mu = 1.81 \cdot 10^{-5}$ Pa s (Dixon, 2007) and $\nabla p = 5\,\mathrm{Pa}$

Referring to the reference system in Figure 2.16, from the boundary conditions the constants A and B are determined:

$$A = 0 \tag{2.69}$$

$$B = C_0 - A - \frac{G_v}{\lambda_{^{222}\mathrm{Rn}}}$$

$$B = C_0 - \frac{G_v}{\lambda_{^{222}\mathrm{Rn}}} \tag{2.70}$$

where $A = 0$ because the radon concentration should be finite at $x \to \infty$ as it happens only for $A = 0$ being $N \geq M \neq 0$. The asymptotic radon concentration deep inside the porous material, i.e. C_{max}, resulted to be the same as in the solo-diffusion case (§2.3.2):

$$C_{max} = \frac{G_v}{\lambda_{\mathrm{Rn}}} \tag{2.71}$$

The resulting radon concentration is:

$$C_{\mathrm{Rn}}(x) = C_0 e^{-(N+M)x} + C_{max}(1 - e^{-(N+M)x})$$

$$C_{\mathrm{Rn}}(x) = C_0 e^{-(N+M)x} + \frac{G_v}{\lambda_{\mathrm{Rn}}}(1 - e^{-(N+M)x}) \tag{2.72}$$

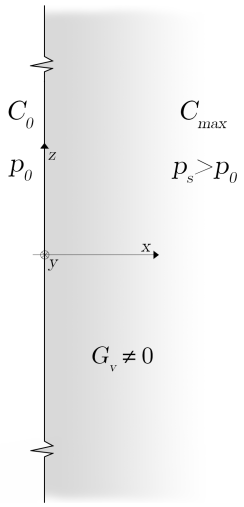

Figure 2.16: Schematic representation of a porous infinite slab, with inner radon sources (i.e. $G_v = \frac{P}{\epsilon} \neq 0$), whose right side surface is free to exhale (at $x = 0$). p_0 and p_s denote the air pressure at $x = 0$ (if the exhalation from the soil is studied, p_0 is the atmospheric pressure at sea level) and at $x \to \infty$, respectively.

The radon concentration function inside the slab is plotted in Figure 2.17 for the same soil (i.e. silt) with different saturation degrees. Analogously to what previously mentioned for the diffusion length, the lower the moisture content, the higher the radon permeability through the soil. By increasing the pressure gradient, the rise to the asymptotic value C_{max} gets smoother, especially for lower saturation degrees.

The exhalation rate, E ($\mathrm{Bq\,m^{-2}\,s^{-1}}$) at $x = 0$. In doing this, attention should be paid to the opposite versus of the x-axis relative to the exhalation process at the free surface: this reflects on to the minus before dx.

$$\begin{aligned} E(0) &= -D\frac{dC_{\mathrm{Rn}}(x)}{-\,dx}\bigg|_{x=0} = \\ &= D(N+M)\Big(C_{max} - C_0\Big) \\ &= D(N+M)\left(\frac{G_v}{\lambda_{\mathrm{Rn}}} - C_0\right) \end{aligned} \tag{2.73}$$

If the radon concentration at the surface is assumed to be approximately zero, Eq. 2.73 turned into :

$$E(0) = D(N+M)\frac{G_v}{\lambda_{\mathrm{Rn}}} \tag{2.74}$$

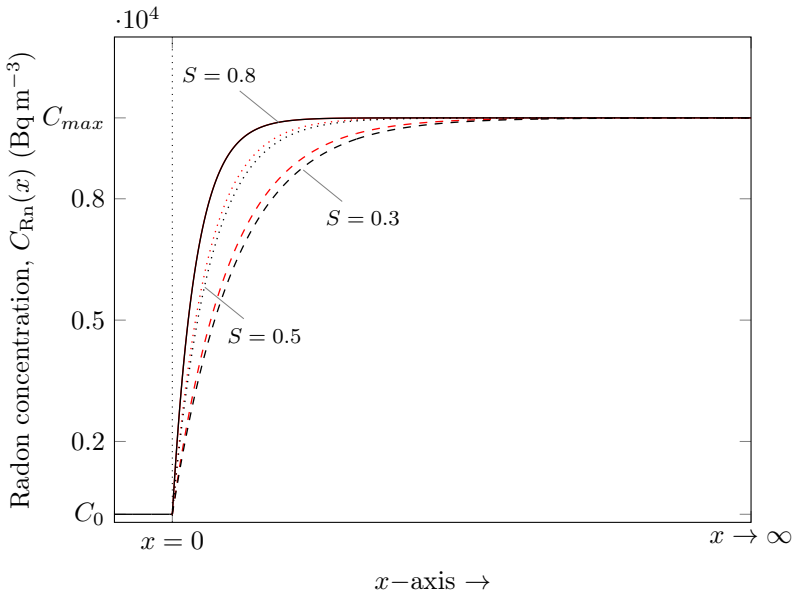

Figure 2.17: Shape of radon concentration along $x-$axis in steady state condition for a silty soil with different saturation degrees, S. The values of the diffusion length R are the same of Fig. 2.9. The permeability of dry soil has been obtained from the Kozeny theory (Nazaroff, 1992) and the values at different saturation degrees by considering the fitting function $\exp(-12S^4)$ (Rogers and Nielson, 1991). The black and red curves have been obtained considering a pressure gradient of 5 and 10 Pa respectively. $\epsilon = 0.5$ (Nazaroff, 1992). The higher the saturation degree, the higher the sum $N + M$ which gets steeper the rise to the asymptotic value C_{max}.

Chapter 3

Design and commissioning of a novel apparatus for measuring radon exhalation rate from wall surfaces

The techniques for measuring radon exhalation rate can be roughly divided in two depending on whether the measurement is intended to be performed with or without making a sample of the existing product.

The method for determining the mass exhalation rate from a building material sample is described by ISO standard 11665-9 (International Organization for Standardization, 2012b), regarding the determination of the free radon exhalation rate from a sample by using air-tight exhalation vessels. Due to the practical difficulty in assuring the perfect airtightness of the exhalation vessel, the standard method is often modified to easily overcome problems linked back diffusion and chamber leakage (Sahoo and Mayya, 2010; Ishimori et al., 2013). The latter approach has been widely adopted through the years using both continuous radon monitors (CCRMs) (e.g. Leonardi et al., 2018; Bavarnegin et al., 2013; Al-Jarallah, 2001; Al-Jarallah et al., 2001; Stranden, 1988) and solid state nuclear track detectors (SSNTDs) (e.g. Sharma et al., 2016; Amin, 2015; Saad et al., 2014; Gupta et al., 2013; Saad et al., 2010).

Despite the practicality that often characterizes the measurements performed on samples, when possible, in-situ – directly from the manufact (i.e. wall, ceiling or floor) surfaces – measurements of radon exhalation rate are often to be preferred. This is why the radon flux from room surfaces is strongly affected by some features of the actual exhalation scenario: *i*) those elements that could be referred to as installation conditions, mainly width and geometry of the slab, how units are laid in and bound together, binding elements and covering layers and *ii*) all the environmental parameters (i.e. the pressure gradient inside and outside the slab, the locals temperature and the air exchange rate) reflecting on properties of the building materials and directly influencing the radon transport phenomena. The three basic approaches for the in-situ measurement of surfaces radon exhalation flux are, according to the classification offered by the IAEA

Technical Report No. 474 (Ishimori et al., 2013), accumulation, flow through systems and adsorption. The accumulation method is based on measuring the radon activity concentration emanating from the surface under investigation inside a container of known volume. Guidelines about this method are provided by the ISO standard 11665-7 (International Organization for Standardization, 2012a).

If examples of radon exhalation rate measurements carried out through the accumulation method are not frequent (e.g. Seo et al., 2018; Yarmoshenko et al., 2018; Vaupotič et al., 2010; Schery et al., 1989), in-situ applications of this method to vertical surfaces, i.e. walls, are even rarer. To the author knowledge, no published study exists documenting measurements performed by sealing an accumulation can directly on a vertical surface of a wall: for measuring radon exhalation rate, a common practise appears to have been sealing the accumulation container to the upper surface of previously prepared samples (Feng and Lu, 2016; Sharma et al., 2014; Saad et al., 2014; Tan and Xiao, 2014, 2013, 2011; Chen et al., 2010; Aldenkamp et al., 1992). This expedient was intended to reduce the radon-rich air leakage from the can inside through the interface with the sample surface by exploiting the weight of the container, and eventually that of the detector, to improve the sealing. This leakage path is, in fact, a well documented source of error when performing such measurements Noverques et al. (2019). Making the container air tight on the surface under investigation can get even worse when operating with surfaces with irregularities. Together with the inadequate air tightness at the sealing, the back-diffusion could introduce radon loss consequently leading to underestimated radon flux (International Organization for Standardization, 2012a).

The solution available on the market for measuring radon exhalation rate from vertical surfaces are generally affected by some problems:

i) they are not specifically designed for vertical surfaces so they are not self-standing apparatuses equipped with a frame supporting the accumulation can,

ii) they are not provided with sealing system of any kind, *iii*) they are sold by the continuous radon monitor manufacturer, so the compatibility is assured only with a specific model of a specific detector,

iv) the air exchanges between inside and outside the accumulation container, other than not being prevented, are not traceable at all,

v) the analysis of the radon concentration registered to obtain the exhalation rate value is a quite slow, multi-step and not automatized process completely up to the operator.

This work deals with the design and the commissioning of the first custom apparatus specifically conceived to in-situ measure the radon exhalation rate directly from walls vertical surfaces. The apparatus hereafter presented and discussed has been already successfully used in some surveys in large buildings in order to reconstruct the likely radon migration path by measuring the surface flux at different locations in different rooms.

3.1 Materials and methods

All the apparatus has been realized by using products available on the market in order to allow all the interested laboratories to build their own systems for exhalation rate measurements.

3.1.1 Accumulation container

The container has been chosen following four criteria: *i*) it should be made of a radon tight material, *ii*) the contact profile should be so as to ensure a large contact between the base of the accumulation container and the surface under investigation, *iii*) the chamber inner surface should be as flat as possible to allow a better computation of the inner volume (according to ISO standard (International Organization for Standardization, 2012a) the volume uncertainty should be lower than 10%), *iv*) the chamber should not result flexible at all in order to avoid the volume to change during the measurement.

Referring to *i*), the high density polyethylene (HDPE) has been found to be a good compromise between cost, rigidity and durability. The HDPE characteristics in terms of radon tightness have been observed to be excellent: the radon diffusion coefficient ranges from $5 \cdot 10^{-12}$ $m^2\,s^{-1}$ to $1 \cdot 10^{-11}$ $m^2\,s^{-1}$ which is considered an optimal range for minimizing the radon transport through diffusion(Jiránek and Hůlka, 2001). The convective transport is not of interest for reasons that will later be clear, so the permeability is not discussed. A thickness of 5 mm has been chosen for the can sides, being such a value well above the insulating minimum thickness recommended for membranes made of HDPE (Jiránek and Hůlka, 2001).

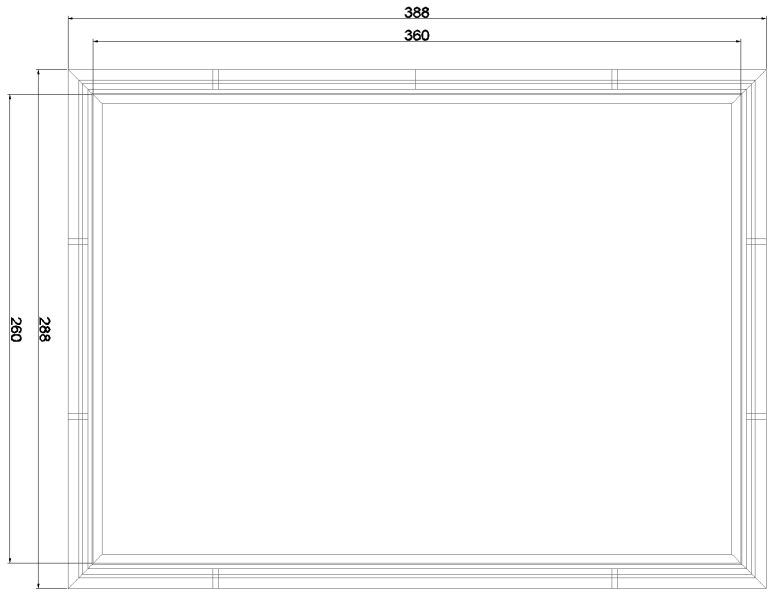

Figure 3.1: Horizontal section of the accumulation chamber at the free-surface level. For both length and width are reported, in millimeters, internal and external dimensions.

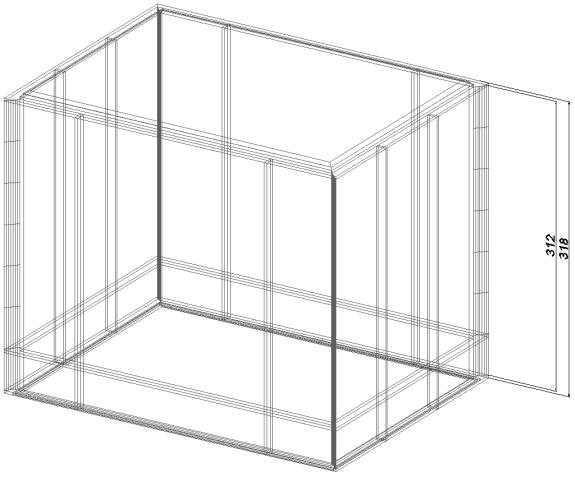

Figure 3.2: Axonometric view of the accumulation chamber. Internal and external heights are reported in millimeters.

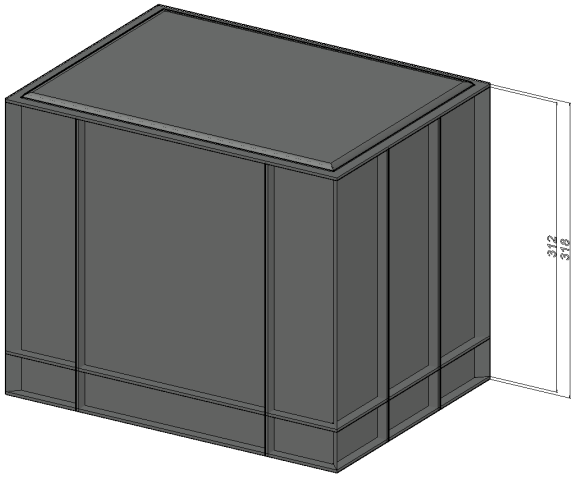

Figure 3.3: Axonometric realistic view of the accumulation chamber. The supports externally running along the chamber are visible as well as the rectangular frame of the free surface. Internal and external heights are reported in millimeters.

The final concept of the accumulation chamber is reported in Figures 3.1, 3.2 and 3.3. The dimensions have been chosen as a compromise between two needs: increasing the volume to retard, and contemporary reduce, the incidence of the back-diffusion phenomenon, and containing the can size to make the overall apparatus compact and portable. In increasing the volume, attention has been paid in making the free-surface wider than the others in order to increase the "resolution" of the exhalation rate returned by the system: the exhalation source term, in fact, influences the radon concentration, being directly proportional to the free-surface area and indirectly to the chamber volume. The final dimensions are listed in Table 3.1 together with the corresponding measurement uncertainties mainly linked with the instrumental accuracy. The relative

uncertainty of the measured inner volume is about 3%, well below the value recommended by the ISO standard 11665-7.

Table 3.1: External and internal dimensions of the accumulation chamber designed for the apparatus to measure radon exhalation rate.

	Internal	External
Length	360±5 mm	388±5 mm
Width	260±5 mm	288±5 mm
Height	312±5 mm	318±5 mm
Volume	29.20±0.84 L	35.53±0.95 L

In order to satisfy the requirement *ii*), the contact surface has been conceived with a rectangular frame 14 mm-thick covering an overall area of 18 cm^2 (±3 cm^2). At the center of such a frame, a rectangular fluting 2 cm-thick and 2 mm-deep has been realized (see Figure 3.4): it allows to insert a 2 mm-thick rectangular frame inside the larger one in case of very flat walls in order to increase to sealing pressure by reducing the contact surface. When the irregularity of the investigated wall are not significant, a reduction of the contact area can be accepted in favor of a higher sealing pressure, the latter obtained without acting on the pushing force.

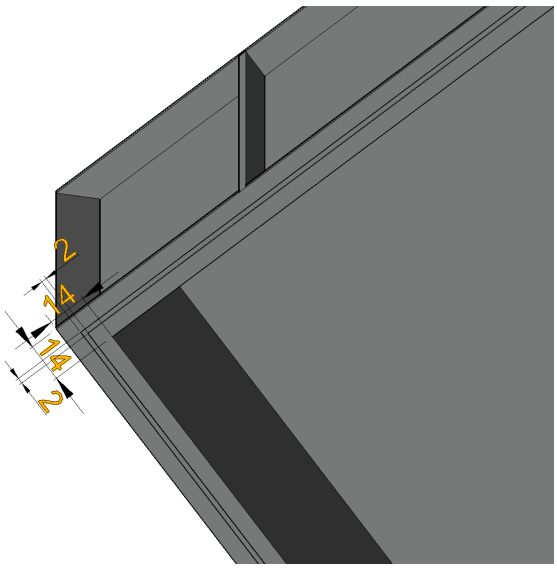

Figure 3.4: Axonometric realistic view of the rectangular frame of the accumulation chamber interface surface. Dimensions are reported in millimeters.

Experiments aiming to evaluate eventual surfaces bend have found that the thickness of 5 mm is not enough to grant the rigidity of the accumulation can so designed. In order to reduce undesired volume changes due to, for example, inside-outside pressure differences, all the lateral surfaces have been equipped with two parallelepipedic supports which externally run along the whole chamber height (see Figure 3.3). At 4 cm from the rectangular a fifth support runs parallel to the frame itself along all the lateral surfaces: this expedient allows

to increase the can rigidity in the most stressed region, i.e. close to the free surface.

3.1.2 Carrying and sealing structure

The all-in-one structure has been designed and assembled with the aim to realize a ready-to-use apparatus capable to minimize and simplify the procedure needed to install the accumulation chamber on the wall and start measuring the radon exhalation rate from the surface. In order to allow other interested laboratories to build their own apparatuses in the easiest and fastest way, all the elements and materials employed have been chosen according to three criteria: *i*) availability on the market; *ii*) low cost and *iii*) ease of installation and processing.

3.1.2.1 Metal chassis

The metal chassis has been entirely realized by an anodized aluminum 30 mm x 30 mm profile whose horizontal section, enriched with all the interest measurements, is reported in Figure 3.5.

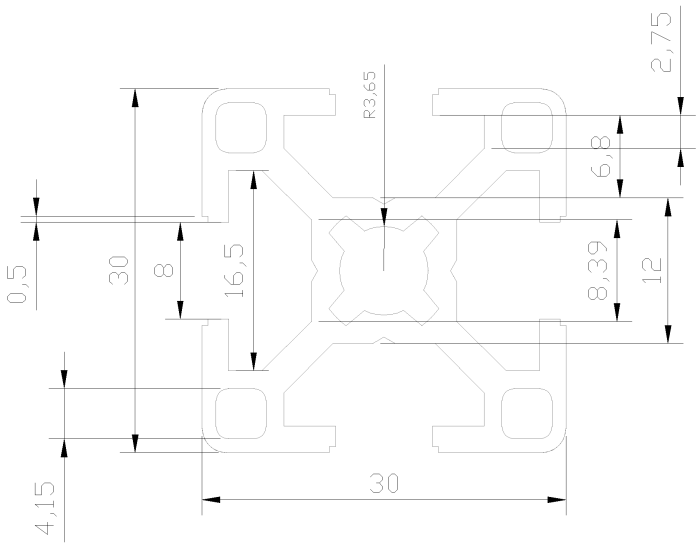

Figure 3.5: Horizontal section of the anodized aluminum profile used to assemble the apparatus chassis. Dimension are in millimeters.

Profile geometry and material are both optimized to assure great flexural strength (section modulus $W = 1.92\,\mathrm{cm}^3$) and low weight (mass per unit length $G = 0.91\,\mathrm{kg\,m}^{-1}$).

Angle brackets have been used to assemble together the different profile pieces. The fastening is assured by a properly shaped nut fitting inside the groove of the profile and screwed on a the bracket bolt. The bracket is kept in the proper position by two fins lodged in the profile grove when the bracket is the right position. Figure 3.6 and Figure 3.7 show the horizontal sections and the two axonometric views of the angle bracket coupled with the corresponding two pairs of bolts and nuts.

Specifically designed rubber stopper have been used to cover the aluminum profiles ends for safety reasons (Figure 3.8).

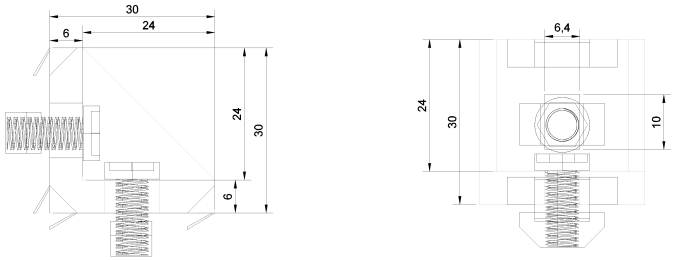

(a) xz Top View (b) yz Top View

Figure 3.6: Angle bracket for aluminum profiles assembling: horizontal sections. Dimensions are in mm.

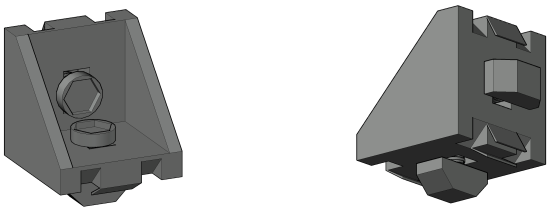

(a) Front View (b) Back View

Figure 3.7: Angle bracket for aluminum profiles assembling: axonometric views.

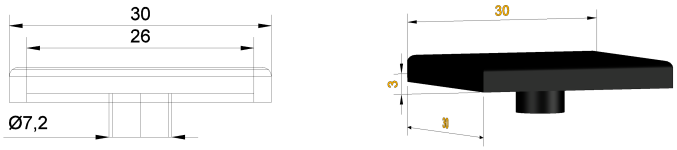

(a) xz Top View (b) Axonometric View

Figure 3.8: Rubber stopper for aluminum profiles ends. Dimensions are in mm.

The resulting metal chassis is reported in Figure 3.9 (a) and (b) and Figure 3.10 (a) and (b). The structure is 40 cm-wide and 80 cm-long whereas its height can vary from 72 cm to 125 cm by simply fixing the horizontal plain at different vertical position (in Figure 3.9 (a) the plain is set at 40 cm from the floor). The idea of realizing a structure that allows to change the position, along the vertical axis, of the accumulation chamber comes from the desire to allow exhalation measurements at different heights with the same apparatus. This feature could provide a significant help in various scenarios: i) in case of electrical wall outlets otherwise making the measurement not feasible, ii) in case of existing

cavities, at unknown positions inside the wall, that could highly influence the returned radon flux, *iii*) when there is the need, and the possibility, to avoid wall irregularities by changing the vertical position of the can.

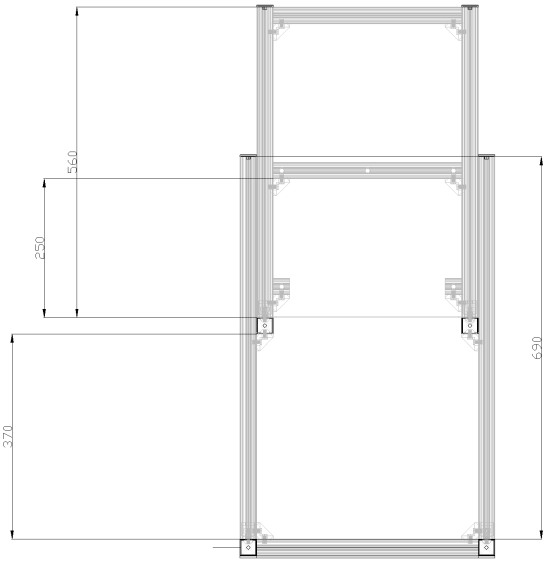

(a) xz Top View

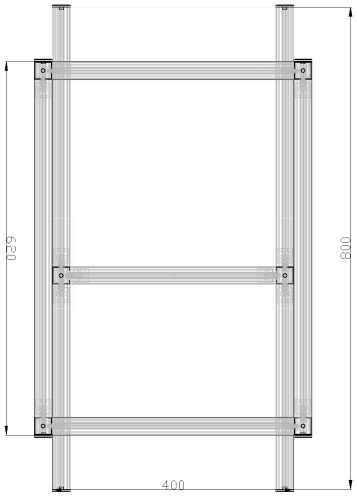

(b) xy Top View

Figure 3.9: Horizontal and vertical section of the designed apparatus metal chassis. Dimensions are in mm.

The bottom surface of the metal chassis is fully covered by a neoprene 4 mm-thick layer (visible in Figure 3.10) with the purpose to increase the friction coefficient between the chassis and the underlying pavement and to avoid the degradation of aluminum profiles composing the bottom rectangular frame.

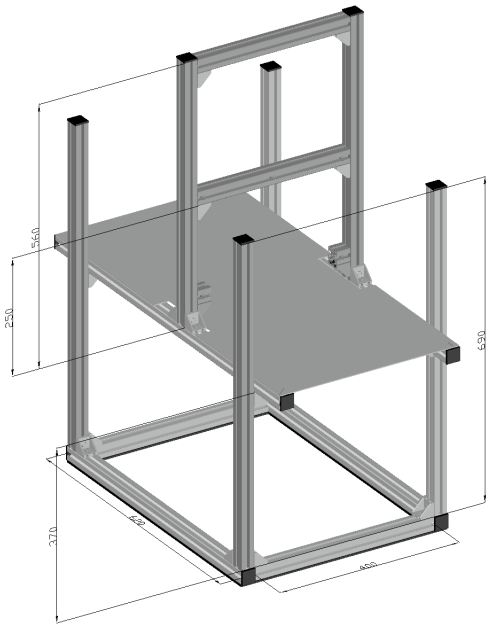

(a) Front View

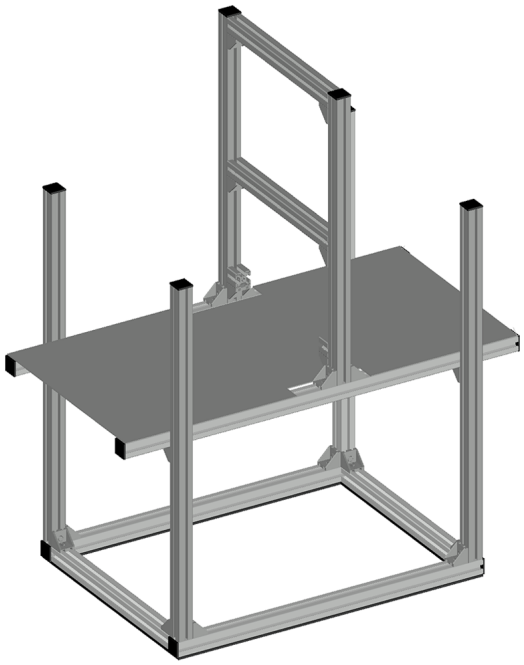

(b) Back View

Figure 3.10: Axonometric views of the designed apparatus metal chassis. Dimensions are in mm.

3.1.2.2 Sealing mechanism

Different techniques to seal the accumulation container have been considered and studied in depth. The adopted solution is reported in Figure 3.11 and it is based on the elastic force exerted by five springs that are mounted on five cylindrical supports passing through the chassis and being blocked by a spine. The cylindrical supports are coupled with wider polyvinyl chloride (PVC) cylindrical stoppers in order to avoid damaging the back of the accumulation can.

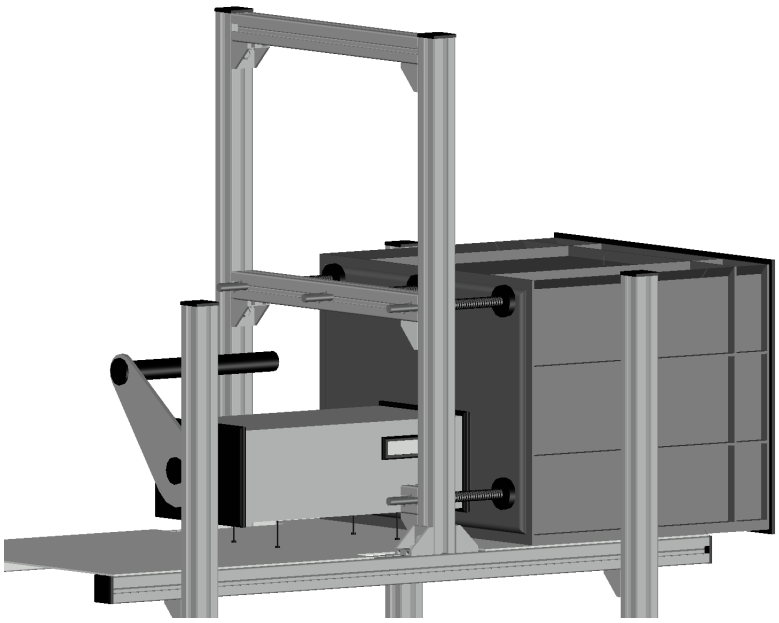

Figure 3.11: Axonometric view of the sealing mechanism designed for the accumulation chamber.

Each spring has been assembled by putting in series two equal 4 cm-long springs for an overall length of 8 cm. The elastic constant of the spring has been evaluated by a lifting experiment performed using a METTLER TOLEDO's 1 kg calibrated weight (ME-216518). A spring lengthening of 4 mm has been observed so leading to $k = 25 \pm 3\,\mathrm{N\,cm^{-1}}$. The elastic constant of each series can be computed as:

$$k_s = \frac{1}{\frac{1}{k_1} + \frac{1}{k_2}} = \frac{k_1 k_2}{k_1 + k_2} \tag{3.1}$$

In the presented case $k_1 = k_2 = k$, so $k_s = \frac{k}{2}$ and $\Delta k_s = \frac{\Delta k}{2}$.

$$k_s = 12 \pm 2\,\mathrm{N\,cm^{-1}} \tag{3.2}$$

The minimum length of each spring series is 3 cm, i.e. the maximum compression is 5 cm (Figure 3.12). The overall elastic force exerted by the five springs in case of full compression can be easily computed as $F_{el} = 5 k_s \Delta x = 300 \pm 60\,\mathrm{N}$. Considering the surface of the rectangular frame $S_f = 18 \pm 3\,\mathrm{cm^2}$, the resulting sealing pressure applied to the wall is $P = \frac{F}{S_f} = \frac{300}{18} = 17 \pm 4\,\mathrm{Pa}$.

As clearly visible in Figures 3.11 and 3.12, the rectangular frame at the chamber open surface has been covered with 4 mm-thick frame made of a radon-tight rubber. Such a layer, when subjected to the sealing pressure P above computed, gets squeezed, increasing its tightness due to both a reduction in the material porosity and a better adherence to the wall surface eventually including irregularities.

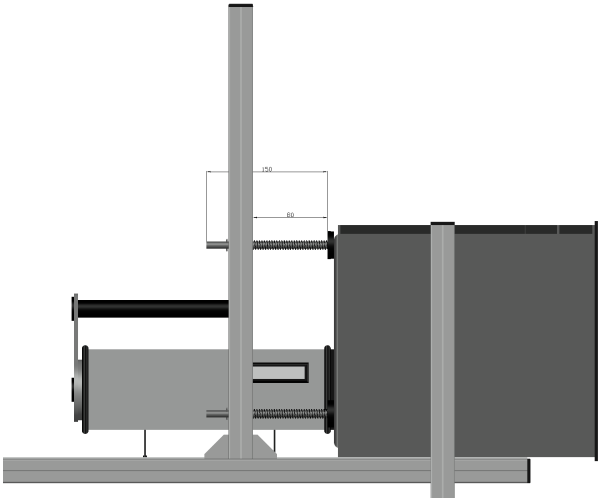

(a) Maximum release phase

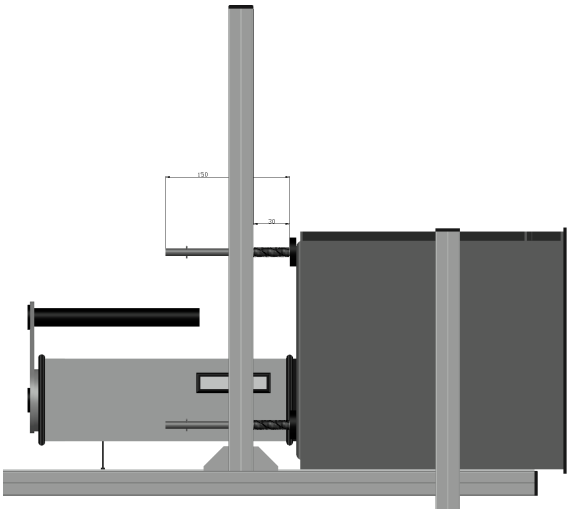

(b) Maximum compression phase

Figure 3.12: Vertical sections of the apparatus during the maximum release (a), i.e. $\Delta x = 0\,\text{cm}$, and the maximum compression (b), i.e. $\Delta x = 5\,\text{cm}$, phases. All the dimensions are in mm.

3.1.3 Continuous Radon Monitor

The apparatus has been designed for a specific continuous radon monitor (in the following often referred to as CRM) model but the configuration can be adapted with few modifications to other commercial radon detectors. This choice was mandatory due to the need of maximizing the radon tightness at the interface between the radon accumulation chamber and the CRM window. The target detector has been the AlphaGUARD (manufactured by Bertin Instruments) PQ2000 Pro but the model PQ2000 is supported as well.

The AlphaGUARD is an ion chamber detector (Genitron InstrumentGmbH, 2012). Its high sensitivity (the highest among active radon detectors), i.e. $0.05\,\mathrm{cpm\,Bq^{-1}\,m^3}$, and wide measuring range, i.e. $2 - 2\,000\,000\,\mathrm{Bq\,m^{-3}}$, have contributed to affirm this detector as a reference instrument for radon metrology. In the model PQ2000 Pro, the radon can enter the chamber driven by concentration or pressure gradient depending on the selected functioning mode: *i*) in diffusion mode the air crosses the filtering window by molecular diffusion only, whereas *ii*) in flow mode an external volumetric pump forces the radon entry into the chamber. When in diffusion mode, the detector returns an updated value of radon concentration once every 10 or 30 minutes. The flow mode significantly increases the number of counts registered within a certain time interval so returning updated radon concentration values every 1 or 10 minutes.

The only known geometrical parameter pertaining to the cylindrical ion chamber is its active volume, V_a=0.56 L. A pretty good estimation of the inner diameter can be obtained by considering that the chamber must be large enough to allow the alpha particles emitted from ^{222}Rn, ^{218}Po and ^{214}Po alpha decays to stop inside the active volume of the chamber. A first diameter approximation could be so obtained by considering the size of the chamber window and the range of the interest alpha particles, i.e. 4 cm in air. For the active volume, a diameter of 7.2 cm and an height of 14 cm is considered likely (Centomani et al., 2018).

The chamber window hosts a large-surface glass fiber filter through which only the gaseous radon-222 may pass, while the radon progeny is prevented to enter the ionization chamber. The filter also acts as a protective barrier against chamber surface contamination by dusty particles.

The center electrode, the cathode, is at 0 V voltage and its output works as the input of the highly sensitive preamplifier unit. The lateral surface is at a potential of +750 V and it is the chamber anode. The signals elaborated by the preamplifer is transmitted to an electronic network for further digital processing. Such a processing is realized by three independent and contemporary signal processing channels, each working with a specific analog-digital converter (ADC) and each analyzing the entering signal simultaneously. Among the three channels, the first operates in pulse mode and is the spectrometric channel of the AlphaGUARD, performing a signal characterization according to voltage pulse height and shape. Channel 2 and 3, the latter operating in current mode, are only effected with high and extreme radon concentrations respectively.

Some details about the AlphaGUARD algorithm have been discussed by Centomani et al. (2018).

3.1.3.1 CRM connection to the accumulation can

The connection of the AlphaGUARD PQ2000 Pro to the accumulation can is crucial to avoid radon losses to the surrounding air. The continuous diffusion measurement method (International Organization for Standardization, 2012a) was chosen because there is no need of prevalence source, i.e. pumps, to drive the air flux inside the detector chamber. Using a pump could lead the air pressure inside the chamber to vary and this could reflect on an overestimation of the exhalation rate measured by the apparatus.

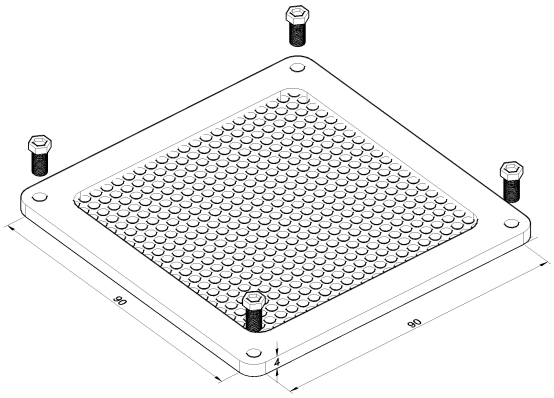

Figure 3.13: Axonometric view of the AlphaGUARD diffusing window grid. The element has been digitized to properly design the CRM-can coupling. Dimensions are in mm.

The CRM-accumulation can coupling has been realized using the AlphaGUARD native diffusing grid (Figure 3.13) inside and a 4 mm-thick neoprene rectangular frame outside as fixing elements. The final assembling is fully visible in Figure 3.14 in both internal (b) and external (a) views.

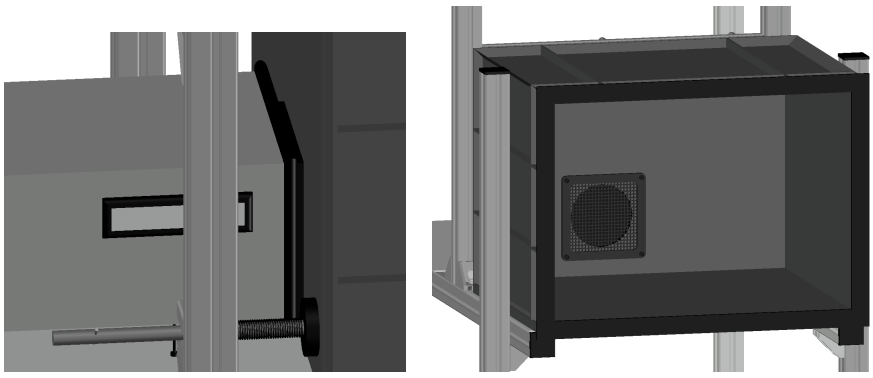

(a) Outside View (b) Inside View

Figure 3.14: Axonometric views of the connection between the CRM's diffusing window and the accumulation container.

The neoprene layer is externally placed between the chamber bottom basis and the detector in order to assure the screwing to be radon-tight. The bolts, in fact, are screwed to the AlphaGUARD window frame passing through the neoprene layer which ends up being compressed by the screwing itself.

3.1.4 Analysis of involved forces

During the maximum springs compression phase, the forces applied on the apparatus are:

- $\boldsymbol{F}_p$, the apparatus overall weight force
- $\boldsymbol{F}_a$, the friction force produced by the interaction of the neoprene bottom layer and the underlying floor
- $\boldsymbol{N}_y$, the vertical constraint reaction exerted by the floor on the apparatus as a reaction to the overall apparatus weight
- $\boldsymbol{N}_x$, the horizontal constraint reaction exerted by the vertical wall on the apparatus as a reaction to the elastic force applied to the wall by the chamber frame.

The apparatus contemporary exerts $\boldsymbol{F}_{ar}$, i.e. the reaction to the friction force, on the floor and $\boldsymbol{F}_{el}$ on the wall due to the springs compression.

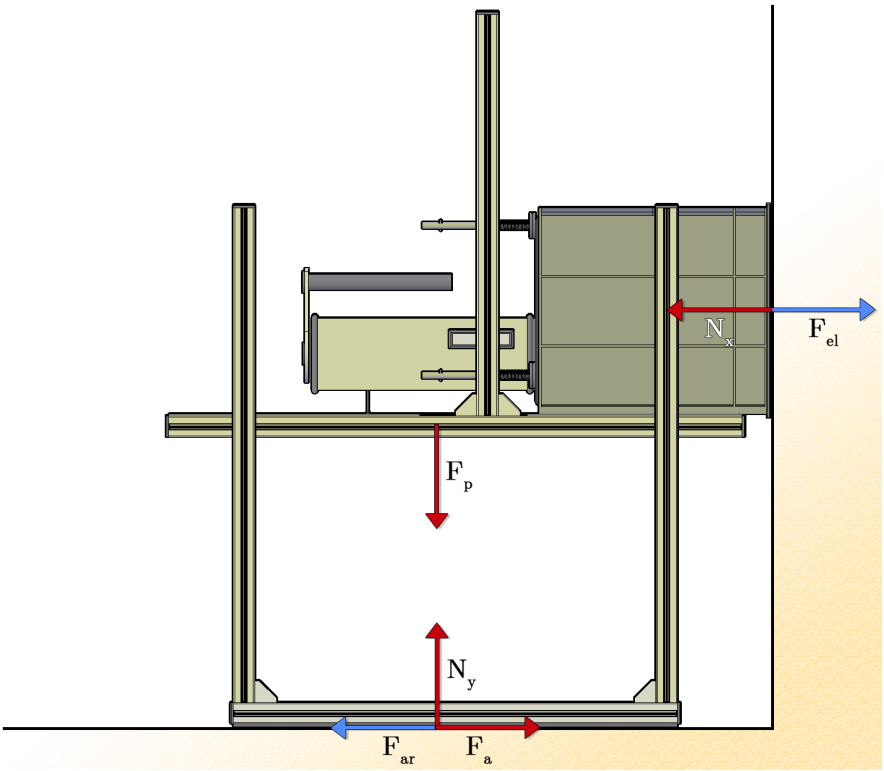

Figure 3.15: Schematic diagram of the forces involved in the sealing of the accumulation container to an investigated vertical wall. In red the forces exerted **on** the apparatus, in light blue those applied **by** the apparatus.

In order to assure the system to be in rest, the forces sum along horizontal and vertical direction should be both equal to zero, i.e. $\sum_{i=1}^{n} F_x = 0$ and $\sum_{j=1}^{n} F_x = 0$.

$$\begin{cases} F_a - N_x = 0 & \text{(3.3a)} \\ N_y - F_p = 0 & \text{(3.3b)} \end{cases}$$

where $F_a = F_{ar}$ and $N_x = F_{el}$. The equality in vertical direction is simply assured by the reaction of the floor to the apparatus weight. Along the x-axis, if the contact between the apparatus and the floor does not determine enough friction, the apparatus tends to move to the left until reaching the position in which the elastic force $F_{el} = N_x$ decreases to F_a. Thus, in order to assure the system to remain in the proper position, i.e. with the springs fully compressed, the friction force should be high enough to counterbalance the elastic force. To do so, the system is equipped with four 2.5 kg portable weights that can serve as ballast, in case of necessity, to increase the weight of the apparatus and in turn the friction force. This complication is made unavoidable by the different floor surfaces an operator could encounter, each characterized by a different friction coefficient with neoprene and each needing a different weight force to assure the apparatus to be in rest.

3.1.5 Connecting the accumulation chamber to the external environment

In normal condition, i.e. no measuring apparatus installed to the wall, the receiving ambient in radon exhalation phenomenon is the room free volume at a certain pressure. When an accumulation can is applied to the wall, especially if the sealing is well designed and realized, the receiving ambient becomes the can volume. The receiving pressure so increases with time during the measurement due to the radon-enriched air exhaled from the wall entering the chamber with no possibility of leaving it. This increasing pressure affect the radon exhalation by reducing the component transported through the wall by the pressure difference, i.e. the advective contribution to radon exhalation decreases with time during measurement. From this the idea of putting in communication the air inside the can to the outside one in order not to introduce perturbation in the measurement of radon exhalation rate. To do so, the air has to be free to escape from the accumulation chamber through a specifically conceived hydraulic connection that assures the pressure equality between inside and outside the chamber. However, the radon contained in the air exchanged through the realized connection has to be considered within the analysis so the amount of air leaving or entering the chamber, and the corresponding radon content, should be monitored, counted and registered.

The connection has been realized by drilling a passing hole (diameter 5 mm) on the bottom surface of the accumulation chamber. Through the hole a taper straight fitting push-on (6/4 mm x G1/8" BSPT-M, made of stainless steel, Figure 3.16) has been installed. An o-ring has been placed outside between the chamber and the hexagonal fixed nut: the sealing is so assured by the o-ring compression granted by the screwing of an internal nut.

The external side of the adapter is connected to a tube made of polytetrafluoroethylene (PTFE), in the following usually referred to simply as teflon) with

inner (ID) and outer (OD) diameters of 6 mm and 8 mm respectively. The tube is fixed to the adapter by a screwing nut (Figure 3.19). PTFE is a radon-tight material traditionally employed in radon facility (e.g. Centomani et al., 2019). The length of the tube has to be reduced as much as possible in order to assure the lowest pressure drop through it.

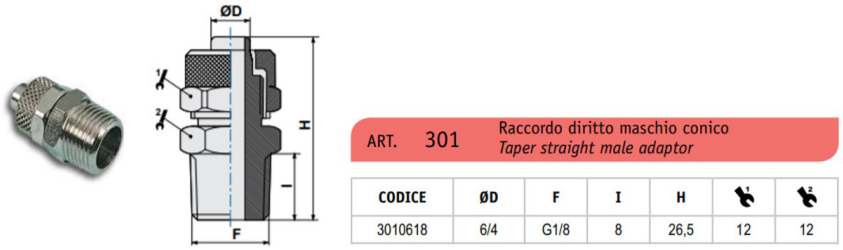

CODICE	ØD	F	I	H	1	2
3010618	6/4	G1/8	8	26,5	12	12

Figure 3.16: Image, longitudinal section and technical specifications of the taper straight male adapter 6/4 mm x G1/8" BSPT-M.

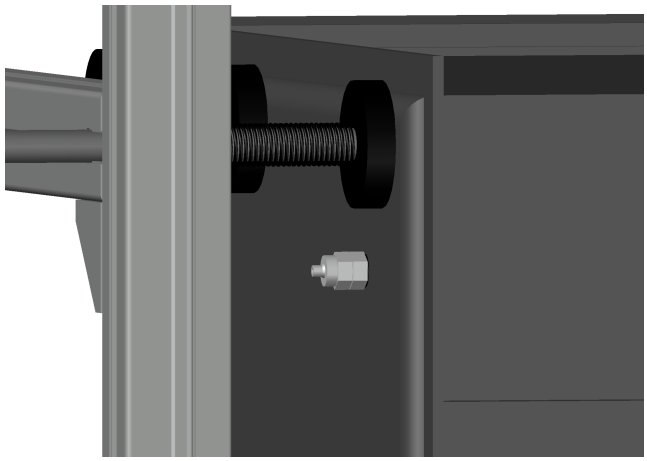

Figure 3.17: Axonometric view of the male adapter connection to the accumulation chamber. In the figure, the hexagonal fixed nut lies on the black o-ring and the screwing nut used for tube fixing is in the bottom end stop, the position to be assured when a tube is connected to the adapter.

Along the PTFE tube the air flow rate is monitored by an high accuracy airflow sensor manufactured by Honeywell (Zephyr Honeywell, 2012). The measuring range of the selected device is ±50 sccm[1]. This range has been chosen among the available standards as the best compromise between measurement resolution – increasing with decreasing range – and avoiding output saturation during normal operation. The device is DC 2.5 V powered and the corresponding output voltage range is [-0.3;2.5]V. The transfer function from the output voltage (in volt) to the measured flow rate (in sccm) is:

$$\Gamma_m = \Gamma_{FS} \frac{\left(\frac{V_o}{V_s} - 0.5\right)}{0.4} \tag{3.4}$$

[1]Standard cubic centimeters per minute. It is a flow rate measuring unit non-SI.

where:

Γ_m is the measured flow rate (sccm)
Γ_{FS} is the full scale flow rate, i.e. 50 sccm
V_o is the output voltage (V)
V_s is the supply voltage, i.e. 2.5 V.

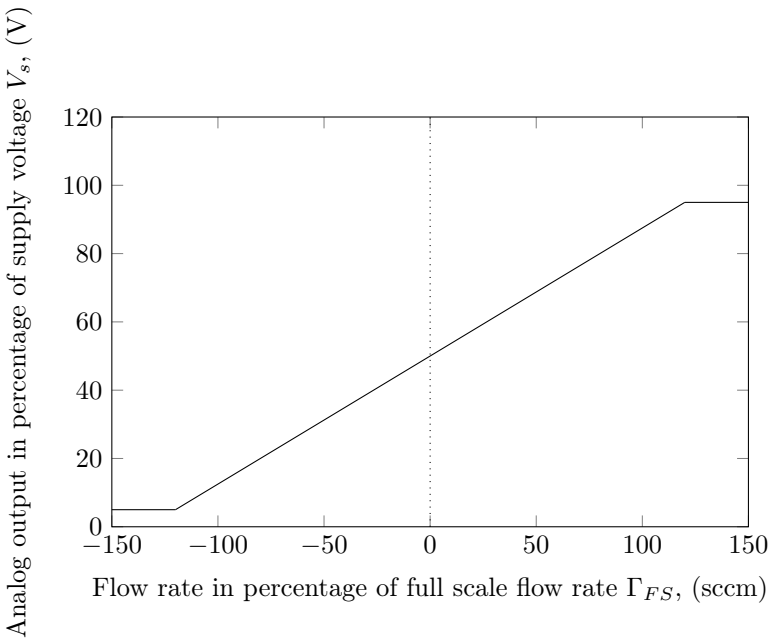

Figure 3.18: Transfer function of Honeywell Zephyr™analog airflow sensor ±50 sccm HAF Series. $\Gamma_{FS} = 50$ sccm and $V_s = 2.5$ V.

The output analog signal (V_{analog} and GND pins) is connected to a multichannel voltage data logger – PicoLog® 1012– manufactured by pico® Technology. The device has a resolution of 10 bits and a sampling rate of 1 kHz. It is powered from a USB port and it is equipped with a software that can be programmed to record the analog signals read (vs. time) and to write them on a file. An example of an output file is here reported.

```
Flow Rate Measurements
Time (s) Voltage (V)

0 1.247
1 1.245
2 1.244
3 1.246
4 1.245
5 1.245
```

In order to convert the voltage array to the corresponding flow rate array, a Python code has been written.

```
#Importing the numpy library.
import numpy as np

#Defining a function to recognize the real numbers.
def isReal (s):
    if len(s)==0:
        return False
    return s.isdigit() or (s[0] in "+-" and s[1:].isdigit()) or
(s.count(".")==1 and (s.replace(".","1")).isdigit())
or (s.count(".")==1 and (s.replace(".","1"))[0]
in "+-" and (s.replace(".","1"))[1:].isdigit())

#Receiving as input the name of the PicoLog 1012 output file.
file_name=raw_input("Flow Rate Input: ")
file_name=file_name+".txt"
#Opening and reading the input file
f_in=open(file_name,"r")
fread=f_in.read()
#Removing the first three rows that do not contain readings.
rows_fread=fread.split("\n")
rows_fread.remove(rows_fread[0])
rows_fread.remove(rows_fread[0])
rows_fread.remove(rows_fread[0])

#Initializing the list of voltages recorded
Voutput=[]

#Selection, for each row, of the voltage value.
#A tab separates time (in seconds) from read voltage (in volt).
#Once selected, each voltage value is appended to Voutput list.
for i in range(len(rows_fread)):
    row=rows_fread[i]
    if "\t" in row:
        row_splitted=row.split("\t")
        Voutput.append(row_splitted[1])

#Converting the voltage values, read as string, to float.
for i in range(len(Voutput)):
    Voutput[i]=float(Voutput[i])

#Converting the list Voutput to the numpy array VOutput.
VOutput=np.array(Voutput) #[V]
#Applying the transfer function to VOutput to obtain the flow rate array
FlowRate=50.*(VOutput*2./5.-0.5)/0.4 #[cm^3 min^-1]
FlowRate=FlowRate*10**(-6)/60. #[m^3 s^-1]

#Opening the output file and writing the FlowRate array on it.
f_out=open("FlowRate_Measurements.txt","w")
for i in range(len(FlowRate)-1):
    f_out.write(str(FlowRate[i]))
```

```
    f_out.write("\n")
f_out.write(str(FlowRate[len(FlowRate)-1]))
#Closing the output file.
f_out.close()
```

3.1.6 Radon concentration inner and outer monitoring

The radon concentration needs to be monitored both inside and outside the accumulation chamber: the reason for this will be later made explicit when dealing with the description of the theoretical model adopted. The monitoring inside the chamber is realized by an AlphaGUARD PQ2000 (or PQ2000 Pro) connected as shown in §3.1.5. The radon concentration in the room indoor air can be monitored by any continuous radon monitor with a sensitivity high enough to assure reliable values of concentration at least every hour. In the experiments later reported, an AlphaGUARD PQ2000 Pro has been used for such a purpose.

Analogously to what introduced for flow-rate output optimization, a Python code has been specifically written to read the radon concentration values from the files downloaded from detectors via the native software (i.e. DataVIEW). The code, hereafter presented, has been joined with that previously presented for flow-rate.

```
import numpy as np

def isReal (s):
    if len(s)==0:
        return False
    return s.isdigit() or (s[0] in "+-" and s[1:].isdigit())
or (s.count(".")==1 and (s.replace(".","1")).isdigit())
or (s.count(".")==1 and (s.replace(".","1"))[0]
in "+-" and (s.replace(".","1"))[1:].isdigit())

#Receiving as input the name of the inner AlphaGUARD PQ2000 Pro
#output file.
file_name=raw_input("Internal AlphaGUARD Data: ")
file_name=file_name+".txt"
#Opening and reading the input file
f_in=open(file_name,"r")
fread=f_in.read()
#Removing thousands separator, if present.
fread=fread.replace(",","")
#Removing the first row that do not contain readings.
rows_fread=fread.split("\n")
rows_fread.remove(rows_fread[0])

#Initializing the list of dates, radon concentration records
#and relative uncertainties.
datei=[]
c_radoni=[]
sigma_c_radoni=[]
```

```
#Selection, for each row, of date, radon concentration
#and relative uncertainty to be appended to the
#corresponding list.
for i in range(len(rows_fread)):
    row=rows_fread[i]
    if "\t" in row:
        row_splitted=row.split("\t")
        datei.append(row_splitted[0])
        c_radoni.append(row_splitted[2])
        sigma_c_radoni.append(row_splitted[3])

#The list datei is checked by looking for non-date entries.
for i in range(len(datei)):
    if ":"in datei[i]:
        datei[i]=str(datei[i])
    else:
        datei.remove(datei[i])
#The list c_radoni is checked by looking for non-real entries.
    if isReal(c_radoni[i])==True:
        c_radoni[i]=float(c_radoni[i])
    else:
        c_radoni.remove(c_radoni[i])
#The list sigma_c_radoni is checked by looking for non-real entries.
    if isReal(sigma_c_radoni[i])==True:
        sigma_c_radoni[i]=float(sigma_c_radoni[i])
    else:
        sigma_c_radoni.remove(sigma_c_radoni[i])

#Converting the list datei to the numpy array Datei.
Datei=np.array(datei) #[dd/mm/yy hh:mm]
#Converting the list c_radoni to the numpy array C_radoni.
C_radoni=np.array(c_radoni) #[Bq/m^3]
#Converting the list sigma_c_radoni to the numpy array Sigma_C_radoni.
Sigma_C_radoni=np.array(sigma_c_radoni) #[Bq/m^3]

#Opening an output file and writing on it the concentration
#records and, separated by a tab, the corresponding uncertainties.
f_out=open("RadonINT_Measurements.txt","w")
for i in range(len(C_radoni)-1):
    f_out.write(str(C_radoni[i]))
    f_out.write("\t")
    f_out.write(str(Sigma_C_radoni[i]))
    f_out.write("\n")
f_out.write(str(C_radoni[len(C_radoni)-1]))
f_out.write("\t")
f_out.write(str(Sigma_C_radoni[len(Sigma_C_radoni)-1]))
#Closing the output files.
f_out.close()
```

```
#-----------------------------------------------

#Receiving as input the name of the outer AlphaGUARD PQ2000 Pro
#output file. From now on, the commands are the same as those written
#for the AlphaGUARD output file.
file_name=raw_input("External AlphaGUARD Data: ")
file_name=file_name+".txt"
f_in=open(file_name,"r")
fread=f_in.read()
fread=fread.replace(",","")
rows_fread=fread.split("\n")
rows_fread.remove(rows_fread[0])

datee=[]
c_radone=[]
sigma_c_radone=[]

for i in range(len(rows_fread)):
    row=rows_fread[i]
    if "\t" in row:
        row_splitted=row.split("\t")
        datee.append(row_splitted[0])
        c_radone.append(row_splitted[2])
        sigma_c_radone.append(row_splitted[3])

for i in range(len(datee)):
    if ":"in datee[i]:
        datee[i]=str(datee[i])
    else:
        datee.remove(datee[i])
    if isReal(c_radone[i])==True:
        c_radone[i]=float(c_radone[i])
    else:
        c_radone.remove(c_radone[i])
    if isReal(sigma_c_radone[i])==True:
        sigma_c_radone[i]=float(sigma_c_radone[i])
    else:
        sigma_c_radone.remove(sigma_c_radone[i])

Datee=np.array(datee) #[dd/mm/yy hh:mm]
C_radone=np.array(c_radone) #[Bq/m^3]
Sigma_C_radone=np.array(sigma_c_radone) #[Bq/m^3]

f_out=open("RadonEXT_Measurements.txt","w")
for i in range(len(C_radone)-1):
    f_out.write(str(C_radone[i]))
    f_out.write("\t")
    f_out.write(str(Sigma_C_radone[i]))
    f_out.write("\n")
f_out.write(str(C_radone[len(C_radone)-1]))
```

```
f_out.write("\t")
f_out.write(str(Sigma_C_radone[len(Sigma_C_radone)-1]))
f_out.close()

if np.array_equal(Datei,Datee):
    f_out=open("Date.txt","w")
    for i in range(len(Datee)-1):
        f_out.write(str(Datee[i]))
        f_out.write("\n")
    f_out.write(str(Datee[len(Datee)-1]))
    f_out.close()

#If successful, displaying the reading-writing procedure outcome.
print "-------------------------------"
print "Input files correctly written."

#The three arrays, together with the one produced by the flow-rate
#optimizing code, are compared to check the length equality.
#Check results are printed on the screen.
print "-------------------------------"
if len(Datei)==len(Datee)==len(C_radoni)==len(C_radone)
==len(Sigma_C_radoni)==len(Sigma_C_radone)
and ((len(Datei)-1)/6*3600+1)==len(FlowRate):
    print "Data check OK."
else:
    print "Error in comparing data."
print "-------------------------------"

#A short summary of measurement details is displayed including
#flow-rate and radon concentration measuring interval.
print "Measuring details:"
print (len(Datee)-1)/6,"hours;"
print "1","s","flow rate measuring interval;"
print "10","m","radon concentration measuring interval;"
```

3.1.7 Activity balance equations for the accumulation can

The radon concentration inside the accumulation chamber can be expressed by the following differential equation in which the positive contribution are in green and the negative ones in red:

$$\frac{dC_{\mathrm{Rn},in}(t)}{dt}V_{ch} = -\lambda_{\mathrm{Rn}}C_{\mathrm{Rn},in}(t)V_{ch} + \Gamma_{in}(T)C_{\mathrm{Rn},out}(t) - \Gamma_{out}(t)C_{\mathrm{Rn},in}(t) + \\ - \frac{D_o S_d}{l_d}(C_{\mathrm{Rn},in}(t) - C_{\mathrm{Rn},out}(t)) + ES_{free} \tag{3.5}$$

where:

$C_{\mathrm{Rn},in}(t)$ is the radon concentration inside the chamber, so registered by the inner detector ($\mathrm{Bq\,m^3}$)

$C_{\mathrm{Rn},out}(t)$ is the radon concentration outside the chamber, so registered by the outer detector ($\mathrm{Bq\,m^3}$)
V_{ch} is the volume of the chamber ($\mathrm{m^3}$)
S_{free} is the exhaling surface, i.e. the free surface of the chamber at the interface with the wall ($\mathrm{m^2}$)
λ_{Rn} is the ^{222}Rn decay constant ($\mathrm{s^{-1}}$)
$\Gamma_{in}(t)$ is the air flow-rate, registered by the corresponding sensor, entering the chamber through the hydraulic connection with the room air ($\mathrm{m^3\,s^{-1}}$)
$\Gamma_{out}(t)$ is the air flow-rate, registered by the corresponding sensor, leaving the chamber through the hydraulic connection with the room air ($\mathrm{m^3\,s^{-1}}$)
E is the radon exhalation rate per unit surface, supposed constant during each measurement ($\mathrm{Bq\,m^{-2}\,s^{-1}}$)
S_d is the section inner area of the PTFE tube used to connect the chamber to the room environment ($\mathrm{m^2}$)
l_d is the distance obtained by summing the PTFE tube length and the path traveled through the sensor and the straight male adapter (m)
D_0 is the radon diffusion coefficient in open air, $D_0 = 1.2 \cdot 10^{-5} \mathrm{m^2\,s^{-1}}$.

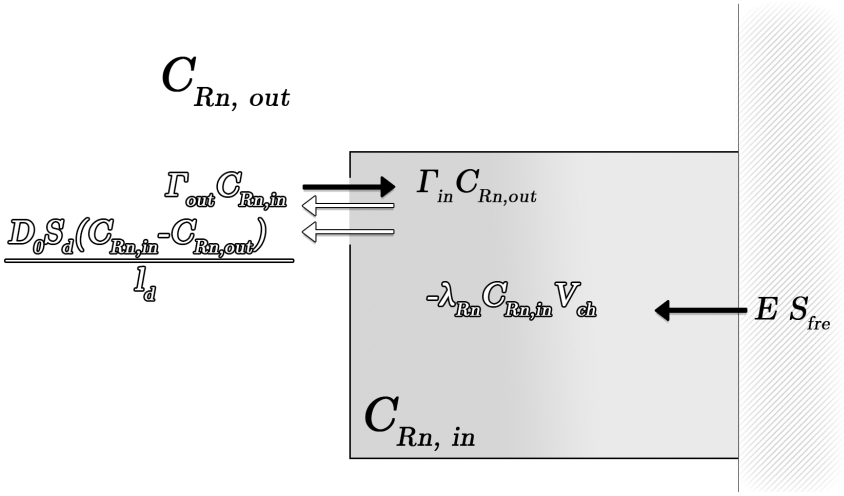

Figure 3.19: Conceptual representation of the activity balance inside the accumulation can volume at a certain time instant t. The positive contributions are represented in black, the negative in white. All the terms are expressed in $\mathrm{Bq\,s^{-1}}$.

The positive contributions are due to the advective air flow entering the chamber and the exhalation from the wall surface. The negative contributions are due to the radon radioactive decay, the advective air flow leaving the chamber and the concentration-gradient-driven diffusion through the PTFE tube. The latter term, in principle, could be either positive or negative, positive is the outer concentration is higher than the inner one, and negative vice versa. Eq. 3.5 remains valid in both scenarios.

The flow-rate sensor measures intensity and versus of the air flow-rate. As the sensor is mounted on the apparatus, being Γ the returned air flow-rate:

i) if ($\Gamma > 0$), the air flux is towards the chamber so $\Gamma_{in} = \Gamma$;

ii) if ($\Gamma < 0$), the air flux is towards the room so $\Gamma_{out} = |\Gamma|$;

3.1.8 Software architecture for data analysis

3.1.8.1 Temporal discretization

The differential equation mathematically describing the accumulation of radon in the chamber during the measurement needs to be discretized in order to be implemented in the functioning algorithm. The radon concentration output cannot be updated faster than once every ten minutes, the latter interval depending on the sensitivity of the detector. On the contrary, measured values of air flow-rate cannot be written on the output file slower than once a minute in order to make the measurement representative enough of the real air exchange phenomenon between the can and the surrounding environment. The time discritization of Eq. 3.5 should rely on time steps short enough to account for the changes of all the variables involved. Summarizing, three different time series exist, each with its own time discretization.

The following input need to be introduced:

- t is the time elapsing between two subsequent radon concentration records, i.e. 10 minutes in the case considered
- T is the overall measurement length, (gg/hh/mm)
- N is the number of t-lasting interval necessary to cover the entire T
- Δt is the time step chosen for the time discretization of the differential equation 3.5 (s)
- n is the number of Δt time steps necessary to cover a t-lasting period.
- p is the number of time interval between two subsequent flow-rate records necessary to cover a t-lasting period
- τ is the time variable, so defined in order to avoid superposition with other symbols, (s).

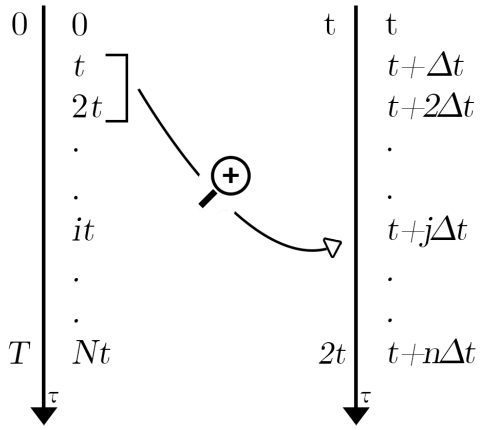

Figure 3.20: Fixed correlation between the time series of radon concentration records and the time discretization of Eq. 3.5. The index j assumes all the $n+1$ integer values in the range $[0; n]$. It is worth noting that $n\Delta t = t$, by definition.

The radon concentration records series can be synchronized with the differential equation discretization as shown by Figure 3.20. Analogously, the radon concentration records series can be so synchronized with the flow-rate records one as shown by Figure 3.21.

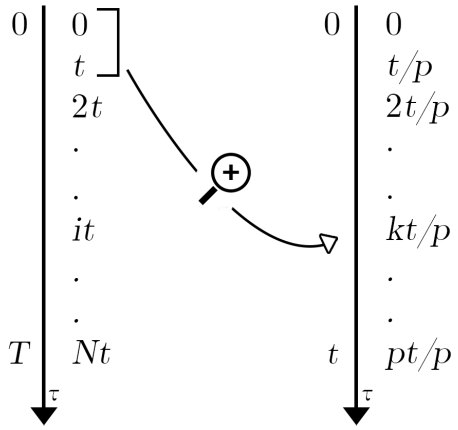

Figure 3.21: Time series of radon concentration records and flow-rate records. The index i assumes all the $N+1$ integer values in the range $[0;N]$. The index k assumes all the $p+1$ integer values in the range $[0;p]$. It is worth noting that $Nt = T$, by definition.

Defining the overall observation (or measurement) time as T, the number of radon concentrations returned will be $N+1$, including the initial value at $\tau = 0$. Analogously, during the time interval between two subsequent radon concentration records, e.g. $it - (i+1)t$ the number of radon concentration values considered by the discretized computation will be $n+1$, including the "experimental" values at $\tau = (i-1)t$ and $\tau = it$. In other words, N, n and p are respectively: the number of intervals among radon concentration records, the number of intervals, for each of the N interval, among concentration values, either recorded or computed, and the number of intervals, for each of the N interval, among flow-rate records.

Referring to the actual apparatus, $t = 600\,\mathrm{s}$ and $n = 6000$. This means that the radon concentration is estimated through Eq. 3.5 every 0.1 s moving from the experimental values returned by the CRM every 600 s. As previously said, the flow-rate values are returned by the corresponding sensor every 1 s, i.e. $p = 600$. Each interval between two available flow-rate values contains $\frac{n}{p} = 10$ intervals of computation. By generalizing, for general i and k, the correlation between flow-rate values intervals and computational time step Δt is reported in Figure 3.22 where the index m assumes all the $\frac{n}{p}+1$ integer values in the range $[0;\frac{n}{p}]$. For the value just declared, $\frac{n}{p} = 10$. In the interval between $it + k\frac{t}{p} + m\Delta t$ and $it + k\frac{t}{p} + (m+1)\Delta t$, the flow-rate, $\Gamma_{i,k,m}$, is computed by linearly interpolating between the flow-rate at $\tau = it + k\frac{t}{p}$ and $\tau = it + (k+1)\frac{t}{p}$:

$$\Gamma_{i,k,m} = \frac{\Gamma_{i,k+1} - \Gamma_{i,k,m}}{\frac{n}{p}} \cdot m + \Gamma_{i,k} \tag{3.6}$$

where $\Gamma_{i,k} = \Gamma_{\tau=it+k\frac{t}{p}}$ and $\Gamma_{i,k+1} = \Gamma_{\tau=it+(k+1)\frac{t}{p}}$.

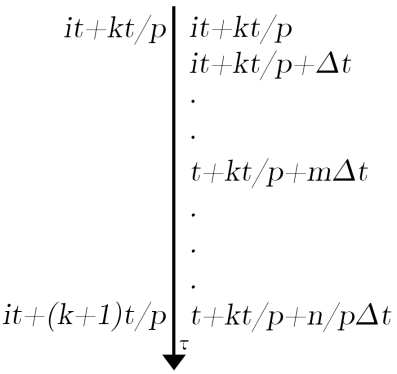

Figure 3.22: Time series of radon flow rate records and computational intervals. The index i assumes all the $N+1$ integer values in the range $[0;N]$. The index k assumes all the $p+1$ integer values in the range $[0;p]$. The index m assumes all the $\frac{n}{p}+1$ integer values in the range $[0;\frac{n}{p}]$. It is worth noting that $n\Delta t = t$ so $it + k\frac{t}{p} + \frac{n}{p}\Delta t = it + (k+1)\frac{t}{p}$.

Passing from continuous to discretized time intervals, Eq. 3.5 becomes:

$$\begin{aligned} C_{\mathrm{Rn},in,i,k,m+1} = C_{\mathrm{Rn},in,i,k,m} + \Delta t \Bigg(& -\lambda_{\mathrm{Rn}} C_{\mathrm{Rn},in,i,k,m} \\ & + \frac{\Gamma_{in,i,k,m} C_{\mathrm{Rn},out,i,k,m}}{V_{ch}} - \frac{\Gamma_{out,i,k,m} C_{\mathrm{Rn},in,i,k,m}}{V_{ch}} \\ & - \frac{D_0 S_d}{l_d V_{ch}} (C_{\mathrm{Rn},in,i,k,m} - C_{\mathrm{Rn},out,i,k,m}) + \frac{E S_{free}}{V_{ch}} \Bigg) \end{aligned} \tag{3.7}$$

where:

$$C_{\mathrm{Rn},in,i,k,m} = C_{\mathrm{Rn},in}(\tau = it + k\frac{t}{p} + m\Delta t) \tag{3.8}$$

$$C_{\mathrm{Rn},in,i,k,m+1} = C_{\mathrm{Rn},in}(\tau = it + k\frac{t}{p} + (m+1)\Delta t) \tag{3.9}$$

$$C_{\mathrm{Rn},out,i,k,m} = C_{\mathrm{Rn},out}(\tau = it + k\frac{t}{p} + m\Delta t) \tag{3.10}$$

$$= \frac{(C_{\mathrm{Rn},out,i+1} - C_{\mathrm{Rn},out,i})}{n} \cdot \left(k\frac{n}{p} + m\right) + C_{\mathrm{Rn},out,i} \tag{3.11}$$

3.1.8.2 Python code for radon exhalation rate estimation

The output files of the previously presented input optimizer software (§3.1.5 and §3.1.6) are then passed as input to the custom software written to estimate the radon exhalation rate from radon concentrations and flow-rates registered by the CRM and the flow-rate sensor, respectively.

The code, written in Python, is hereafter reported including several comments useful to understand the purpose of the various code sections. The general aim of this code is to identify the value of the radon exhalation rate that, put in Eq.3.5, returns the best estimation of radon concentration inside the chamber during the experiment. In other words, the residual, i.e. the sum of the squared differences between estimated and measured radon concentrations for $\tau \in [0, T]$, should be minimized by the best choice of the exhalation rate. To do so, the code accepts as inputs lower and upper boundaries of the exhalation rate range and looks for the value minimizing the residual through subsequent iterations.

```
# -*- coding: cp1252 -*-
import numpy as np
import copy as cp
import winsound as ws
from math import *
from matplotlib.pyplot import *

def isReal (s):
    if len(s)==0:
        return False
    return s.isdigit() or (s[0] in "+-" and s[1:].isdigit())
or (s.count(".")==1 and (s.replace(".","1")).isdigit())
or (s.count(".")==1 and (s.replace(".","1"))[0]
in "+-" and (s.replace(".","1"))[1:].isdigit())

#-----------------------------------------------------------------
#Defining nuclear and diffusion data for radon.

lambda_222Rn=2.09838*(10**(-6)) #[s^-1]
D_0=1.2*10**(-5) #[m^2 s^-1]

#-----------------------------------------------------------------
#Defining the dimensions of the accumulation can.

length=36.0 #[cm]
width=26.0 #[cm]
height=31.2 #[cm]

V_ch=length*width*height*(10**(-6)) #[m^3]

#-----------------------------------------------------------------
#Defining the dimensions of hydraulic connection between
#can and room air.

d_d=0.004 #[m]
S_d=np.pi/4*d_d**2 #[m^2]
l_d=0.1 #[m]

#-----------------------------------------------------------------
```

```
#Receiving as input the measuring interval details.

print("Measuring Interval Details:")
day=input("Days: ")
hour=input("Hours: ")
minute=input("Minutes: ")
T=day*24*3600+hour*3600+minute*60. #Measurement duration, [s].

#-----------------------------------------------------------------
#Defining the intervals between records of radon
#concentration and flow-rate.

t=600. #Interval between two following CRM outputs, [s].
N=T/t #n° of t-lasting interval to cover the measurement period.
p=600 #n° of intervals between two following flow-rate outputs
#for each t-lasting interval.

#-----------------------------------------------------------------
#Defining the discretization details.

n=6000. #n° of computation intervals for each t-lasting interval.
deltat=t/n  #Time step length used for discretization.

#-----------------------------------------------------------------
#Reading the radon concentration records, with the corresponding
#uncertainties, from the optimized output of the inner detector.

file_input="RadonINT_Measurements.txt"
Radonin_in=open(file_input,"r")
Radonin_text=Radonin_in.read()
Radonin_list=Radonin_text.split("\n") #[Bq/m^3]

#Initializing the list of concentration and uncertainty values.

cin_222Rn=[]
sigmain_222Rn=[]

for i in range(len(Radonin_list)):
    raw=Radonin_list[i]
    if "\t" in raw:
        cin_222Rn.append(raw.split("\t")[0])
        sigmain_222Rn.append(raw.split("\t")[1])
    else:
        Radonin_list.remove(raw)

#Radon concentration and uncertainty values, read as string,
#are transformed into float numbers, after a further check
#through the isReal() function.

for i in range(len(cin_222Rn)):
```

```
    if isReal(cin_222Rn[i])==True:
        cin_222Rn[i]=float(cin_222Rn[i])
    else:
        cin_222Rn.remove(cin_222Rn[i])

for i in range(len(sigmain_222Rn)):
    if isReal(sigmain_222Rn[i])==True:
        sigmain_222Rn[i]=float(sigmain_222Rn[i])
    else:
        sigmain_222Rn.remove(sigmain_222Rn[i])

#sigmain_222Rn and cin_222Rn lists are transformed into
#numpay arrays.

sigmain_222Rn=np.array(sigmain_222Rn) #[Bq/m^3]
cin_222Rn=np.array(cin_222Rn) #[Bq/m^3]

#Computing the number of radon atoms from the radon
#concentration array.

Min_222Rn=cin_222Rn*V_ch/lambda_222Rn #[atoms]

#If data have been properly acquired, the number of radon
#concentration records should be equal to N+1.

if len(cin_222Rn)==N+1:
    check_Radonin=True
else:
    check_Radonin=False

#-----------------------------------------------------------------
#Reading the radon concentration records, with the corresponding
#uncertainties, from the optimized output of the inner detector.
#The same comments seen for the inner radon monitor identically
#applies to the outer one.

file_input="RadonEXT_Measurements.txt"
Radonout_in=open(file_input,"r")
Radonout_text=Radonout_in.read()
Radonout_list=Radonout_text.split("\n") #[Bq/m^3]
cout_222Rn=[]
sigmaout_222Rn=[]

for i in range(len(Radonout_list)):
    raw=Radonout_list[i]
    if "\t" in raw:
        cout_222Rn.append(raw.split("\t")[0])
        sigmaout_222Rn.append(raw.split("\t")[1])
    else:
        Radonout_list.remove(raw)
```

```
for i in range(len(cout_222Rn)):
    if isReal(cout_222Rn[i])==True:
        cout_222Rn[i]=float(cout_222Rn[i])
    else:
        cout_222Rn.remove(cout_222Rn[i])

sigmaout_222Rn=np.array(sigmaout_222Rn) #[Bq/m^3]
cout_222Rn=np.array(cout_222Rn) #[Bq/m^3]

#The outer radon concentration is used to obtain the array of
#radon atoms per unit volume.

Mout_222Rn=cout_222Rn/lambda_222Rn #[atoms/m^3]

if len(cout_222Rn)==N+1:
    check_Radonout=True
else:
    check_Radonout=False

#-----------------------------------------------------------------
#Initializing the lists of alpha-emitting short-lived radon
#daughters.

N_222Rn=np.ones(int(N)+1) #[atoms]
N_222Rn[0]=Min_222Rn[0]
n_222Rn=np.ones(int(n)+1)

#-----------------------------------------------------------------
#Reading the flow rate records from the optimized output of
#the flow rate sensor.

file_input="Portata_Measurements.txt"
Gamma_in=open(file_input,"r")
Gamma_lista=Gamma_in.read()
Gamma_222Rn=Gamma_lista.split("\n")
for i in range(len(Gamma_222Rn)):
    if len(Gamma_222Rn)>0:
        Gamma_222Rn[i]=float(Gamma_222Rn[i])
    else:
        Gamma_222Rn.remove(Gamma_222Rn[i])
Gamma_222Rn=np.array(Gamma_222Rn) #[m^3/s]

#Being T the measurement duration (in seconds), the number of
#flow rate records, registered once a second, should equal T+1.

if len(Gamma_222Rn)==T+1:
check_Gamma=True
else:
check_Gamma=False
```

```
#-------------------------------------------------------------
#The exhalation rate value best fitting the radon concentration
#trend measured is obtained through subsequent iteration.
#The discretized differential equation governing the accumulation
#should be solved separately for R_ExInf and R_ExSup. For each
#of the two solutions, the residual is then computed relative to
#the measured trend.

r_ExInf=0. #[mBq/(m^2*h)]
R_ExInf=r_ExInf/1000*length*height*(10**(-4))/lambda_222Rn/3600
#[atoms_222Rn/s]
r_ExSup=50000. #[mBq/(m^2*h)]
R_ExSup=r_ExSup/1000*length*height*(10**(-4))/lambda_222Rn/3600
#[atoms_222Rn/s]

#-------------------------------------------------------------
#Opening the output file after received, as input, its name.

file_output=raw_input("Results File Name: ")
f_out=open(file_output+".txtr","w")

#The exhalation rate value best fitting the radon concentration
#trend measured is obtained through subsequent iterations.
#Three variables need to be initialized before starting.

counter=1 #Counter to account for number of iterations done.
ResInf=0 #This variable will contain the "lower residual".
ResSup=0 #This variable will contain the "upper residual".

#The research of the exhalation value best fitting the radon
#concentration trend measured is designed to end when the
#residual is lower than a certain value or when a certain
#number of iterations has been performed.
#ResTot is a variable that equals the lowest residual
#between ResInf and ResSup. Such a variable has to be
#initialized at a starting value higher than the minimum
#residual such to determine the end of the exhalation rate
#research.

ResTot=1000001

#-------------------------------------------------------------
#Iterative process to find the radon exhalation rate best-fitting
#the experimental data.

#All the acquired arrays should have passed the length check.
#The while cycle contains the two exit conditions previously
#discussed and described.
if check_Radonin==True and check_Radonout==True
```

```
and check_Gamma==True:
    while (counter<=15 and ResTot>1000000.):
    #The following equations estimate the radon concentration
    #if the exhalation rate equals R_ExInf.
        for i in range(int(N)):
        #For each interval between radon records.
        #Initializing three support variables whose
        #first value equals the measured radon
        #concentration at the beginning of the
        #corresponding interval.
            n_222Rn[0]=N_222Rn[i]
            for k in range(int(p)):
            #For each interval between flow rate records
            #within the same radon records interval.
                for m in range(int(n/p)):
                #For each computation interval within
                #the same flow rate interval.
                    Gamma_222Rn_m=(Gamma_222Rn[k+1]
                    -Gamma_222Rn[k])/(n/p)*m+Gamma_222Rn[k]
                    Mout_222Rn_m=(Mout_222Rn[i+1]
                    -Mout_222Rn[i])/n*(k*(n/p)+m)+Mout_222Rn[i]
                    #The flow rate measured by the sensor cannot be
                    #simultaneously positive and negative so the
                    #following if cycle chooses the proper
                    #formulation of Eq. 3.5 relative to the flow
                    #rate sign.
                    if Gamma_222Rn_m>=0:
                        n_222Rn[int(k*(n/p)+m+1)]=n_222Rn[int(k*
                        (n/p)+m)]
                        +deltat*(-lambda_222Rn*n_222Rn[int(k*(n/p)
                        +m)]
                        +(Gamma_222Rn_m*Mout_222Rn_m)
                        +R_ExInf-D_0*S_d/(l_d*V_ch)*
                        (n_222Rn[int(k*(n/p)+m)]-Mout_222Rn_m*
                        V_ch))
                    else:
                        n_222Rn[int(k*(n/p)+m+1)]=n_222Rn[int(k*
                        (n/p)+m)]
                        +deltat*(-lambda_222Rn*n_222Rn[int(k*(n/p)
                        +m)]
                        +(-Gamma_222Rn_m*n_222Rn[int(k*(n/p)+m)]/
                        V_ch)
                        +R_ExInf-D_0*S_d/(l_d*V_ch)*
                        (n_222Rn[int(k*(n/p)+m)]-Mout_222Rn_m*
                        V_ch))
            #The last value computed within the i-interval
            #between radon concentration records is written
            #in the i+1 value of radon concentration array.
            N_222Rn[i+1]=n_222Rn[int(n)]
        #The radon concentration array is copied.
```

```
N_222RnInf=cp.copy(N_222Rn)
#The following cycle computes the lower residual.
for i in range(len(N_222RnInf)):
    ResInf+=(N_222RnInf[i]-Min_222Rn[i])**2

for i in range(int(N)):
    n_222Rn[0]=N_222Rn[i]
    for k in range(int(p)):
    #For each interval between flow rate records
    #within the same radon records interval.
        for m in range(int(n/p)):
        #For each computation interval within
        #the same flow rate interval.
            Gamma_222Rn_m=(Gamma_222Rn[k+1]
            -Gamma_222Rn[k])/(n/p)*m+Gamma_222Rn[k]
            Mout_222Rn_m=(Mout_222Rn[i+1]
            -Mout_222Rn[i])/n*(k*(n/p)+m)+Mout_222Rn[i]
            if Gamma_222Rn_m>=0:
                n_222Rn[int(k*(n/p)+m+1)]=n_222Rn[int(k*
                (n/p)+m)]
                +deltat*(-lambda_222Rn*n_222Rn[int(k*(n/p)
                +m)]
                +(Gamma_222Rn_m*Mout_222Rn_m)
                +R_ExSup-D_0*S_d/(l_d*V_ch)*
                (n_222Rn[int(k*(n/p)+m)]-Mout_222Rn_m*
                V_ch))
            else:
                n_222Rn[int(k*(n/p)+m+1)]=n_222Rn[int(k*
                (n/p)+m)]
                +deltat*(-lambda_222Rn*n_222Rn[int(k*(n/p)
                +m)]
                +(-Gamma_222Rn_m*n_222Rn[int(k*(n/p)+m)]/
                V_ch)
                +R_ExSup-D_0*S_d/(l_d*V_ch)*
                (n_222Rn[int(k*(n/p)+m)]-Mout_222Rn_m*
                V_ch))
    #The last value computed within the i-interval
    #between radon concentration records is written
    #in the i+1 value of radon concentration array.
    N_222Rn[i+1]=n_222Rn[int(n)]
#The radon concentration array is copied.
N_222RnSup=cp.copy(N_222Rn)
#The following cycle computes the lower residual.
for i in range(len(N_222RnSup)):
    ResSup+=(N_222RnSup[i]-Min_222Rn[i])**2

#The following commands allow to print a specific report
#displaying, for each iteration, lower and upper
#residuals.
print(counter," "*(3-len(str(counter))),"|"," "*0,
```

```
        round(R_ExInf*1000*lambda_222Rn*3600/
        (length*height*(10**(-4))),2)," "*(10-
        len(str(round(R_ExInf*1000*lambda_222Rn*3600/
        (length*height*(10**(-4))),2)))),"|"," "*0,
        round(ResInf,2)," "*(20-len(str(round(ResInf,2)))),"|",
        " "*0,round(R_ExSup*1000*lambda_222Rn*3600/
        (length*height*(10**(-4))),2)," "*(10-len(str(round
        (R_ExSup*1000*lambda_222Rn*3600/(length*
        height*(10**(-4))),2)))),"|"," "*0,round(ResSup,2))
        f_out.write(str(counter)+" "*(3-len(str(counter)))+
        " "*1+"|"+" "*1+str(round(R_ExInf*1000*lambda_222Rn*
        3600/(length*height*(10**(-4))),2))+" "*(10-
        len(str(round(R_ExInf*1000*lambda_222Rn*3600/
        (length*height*(10**(-4))),2))))+" "*1+"|"+" "*1+
        str(round(ResInf,2))+" "*(20-len(str(round(ResInf))))+
        " "*1+"|"+" "*1+str(round(R_ExSup*1000*lambda_222Rn*
        3600/(length*height*(10**(-4))),2))+" "*(10-
        len(str(round(R_ExSup*1000*lambda_222Rn*3600/
        (length*height*(10**(-4))),2))))+" "*1+"|"+" "*1+
        str(round(ResSup,2)))
        f_out.write("\n")

        #The following commands aim to define a new upper and
        #lower boundaries for the exhalation rate. Among the
        #previous boundaries, the one characterized by the lower
        #residual is confirmed, the other changed following the
        #binomial goal seeking.
        if ResInf<=ResSup:
            ResTot=ResInf
            R_ExInf=R_ExInf
            R_ExSup=(R_ExSup-R_ExInf)/2+R_ExInf
            N_222Rn=N_222RnInf
            N_218Po=N_218PoInf
            N_214Pb=N_214PbInf
            R=R_ExInf
        elif ResSup<ResInf:
            ResTot=ResSup
            R_ExSup=R_ExSup
            R_ExInf=R_ExSup-(R_ExSup-R_ExInf)/2
            N_222Rn=N_222RnSup
            N_218Po=N_218PoSup
            N_214Pb=N_214PbSup
            R=R_ExSup
        #The residuals are zeroed and the counter increased by 1.
        ResInf=0
        ResSup=0
        counter+=1

#Reproducing a beep when the goal seeking finishes and
#printing the results on both the screen and the output
```

```
#file.
ws.Beep(400,500)
R=R*1000*lambda_222Rn*3600/(height*length*(10**(-4)))
print"The estimated radon exhalation rate is",R,"mBq/(h*m^2)"
f_out.write("\n")
f_out.write("The estimated radon exhalation rate is"+" "+
str(round(R,2))+" "+"mBq/(h*m^2)")
f_out.close()

#-----------------------------------------------------------------
#Assembling the arrays of radon activity and activity concentration.

A_222Rn=N_222Rn*lambda_222Rn #[Bq]

a_222Rn=A_222Rn/V_ch #[Bq/m^3]

#-----------------------------------------------------------------
#Printing on a second output file the radon concentration trend
#corresponding to the returned exhalation rate.

f_out=open(file_output+".txto","w")
for i in range(len(a_222Rn)-1):
f_out.write(str(cin_222Rn[i]))
f_out.write(" "*(22-len(str(cin_222Rn[i]))))
f_out.write(str(a_222Rn[i]))
f_out.write("\n")
f_out.write(str(cin_222Rn[len(a_222Rn)-1]))
f_out.write(" "*(22-len(str(cin_222Rn[len(a_222Rn)-1]))))
f_out.write(str(a_222Rn[len(a_222Rn)-1]))
f_out.close()

#-----------------------------------------------------------------
#The last code section is dedicated to the graphic representation
#of both the measured and the estimated radon concentration trend.

plt.figure(figsize=(10,5),dpi=200)
plt.plot(cin_222Rn,color="darkmagenta", linestyle="-",
linewidth=0.7,label="Measured $^{222}$Rn concentrations")
plt.errorbar(list(range(0,len(cin_222Rn))),cin_222Rn,
yerr=(sigmain_222Rn,sigmain_222Rn),color="darkmagenta",
marker='.',markersize=5,markeredgewidth=0.5, linewidth=0.2,
markeredgecolor='darkmagenta',markerfacecolor='magenta',
ecolor='magenta',capsize=2)
plt.plot(a_222Rn,color="green",linestyle="--",linewidth=0.7,
label="Estimated $^{222}$Rn concentrations")
plt.xlim(0,len(cin_222Rn)-1)
plt.ylim(0,max(cin_222Rn)*1.5)
pHours=1
plt.xticks(np.arange(0,len(cin_222Rn),pHours*6),(np.arange
(0,len(cin_222Rn),pHours*6)/6).astype(int))
```

```
plt.yticks(np.arange(0,max(cin_222Rn*1.5),100))
plt.minorticks_on()
plt.grid(b=True, which='minor', color='whitesmoke',
linestyle='--',linewidth=0.3)
plt.grid(b=True,which='major', color='gainsboro',linestyle='-',
linewidth=0.3)

plt.xlabel(u"Measuring time (hours)")
plt.ylabel(u"$^{222}$Rn concentrations (Bq m$^{-3}$)")
plt.legend(loc="best")
plt.title("Comparison between estimated and measured trend")
plt.img_output=file_output+".png"
plt.savefig(plt.img_output)
plt.show()
```

While the code is running, general information about the specific iteration just completed are displayed on the screen. In particular, they contain lower and upper residuals other than the two exhalation values the code has just evaluated (Figure 3.23).

```
Results File Name: 15Oct_2019
1    |  0.0         |  3703224010714898.0    |  50000.0     |  3703224010714898.0
2    |  0.0         |  3703224010714898.0    |  25000.0     |  3703224010714898.0
3    |  12500.0     |  540679998653572.94    |  25000.0     |  540679998653572.94
4    |  18750.0     |  57888984233151.38     |  25000.0     |  57888984233151.38
5    |  18750.0     |  57888984233151.38     |  21875.0     |  57888984233151.38
6    |  18750.0     |  57888984233151.38     |  20312.5     |  57888984233151.38
7    |  19531.25    |  49031403912325.18     |  20312.5     |  49031403912325.18
8    |  19531.25    |  49031403912325.18     |  19921.88    |  49031403912325.18
9    |  19726.56    |  48604901071069.5      |  19921.88    |  48604901071069.5
10   |  19726.56    |  48604901071069.5      |  19824.22    |  48604901071069.5
11   |  19726.56    |  48604901071069.5      |  19775.39    |  48604901071069.5
12   |  19726.56    |  48604901071069.5      |  19750.98    |  48604901071069.5
13   |  19738.77    |  48601990087287.9      |  19750.98    |  48601990087287.9
14   |  19744.87    |  48601582188507.48     |  19750.98    |  48601582188507.48
15   |  19744.87    |  48601582188507.48     |  19747.92    |  48601582188507.48
The estimated radon exhalation rate is 19744.87 mBq/(h*m^2)
```

Figure 3.23: Example of the report displayed when the code run ends. From left to right: the iteration counter, the lower exhalation rate boundary, the lower residual, the upper exhalation rate boundary and the upper residual.

The code, once found the exhalation rate best fitting the experimental data, returns three different files: a .txto that contains both the concentration values measured and the results of the model for the chosen exhalation rate, a .txtr that reports the same information displayed right after the end of the goal seeking and .png plot showing the comparison between the experimental and the estimated radon concentration trend. All these three output files share the same name, chosen by the operator as input.

An equivalent code has been further developed in case of apparatus operation without the hydraulic connection between its inner volume and the surrounding environment. The algorithm structure is absolutely the same but both the diffusive and the advective radon migration terms are excluded from Eq. 3.5.

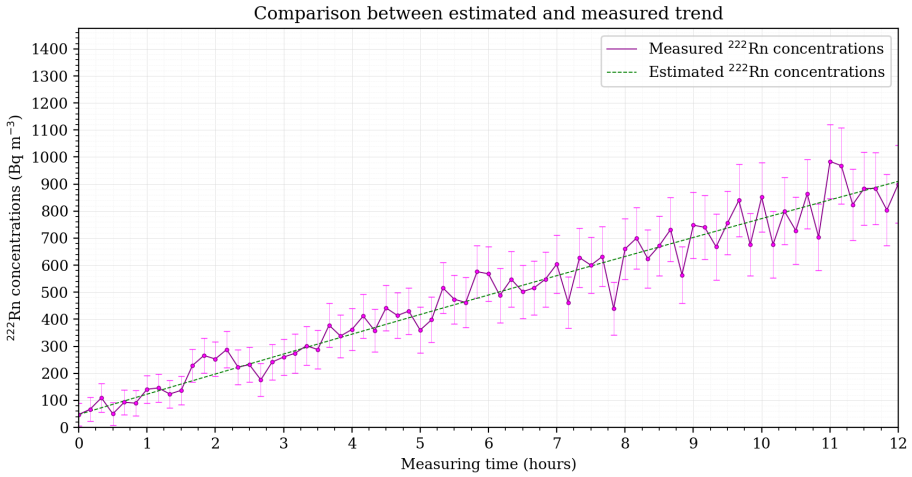

Figure 3.24: Example of the plot automatically produced by the code once found the best exhalation rate for fitting the experimental data. In dashed green the model results for the exhalation rate value chosen and in purple the measured trend with the corresponding error bars.

3.2 Procedures and results

The commissioning procedure included several and strictly subsequent steps: *i*) verifying the air-tightness of the accumulation chamber excluding the interface with the exhaling surface (i.e. the vertical wall), *ii*) extending the results to the interface with the wall, *iii*) studying the repeatability of the measuring system and *iv*) optimizing the measurement duration.

3.2.1 Accumulation chamber air-tightness

The operation of the apparatus requires to perform an air-tightness test aiming to verify both the tightness of the chamber - considering it with all its penetrations previously presented - and of the sealing at the wall interface.

For the first purpose, the accumulation chamber was disassembled from the apparatus and coupled with a 2 cm-thick plexiglass plate, long and wide enough to cover the entire free surface of the can. The sealing was realized by 20 bolts, that screwing through the plexiglass were clumped by 20 nuts to aluminum frames installed below the HDPE frame of the chamber. The bolts were screwed outside the radon-tight rubber covering the rectangular frame of the chamber in order to prevent the bolts from compromising the sealing integrity and from representing themselves routes for air escaping.

The air, in application far from critical condition ($P_c = 3769.290\,\text{kPa}$ and $T_c = -140.6\,^\circ\text{C}$), is to be considered a perfect gas: as a consequence, if the chamber has been correctly designed such to avoid air leakage, density, pressure and temperature should obey to the perfect gas state equation.

$$\frac{P}{T} = R_{air}\rho_{air} \tag{3.12}$$

where:

P is the air pressure, (Pa)
T is the air temperature, (K)
R_{air} is the individual air gas constant, $287.05\,\mathrm{J\,kg^{-1}\,K^{-1}}$
ρ_{air} is the air density, varying both with pressure and temperature, $(\mathrm{kg\,m^{-3}})$.

Pressure, temperature and relative humidity were monitored by two different sensors inserted within the chamber (i.e Sensirion SHT75 for temperature and humidity and Bosch Sensortec GY-BMP280-3.3. for high resolution measuring of the absolute pressure). Both power supply and signal transmission were assured using two MIL-C-5015 Amphenol 4-pins connectors (Figure 3.25). The male one (MS3102A) was installed right on the plexiglass plate with its pins soldered to the sensors signal outputs and the power inputs. The female one (MS3106A) pins were soldered to signal and power cables outside the chamber. The male connector, properly sealed by an o-ring on the plate and externally screwed to the female one, assured the air tightness of the electrical penetrations.

Figure 3.25: Male and female MIL-C-5015 Amphenol 4-pins connectors screwed on the top of the plexiglass plate.

Temperature and pressure trends over a measuring period of 24 hours are reported in Figure 3.26 and Figure 3.27.

The tightness effectiveness was evaluated by comparing two quantities, in the following referred to as measured mass (M_m) and computed mass (M_c). The first one is that computed as the product of the chamber volume by the air density function of pressure and temperature. In doing so, a compressibility factor $Z \approx 1$ was assumed(Ahmed, 2013). The second one is that obtained through a mass balance accounting for the starting mass value and all the following air exchanges through the flow rate sensor. So:

$$M_{m,i} = V_{ch} \frac{P_i}{T_i R_{air}} \tag{3.13}$$

$$M_{c,i} = M_{c,i-1} + \Gamma_i \frac{P_i}{T_i R_{air}} \Delta t \tag{3.14}$$

where:

Δt is the time elapsing between two subsequent sensors records, i.e. 1 s

i is the progressive number associated to the discrete number of sensors records, i.e. $i \in [1, T \cdot 3600]$ where T is the measurement duration

Γ_i is the flow rate measured by the corresponding sensor, positive if air is entering the chamber and negative otherwise.

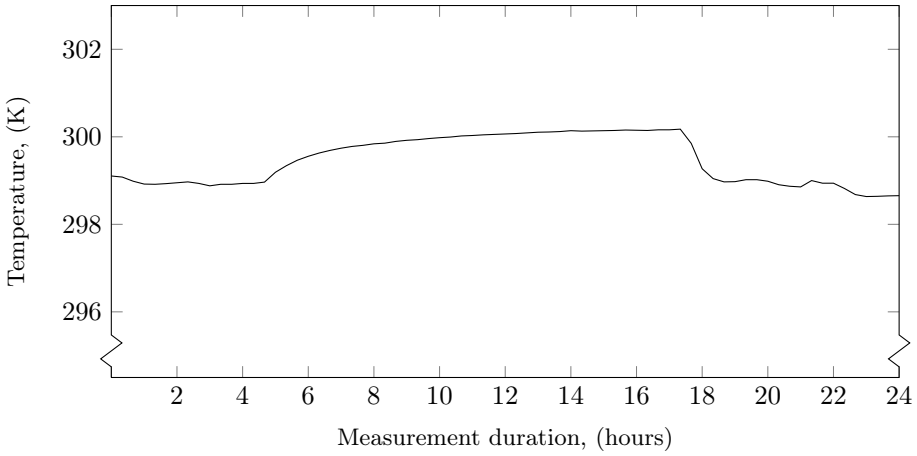

Figure 3.26: Temperature trend during the monitored period. The plotted values are affected by instrumental uncertainty of 1 K (Sensirion, 2011).

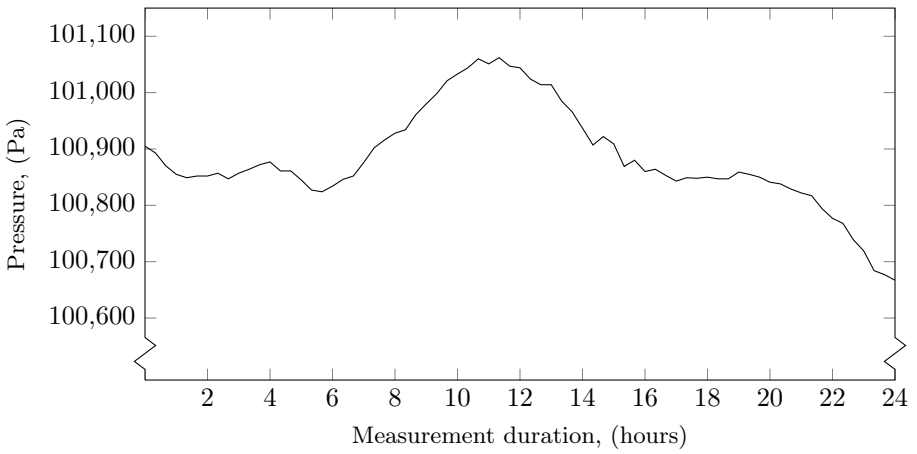

Figure 3.27: Pressure trend during the monitored period. The plotted values are affected by a fixed instrumental uncertainty of 100 Pa (Bosch Sensortec, 2009).

If the computed mass equals the measured one, it can be stated that no mass losses happened during the experiment other than the air leaving (or entering) the chamber through the monitored channel. The comparison results are displayed in Figure 3.28. The uncertainty of both series considered, measured and computed mass resulted to be the same during the whole measuring period. This statement is further supported by the length of the observation period, i.e. 24 hours, at least twice the maximum length to be considered for in-situ measurements of the actual radon exhalation rate. The maximum difference,

in absolute value, is 0.1 g, well below the average uncertainty (evaluated with a coverage factor $k = 1$) of each series, i.e. 0.2 g.

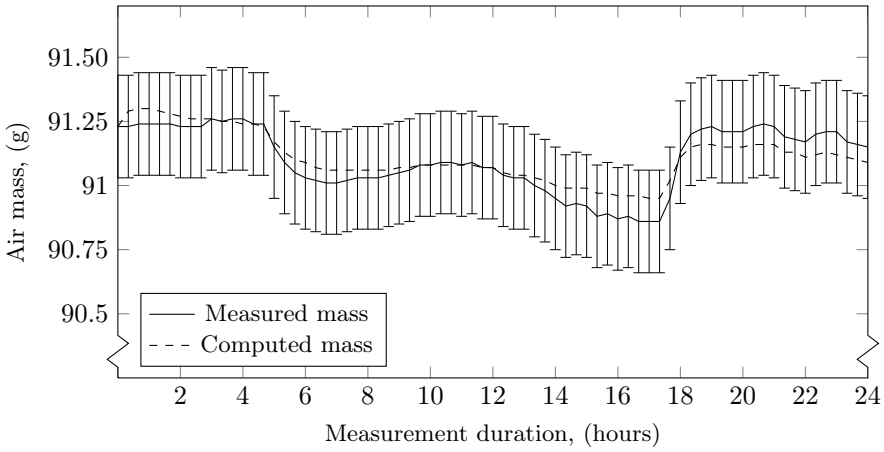

Figure 3.28: Comparison between measured mass and computed mass, both defined as explained in §3.2.1. For the sake of clarity, only the error bars of the measured mass trend are displayed on the graph.

3.2.2 Air-tightness at the interface between the accumulation can and the exhaling vertical surface

A specific experiment was designed to study the radon-tightness at the interface between the accumulation chamber and the exhaling vertical surface. Two identical prototypes of the same apparatus were realized and then applied to the same wall, one next to the other. The wall was chosen large enough to host both the measuring apparatuses at a distance such to avoid any interference among them. Furthermore, the wall surface was verified to be uniform and without significant imperfections such to affect the can cohesion to the vertical surface.

The measuring apparatuses were identical a part from the sealing mechanism. One of them, in the following referred to as Pr#B, was connected to the wall by using eight bolts screwed directly to the wall passing through four aluminum frames placed on the neoprene frame of the accumulation chamber itself. In other words, the can was sealed to the wall in the same way it was closed to the plexiglass plate in the previous experiment (Figure 3.29). The tightness of Pr#B was so assured by the results shown by §3.2.1. The other apparatus, in the following referred to as Pr#S, was the one to be commissioned. It was so equipped with the sealing mechanism described by §3.1.2.2 and it shown in Figure 3.30.

The apparatuses were placed side by side and a first measurement, lasting 12 hours, was started. Data were automatically collected from inner and outer AlphaGUARDs other than from the airflow sensor and the analysis performed through the Python code previously described (results in Figure 3.31). The exhalation rate resulted to be 23 $\mathrm{kBq\,h^{-1}\,m^{-2}}$ and 14 $\mathrm{kBq\,h^{-1}\,m^{-2}}$ for Pr#B and Pr#S, respectively.

In order to understand if such a difference was due to the bad tightness of

Figure 3.29: Pr#B apparatus used as reference in the experiment aiming to evaluate the effectiveness of the sealing mechanism of the apparatus under commission, i.e. Pr#S. The chamber is fixed to the wall using eight bolts, two for each side. Four aluminum frames, one for each side, serve both to distribute the pressure exerted over a wider portion of the chamber frame and to avoid penetrations in the frame itself.

Figure 3.30: Pr#S configuration of the experimental apparatus representing the one to be commissioned. Looking at the photo, several elements could be recognized on the metal chassis: the black plastic small box containing the Honeywell airflow sensor, the multi-channel voltage data logger PicoLog®, a mini PC collecting data from data logger and the CRM used to monitor the radon concentration inside the chamber.

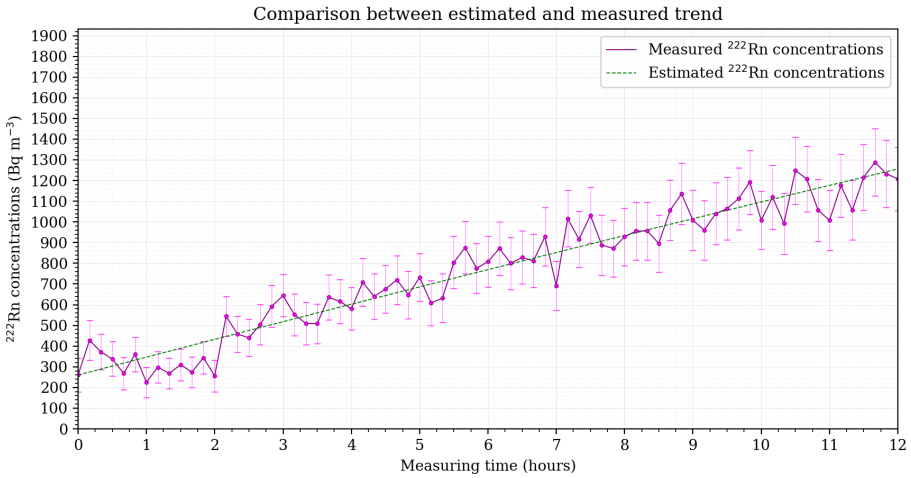

(a) Radon concentration in Pr#B during the measurement.

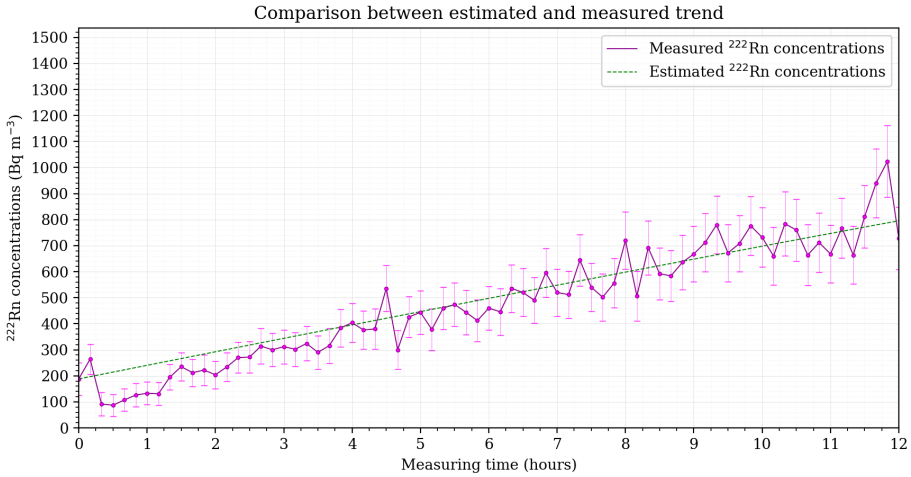

(b) Radon concentration in Pr#S during the measurement.

Figure 3.31: Measured radon concentrations in both the apparatuses during the first tightness measurement plotted together with the corresponding fits. These figures are taken directly from the code output without any elaboration.

the Pr#S, the position of the chambers was switched and a second 12 hours-lasting measurement was started. This attempt aimed to exclude the wall inner structure from the factors influencing the measurement results. The registered radon concentration trends, plotted in Figure 3.32, resulted in radon exhalation values of $14\,\mathrm{kBq\,h^{-1}\,m^{-2}}$ and $22\,\mathrm{kBq\,h^{-1}\,m^{-2}}$ for Pr#B and Pr#S, respectively.

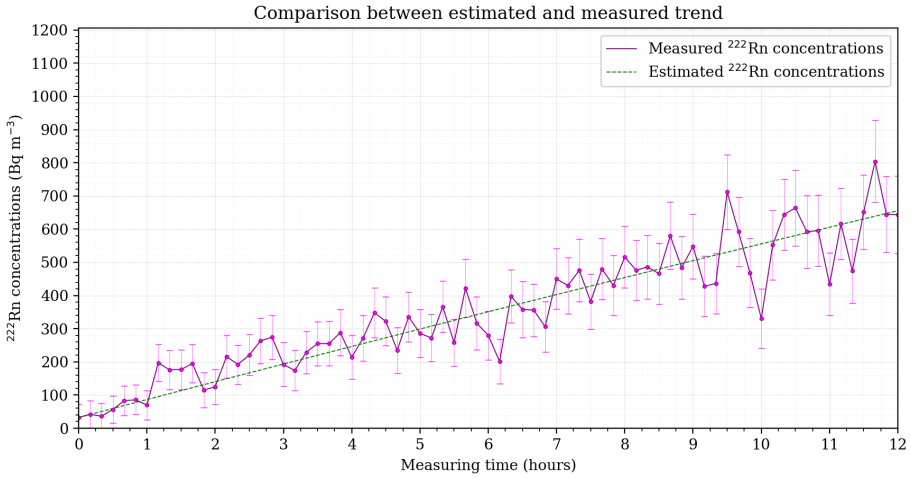

(a) Radon concentration in Pr#B during the measurement.

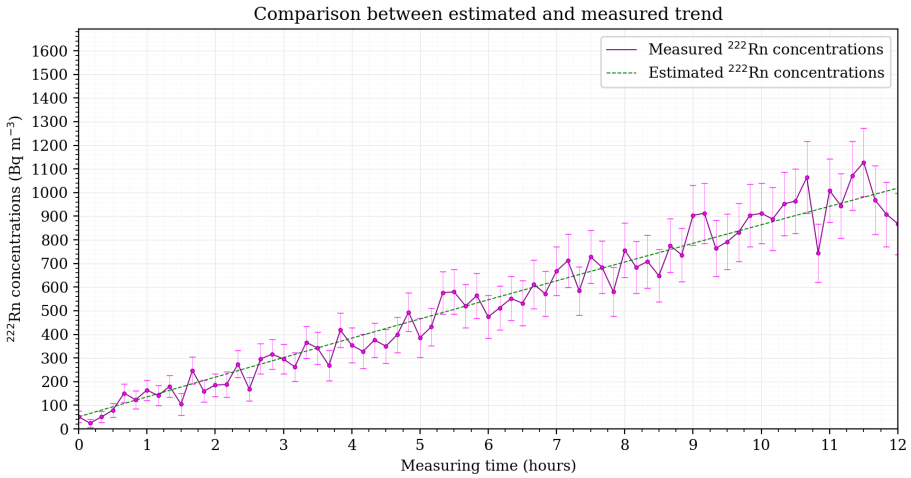

(b) Radon concentration in Pr#S during the measurement.

Figure 3.32: Measured radon concentrations in both the apparatuses during the second tightness measurement plotted together with the corresponding fits. The position of Pr#B and Pr#S was switched relative to the first experiment. These figures are taken directly from the code output without any elaboration.

The results of the second experiments resulted to be, for each position, exactly the same as the first one. Several measurements were so carried out [2] with the corresponding results confirming this finding. The radon exhalation

[2] Basing on what previously said about the different environmental parameters – mainly pressure difference between the wall structure and the room air – affecting in-situ radon exhalation from building materials, all the measurements described in this section have been

measured in each position was about the same in all the experiments but sensibly different from that found in the other position. Hence, the results at each position did not depend on the sealing mechanism of the apparatus used. Such evidences proved the goodness of Pr#S sealing system compared to the Pr#B one, whose effectiveness was previously verified through the experiment described in §3.2.1.

3.2.3 Measurements repeatability

The repeatability (of results of measurements) is defined as the closeness of the agreement between the results of successive measurements of the same measurand carried out under the same conditions of measurement (Joint Committee for Guides in Metrology, 2008). The so-called repeatability conditions, in the case of the apparatus under commissioning, include: *i*) the same measurement procedure, *ii*) the same operator performing the measurement, *iii*) the same code used for data analysis, *iv*) the same instrument to measure radon concentration and flow-rate, *v*) the same environmental parameters at the same location and *vi*) a short time elapsing between the measurements. The repeatability evaluation was performed with respect to $q = 2$ measurand levels, different walls with significantly different radon exhalation rates, by relying on $n = 4$ measurements of each measurand. The total number of measurements has been $q \cdot n = 8$.

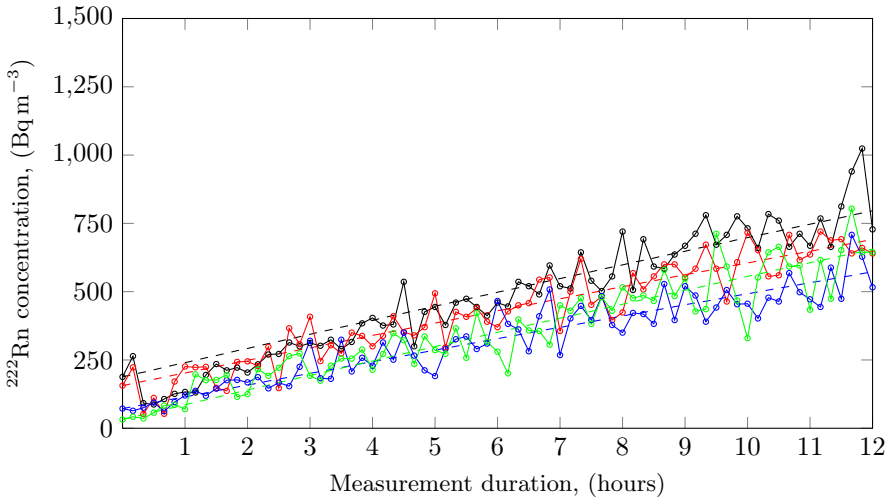

Figure 3.33: Measured and fitted radon concentration trends from the four measurement repetitions of the first measurand level. Each repetition is colored differently. In full line the experimentally measured trend whereas in dashed line the fitted one.

Results of measurements of first and second measurand levels, together with the corresponding data fit, are reported in Figure 3.33 and Figure 3.34, respectively. The repeatability was then evaluated by computing, for each of the two

performed under the same conditions. This expedient allows to exclude the influence of meteorological changes on the evaluated radon exhalation rate.

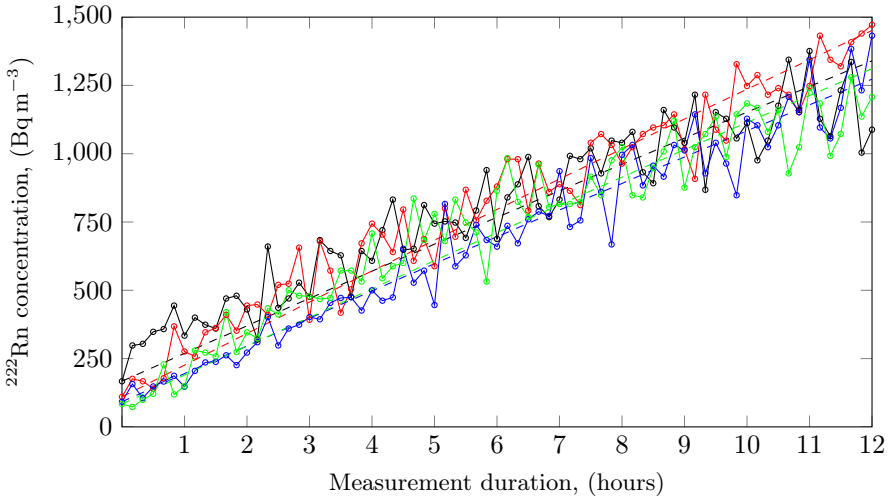

Figure 3.34: Measured and fitted radon concentration trends from the four measurement repetitions of the second measurand level. Each repetition is colored differently. In full line the experimentally measured trend whereas in dashed line the fitted one.

measurand level q^*, the coefficient of variation:

$$CV_{q^*} = \sqrt{\frac{1}{n-1}\frac{\sum_{i=1}^{n}(R_{i,q^*} - \mu_{q^*})^2}{\mu_{q^*}^2}} \tag{3.15}$$

where:

R_{i,q^*} is the radon exhalation rate value returned by the i-measurement of the measurand q^*, (Bq h^{-1} m^{-2})

μ_{q^*} is the arithmetic mean of $n = 4$ experimental determination of the q^* radon exhalation rate, i.e. (Bq h^{-1} m^{-2})

As shown by Table 3.2, the measurement repeatability resulted to be below 10% for both measurand levels. In particular, it slightly decreased with increasing radon exhalation rate measured. This result seems in agreement with the reduction of the statistical uncertainty associated to the single CRM output with increasing radon concentration. In evaluating the results obtained, it should be considered that assuring the fifth repeatability condition, i.e. the same environmental parameters affecting either the inner characteristics of the building materials or the phenomena leading to radon migration, is not easy at all. Excluding to control the environmental parameters in this kind of measurements, the possibility to assure the "same" measuring conditions lies on monitoring such parameters and waiting until they assume values similar enough. The temperature, affecting the emanation coefficient of building materials (Zhang et al., 2019), can be easy monitored during the measurement. The same does note apply to the air exchange rate of locals, influencing the indoor radon concentration (Vasilyev et al., 2015), and to the pressure gradient between inside and outside the slab, the latter affecting directly the advective transport and the permeability of the slab (Chauhan and Kumar, 2015). In view of this, a coefficient of variation of less than 10%, obtained for measurements performed

on different days chosen mainly looking at temperature and absolute pressure similarity, is to be considered extremely satisfying when evaluating the goodness of the apparatus performance.

Table 3.2: Results of repeatability tests on the apparatus under commissioning for measuring radon exhalation rate from vertical wall surfaces. The measurand levels are identified through the j-index that assumes all the integer values in the range $[1; q]$ where $q = 2$. The results of the $n = 4$ measurements performed, for each q^* measurand level, are simply referred to through the i-index that assumes all the integer values in the range $[1; n]$. The last two rows report the arithmetic mean and the coefficient of variation for both the measurand levels.

Radon Exhalation Rate ($\mathrm{Bq\,h^{-1}\,m^{-2}}$)		
	$j = 1$	$j = 2$
$i = 1$	13.9	26.9
$i = 2$	12.4	30.6
$i = 3$	11.5	26.9
$i = 4$	14.2	28.0
μ	13.0	28.1
σ	1.3	1.7
CV (%)	**9.8**	**6.2**

3.2.4 Measurement length

Choosing the proper measurement length is crucial to assure reliability of results. A short duration allows to increase the number of measurements per day by reducing the turnaround time. However, reducing the measurement length means reducing the number of points available to the algorithm for estimating the radon exhalation rate: this makes the result more dependent on short-term fluctuations of radon concentration (both inside and outside the chamber) due to sudden and strong changes in environmental parameters. On the other side, the long measurements are less affected by such disturbing short-term effects but the turnaround time increases and, during the accumulation process, variations in the external and internal container conditions are more likely to happen. Furthermore, the back-diffusion effect progressively gains relevance with time, the radon exhalation rate fixed. The ISO Standard 11665-7 (International Organization for Standardization, 2012a) does not contain specific indications: it only suggests to perform measurements lasting few hours. No suggestions arise from literature publications as well. The response vs. time of the apparatus under commissioning was so experimentally studied in order to identify the best measurement length.

Referring to short-term phenomena affecting radon accumulation process, they were found to be quite not rare. They happens especially in case of sudden drops in the room absolute pressure that leads, as a consequence, to a loss of tightness by the accumulation chamber sealing. The result is a sudden drop in radon concentration inside the chamber as shown by Figure 3.35.

Long-term variations of measurable environmental parameters were observed in several measurements. Figure 3.36, which reports two temperature trends observed during two measurements performed at the same hours and at the

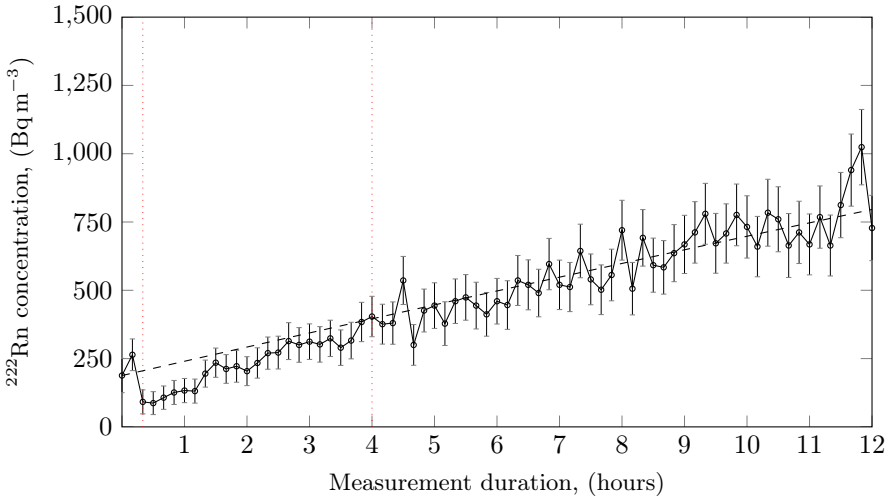

Figure 3.35: Radon concentration trend during a 12-hours lasting measurement. During the first 4 hours (i.e. the exact period is identified by two vertical dotted red line in the graph), the radon concentration does not follow the overall trend due to a sudden loss of air tightness. The latter leads the a fraction of radon contained in the accumulation can to escape towards the surrounding air volume.

same room in two subsequent working days, shows two very significant points: even at the same location with unchanged occupancy patterns and habits and despite the short time interval between the measurements both absolute values (*i*) and relative trends (*ii*) during the measurement can vary a lot.

Pertaining to back-diffusion effect, it was observed that the greater is the radon exhalation rate, the greater is the dependence of such a value on the measurement length. This disturbing phenomenon also gains relevance with high radon exhalation rate, i.e. $> 50\,\mathrm{Bq\,m^{-2}\,h^{-1}}$ for the size of the accumulation chamber under commissioning. The correlation between results (in terms of exhalation rates) and measurement duration was studied for walls different for composition and exhaling scenario. Figure 3.37 graphically reports results for a high-exhaling wall, i.e. $R \approx 300\,\mathrm{Bq\,m^{-2}\,h^{-1}}$, in case of four different measurement length, i.e. 3, 6, 9 and 12 h. In it, the effects of back-diffusion are evident: the slope of the measured radon concentrations (in full line) gradually reduces and this reflects on the slope reduction of trends (in dashed lines) obtained from the equilibrium equation (Eq. 3.7) solved for the exhalation value best fitting the measured trend in case of 3, 6, 9 and 12 hours-lasting measurements (in green, red, blue and black dashed lines, respectively). Considering the shorter measurement (i.e. 4 hours) as the most reliable, the radon exhalation returned by the method experiences a reduction of about 20%, 35% and 50% if the measurement length is 6, 9 or 12 hours. Such differences gradually decrease with decreasing exhalation magnitude of the wall under examination.

In light of the above, the following recommendation can be formalized for choosing the best measurement duration:

i) it is suggested to perform a first 6 hours-lasting measurement, then:

- if the radon exhalation value obtained by considering only the first

4 hours of measurement is less than $50\,\mathrm{Bq\,m^{-2}\,h^{-1}}$, the radon exhalation process should be weakly affected by the back-diffusion affect. If so, the radon exhalation values obtained by considering 4 and 6 hours of measurement should be very close to each other (i.e. relative difference of few percent). If not, some short-term phenomena have occurred and the measurement should so be repeated by increasing its duration up to 12 hours.

- if the radon exhalation value obtained by considering only the first 4 hours of measurement is more than $50\,\mathrm{Bq\,m^{-2}\,h^{-1}}$, the back-diffusion could strongly have affected measurement results. The best estimation of the radon exhalation rate is given by considering the shorter measuring interval (i.e. 3-4 hours) after having checked that no short-term phenomena had happened during the measurement. This can be verified by looking at the measured radon concentration trend (see Figure 3.35).

ii) measurement lasting less than 4 hours are discouraged because in case of short-term disturbing phenomena they become unreliable and no solution exists other than repeating the measurement. This would frustrate the only advantage of short measurement, i.e. the time saving.

iii) during the measurement, at least temperature, absolute pressure and relative humidity of room air should be monitored in order to check if significant fluctuations happen such to affect the reliability of the radon exhalation rate returned.

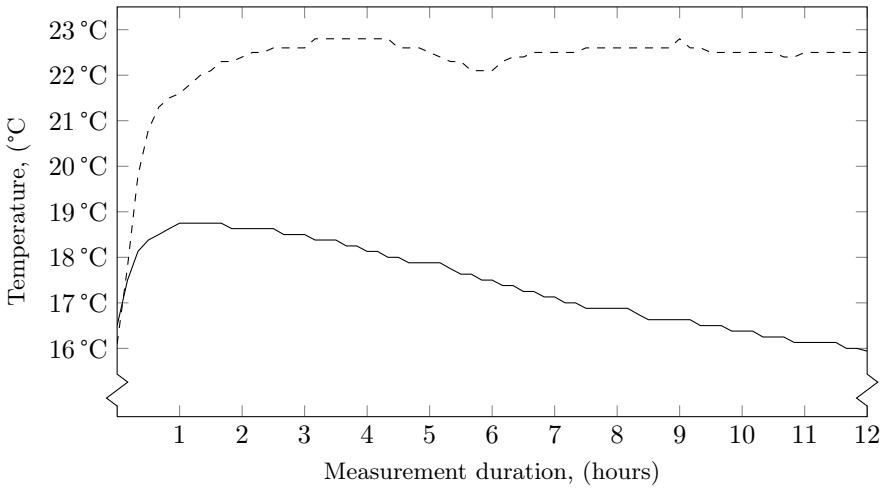

Figure 3.36: Temperature trend during two different measurement. The dashed one is flat, no significant fluctuations exist. The full one is affected by a sudden and significant drop of more than 2 °C. The measurements have been carried out at the same room, in two subsequent days at the same hour: this just to show the extremely high variability of both the absolute value and the relative temperature trend could experience during measurements. The plotted temperature values are affected by a measurement uncertainty of 0.5 °C.

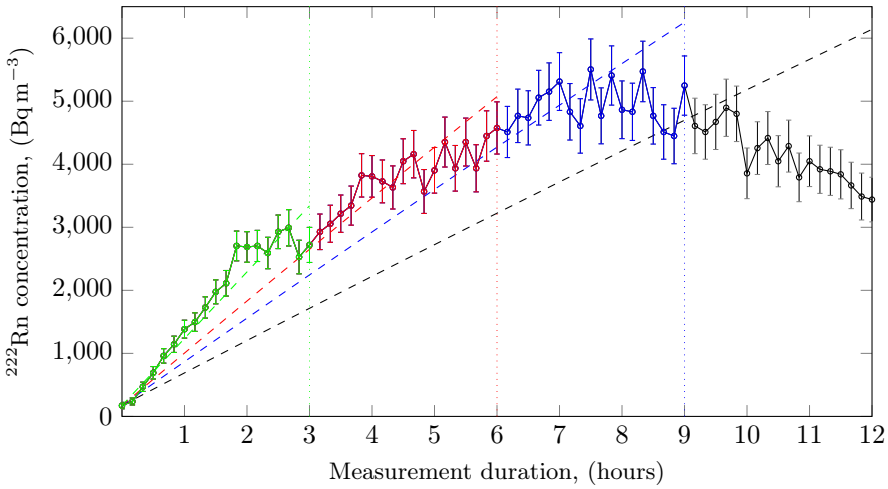

Figure 3.37: Radon concentration trend (full lines) in case of very high radon exhalation rate (i.e. $\approx 300\,\mathrm{Bq\,m^{-2}\,h^{-1}}$) and the trends corresponding to the estimated exhalation rates obtained from measurements of different duration (dashed lines). A duration of 3, 6, 9 and 12 hours has been separately considered in drawing the trends in dashed green, red, blue and black, respectively.

3.2.5 A case study of prototype application: identifying the best remediation strategy in large public buildings

The experience in large public buildings remediation is poor and it generally comes from lesson learned in remediating kindergartens and schools which are large but not very complex. In addition to this, most large public buildings are historical buildings usually with thick walls, missing or inaccurate blueprints and few information on building foundations. A survey was designed to measure the radon concentration in a historical big building in Rome. It was built in the second half of 19^{th} century and it has more than 1200 rooms, distributed on 5 floors plus the basement. The foundation is structured in several blocks, some connected to some others.

Table 3.3: Results of radon concentration measurements performed in a sample of 567 rooms. $300\,\mathrm{Bq\,m^{-3}}$ is the maximum reference level considered appropriate by the Council Directive 2013/59/Euratom (European Commission, 2014).

Floor	Measured rooms	Rooms with $C_{^{222}\mathrm{Rn}} > 300\,\mathrm{Bq\,m^{-3}}$	% of rooms with $C_{^{222}\mathrm{Rn}} > 300\,\mathrm{Bq\,m^{-3}}$
-1	12	2	17%
0	83	1	1%
1	103	37	36%
2	173	54	31%
3	192	37	19%
4	4	1	25%
	567	132	23%

The radon concentration was measured in a sample of rooms (i.e. 567) and results showed high radon levels also at higher floors (i.e. 2^{nd} and 3^{rd} floor). This behavior seemed quite peculiar. A possible explanation for this was found by looking at the foundations blocks: at the underground level, entrances of the ancient tunnels used to heat the upper floors were visible (see Figure 3.38). The original blueprints of the building also revealed the existence of pipes running through the external walls and stopping at different floor levels. Those pipes belonged to the ancient building heating system as well and connected the underground level to each room of the upper floors.

Figure 3.38: Tunnel entrances, at the foundations level, of the original heating system.

3.2.5.1 Identifying the main route for radon entry

A first explanation for high radon concentrations at upper floors was given by considering such pipes as low-resistance paths for radon accumulated in foundations that, once entered the pipes by the underground entrances (Figure 3.38), went up due to the natural pressure difference. If so, the radon should enter each room (especially those at the upper floors) mainly by exhalation from walls and a strong difference should exist between the exhalation rate from the wall hosting the discharge side of pipes connected to foundations and that from walls with nothing similar inside. In order to prove this, two different rooms, located one above the other (at 2^{nd} and 3^{rd} floor), were chosen and two apparatuses were positioned in each of them. In particular, for each room, the radon exhalation rate was contemporary measured from the external wall and from another wall (setup in Figure 3.39). The latter was chosen similar for building characteristics (i.e. thickness and composition) to the external one in order not to introduce disturbing variables into the process. In other words, the idea was to realize two contemporary measurements in both rooms avoiding confounding effects in order to attribute any difference in results to the radon source term only. The need for performing measurement in two rooms, one above the other, lied in trying to give a further confirmation to the direction followed by radon: if radon actually followed the tube length from foundations to discharges in rooms, the exhalation rate from the external walls should have decreased passing from the 2^{nd} to the 3^{rd} floor. Each set of 4 contemporary measurements lasted 6 hours according to the recommendations given in §3.2.4. The measurements were repeated 3 times, in 3 subsequent days, for a total of 12 data acquisitions, during the late afternoon (between 04:30 p.m. and 10:30 p.m.). The repetitions served to confirm the repeatability of the measuring technique also in that scenario.

Figure 3.39: Experimental setup designed for the experiment aiming to demonstrate the main carrying path of radon from foundations to rooms at upper levels. The first apparatus was closed to the wall on the left with no connection to foundations. The accumulation chamber was placed quite high (i.e. $\approx 120\,\text{cm}$) from the ground) in order to avoid disturbing effects due to unknown penetrations in the wall itself, e.g. those hosting electrical or internet network cables. The second apparatus was closed to the external wall at the end of the room (close to the window), after having checked that the wall was served by the ancient heating system. The accumulation chamber height (i.e. $\approx 50\,\text{cm}$) was chosen such to allow the can free surface to cover all the tube discharge side, whose position was assumed according to the information collected from original rooms blueprints.

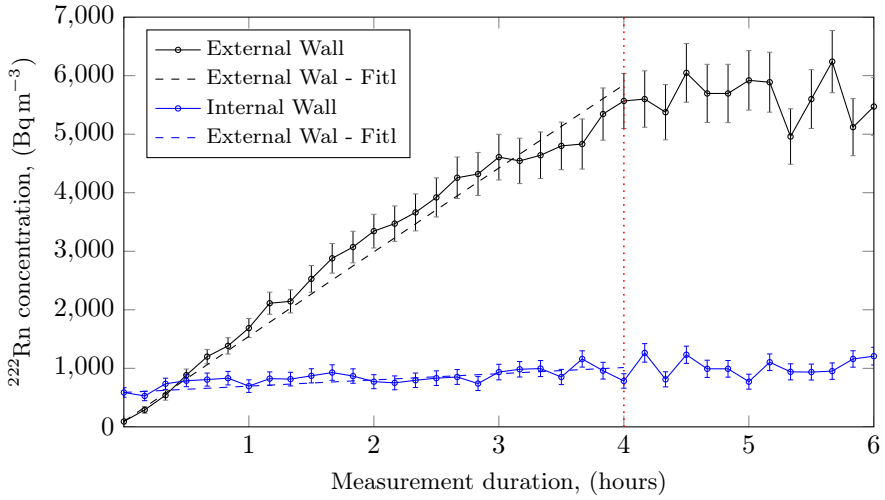

Figure 3.40: Radon concentration trends for external and internal walls measured in the room located at the second floor. For the external wall, due to the very high radon exhalation rate, the accumulation process is affected by the back-diffusion effect. According to the suggestions of §3.2.4, the radon exhalation rate is evaluated by considering only the first four hours of measurement, delimited by the vertical dotted red line.

The absolute value of the radon exhalation rate measured at the external wall of the room at the second floor was extremely significant, i.e. $380\,\mathrm{Bq\,m^{-2}\,h^{-1}}$, whereas no appreciable contribution was found from the internal wall (Figure 3.40). From such results, the following was stated: *i*) considering also the floor level, the exhalation from the walls could be considered as the main route for radon entry into that room and *ii*) the exhalation mainly took place from the external wall, the one hosting the discharge side of the tubes pertaining to the ancient heating system. The role played by such tubes in transporting radon from foundations to rooms at the upper floors seemed to be confirmed by this first set of measurements.

The scenario at the third floor, shown by Figure 3.41 was found to be slightly different. The radon exhalation rate from the external wall was significant too but not as in the room below, i.e. $103\,\mathrm{Bq\,m^{-2}\,h^{-1}}$. This decrease in the exhalation rate from the external wall was counterbalanced by a significant increase of the contribution form the internal wall which was found to exhale $195\,\mathrm{Bq\,m^{-2}\,h^{-1}}$. The suspect was that radon, once reached the third floor through the vertical pipes running through the external building walls, did not exhale exclusively from the external wall itself but, due to some wall constructive peculiarities, found its way crossing both the internal and the external wall.

Summarizing, the radon exhalation rate from the external wall strongly depends on the floor level, despite the rooms were located one above the other and the walls had analogous composition. Furthermore, exactly the same applies to the internal walls, different in exhalation magnitude but absolutely the same in constructive features. All this lead to the following statements:

i) the contribution to indoor radon concentration due to building materials of internal walls was negligible. If assumed that the composition of internal and external walls is similar, such a statement can be extended also to the external walls, regardless the floor level.

ii) the main contribution to indoor radon concentration came from radon transported from other places due to the existing pressure difference. The results of measurements performed at the second floor, together with the discovered heating system previously described, seemed to suggest the main role played by the vertical tubes that connect foundations to each room in transporting the radon to the upper floors.

Furthermore, the overall (i.e. from both walls considered) radon exhalation rate at third floor resulted to be about 20% smaller than the corresponding value found at the second floor. This was interpreted as a further clue of the route followed by radon: if it came from foundations and if it travelled along vertical pipes running through the external building walls, it appeared reasonable that the exhalation decreased with increasing floor level.

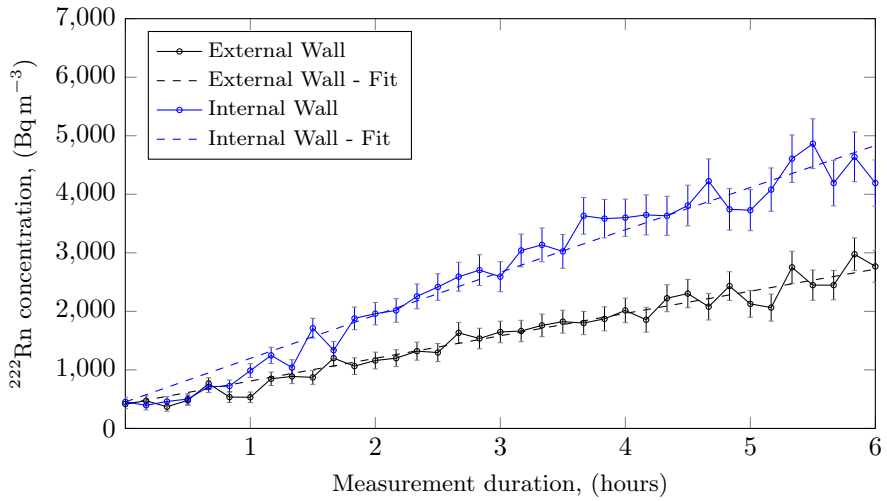

Figure 3.41: Radon concentration trends for external and internal walls measured in the room located at the third floor. Some minor short-term effects seem to slightly affect the accumulation process during the very first hours measurements.

3.2.5.2 Choosing the best remediation strategy and evaluating its performances

Moving from the hypotheses done about how radon entered the rooms at the upper floors, the remediation strategy applied consisted in installing ventilators, together with the corresponding power controls on each of the tunnel identified as belonging to the heating system. To do so, the first step was, in fact, excluding the tunnels in foundations with different purposes. Then, the entrances of all the heating system tunnels were sealed with different techniques and materials previously tested at the Laboratory of Radioactivity of the Italian National

Institute of Health. Techniques and materials used, including tests conceived and performed to prove their effectiveness for such a purpose, will be addressed by a specific paper and they are not to be considered as subjects of this thesis. Centrifugal fans were chosen as the best solution for the application considered mainly due to the large flow-rate they are capable of elaborating. In particular, once installed, the flow-rate was measured to be variable between 100 and 2470 $m^3\,h^{-1}$ according to the power supply assured. The fans were installed in a way such to draw radon-rich air from each tunnel and discharge it at the underground level. Further fans were installed to draw air from foundations and discharge it outside at a height such to avoid dangerous reentries through the windows of rooms located at the upper floors.

A second set of measurements was later conceived in order to study the effectiveness of the fans installed as a remedial action against high radon concentration at second and third floors. In the same two rooms previously considered, positioned at second and third floor, two measuring apparatuses were closed one to the external wall and the other to the internal one. The positions of the accumulation chambers were exactly the same as in §3.2.5.2. The measurements were performed in 3 consecutive days with environmental parameters assuming values similar to the ones observed during the first set. They were also performed during the same time of the day, i.e. late afternoon between 04:30 p.m. and 10:30 p.m.. All these precautions were aimed to make results of the two sets of measurements comparable one to each other.

Measurements results are shown in Figure 3.42 and 3.43 for the 2nd floor room and in Figure 3.44 and 3.45 for the 3rdfloor one.

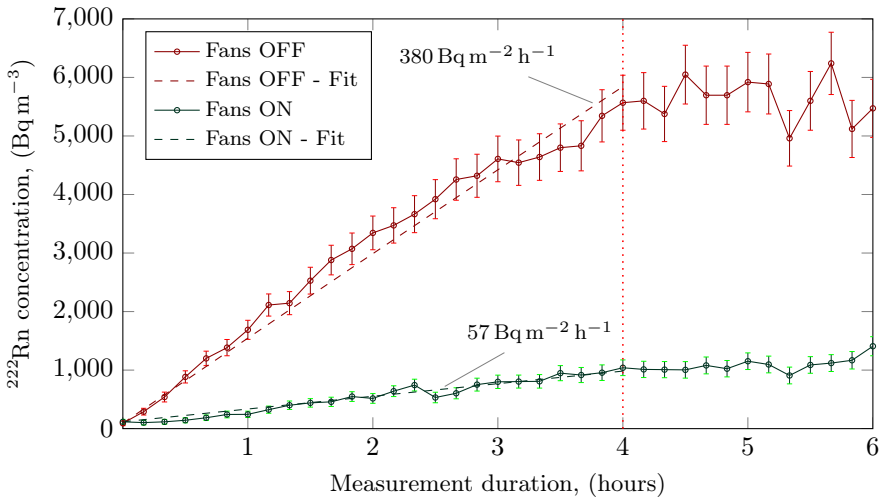

Figure 3.42: Radon concentration trends from the external wall of the room at the second floor when the underground fans were OFF and ON, plotted in red and green respectively. According to the suggestions of §3.2.4, the radon exhalation rate is evaluated in both cases by considering only the first four hours of measurement, delimited by the vertical dotted red line. This just to avoid the disturbing effect of back-diffusion. Radon exhalation rate values returned by the algorithm are reported close to the corresponding fit dashed line.

For all walls considered a strong reduction was found in the radon exhalation

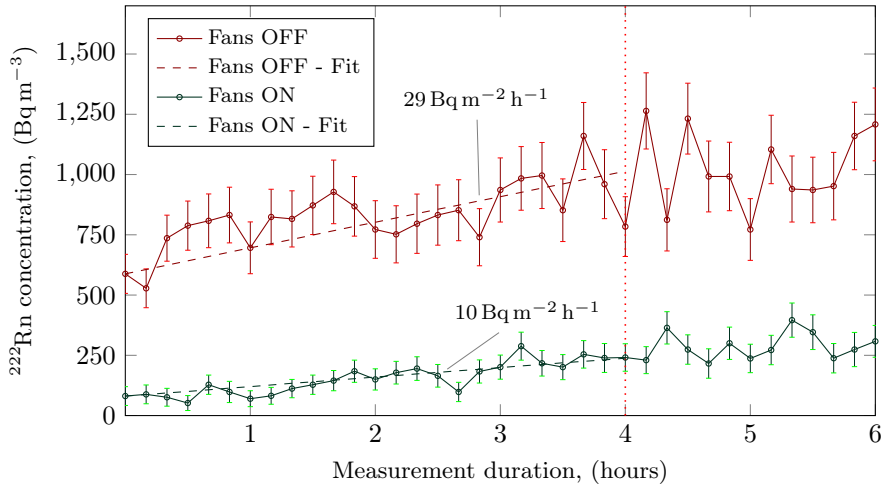

Figure 3.43: Radon concentration trends from the internal wall of the room at the second floor when the underground fans were OFF and ON, plotted in red and green respectively. According to the suggestions of §3.2.4, the radon exhalation rate is evaluated in both cases by considering only the first four hours of measurement, delimited by the vertical dotted red line. Radon exhalation rate values returned by the algorithm are reported close to the corresponding fit dashed line.

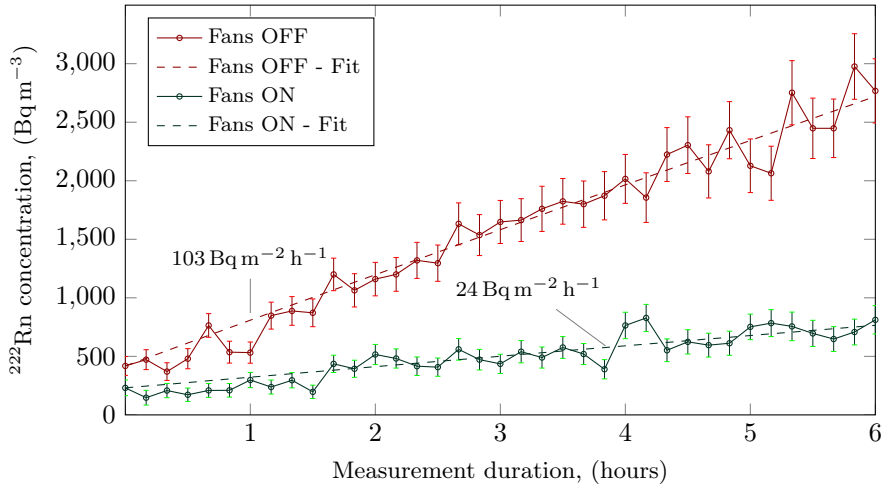

Figure 3.44: Radon concentration trends from the external wall of the room at the third floor when the underground fans were OFF and ON, plotted in red and green respectively. According to the suggestions of §3.2.4, the radon exhalation rate is evaluated in both cases by considering the whole measuring period of 6 hours. Radon exhalation rate values returned by the algorithm are reported close to the corresponding fit dashed line.

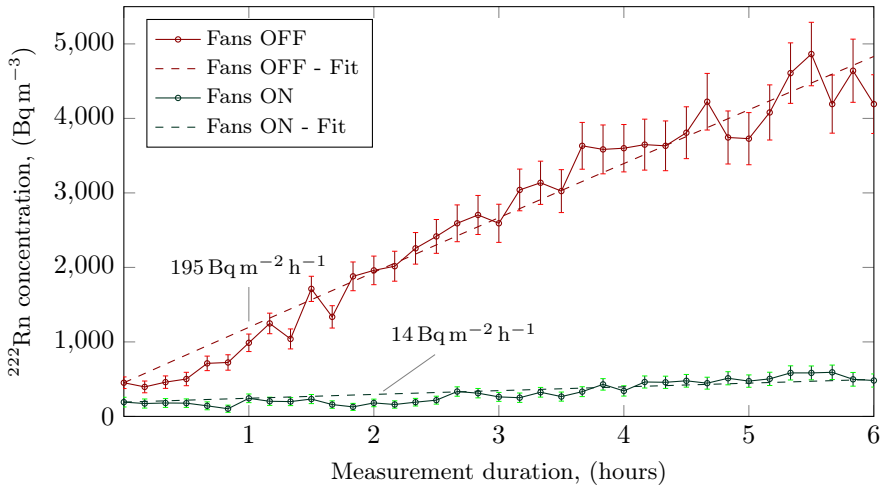

Figure 3.45: Radon concentration trends from the internal wall of the room at the third floor when the underground fans were OFF and ON, plotted in red and green respectively. According to the suggestions of §3.2.4, the radon exhalation rate is evaluated in both cases by considering the whole measuring period of 6 hours. Radon exhalation rate values returned by the algorithm are reported close to the corresponding fit dashed line.

rate due to the fans functioning at the underground floor. Relative to the external walls, the ones hosting the discharge sides of the heating system tunnels, relative reductions of 85% and 77% were found at 2nd and 3rd floor, respectively. The internal walls experienced a relative reduction of 66% and 93% at 2nd and 3rd floor, respectively. These results, here briefly discussed, represented a very clear demonstration of the effectiveness of the tested remedial systems. The performances of the underground fans were then evaluated by performing measurements in a wider set of rooms positioned all over the building and repeating such measurements under different climatic conditions in order to extend both spatially and temporarily the validity of results obtained.

3.3 Conclusions

An innovative experimental apparatus to measure the radon exhalation rate directly in-situ from vertical surfaces of walls has been conceived, designed and realized at the Laboratory of Radioactivity of the Italian National Institute of Health. The main innovation stands in the apparatus itself: in fact, no measuring setup, with similar purposes, exists in literature. This lack explains why no previous works addressed the measurement of the exhalation rate directly on site through the so-called accumulation method as described by the ISO 11665-7. The project is completely open access. All the files needed by a laboratory to build its own measuring apparatus and start measuring are available on Github at this LINK. This could promote a wider spread of this technology allowing both to increase the number of in-situ measurements available on literature and improving the functioning of the apparatus itself due to collaborations, or simply inputs, from all over the world. All the instrumentation used, including the

radon detectors, have been chosen according to the general criteria of prompt availability and inexpensiveness.

The prototype is intended to solve the main critical issues associated to this kind of measurements that, until now, have prevented a similar apparatus from being commercially available on the market of radon industries: mechanically sustaining the accumulation can during the measurement without interfering with the measurements itself (*i*) and assuring the sealing of the chamber relative to the radon detector (*ii*) and the wall under investigation (*iii*). The prototype also aims to avoid the interfering effect of the chamber pressurization during the measurement and to reduce the effect of the back-diffusion on the accumulation process.

The apparatus has undergone a full commissioning that included: *i*) an air tightness test, *ii*) a repeatability analysis and *iii*) the development of a practical guide concerning the best duration of measurements in different scenarios. The air tightness test was split in two parts, the first one aiming to demonstrate the tightness of the chamber with all its penetrations and connections with the exception of the free surface interface. The latter was specifically investigated by the second part intending to extend the results of the first one to the interface with the most common wall surfaces.

In the framework of a study on a large historical building in Italy, the measuring apparatus has been used to identify the main route of radon entry into the rooms at the upper floors, to suggest the best remediation strategy accordingly and to verify its effectiveness.

The main further applications will comprehend, other than a more extended usage in the field of remedial actions against high radon concentrations in case of high contribution from building materials, a comprehensive and systematic study aiming to analyze the eventual relationship between radon exhalation rate measured at the laboratory on samples and the same rate measured directly in-situ on the finished product (i.e. the wall).

Chapter 4

Design and commissioning of an innovative radon chamber for radon detectors testing and calibration

4.1 Introduction

The growth of interest in radon measurements has led to the development of a wide range of radon detectors for both professional and "domestic" measurements in the framework of the increasing attention given to the so-called citizen science and of the improved awareness of the population about risks linked to radon exposure. The direct consequence of this has been increasing the request of testing facilities and calibration apparatuses. These facilities should always rely on radon chambers that are designed to produce reference atmospheres whose radon activity concentration depends on the radium source employed and on the chamber volume. These facilities can be roughly divided into two families (Azimi-Garakani, 1992): radon "boxes" with a volume of a few cubic meters (e.g. the radon facility at Naples University with a volume of 33 L (Venoso et al., 2009)), and radon "walk-in chambers" characterized by a larger volume (e.g. the ENEA-INMRI 'walk-in' radon chamber with a volume 18 m^3 (Cardellini et al., 2016)). Dealing with the calibration of active detectors, much bigger than the passive ones, the first kind of radon chamber is often suitable to host only a very limited number of monitors and the walk-in radon chambers end up representing the only facilities to make feasible calibrating several (i.e. > 10) radon continuous monitors in parallel. The same consideration applies to the investigation of the influence of environmental parameters, i.e. temperature, relative humidity, absolute pressure and aerosol concentration and granulometric distribution, on detector response. Similar tests are performed in facility designed in a way such to allow the climate control, e.g. (Honig et al., 1998).

Dealing with radon chamber, the international standard IEC 61577-4 (International Electrotechnical Commission, 2009) lays down requirements for radon chambers, defined as the "System for Test Atmospheres with Radon" (STAR),

needed for testing, in a reference atmosphere, the instruments measuring radon and its decay products. Such a standard provides guidance for those facing problems associated with the production of equipment for setting up reference atmospheres for radon and its decay products.

According to the current state of the art, radon chambers are characterized by significant costs as design, construction, commissioning, and maintenance are concerned. In particular, critical issues are *i*) materials used for the structure and the sealing, *ii*) fan system for concentration homogenization, *iii*) source–chamber interface circuit and *iv*) control instrumentation. Moreover, current radon chambers are typically managed by a trained technician, manually operating on the apparatus due to lack of remote monitoring and control. This is also required considering that the radon concentration established inside the chamber can be varied only by changing the ^{226}Ra source interfaced to the chamber, i.e. by changing the activity of the parent nuclide. This happens because a certain activity concentration of ^{222}Rn is realized via a radon gas activity standard (i.e. a ^{226}Ra source whose activity is stated at a given time) circulated inside a calibration volume, both values traceable to national standards (Röttger and Honig, 2011). Only changing the source activity, other than varying the calibration volume, would result in a variation of the radon concentration inside the chamber. As a result, industries, agencies or institutions managing a radon chamber need as many radium sources as the radon concentrations required by the different calibration protocols. But, as a matter of fact, holding more than one source complicates the licensing requirements concerned with radioactive materials possession established by the national transpositions of the Council Directive 2013/59/Euratom (European Commission, 2014). Another issue frequently discouraging laboratories from realizing, or acquiring, radon chambers is given by the significant dimensions of such apparatuses (similar systems are specifically addressed by Lee et al., 2004; Vargas et al., 2004), notwithstanding the most frequent operation is the calibration of very small devices such as passive solid state nuclear tracks detectors (SSNTDs) (e.g. Mamont-Cieśla et al., 2010).

This work describes an innovative 0.1 m^3 radon chamber fully designed, built and tested at the laboratory of Radiation Protection of Sapienza - University of Rome. It has been conceived as and easy-to-assemble, cheap, and small facility dedicated to research on radon and calibrations services. The main innovation stands in the way radon activity concentration is varied and controlled within the chamber atmosphere: the system, in fact, may allow to establish a wide range of ^{222}Rn concentrations through a single ^{226}Ra source placed outside the control volume and by means of two air circulation circuits controlled by specific electric pumps remotely controlled and actuated. Such a system is intended to allow the calibration of detectors according to standard calibration procedure and to evaluate the instruments' dynamic response to radon-concentration variation in time.

4.2 Materials and methods

The radon chamber has been conceived as a plexiglass-made structure. The choice of plexiglass (polymethyl methacrylate, PMMA) has been done according to three fundamental criteria: *i*) the material should be transparent in order

to monitor the displays of the instrumentation placed inside the chamber during the measurements, *ii*) the material should be as resilient as possible and *iii*) the material should be as light as possible in order not to introduce requirements about the load resistance of the structure mechanically sustaining the chamber. The PMMA is better than glass in all these fields: compared to glass, it guarantees a better transparency because it is less affected by light reflexes and it is more resilient and lighter ($\rho = 1.19\,\mathrm{g\,cm^{-3}}$). Furthermore, its permeability to radon migration is lower than for glass (Arafa, 2002). It is also relatively cheap and easy to work and assemble.

The chamber length, width and height are 50 cm, 40 cm and 51.4 cm, respectively. The lateral sides have a thickness of 1.5 cm whereas the basis and is 2 cm-thick. The overall height is comprehensive of the upper plexiglass plate that is 1.4 cm-thick. The access to the inner volume is granted by such a plate that is removable.

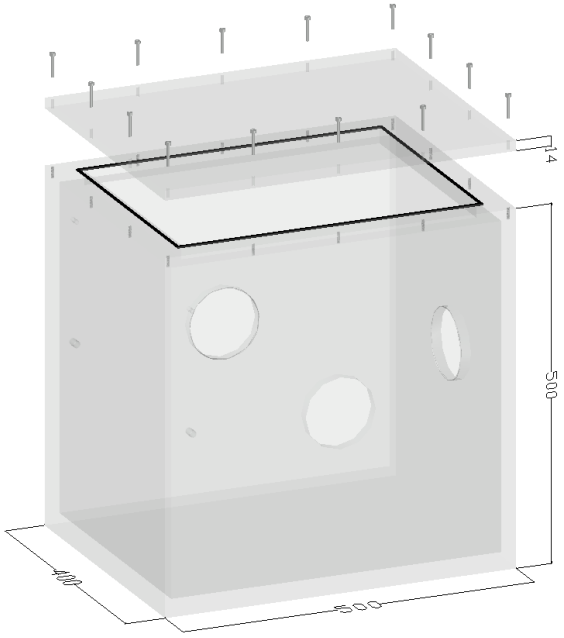

Figure 4.1: Axonometric view of the radon chamber external structure. The top side is represented when not fixed to the lower part. All dimensions are reported in millimeters.

The sealing between the top side and the lower 5-sides structure is provided by a square shaped o-ring made of radon tight rubber with a diameter of 4 mm. This o-ring is housed in 3.5 mm-wide rectangular groove realized on the upper frame of the lower part of the chamber. Using an o-ring slightly larger than the corresponding housing aims to assure the air tightness in case of rubber tensing due to thermal effect. The upper plexiglass plate is closed to the underneath structure by 14 screws whose housings are on the lateral surfaces frame, externally to the o-ring position.

Table 4.1 reports internal and external dimensions of the radon chamber. However, the internal volume reported in the table does not consider the volume

delimited by the upper vertical frame below the removable top side, i.e. 2.7 ± 0.1 L. So, the total inner volume of the void radon chamber is 82.7 ± 0.4 L. All the geometrical details are shown by Figure 4.2 that presents the two chamber vertical sections.

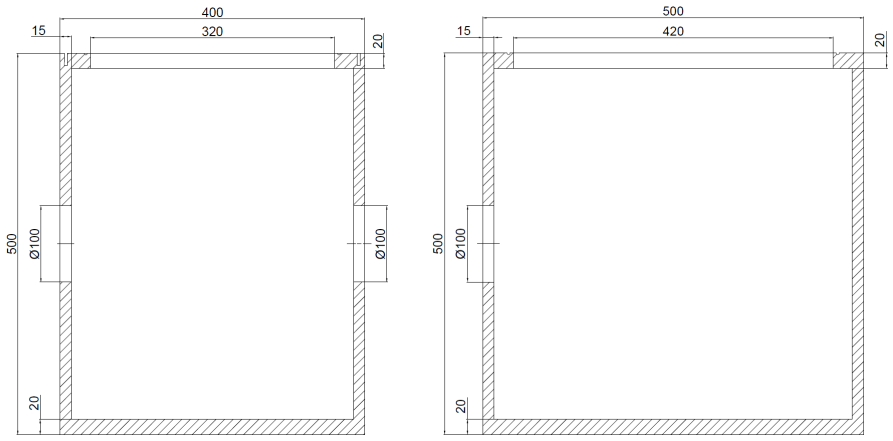

(a) Width-Height Top View (b) Length-Height Top View

Figure 4.2: Vertical sections of the radon chamber external structure. Dimensions are in mm.

Table 4.1: External and internal dimensions of the radon chamber. [a] By internal height it is meant the distance between the basis and the upper rectangular frame lower surfaces.

	Internal	External
Length	470±5 mm	500±5 mm
Width	370±5 mm	400±5 mm
Height	260[a] ±5 mm	514±5 mm
Volume	80.0±0.3 L	102.8±0.4 L

4.2.1 Hydraulic connections

A first circular penetration has been realized on the short lateral surface of the chamber to assure hydraulic connection between inside and outside the chamber. Their diameter is 10 cm.

The hole, female threaded, hosts a brass porthole made of two parts: the first component (left side of Figure 4.3), male threaded, is screwed to the hole thread from the outside while the second one (right side of Figure 4.3) acts like a brass nut, securing the first component from the inside. The sealing is assured by the thread itself and a by specific o-ring, located between the internal surface of the chamber lateral side and the second component of the porthole (right side of Figure 4.3) just described.

Inside the porthole, 4 holes have been realized with Whitworth BSPP G1/8 thread. Internal and external diameter are 8.566 mm and 9.728 mm, respectively. Each hole hosts a stainless steel taper straight male adapter 6/4 mm x

G1/8" BSPT-M (§4.5, Figure 4.31). The assembling is reported in Figure 4.4. Such straight male adapters have been chosen in order to allow the connection with teflon (PTFE, material frequently employed in application concerning radon due to its tightness (Jobbágy et al., 2020)) tubes with inner and outer diameter of 4 and 6 mm, respectively.

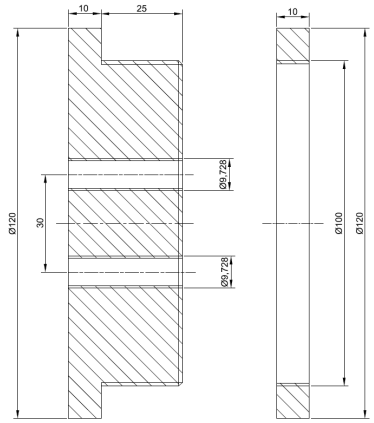

Figure 4.3: Vertical section of the brass porthole screwed inside the 10 cm hole on the short lateral side of the chamber. Its two components, acting like the bolt and the corresponding nut, are separately represented. All dimensions are reported in millimeters.

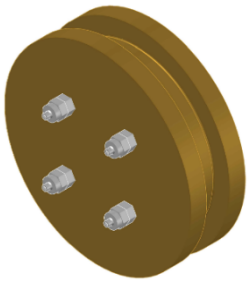

Figure 4.4: Axonometric view of the brass porthole screwed inside the 10 cm hole on the short lateral side of the chamber. Its two components, acting like the bolt and the corresponding nut, are represented screwed one to each other.

Two further holes with a diameter of 1 cm have been realized on the long lateral sides of the chamber, one for each. The holes have been female threaded in order to host a male screwed brass cylinder. Such cylinder is secured outside and inside the chamber by brass hexagonal nuts. The sealing is assured by the thread itself and by a specific o-ring, located between the internal surfaces of the chamber lateral sides and the internal nut. Both nuts have been female threaded in a way such to host two stainless steel taper straight male adapters 6/4 mm x G1/8" BSPT-M, one for each side. The overall assembly is reported by Figure 4.5.

The radon chamber with all its hydraulic equipment mounted on appears

like displayed by Figure 4.6.

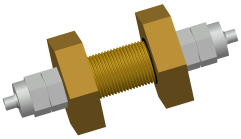

Figure 4.5: Axonometric view of the brass cylinder screwed inside the holes on both long lateral sides of the chamber. On each side a male adapter is connected. The o-ring is placed exclusively at the internal side before the securing brass nut.

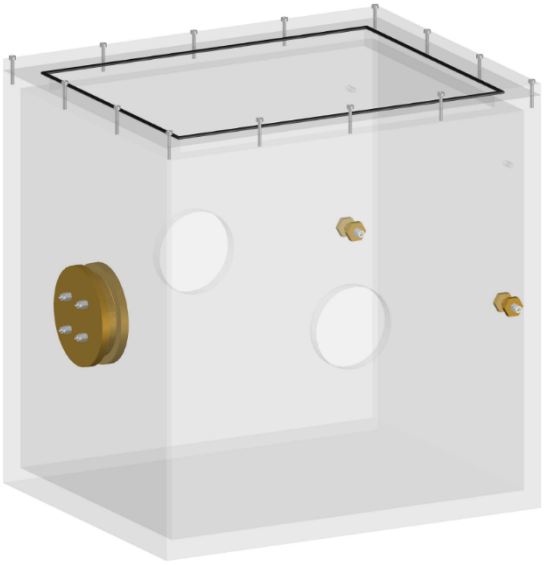

Figure 4.6: Axonometric view of the radon chamber equipped with all the hydraulic connectors. The top side is represented closed to the lower. The porthole is mounted on the short lateral side, whereas the cylinders are on the long lateral sides, one for each.

4.2.2 Electrical connections

The electrical connections, i.e. power supply and data transfer, between inside and outside the chamber have been realized by a specific brass porthole screwed to the threaded hole drilled on one of the long chamber sides. Two couples of penetrations have been realized in the porthole with diameters of 20 mm and 26 mm, respectively. Their sections are reported in Figure 4.7. The sealing is assured, other than by the crewing itself, by a brass ring that secures the porthole from the inside while pressing against an o-ring.

Proper connectors have been screwed to the brass porthole. The main issue was avoiding that such connectors could represent a route for radon leakage towards the outdoor environment. This has been assured by using MIL connectors

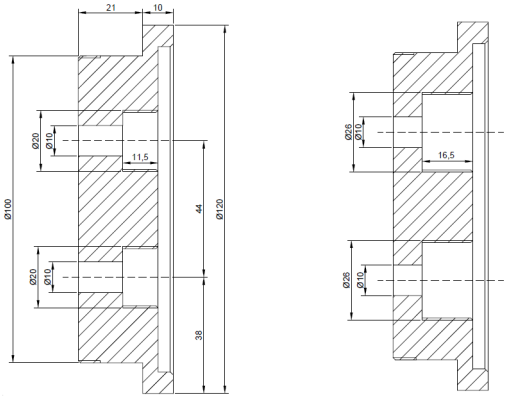

Figure 4.7: Vertical sections of the brass porthole screwed inside the 10 cm hole on one of the long lateral sides of the chamber (on the left) and of the corresponding securing brass ring (on the right). The two components, acting like the bolt and the corresponding nut, are separately represented. All dimensions are reported in millimeters.

(class A and series MS) satisfying high standards in terms of air tightness. The chosen connectors are manufactured by Amphenol® and are listed in Appendix B. Four MIL straight male connectors, two with 4 pins (Figure 4.38) and two with 10 pins (Figure 4.40), have been screwed to the brass porthole from outside the chamber. The corresponding female connectors (Figure 4.39 and Figure 4.41) can be connected to the male ones from outside. The air tightness is assured, other than by the connectors themselves, by 4 o-rings with a diameters of 0.6 mm. The axonometric view of the so-equipped brass porthole is reported by Figure 4.8. In such a way, 28 pins have been made available for air-tight connections between inside and outside the chamber. The electrical continuity between inside and outside the chamber has been easily realized by soldering the cables sides to the internal pins of male connectors and to the external pins of the female ones. The pins have been connected as follows:

3 pins connected to the main power supply of inner devices;

10 pins dedicated to the RS-232 Serial Port connecting the reference detector inside the chamber to an external PC;

10 pins (5+5) dedicated to 2 USB Serial Ports providing connection for further internal devices;

5 controlling 4 external solenoid valves, on both air circulation circuits, by an internal Arduino microcontroller.

Further details on all the connections made will be provided in the following.

On the opposite lateral long side of the chamber, a third pothole has been installed. This porthole has no specific purposes and it is currently hosting a PTFE disk just to ensure its tightness. It has been realized with the aim to avoid any mechanical processing on the chamber. In such a way, if new needs of realizing further connections between inside and outside the chamber should rise in the future, the current porthole (with the PTFE disk) could be easily

substituted with one specifically designed for the desired function. The securing and sealing mechanism of this porthole is absolutely the same the other two portholes presented. Vertical sections of porthole and securing ring are shown in Figure 4.9.

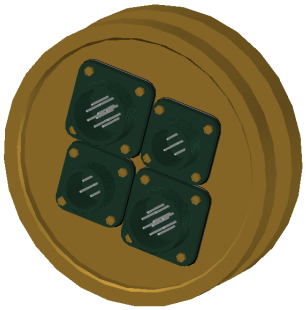

Figure 4.8: Axonomertric view of the brass porthole used for power supply and data transfer of internal instrumentation. In this representation its two components, acting like the bolt and the corresponding nut, are assembled together.

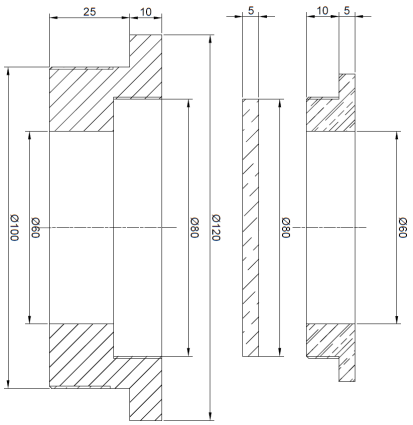

Figure 4.9: Vertical sections of the customizable brass porthole hosting the PTFE disk (on the left) and of the corresponding securing brass ring (on the right). The two components, acting like the bolt and the corresponding nut, are separately represented. All dimensions are reported in millimeters.

4.2.3 Monitoring of environmental parameters

The chamber has been equipped with two sensors, and the relative transmitters, of environmental parameters. The first (II SERIE RHP MS2-X101, manufactured by Dwyer®) is aimed to measure the pressure difference between inside and outside the chamber and the second (RHP-3D33-LCD, manufactured by Dwyer®) monitors the relative humidity and the temperature inside the chamber. Both sensors, whose specifics are reported in Appendix C, are equipped with a display, for a prompt communication of the values registered to the op-

erator, but contemporary elaborate an analogue signal to be sent as input to a microcontroller for data logging or analysis. An Arduino UNO Rev3 (Ard, a) has been employed for such purposes, coupled with a Wireless SD Shield [1] and a Real Time Clock (RTC) module DS3231[2]. The functioning code of the Arduino board is reported in the following.

```
#include <DS3232RTC.h>
// Library of the RTC.
#include <SD.h>
// Library of the SD Shield.
#include <SPI.h>
// Library for the Serial Peripheral Interface
#include <Time.h>
// Library including commands about time.

char c;
String stringa;
File myFile;
//Three variables (1 char, 1 string and 1 file) are initialized.
DS3232RTC myRTC(false);
//The I2C bus is not initialized.

void setup() {
    Serial.begin(9600);
    Serial.print("Initializing SD card...");

    if (!SD.begin(4)) {
      Serial.println("Initialization failed!");
      while(1);
    }
    Serial.println("Initialization done.");
//4 is the pin connected to the chip select line of the SD card.

    myRTC.begin();
    myFile=SD.open("filename.txt", FILE_WRITE);
//Opening a file called "filename" on the SD.

    if (myFile) {
      Serial.println("First file raw: ");
//The code ask to write on the serial the string desired as first
//raw of the file just opened.
      while(!Serial.available()){
      }
      stringa="";
      do{
```

[1]The Wireless SD shield allows an Arduino board to communicate wirelessly using a specific module. The module can communicate up to 30 meters indoors or 90 meters outdoors (with line-of-sight). Included on board is a SD card slot. (Ard, b)

[2]The DS3231 is a low-cost, highly accurate Real Time Clock which can maintain hours, minutes and seconds, as well as, day, month and year information. It is needed due to the lack of an internal clock by the th Arduino UNO.

```
        if (Serial.available()){
          c=Serial.read();
          stringa+=c;
        }
//The typed string is acquired as a succession of single characters.
      } while (c != '\n');
//The new line command stops the raw acquisition.

     Serial.print(stringa);
//The serial monitor displays what just typed.
     myFile.println(stringa);
//The acquired string is printed on the file.
     myFile.println("Date and hour; Temperature [°C]; Pressure [Pa];
Relative Humidity [%]");
//Column headings are printed on the file as second raw.
     myFile.close();
    }
    else {
      Serial.print("errore");
    }
}

void loop () {
    myFile=SD.open("filename.txt", FILE_WRITE);

    if (myFile) {
    Serial.println ("Writing on SD...");

    tmElements_t tm;
    RTC.read (tm);
//The following commands write on the file day, month, year,
//hour, temperature, pressure and relative difference read.
    myFile.print (tm.Day, DEC);
    myFile.print ('/');
    myFile.print (tm.Month, DEC);
    myFile.print ('/');
    myFile.print (tm.Year+1970, DEC);
    myFile.print ("; ");
    myFile.print (tm.Hour, DEC);
    myFile.print (':');
    myFile.print (tm.Minute, DEC);
    myFile.print (':');
    myFile.print (tm.Second, DEC);
    myFile.print (" ; ");
    myFile.print (map(analogRead(A0),0,1023,0,100)-40);
//Temperature analogue reading is mapped considering that the
//sensor range is [-40;60]°C.
    myFile.print (" ; ");
    myFile.print(map(analogRead(A1),0,1023,0,125));
//Pressure reading is mapped considering that the sensor range is
```

```
//[0;125]Pa
    myFile.print(" ; ");
    myFile.println(map(analogRead(A2),0,1023,0,100));
//Relative humidity reading is mapped considering that the sensor
//range is [0;100]%.
    myFile.close();
    delay(5000);
//This is delay between two subsequent data acquisition: 5 seconds.
    }
    else{
    Serial.println("errore");
    while(1);
    }
}
```

The output of the code just described is a .txt file, saved on the SD card, containing all the temperature, pressure and relative humidity values recorded during the acquisition. The time elapsing between subsequent data logged is not an explicit code input but can be easily modified as well (see the code comments above).

The power (24 V) is supplied to the sensors outside the chamber.

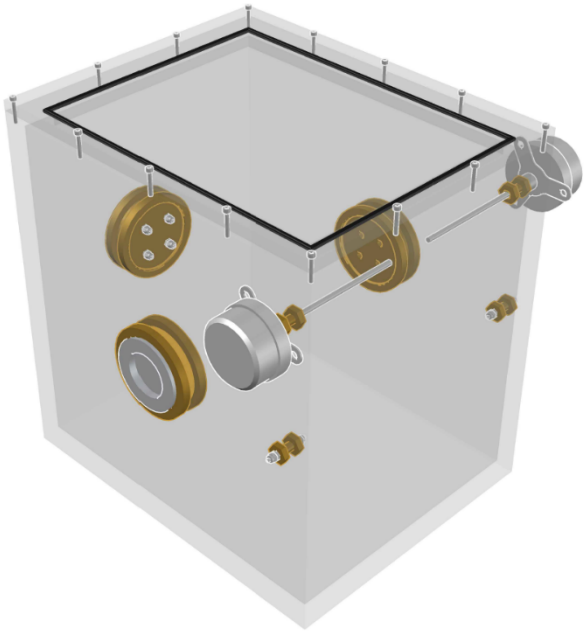

Figure 4.10: Axonometric view of the radon chamber with all the elements described: the three portholes, the two sensors and the additional connection with the external environment.

The sensors are designed in a way such to allow the sensitive element to be inside the chamber while all the other components, the display included, are left outside. By employing the same brass cylinders seen above (Figure 4.5), the sensitive element of both the sensors are positioned inside the chamber by

crossing two further holes realized on the two opposite long sides of the chamber. The final configuration of the radon chamber is shown in Figure 4.10.

4.2.4 Radon source

The ^{222}Rn hosted inside the chamber is produced from the radioactive decay of a ^{226}Ra source connected to the chamber itself. The source is not certified and it has been fully realized at the Laboratory of Radiation Protection of Sapienza - University of Rome moving from the availability a radium limescale settled on the bottom of a glass beaker, anciently used to enrich water with radon by bubbling technique.

Figure 4.11: ^{226}Ra source specifically designed for the operation of the radon chamber. The picture clearly shows the brass external cylinder and the PTFE top side secured to the lower part by six screws. The inlet connection is on the top and it is realized through an elbow taper male adaptor (Figure 4.34). The outlet connection is placed at the bottom of the brass cylinder and it is obtained through the same elbow adapter. Both on outlet and inlet, a ball-valve with Whitworth G1/8" BSPP-F thread serves to keep the radon-rich air inside the source during the accumulation period, i.e. 4-5 times the half life of ^{222}Rn.

A brass cylinder ($OD = 10\,\text{cm}$) has been designed and realized to encapsulate the beaker and providing adequate shielding for ^{226}Ra γ-rays, essentially the 186.211 keV. The top side is a 1.5 cm thick PTFE cap, secured to the brass upper flange ($OD = 15\,\text{cm}$) by screws equal to those used for the radon chamber. Inside the brass cylinder, a coaxial glass cylinder ($OD = 6\,\text{cm}$) with a shorter diameter hosts the radium source at its basis. The latter is suspended from the brass basis by a PLA spacer realized by a 3D printer. The inlet connection has been so set on the top of the brass cylinder and it extends itself inside the

glass beaker through a PTFE 1/8" tube ($ID = 4\,\text{mm}$). Such a configuration aims to prevent the radon-charged air from layering and bedding. The outlet connection has been set on the bottom of the brass cylinder in order not to make the suction interfere with the inlet air flow. Attention has been paid in connecting the outlet to the volume between the brass and glass cylinder. This to prevent the outlet flow rate from damaging the radium limescale. The ^{226}Ra retained inside the limescale solid matrix, in fact, could be re-suspended by high flow rate if a proper distance, or specific obstacles, do not exist between the outlet and the source itself.

The need for the source to be self-shielding arose from the desire to reduce the distance existing between the source itself and radon chamber in order to contain the distributed head losses. The shielding has been designed by the Monte Carlo N-Particle eXtended Transport Code (MCNPX) (Pelowitz, 2011) with the aim to make negligible the effective dose 1 cm far from the brass cylinder relative to the existing gamma dose rote due to the natural background, i.e. $\approx 0.3\,\mu\text{Sv}\,\text{h}^{-1}$.

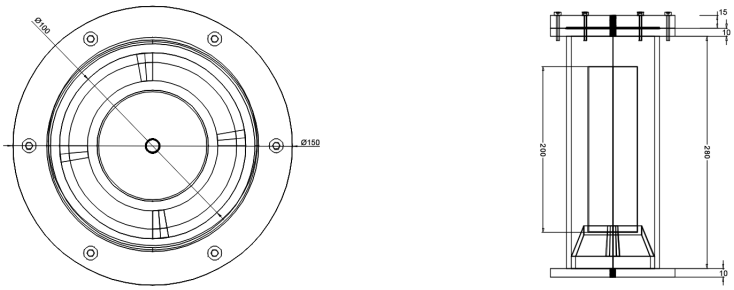

(a) Horizontal Section (b) Vertical Section

Figure 4.12: Horizontal and vertical sections of the ^{226}Ra source connected to the radon chamber. Dimensions are in mm.

4.2.5 Air circulation circuits

The regulation of the radon concentration inside the chamber is conceived to be the result of the contemporary operation of two air circuits, the first connecting the radium source to the chamber and the second one putting in communication the chamber to the outdoor air. The source-chamber circuit has been realized before the apparatus commissioning here discussed whereas the chamber-outdoor circuit, despite having been designed together with the first one, has been realized later. This choice has been motivated by the need of taking into consideration all the lessons learned from the realization of the source-chamber circuit while implementing the communication circuit with the outdoor air.

4.2.5.1 Air circuit between the ^{226}Ra source and the radon chamber

The components of the circuit moving the radon-rich air from the source to the chamber and back, whose scheme in reported in Figure 4.14, are fully described in Appendix D.

The inlet leg has been designed to host, outside the chamber, an electrovalve SBSV-B1N4 Dwyer® (§4.8.3) and a ball valve manually operated. On the same

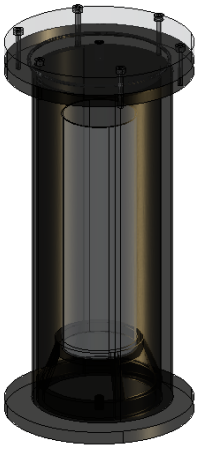

Figure 4.13: Axonometric view of the ^{226}Ra source including all the internals. This view allows to see the position of the PLA spacer that, lying on the brass lower flange, suspends the internal glass coaxial cylinder.

leg, inside the chamber, a flowmeter VFA-21 Dwyer® (§4.8.1) has been placed before, referring to the air flow rate direction, a micro diaphragm gas pump NMP 09L KNF® (§4.8.6). In order to avoid pump overheating, a DC brushless axial fan SUNON (§4.8.5) has been placed close the pump itself.

The outlet leg has not been equipped with a pump so the overpressure due to the inlet pump operation is designed to be the only responsible for the air leaving the chamber towards the radium source. The outlet flow rate is monitored inside the chamber by an other flowmeter VFA-21 Dwyer®. Outside the chamber, between a manually operated ball valve and an electrovalve SBSV-B1N4 Dwyer®, a check valve BICV-0F01 Dwyer® (§4.8.4) is aimed to prevent radon-rich air from flowing back to the chamber through the outlet leg. The position of the check valve is justified by the need of a safe maintenance in case of malfunctioning: in this way, closing both the shut-off valves would be sufficient to isolate the part of the circuit with the check valve.

Pump flow rate characterization The micro diaphragm gas pump NMP 09L KNF® (§4.8.6) has undergone a full characterization process aiming to experimentally verify the air flow rate processed by the pump either in no-load (i.e. pump operating in free air) and in actual-load conditions (i.e. pump properly connected to the chamber-source circuit).

The results of both tests (Figure 4.15) demonstrate the possibility to perform a regulation of the air flow rate by operating on the power supply voltage with the only condition of not exceeding the nominal value indicated by the manufacturer.

Voltage divider A custom voltage divider has been specifically designed in order to allow variation of the power supply voltage of the pump. Such a voltage divider has been conceived as a fully remote-controlled device and its functioning is based on the contemporary operation of four different relays. The

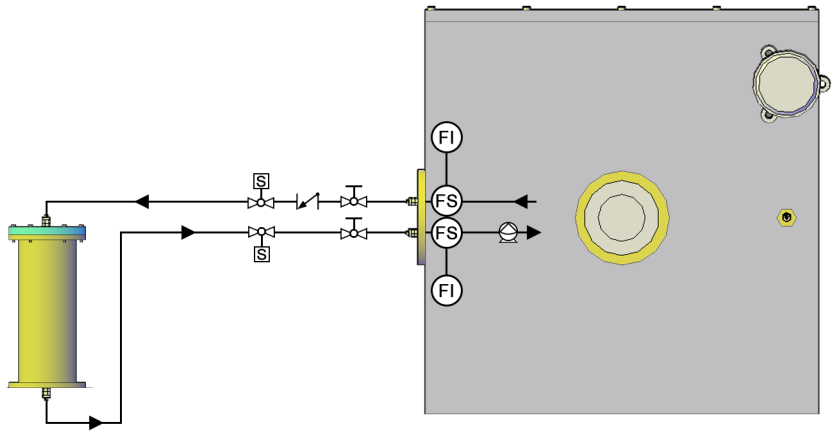

Figure 4.14: Scheme of the circuit connecting the radon chamber to the radium source. The pump has been installed inside the radon chamber on the inlet leg. The flowmeters have been mounted on both legs inside the chamber in a way such to be visible from the outside. Outside the chamber, on each legs, a ball valve manually actuated has been coupled with an electrovalve actuated by a solenoid. On the chamber-to-source leg (i.e. outlet leg), a check valve prevents the air from flowing back from the source to chamber. All the components are represented through the corresponding P&ID symbols.

Table 4.2: Power supply voltage of the micro pump, operating in the chamber-source circuit, as a function of the relays switches positions in no-load and full-load conditions. "1" and "0" states stand for switch closed and open, respectively.

	Relay				No-Load V	Full-Load V
	#1	#2	#3	#4	(V)	(V)
V_1	1	0	0	0	6.6	6.6
V_2	0	1	0	0	6.2	5.3
V_3	0	0	1	0	5.6	4.2
V_4	0	0	0	1	5.1	3.5

power supply voltage of the pump can be so regulated by acting on the relays switches (Table 4.2).

The four relays are both powered (the power supply voltage is 5 V) and controlled by an Arduino UNO WiFi Rev2 (Ard, c). The switches are connected in normally open configuration for the pump safeguard. The scheme of the electrical connections between the microcontroller and the relays is reported by Figure 4.17. The four relays are positioned inside the radon chamber, as well as the pump power supply and the Arduino UNO WiFi Rev2 used to control the whole system.

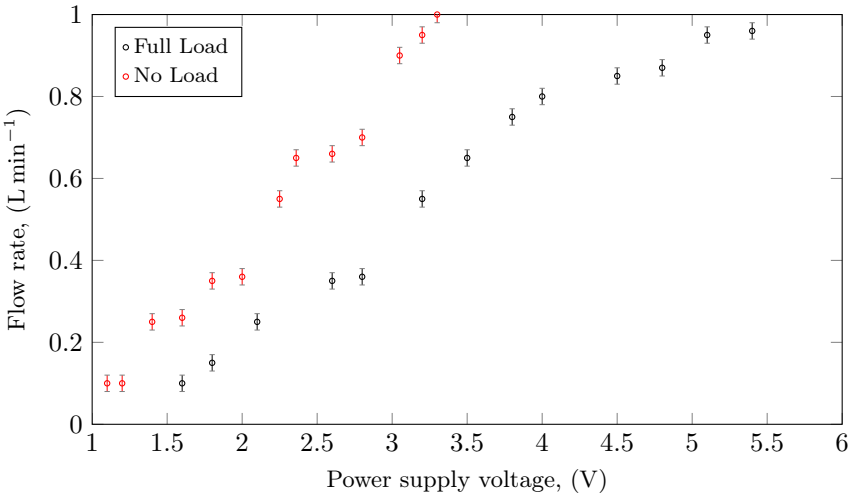

Figure 4.15: Air flow rate processed by the micro pump at no-load and full-load conditions. The no-load test has been stopped at $\Delta V = 3.4\,\mathrm{V}$ in order to avoid flow rate values exceeding the range declared by the manufacturer. The full-load test has been stopped at $\Delta V = 6\,\mathrm{V}$ in order to prevent overvoltage operation of the pump.

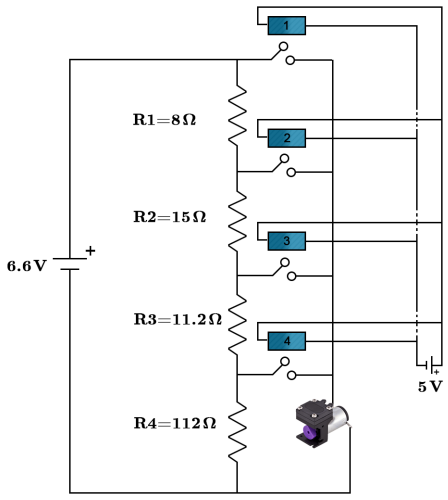

Figure 4.16: Voltage divider designed to vary the power supply voltage of the micro pump operating in the chamber-source circuit. The ideal voltage generator at 6.6 V stands for the power supply of the pump whose nominal and no-load voltage are 6 V and 6.6 V, respectively.

4.2.5.2 Air circuit between the radon chamber and the outdoor air

The components of the circuit moving the radon-rich air from the chamber to the outdoor air and back, whose scheme in reported in Figure 4.18, are similar to those previously seen for the source-chamber circuit and are anyway fully described in Appendix D.

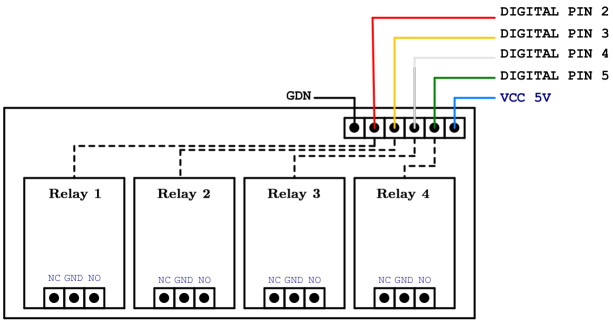

Figure 4.17: Scheme of the electrical connections between the Arduino UNO WiFi and the four relays used to control the voltage divider of the chamber-outdoor circuit.

Unlike the chamber-source circuit, a micro diaphragm gas pump NMP 09L KNF® (§4.8.6) has been mounted on the outlet leg, inside the chamber together with a flowmeter VFA-22 Dwyer® (§4.8.2). Outside the chamber, the same leg has been equipped with a ball valve manually operated and an electrovalve SBSV-B1N4 Dwyer® (§4.8.3). A DC brushless axial fan SUNON (§4.8.5) has been placed close to the pump to prevent its overheating.

The inlet leg has not been equipped with a pump so the underpressure due to the outlet pump operation is designed to be the only responsible for the air entering the chamber from the outdoor air. The inlet flow rate is monitored inside the chamber by a second flowmeter VFA-22 Dwyer®. Outside the chamber, between a manually operated ball valve and an electrovalve SBSV-B1N4 Dwyer®, a check valve BICV-0F01 Dwyer® (§4.8.4) is aimed to prevent air from flowing back to the outdoor through the inlet leg.

Voltage divider A similar voltage divider has been designed to be coupled with the pump operating in the chamber-outdoor circuit. The criterion underlying the choice of the employed resistance has been the need to obtain flow rates much higher than those circulating between the chamber and the radium source. The four relays are both powered (the power supply voltage is 5 V) and controlled by the same Arduino UNO WiFi Rev2 (Ard, c) used for the chamber-outdoor circuit. The switches are connected in normally open configuration for the pump safeguard. The scheme of the electrical connections between the microcontroller and the relays is reported by Figure 4.20.

The pump is powered by a second power supply, identical to the first one used in the chamber-source circuit.

Relays and pump power supply are placed inside the radon chamber.

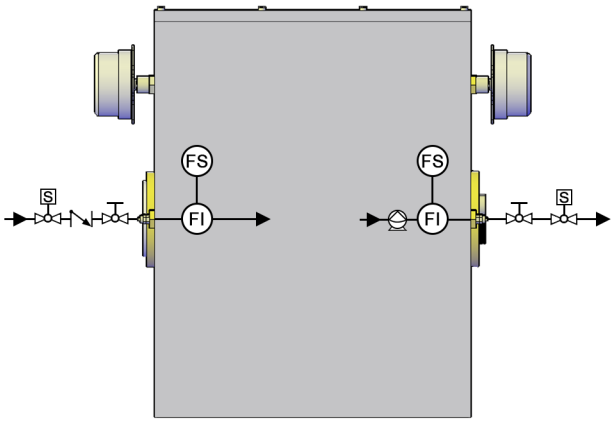

Figure 4.18: Scheme of the circuit connecting the radon chamber to the outdoor air. The pump is installed inside the radon chamber, as well as the mechanical flow-meters. Outside the chamber, on each legs, a ball valve manually actuated is coupled with an electrovalve actuated by a solenoid. On the outdoor-to-chamber leg, i.e. the inlet leg, a check valve prevents the air flow from flowing back from the chamber to the outdoor air. All the components are represented through the corresponding P&ID symbols.

Table 4.3: Power supply voltage of the micro pump, operating in the chamber-source circuit, as a function of the relays switches positions in no-load and full-load conditions. "1" and "0" states stand for switch closed and open, respectively.

	Relay				No-Load V	Full-Load V
	#1	#2	#3	#4	(V)	(V)
V_1	1	0	0	0	6.6	6.6
V_2	0	1	0	0	6.3	5.5
V_3	0	0	1	0	6.0	4.9
V_4	0	0	0	1	5.9	4.2

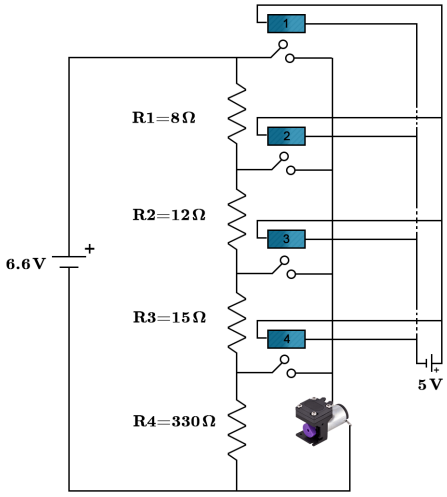

Figure 4.19: Voltage divider designed to vary the power supply voltage of the micro pump operating in the chamber-outdoor circuit. The ideal voltage generator at 6.6 V stands for the power supply of the pump whose nominal and no-load voltage are 6 V and 6.6 V, respectively.

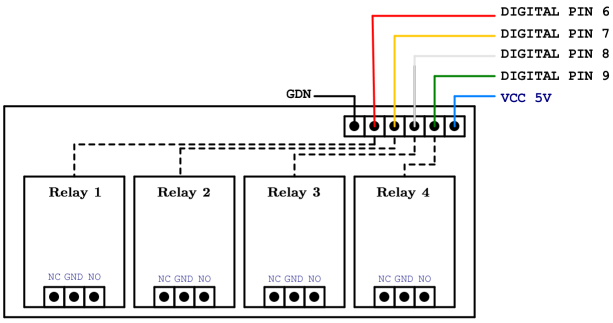

Figure 4.20: Scheme of the electrical connections between the Arduino UNO WiFi and the four relays used to control the voltage divider of the chamber-outdoor circuit.

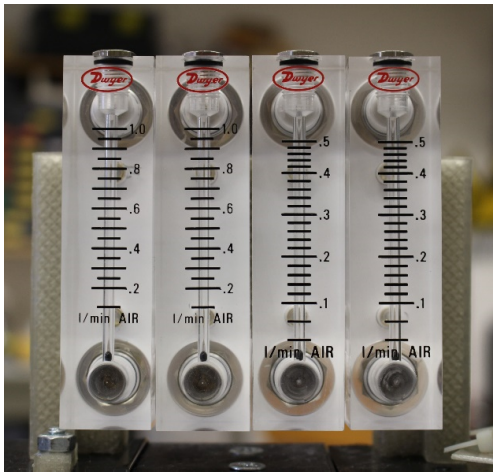

(a) Front View

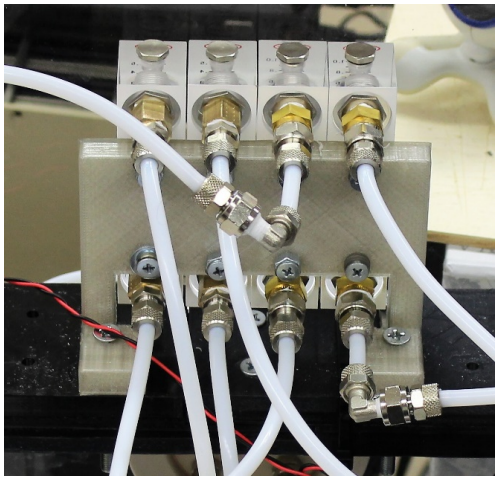

(b) Back View

Figure 4.21: Front and back view of the 4 flowmeters, 2 pertaining to the chamber-source circuit (on the right in front view) and 2 to the chamber-outdoor one (on the right in front view). Such devices are placed inside the chamber, in a position that allows an easy view of the values being measured.

4.2.6 Regulation and control system

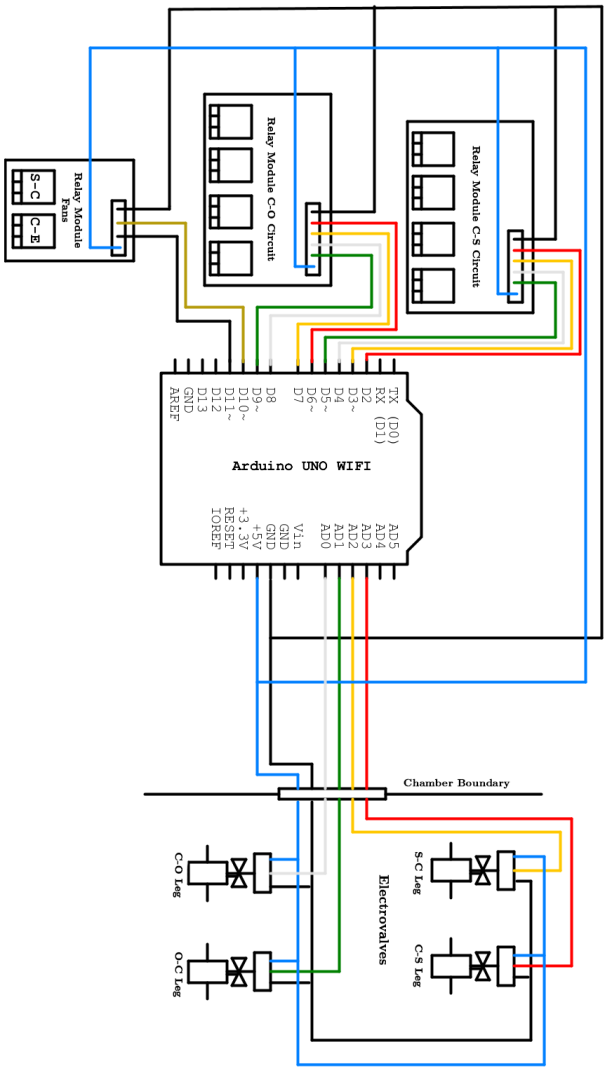

Figure 4.22: Scheme of the logical connections between the Arduino UNO WiFi and all the elements controlled and actuated in the apparatus: *i*) the pump voltage dividers, *ii*) the pump cooling fans and *iii*) the external electrovalves.

Other than the voltage dividers coupled with the micro pumps of the chamber-source and chamber-outdoor circuits, the two cooling axial fans and the four electrovalves are controlled by the Arduino UNO WiFi placed inside the chamber and therein powered. The ON-OFF regulation of the cooling fans is realized by two distinct relays placed on the phase wire of the common 12 V power supply. The electrovalves are actuated by four relays, placed outside the chamber and therein powered, located on the phase wires of two distinct 24 V power supplies, one for each couple of electrovalves. The Arduino code can be updated

remotely from the outside, so modifications can be done to the functioning routine of pumps and valves even during measurements, when the concentration inside the chamber can be very high. This feature opens the way to the possibility of changing the desired radon concentration inside the chamber without opening it and loosing the radon accumulated by the source in a quite long time. This helps reducing the dead time between two subsequent measurements considering that the time required by the source to make the radon reach the secular equilibrium inside its vessel is of about 20 days, i.e. 4-5 time its half life.

4.2.7 Activity balance equations for the radon chamber and source vessel control volumes

The theoretical model underlying the project has been drawn up on a Eulerian approach, considering the inner volume of the chamber as a control volume and the number of radon atoms as the fluid particles entering and leaving the chamber across the boundaries. The radium source and the outdoor environment are treated as further control volumes. Considering the continuity principle, the variation of radon concentration vs. time is expressed by a system of two differential equations. Radon concentration inside each control volume is supposed to be uniform. Referring to the chamber inner volume, the proposed model considers:

i) the ^{222}Rn atoms radioactive decaying;

ii) the ^{222}Rn atoms entering the chamber from the source;

iii) the ^{222}Rn atoms entering the chamber from the outdoor environment;

iv) the ^{222}Rn atoms leaving the chamber towards the source;

v the ^{222}Rn atoms leaving the chamber towards the outdoor environment;

$$\frac{dC_{\mathrm{Rn},c}(t)}{dt}V_{ch} = -\lambda_{\mathrm{Rn}}C_{\mathrm{Rn},c}(t)V_{ch} + \Gamma_{s\to c}(t)C_{\mathrm{Rn},s}(t) + \Gamma_{o\to c}(t)C_{\mathrm{Rn},o}(t) - \Gamma_{c\to s}(t)C_{\mathrm{Rn},c}(t) - \Gamma_{c\to o}(t)C_{\mathrm{Rn},c}(t) \qquad (4.1)$$

where:

$C_{\mathrm{Rn},c}(t)$ is the radon concentration inside the chamber, so registered by the inner detector ($\mathrm{Bq\,m^3}$)
$C_{\mathrm{Rn},s}(t)$ is the radon concentration inside the source vessel ($\mathrm{Bq\,m^3}$)
$C_{\mathrm{Rn},c}(t)$ is the outdoor radon concentration ($\mathrm{Bq\,m^3}$)
V_{ch} is the volume of the chamber ($\mathrm{m^3}$)
λ_{Rn} is the ^{222}Rn decay constant ($\mathrm{s^{-1}}$)
$\Gamma_{s\to c}(t)$ is the air flow-rate, registered by the corresponding sensor, entering the chamber from the source vessel ($\mathrm{m^3\,s^{-1}}$)
$\Gamma_{o\to c}(t)$ is the air flow-rate, registered by the corresponding sensor, entering the chamber from the outdoor environment ($\mathrm{m^3\,s^{-1}}$)
$\Gamma_{c\to s}(t)$ is the air flow-rate, registered by the corresponding sensor, leaving the chamber towards the source vessel ($\mathrm{m^3\,s^{-1}}$)

$\Gamma_{c\to s}(t)$ is the air flow-rate, registered by the corresponding sensor, leaving the chamber towards the outdoor environment ($m^3\,s^{-1}$)

Referring to the radium source control volume, the radioactive decay of radium and the radon atoms coming from the chamber represent the positive terms (in green). The long half-life of radium ($\approx$ 1602 years) allows to assume the ^{226}Ra activity as a constant. Radioactive decay and advective flow towards the chamber contribute to radon removal. The model adopted is shown below.

$$\frac{dC_{\mathrm{Rn},s}(t)}{dt}V_v = -\lambda_{\mathrm{Rn}}C_{\mathrm{Rn},s}(t)V_{ch} + \lambda_{\mathrm{Rn}}A_{\mathrm{Ra},s}(t) + \Gamma_{c\to s}(t)C_{\mathrm{Rn},c}(t) + - \Gamma_{s\to c}(t)C_{\mathrm{Rn},s}(t) \tag{4.2}$$

where:

$C_{\mathrm{Rn},c}(t)$ is the radon concentration inside the chamber, so registered by the inner detector ($Bq\,m^3$)
$C_{\mathrm{Rn},s}(t)$ is the radon concentration inside the source vessel ($Bq\,m^3$)
V is the volume of the source vessel (m^3)
λ_{Rn} is the ^{222}Rn decay constant (s^{-1})
$\Gamma_{s\to c}(t)$ is the air flow-rate, registered by the corresponding sensor, entering the chamber from the source vessel ($m^3\,s^{-1}$)
$\Gamma_{c\to s}(t)$ is the air flow-rate, registered by the corresponding sensor, leaving the chamber towards the source vessel ($m^3\,s^{-1}$)
A_{Ra} is the radium activity of the source (Bq).

Boundary condition fixed, i.e. $C_{\mathrm{Rn},c}(t=0) = C^0_{\mathrm{Rn},c}$ and $C_{\mathrm{Rn},s}(t=0) = C^0_{\mathrm{Rn},s}$, the numerical solution of the differential equations system provides the radon concentration trend vs time, as a function of air flow rates in the two circuits.

4.3 Procedures and results

The commissioning procedure included several and strictly subsequent step: *i*) verifying the air-tightness of the radon chamber excluding the connection circuit with the source and the source vessel volume *ii*) extending the results, in terms of radon-tightness, to all the components of the chamber-source circuit, i.e. radon chamber, source vessel and both connecting legs.

4.3.1 Radon chamber air-tightness

The operation of the apparatus requires to perform an air-tightness test aiming to verify both the tightness of the chamber - considering it with all its penetrations previously presented - and of the sealing at the wall interface.

The air, in application far from critical condition (P_c = 3769.290 kPa and T_c = −140.6 °C), is to be considered a perfect gas: as a consequence, if the chamber has been correctly designed such to avoid air leakage, density, pressure

and temperature should obey to the perfect gas state equation.

$$PV = nRT \tag{4.3}$$

$$\frac{P}{\rho_{air}} = R_{air}T \tag{4.4}$$

where:

- P is the air pressure, (Pa)
- T is the air temperature, (K)
- R is the universal air gas constant, $8.314\,\mathrm{J\,kg^{-1}\,K^{-1}}$
- ρ_{air} is the air density, varying both with pressure and temperature
- R_{air} is the individual air gas constant, $287.05\,\mathrm{J\,kg^{-1}\,K^{-1}}$
- V is the volume of the radon chamber, comprehensive of the very small air volume contained in outlet and inlet legs until the ball valves.

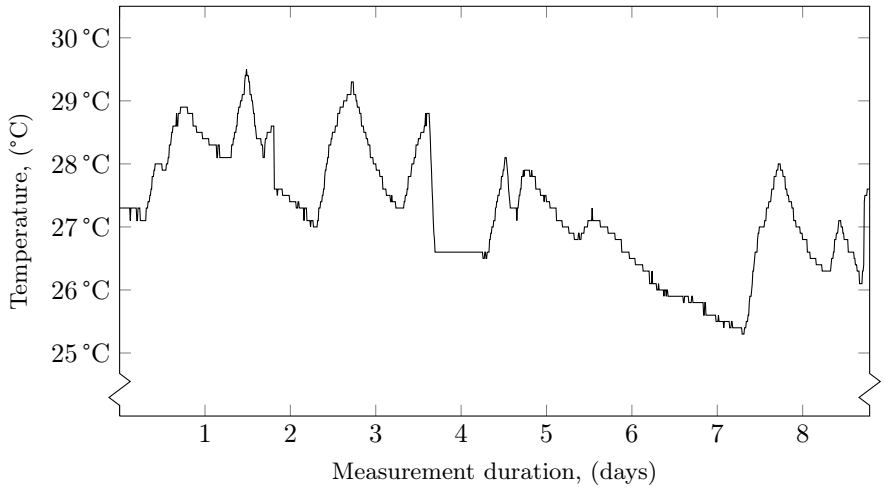

Figure 4.23: Temperature trend during the air-tightness test performed on the the radon chamber. The temperature values returned by the AlphaGUARD PQ2000 sensor are affected by an uncertainty of 0.1 °C, not reported on the graph for the sake of plot clarity.

Pressure, temperature and relative humidity were monitored by the corresponding native sensors of the AlphaGUARD PQ2000 that was inserted in the chamber during the tightness test.

Temperature trend over the whole measuring period (about 10 days) are reported in Figure 4.23.

The tightness effectiveness can be evaluated through the comparison between actual values of measured pressure and theoretical trend obtained through the perfect gas state equation by assuming a compressibility factor $Z \approx 1$(Ahmed, 2013). The minimum and maximum differential pressure between inside and outside the chamber have been 2000 Pa and −20 000 Pa, respectively. The mean air density measured during the measurement has been $1178.26\,\mathrm{g\,m^{-3}}$ with a standard deviation of $1.56\,\mathrm{g\,m^{-3}}$.

Air losses during the test have been estimated to be of about 0.6 g that correspond to about 53.5 Bq. In view of this, considering also the uncertainty

characterizing pressure and temperature measurements, the air-tightness of the chamber should be considered reliable, despite minor air losses corresponding to strong pressure difference experienced between inside and outside the chamber.

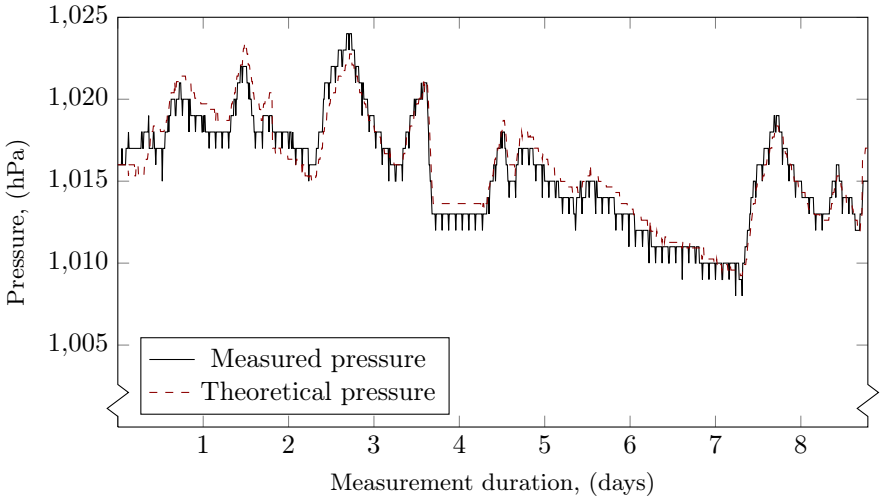

Figure 4.24: Measured and theoretical pressure trends during the air-tightness test performed on the the radon chamber. The measured pressure values returned are affected by an uncertainty of 0.5 Pa.

4.3.2 Chamber-source circuit radon-tightness

Once checked the air-tightness of the radon chamber, a further experiment has been carried out with the aim to extend the conclusions to the whole chamber-source circuit, i.e. including also the source vessel and the communications legs. In order to do so, radon has been introduced in the chamber throughout the inlet leg connecting the ^{226}Ra source to the chamber. Radon concentration has been measured inside the chamber by the AlphaGUARD PQ2000 set in diffusion mode and returning measurement once every ten minutes. After opening both couples of ball valves and electrovalves, the radon source vessel has been purged by blowing away its gaseous content by means of an external volumetric pump. The obtained experimental trend has been compared to the theoretical solution of differential equations system developed within the model. Eq.s 4.2 and 4.3 are representative of the scenario considered with the following boundary conditions:

$$\begin{cases} C_{\mathrm{Rn},c}(t=0) \approx 0\,\mathrm{Bq\,m^{-3}} & \text{(4.5a)} \\ C_{\mathrm{Rn},s}(t=0) \approx 0\,\mathrm{Bq\,m^{-3}} & \text{(4.5b)} \\ \Gamma_{s\to o}(t) = 0\,\mathrm{m^3\,s^{-1}} & \text{(4.5c)} \\ \Gamma_{o\to s}(t) = 0\,\mathrm{m^3\,s^{-1}} & \text{(4.5d)} \\ \Gamma_{s\to c}(t) = \Gamma_{c\to s}(t) & \text{(4.5e)} \end{cases}$$

The flow rate circulating in inlet and outlet legs has been modeled, by properly acting either on electrovalves and pump by the Arduino UNO WiFi microcontroller, as a step function. The micro-pump has been operated $\Delta t_1 = 60\,\mathrm{s}$

ON ($\Gamma_{s\to c}(t) = \Gamma_{c\to s}(t) = 0.5\,\mathrm{L\,min^{-1}}$) and $\Delta t_2 = 600\,\mathrm{s}$ OFF ($\Gamma_{s\to c}(t) = \Gamma_{c\to s}(t) = 0\,\mathrm{L\,min^{-1}}$).

The chamber free volume and the source vessel volume, the latter including also the inner volume of outlet and inlet legs of the chamber-source circuit, have been estimated to be $0.068\,\mathrm{m^3}$ and $0.0005\,\mathrm{m^3}$, respectively, on the basis of AutoCAD 3D modeling. The theoretical final concentration to be reached inside the chamber has been so estimated to be $\frac{20\,000\,\mathrm{Bq}}{0.068+0.005\,\mathrm{m^3}} = 292\,\mathrm{kBq\,m^{-3}}$. The radon concentration measured during the test is reported in Figure 4.25.

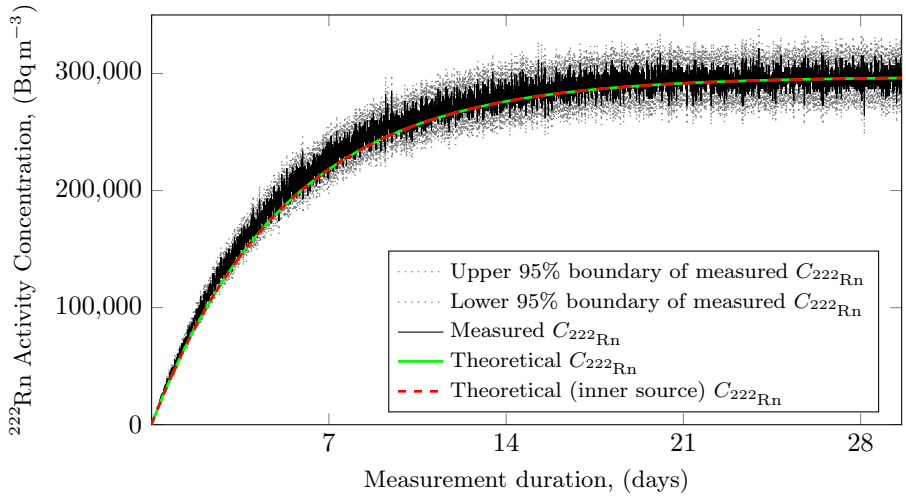

Figure 4.25: Comparison between radon concentrations measured during the build-up test (black full line), the estimations obtained by solving, by means of the finite differences method, Eqs. 4.2 and 4.3 (green dashed line) and the estimation obtained by considering the radium source inside a control volume given by the sum of vessel (V_v) and chamber (V_{ch}) volume (dashed red line). In grey the 95% confidence interval of the measured values obtained considering both systematic and statistical uncertainties of the AlphaGUARD PQ2000.

The actual concentration reached after about 1 month ($\approx 5T_{1/2}$), averaged over the last 16 hours (i.e 100 measurements), resulted to be $297.2 \pm 16.5\,\mathrm{kBq\,m^{-3}}$, in full agreement with the value supposed on the basis of the source activity and the overall volume of the apparatus during the chamber-circuit functioning.

Solution of Eqs. 4.2 and 4.3 by the finite differences method is graphically represented by the full green line in Figure 4.25. The agreement between such analytical solution and the experimentally measured values (full black line) turned out to be very good, considering that the green line appears to be well within the 95% confidence interval of the experimental values. This comparison demostrates the air tightness of the chamber because the experimental trend is well fitted by the analytical solution of the model, the latter not considering any kind of leakages.

The red dashed line graphically represents the analytical solution of the differential equation describing the radon concentration build-up in case of radium source contained inside a theoretical volume given by the sum of vessel (V_v) and chamber (V_{ch}) volume. In other words, it stands for the graphical solution of

the following equation:

$$C_{^{222}\mathrm{Rn},c+s}(t) = C^{0}_{^{222}\mathrm{Rn},c+s} e^{-bt} + C^{\infty}_{^{222}\mathrm{Rn},c+s}(1 - e^{-bt}) \tag{4.6}$$

where:

$C^{0}_{^{222}\mathrm{Rn},c+s}$ is the radon concentration at $t = 0$ in $V = V_{ch} + Vv$, ($\mathrm{Bq\,m^{-3}}$)
$C^{\infty}_{^{222}\mathrm{Rn},c+s}$ is the radon concentration once the steady state is reached in $V = V_{ch}+Vv$, ($\mathrm{Bq\,m^{-3}}$)
b is the ^{222}Rn decay constant, $\lambda_{^{222}\mathrm{Rn}} = 2.09838 \cdot 10^{-6}$ ($\mathrm{s^{-1}}$)

Such analytical solution pefectly fits the dashed green line representing the general solution. This is justified by considering that time characterizing source emptying is much smaller than radium decay constant and so everything occurs as if the radium source was inside the chamber.

If instead of the proper trend of the air flow rate (for $\Delta t_1 = 60\,\mathrm{s}$ $\Gamma_{s\to c} = \Gamma_{c\to s} = 0.5\,\mathrm{L\,min^{-1}}$ and for $\Delta t_2 = 600\,\mathrm{s}$ $\Gamma_{s\to c} = \Gamma_{c\to s} = 0\,\mathrm{L\,min^{-1}}$), a mean value ($\bar{\Gamma} = \frac{\Gamma_1\Delta t_1+\Gamma_2\Delta t_2}{\Delta t_1+\Delta t_2} = 0.045\,\mathrm{L\,min^{-1}}$) was considered the resulting trend obtained by solving Eq. 4.2 would result to perfectly overlap the other two theoretical trends just discussed. This demonstrates the feasibility of this further assumption to make it easier the solution of the balance equation.

4.3.3 Radon chamber radon-tightness

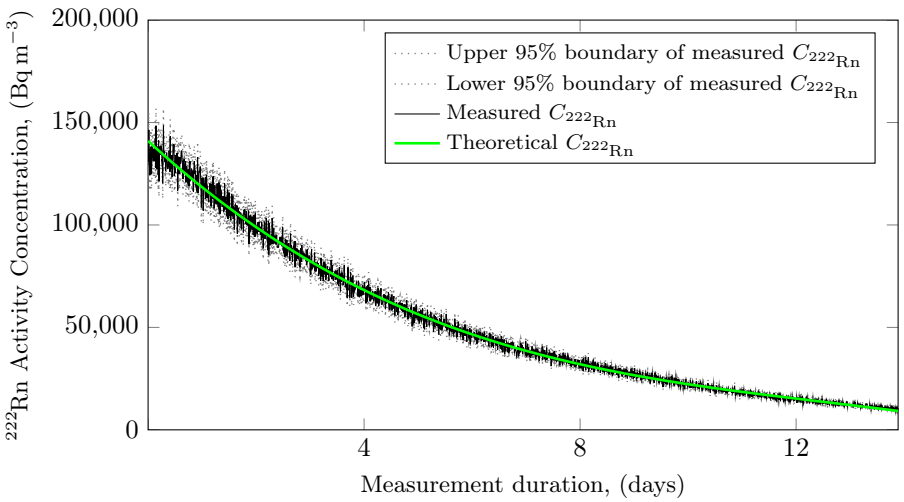

Figure 4.26: Comparison between radon concentrations measured during the natural decay test (black full line) and the estimations obtained by solving, by means of the finite differences method, Eq. 4.2 (green full line). In grey the 95% confidence interval of the measured values obtained considering both systematic and statistical uncertainties of the AlphaGUARD PQ2000.

A further experiment has been required by the need of excluding the radon diffusion through the boundaries of the chamber. Once reached the steady state for radon concentration value inside the chamber, all the valves have been

closed in order to observe the negative exponential trend due to only the natural radioactive decay of ^{222}Rn. Indeed, there are no flow rates entering or leaving the chamber so the governing balance equation accounts only for the radon radioactive decay.

Figure 4.26 shows that the experimental trend (black full line) is properly interpolated by the typical exponential decay function (green full line), $C_{^{222}\mathrm{Rn},c}(t) = C^0_{^{222}\mathrm{Rn},c} e^{-bt}$ with $b = \lambda_{^{222}\mathrm{Rn}} = 2.09838 \cdot 10^{-6}\mathrm{s}^{-1}$ and $C^0_{^{222}\mathrm{Rn},c} = 297.2\,\mathrm{kBq\,m^{-3}}$. This perfect fit demonstrates the radon-tightness of the radon chamber.

4.3.4 Dynamic functioning: operating the radon recirculation circuit with the outdoor air

Lessons learned in §4.3.2 make legit assuming that the radon source is contained inside the radon chamber. Now, if the chamber-source and chamber-outdoor circuits are contemporary operated, the radon concentration inside the radon chamber can be modelled as follow:

$$\begin{aligned}\frac{dC_{\mathrm{Rn},c}(t)}{dt}V = {} & A_{^{226}\mathrm{Ra}}\lambda_{^{222}\mathrm{Rn}} - \lambda_{\mathrm{Rn}}C_{\mathrm{Rn},c}(t) \\ & + \Gamma_{o\to c}(t)C_{\mathrm{Rn},o} - \Gamma_{c\to o}(t)C_{\mathrm{Rn},c}(t)\end{aligned} \tag{4.7}$$

4.3.4.1 Different radon concentration at steady state

The steady state reached, the radon concentration inside the chamber, obtained by considering $\frac{dC_{\mathrm{Rn},c+s}(t)}{dt} = 0$, is:

$$C^{\infty}_{\mathrm{Rn},c+s} = \frac{A_{^{226}\mathrm{Ra}}}{V}\frac{1 + \frac{\bar{\Gamma}_{c\to o}C_{\mathrm{Rn},o}}{\lambda_{^{222}\mathrm{Rn}}A_{^{226}\mathrm{Ra}}}}{1 + \frac{\bar{\Gamma}_{c\to o}}{V\lambda_{^{222}\mathrm{Rn}}}} \tag{4.8}$$

where $C^{\infty}_{^{222}\mathrm{Rn},c+s}$ is the radon concentration, in steady state conditions, reached in $V = V_{ch} + V_v$ and $\bar{\Gamma}_{c\to o}$ is the air flow rate in the chamber-outdoor circuit averaged over the pump cycle. This value differs from the corresponding steady state radon concentration with no recirculation with outdoor air (i.e. $C^{\infty}_{\mathrm{Rn},c+s} = \frac{A_{^{226}\mathrm{Ra}}}{V}$) by the second term of the right hand side of Eq.4.8.

As theoretically shown, the contemporary operation of source-chamber and chamber-outdoor circuit opens the way to the possibility of realizing in the controlled atmosphere of the radon chamber a wide range of equilibrium concentrations, by means of a single radium source. A key parameter in regulating the radon concentration at steady state is the flow rate circulating in both inlet and outlet legs of the chamber-outdoor circuit. The way it influences the final concentration value can be observed by considering the trends reported in Figures 4.27, 4.28 and 4.29. Therefore, given a maximum concentration of about $300\,000\,\mathrm{Bq\,m^{-3}}$, it is possible establishing even lower equilibrium concentration by varying the flow rate in the chamber–outdoor circuit. Figures 4.27 and 4.28 shown how the steady state radon concentration can be changed by varying the flow rate circulating in the chamber-outdoor inlet and outlet legs when the source is initially empty (i.e. $C_{^{222}\mathrm{Rn},s}(t=0) \approx 0$).

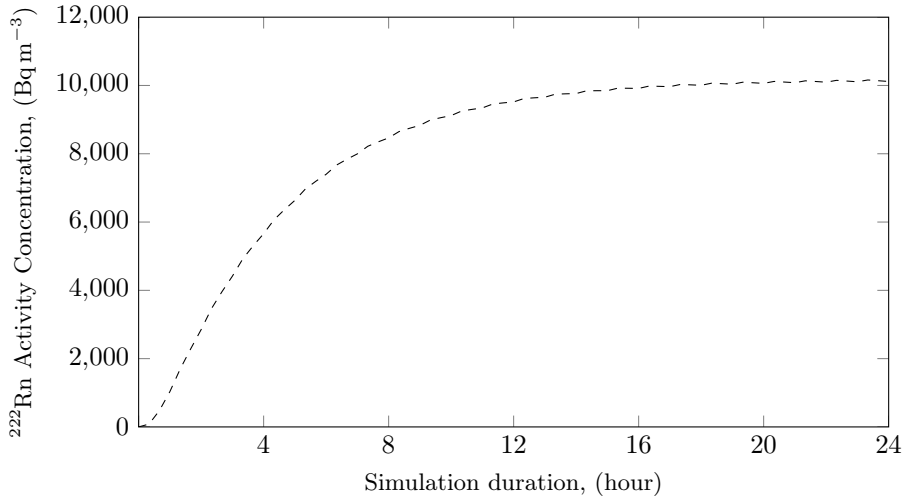

Figure 4.27: Radon concentration trend in the radon chamber obtained by considering the following duty cycle for the two pumps working on chamber-source and chamber-outdoor circuits. For $\Delta t_1 = 120\,\mathrm{s}$ $\Gamma_{s\to c} = \Gamma_{c\to s} = 0.1\,\mathrm{L\,min^{-1}}$ and for $\Delta t_2 = 600\,\mathrm{s}$ $\Gamma_{s\to c} = \Gamma_{c\to s} = 0\,\mathrm{L\,min^{-1}}$ and for $\Delta t_1 = 120\,\mathrm{s}$ $\Gamma_{c\to o} = \Gamma_{o\to c} = 0.8\,\mathrm{L\,min^{-1}}$ and for $\Delta t_2 = 240\,\mathrm{s}$ $\Gamma_{c\to o} = \Gamma_{o\to c} = 0\,\mathrm{L\,min^{-1}}$.

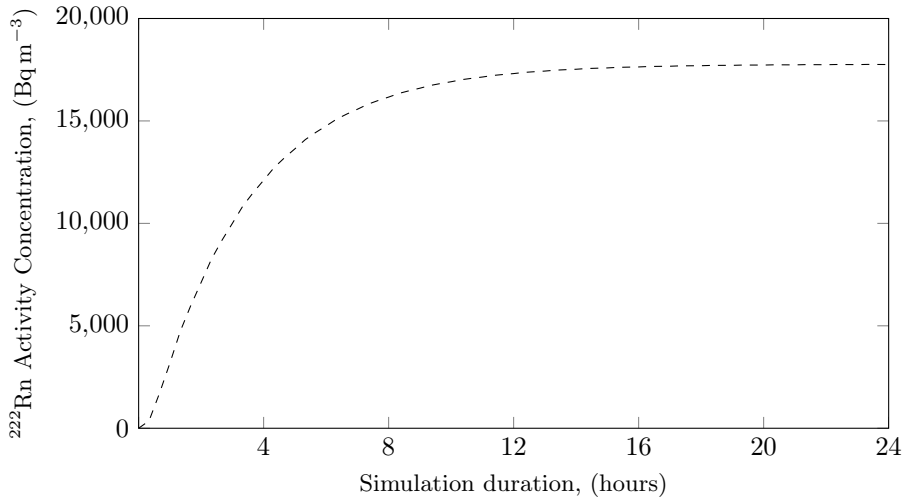

Figure 4.28: Radon concentration trend in the radon chamber obtained by considering the following duty cycle for the two pumps working on chamber-source and chamber-outdoor circuits. For $\Delta t_1 = 120\,\mathrm{s}$ $\Gamma_{s\to c} = \Gamma_{c\to s} = 0.1\,\mathrm{L\,min^{-1}}$ and for $\Delta t_2 = 600\,\mathrm{s}$ $\Gamma_{s\to c} = \Gamma_{c\to s} = 0\,\mathrm{L\,min^{-1}}$ and for $\Delta t_1 = 120\,\mathrm{s}$ $\Gamma_{c\to o} = \Gamma_{o\to c} = 0.8\,\mathrm{L\,min^{-1}}$ and for $\Delta t_2 = 600\,\mathrm{s}$ $\Gamma_{c\to o} = \Gamma_{o\to c} = 0\,\mathrm{L\,min^{-1}}$.

Similar results can be also obtained in case of secular equilibrium established in the source vessel between ^{226}Ra and ^{222}Rn. The feasibility of this second process is demonstrated by the simulation plotted in Figure 4.29.

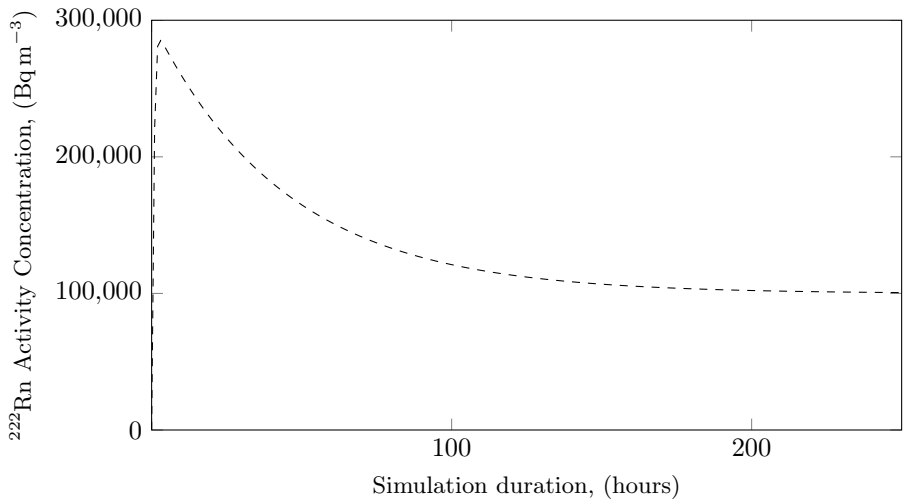

Figure 4.29: Radon concentration trend in the radon chamber obtained by considering the following duty cycle for the two pumps working on chamber-source and chamber-outdoor circuits. For $\Delta t_1 = 300\,\mathrm{s}$ $\Gamma_{s\to c} = \Gamma_{c\to s} = 0.1\,\mathrm{L\,min^{-1}}$ and for $\Delta t_2 = 1500\,\mathrm{s}$ $\Gamma_{s\to c} = \Gamma_{c\to s} = 0\,\mathrm{L\,min^{-1}}$ and for $\Delta t_1 = 300\,\mathrm{s}$ $\Gamma_{c\to o} = \Gamma_{o\to c} = 0.1\,\mathrm{L\,min^{-1}}$ and for $\Delta t_2 = 1500\,\mathrm{s}$ $\Gamma_{c\to o} = \Gamma_{o\to c} = 0\,\mathrm{L\,min^{-1}}$.

Calibrating a passive or active monitor, in fact, generally means exposing the device to different radon concentration plateaux each realized inside radon chambers by means of as specific radium source. So, the calibrating laboratory needs as many radium sources as the calibration points required by the consumer. The just introduced potentiality of the radon chamber under discussion would be translated in the possibility, for the laboratories, to perform calibrations of passive and active detectors owning a single radium source.

4.3.4.2 Sudden changes of radon concentration

Another interesting possibility offered by the contemporary operation of both the designed circuits is realizing concentration trends with sudden variations among different plateaux. Similar radon concentration trends are extremely useful to evaluate the dynamic response of the active monitors, i.e. the capability of following sudden changes in the measured concentration. An example of this is shown by Figure 4.30 that illustrates the trend resulting from subsequent changes in operation status of chamber-source and chamber-outdoor circuits. The initial steady state condition is achievable simply opening the valves on the chamber-source legs and waiting for the steady state establishing (Figure 4.25). For the initial 3 hours, the boundary conditions are kept unchanged then the chamber-outdoor pump is started and intercepting valves opened, so $\Gamma_{c\to o} = \Gamma_{o\to c} = 1\,\mathrm{L\,min^{-1}}$. For the following two hours the chamber-outdoor flow rate is kept unchanged and the chamber-source circuit intercepted. After 1 hours the chamber-outdoor circuit is intercepted as well, and the pump stopped.

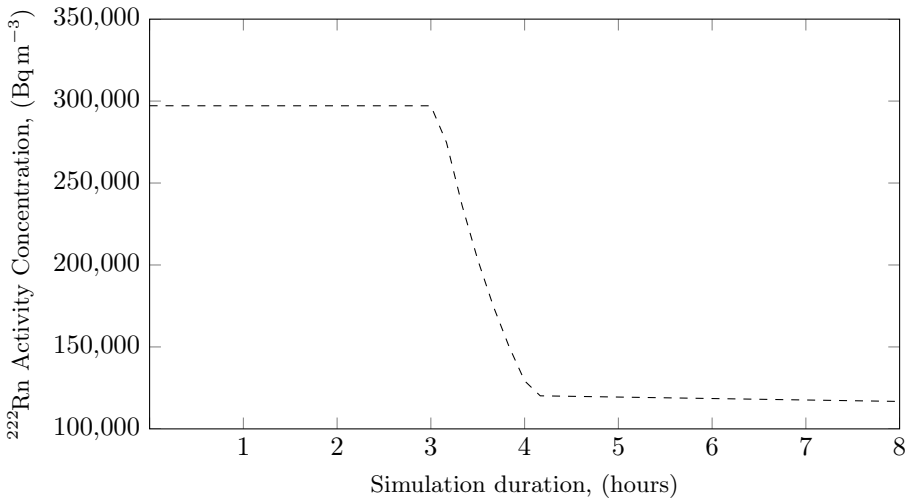

Figure 4.30: Radon concentration trend in the radon chamber obtained by alternatively operating the chamber-source and the chamber-outdoor circuit.

The same procedure can be repeated several times over a wider time interval in order to realize subsequent sudden radon concentration changes and so study the response of continuous radon monitors in extremely stressing scenarios.

4.4 Conclusion

An innovative, either for how it has been conceived and realized, radon chamber has been built at the Laboratory of Radiation Protection of Sapienza - University of Rome. The main innovation aspects are, mainly, its small size (i.e. the inner volume is 68 L), its cheapness, the allowed remote control for all the chamber different functions and the possibility to perform calibrations by means of a single ^{226}Ra source.

The chamber has been equipped with two circuits: the first one realizing the communication of the chamber control volume with the radium source, and the second providing the communication with the outdoor environment of the chamber itself. The first circuit has undergone a full commissioning test aiming to verify its functioning as well as its air- and radon-tightness. In particular the tightness of circuits, valves, connections, source vessel and chamber boundaries have been addressed by specific experimental tests and so verified. The chamber-outdoor circuit will be soon subjected to the same tests. The proper operation of mechanical and electrical components has been demonstrated. The remote control of each components (valves, pump, fans and USB-connected inner device) obtained thanks to the extensive use Arduino UNO Wi- Fi microcontrollers, has been demonstrated to be capable of avoiding entering the laboratory to control radon concentration and chamber operating state.

A Python code implementing the theoretical model underlying the radon chamber has been developed. All the radon chamber operation scenarios have been so simulated through the code. Simulations results have been shown to

very well fit the actually measured radon concentration trends. Further research will address the experimental demonstration of the trends obtainable through the chamber-outdoor circuit.

Different radon equilibrium concentrations have been demonstrated to be achievable inside the radon chamber control volume by operating the two hydraulic circuits connecting the chamber to the radium source and the outdoor air. On view of this, the apparatus is intended to be employed in several applications, such as:

i) calibrating at different radon concentrations both passive and active radon detectors;

ii) checking the response linearity of both passive and active radon detectors;

iii) studying the dynamic response of the continuous radon monitors to sudden changes in radon concentration, considering the influence of the radon concentration absolute values before and after the variation and the length of the transitory state;

iv) allowing the development and testing of new and innovative solutions to measure radon concentration in air;

v) studying the influence of atmospheric parameters, i.e. pressure, temperature and relative humidity, on both passive and active detectors response;

To the authors opinion, the proposed instrumentation could promote a wider spread of the radon chamber technologies, thanks to the cheapness and easy availability on the market of all the materials and instrumentation employed. The possibility offered to perform passive and active detectors calibrations by detaining only one radium source would reveal extremely appealing for all those laboratories interested in reducing the regulatory burden imposed by the single national authorities about the detention of radioactive material.

Further details about this apparatus can be found in the paper recently published by Nuclear Instruments and Methods in Physics Research (Section A) (Centomani et al., 2019).

4.5 Appendix A: hydraulic adapters

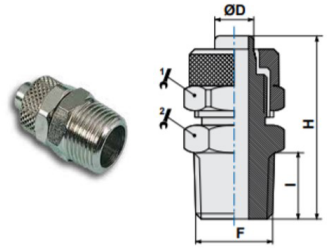

ART. 301 — Raccordo diritto maschio conico / *Taper straight male adaptor*

CODICE	ØD	F	I	H		
3010618	6/4	G1/8	8	26,5	12	12

Figure 4.31: Image, longitudinal section and technical specifications of the taper straight male adapter 6/4 mm x G1/8" BSPT-M.

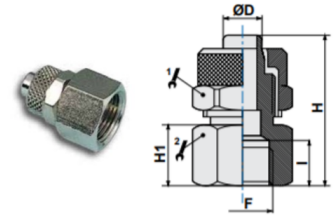

ART. 302 — Raccordo diritto femmina / *Straight female adaptor*

CODICE	ØD	F	I	H	H1		
3020618	6/4	G1/8	8	25	10	12	14

Figure 4.32: Image, longitudinal section and technical specifications of the taper straight female adapter 6/4 mm x G1/8" BSPT-M.

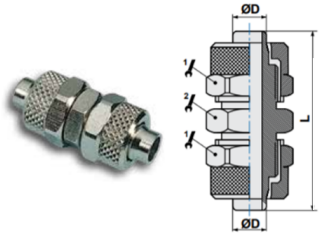

ART. 303 — Raccordo diritto intermedio / *Straight connector*

CODICE	ØD	L					
3030600	6/4	32			12	12	100

Figure 4.33: Image, longitudinal section and technical specifications of the straight connector 6/4 mm.

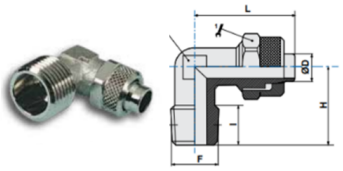

ART. 305 Raccordo ad L maschio conico
Elbow taper male adaptor

CODICE	ØD	F	I	H	L			
3050618	6/4	G1/8	8,5	17	20,5	12	10	100

Figure 4.34: Image, longitudinal section and technical specifications of the elbow taper male adapter 6/4 mm x G1/8" BSPT-M.

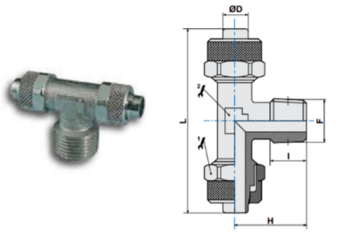

ART. 307 Raccordo T centrale
Central Tee adaptor

CODICE	ØD	F	I	H	L			
3070618	6/4	G1/8	8,5	17	41	12	8	100

Figure 4.35: Image, longitudinal section and technical specifications of the central tee adapter 6/4 mm x G1/8" BSPT-M.

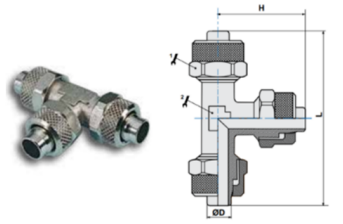

ART. 309 Raccordo T intermedio
Tee connector

CODICE	ØD	H	L			
3090600	6/4	20,5	41	12	8	50

Figure 4.36: Image, longitudinal section and technical specifications of the tee connector 6/4 mm.

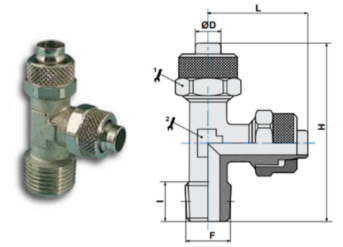

ART. 308 Raccordo T laterale
Off-set Tee adaptor

CODICE	ØD	F	I	L	H			
3080618	6/4	G1/8	8,5	20,5	37,5	12	8	100

Figure 4.37: Image, longitudinal section and technical specifications of the off-set tee connector 6/4 mm.

4.6 Appendix B: electrical connectors

(a) Front View (b) Back View

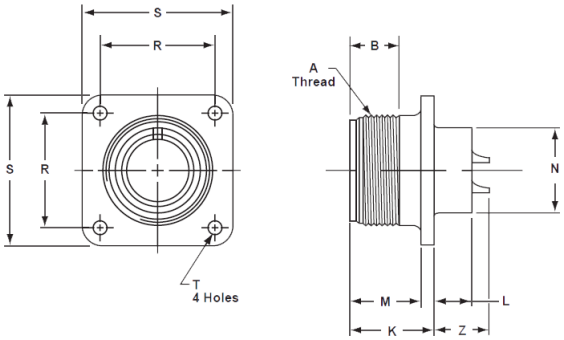

(c) Horizontal and Vertical Sections

Figure 4.38: Circular 4 pins straight male connector, MIL-C-5015 MS3102A (Amphenol®).

Table 4.4: Critical dimensions, in (cm), of the Amphenol® connector in Figure 4.38.

Shell size	A	B	K	L	M	N	R	S	T	Z
14S	2.2-20UNEF	1.14	1.71	0.75	1.43	1.91	2.30	3.02	0.30	1.07

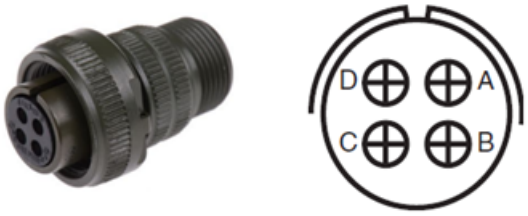

(a) Front View and Pin Coding

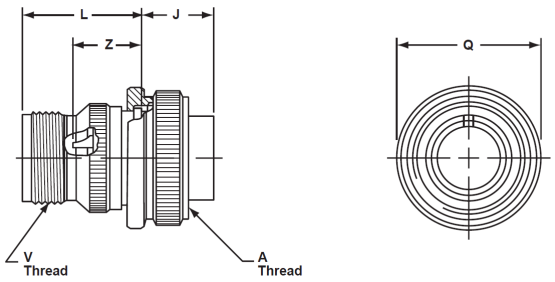

(b) Horizontal and Vertical Sections

Figure 4.39: Circular 4 pins straight female connector, MIL-C-5015 MS3106A (Amphenol®).

Table 4.5: Critical dimensions, in (cm), of the Amphenol® connector in Figure 4.39.

Shell size	A	J	L	Q	V	Z
14S	2.2-20UNEF	1.35	2.38	2.85	1.9-20UNEF	1.43

(a) Front View

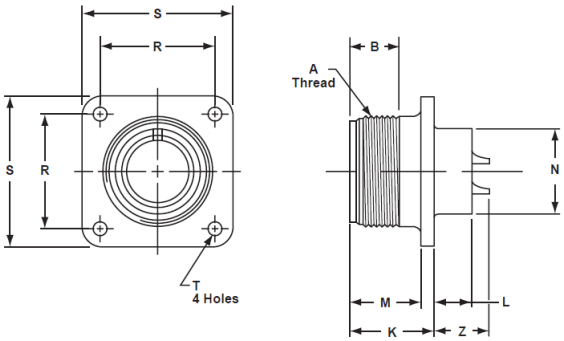

(b) Horizontal and Vertical Sections

Figure 4.40: Circular 10 pins straight male connector, MIL-C-5015 MS3102A (Amphenol®).

Table 4.6: Critical dimensions, in (cm), of the Amphenol® connector in Figure 4.40.

Shell size	A	B	K	L	M	N	R	S	T	Z
18	2.9-28UNEF	1.59	2.26	1.15	1.91	2.54	2.70	3.49	0.30	1.63

(a) Front View and Pin Coding

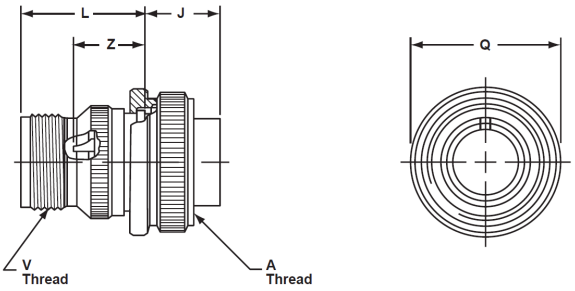

(b) Horizontal and Vertical Sections

Figure 4.41: Circular 10 pins straight female connector, MIL-C-5015 MS3106A (Amphenol®).

Table 4.7: Critical dimensions, in (cm), of the Amphenol® connector in Figure 4.41.

Shell size	A	J	L	Q	V	Z
18	2.9-20UNEF	1.83	3.10	3.39	2.5-20UNEF	2.06

4.7 Appendix C: environmental parameters sensors

4.7.1 Temperature and relative humidity sensor RHP-3D33-LCD Dwyer®

Table 4.8: Specifics of temperature (T) and relative humidity (RH) sensor "RHP-3D33-LCD" Dwyer®.

Relative Humidity Range	0 to 100%
Temperature Range	$-40\,°C$ to $60\,°C$
Relative Humidity Accuracy	$\pm 3\%$ if $RH \in [20\%; 80\%]$ at $25\,°C$
Temperature Accuracy	± 0.22 at $25\,°C$
Hysteresis	$\pm 1\%$
Repeatability	$\pm 0.1\%$
RH Display Resolution	$\pm 0.1\%$
T Display Resolution	$\pm 0.1\,°C$
Allowed Power Supply Voltage	$[15; 35]$ VDC

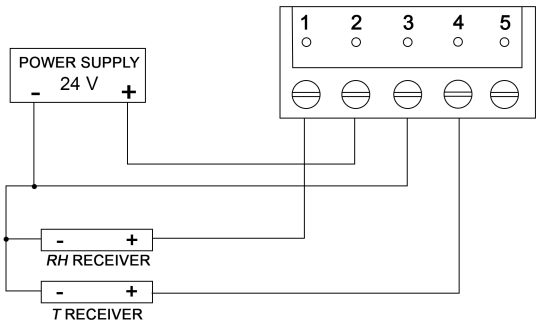

Figure 4.42: Scheme of the electrical contacts of the sensor RHP-3D33-LCD Dwyer®.

The chosen voltage for the sensor power supply is 24 V in DC. The phase wire should be connected to the second contact whereas the ground wire, common between the sensors output receiver (i.e. Arduino UNO Rev3) and the power supply, should be connected to the third one. The analogue (0–5 V) RH and T outputs come from the first and the fourth contacts, respectively.

4.7.2 Pressure difference sensor RHP MS2-X101 Dwyer®

Table 4.9: Specifics of pressure sensor II SERIE RHP MS2-X101 Dwyer®.

Differential Pressure Range	125 Pa
Accuracy	±1%
Allowed Power Supply Voltage	[15; 35] VDC

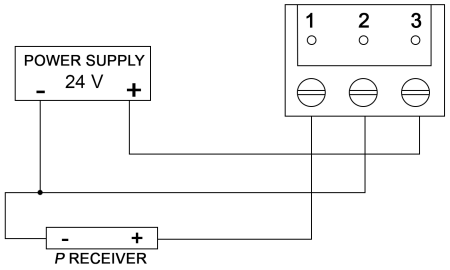

Figure 4.43: Scheme of the electrical contacts of the sensor II SERIE RHP MS2-X101 Dwyer®.

The chosen voltage for the sensor power supply is 24 V in DC. The phase wire should be connected to the third contact whereas the ground wire, common between the sensor output receiver (i.e. Arduino UNO Rev3) and the power supply, should be connected to the second one. The analogue (0–5 V) P output comes from the first contact.

The sensor has also some analogue dials, accessible from behind the display, that allows to make some changes in the transmitter functioning. In particular, the switch number 6 is capable of changing the voltage range of the analogue output between 0–10 V and 0–5 V, the latter chosen for the application considered. Among the others, switches 4 and 5 allow to select the desired measuring unit between kPa, Pa, mm or in of w. c..

4.8 Appendix D: air circuit components

4.8.1 Flow-meter Visi-Float VFA-21 Dwyer®

These flowmeters have a clear acrylic body suitable for gas applications (Dwyer Instruments, a). The VFA model has inlet and outlet connections with brass thread 1/8" NPT. To realize the connection with the adapters described in Appendix A, brass adapters 1/8"NPT-M, 1/8"BSP-M are required.

Figure 4.44: Flow-meter Visi-Float VFA-21 Dwyer®.

The flow rate range is 0.06–0.5 L min^{-1}.

4.8.2 Flow-meter Visi-Float VFA-22 Dwyer®

The only difference with respect to the model VFA-21 is the flow rate range: 0.15–1 L min^{-1}.

Figure 4.45: Flow-meter Visi-Float VFA-22 Dwyer®.

4.8.3 Brass electrovalve SBSV-B1N4 Dwyer®

These valves, solenoid actuated, are normally closed and powered at 24 VDC (Dwyer Instruments, b). The inlet and outlet threads are 1/8"NPT-F so brass adapters 1/8"NPT-F, 1/8"BSP-F are required.

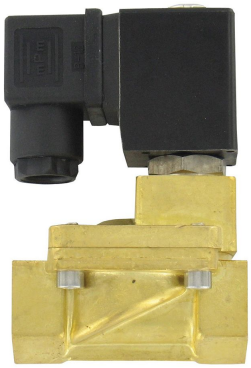

Figure 4.46: Brass electrovalve solenoid actuated SBSV-B1N4 Dwyer®.

4.8.4 Brass inline check valve BICV-0F01 Dwyer®

It is a spring-loaded check valve with an opening pressure required of 0.04 bar (Dwyer Instruments, c). They incorporate a soft seat for a bubble-tight shutoff and are spring-loaded for rapid reseating at high and low temperatures. The low (0.5 psi = 0.04 bar) cracking pressure and patented guided-disc technology ensure reliability at low and high service pressure. Inlet and outlet connections are threaded 3/8" NPT. To realize the connection with the adapters described in Appendix A, reducers 3/8"BSP 1/8"BSP are required.

Figure 4.47: Brass inline check valve BICV-0F01 Dwyer®.

4.8.5 DC brushless axial fan SUNON®

The power supply voltage is 12 V. At rated voltage, the fan frequency is 5000 rpm (SUNON). The fan is moved by a 2 phases, 4-poles brushless DC motor.

Figure 4.48: DC brushless axial fan SUNON®.

4.8.6 Micro diaphragm gas pump NMP 09L KNF®

The micro diaphragm gas sampling pumps from KNF are based on an elastic diaphragm that, fixed on its edge, moves up and down its central point by means of an eccentric. In this way the air is transferred using automatic valves (KNF). They assure a high level of gas tightness thanks to the closed diaphragm surface and special sealing system. The power supply voltage is 6 V. The maximum pressure overtakable and the vacuum obtainable are 0.65 bar and 500 mbar. The declared maximum flow rate is $0.9\,\mathrm{L\,min^{-1}}$.

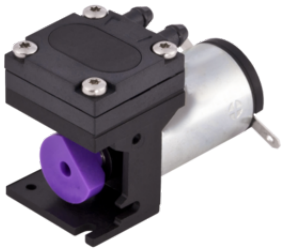

Figure 4.49: Micro diaphragm gas pump KNF®.

Chapter 5

Quality assurance for radon-in-water measurements by emanometry technique

5.1 Introduction

Exposure to radon dissolved in drinking waters can derive indirectly from the inhalation of air containing radon degassed from water (as during showers or dishwashing, due to the volatility of dissolved radon gas which increases with temperature) and directly from ingestion of water (World Health Organization, 2017, 2018). Due to the relatively low solubility of radon in water, about 90% of the dose attributable to radon in drinking waters comes from inhalation rather than ingestion(United Nations Scientific Committee on the Effects of Atomic Radiation, 1993). Nevertheless, the latter exposure pattern should not be neglected as a potential risk for public health (Kendall and Smith, 2002).

The Directive 2013/51/Euratom (European Commission, 2013) for the protection of the health of the general public with regard to radioactive substances in water intended for human consumption contains several requirements to Member States about radon concentration in water, including: *i*) to adopt a parametric value (equal to $100\,\mathrm{Bq\,L^{-1}}$) above which the risk has to be evaluated and remedial actions have to be considered, and *ii*) to carry out representative surveys in order to identify water sources whose radon content might exceed such a parametric value.

The implementation of the such Council Directive has led to a considerable increase of radon concentration measurements in drinking waters. The Directive indicates for the method of analysis a minimum limit of detection (or detection limit, DL) of $10\,\mathrm{Bq\,L^{-1}}$, i.e. 10% of the parametric value. Test methods capable of measuring radon activity concentration satisfying this limit are, mainly, gamma-ray spectrometry, liquid scintillation counting, and emanometry, whose achievable lowest detection limit are 10, 0.05 and $0.04\,\mathrm{Bq\,L} - 1$, respectively (Jobbágy et al., 2017). Findings from previous studies showed no statistically significant differences between results from the three different measuring technique (Pujol and Pérez-Zabaleta, 2017).

The test method using emanometry, regulated by the international standard ISO 13164-3 (International Standard Organization, 2013), has been used in several surveys thanks to its advantages: mainly, the possibility to use different detectors with low-to-moderate costs (i.e. 1-20 k€), the low achievable uncertainty (i.e. up to 5%)(Jobbágy et al., 2017), the suitability for in-situ measurements and the very short turnaround time (International Organization for Standardization, 2014). The related disadvantages primarily refer to the need of sub-sampling with likely radon loss during water sample transfer from transport container to degassing circuit (Jobbágy et al., 2019).

In order to increase the number of measurements performed, i.e. samples analysed per day, laboratories frequently choose to contemporary measure water samples through more than one measuring chain. Referring to emanometry test method, the issue is particularly sensitive: in fact, if it is true that measurement cycle lasts less than 1 hour, water samples have to be analysed one at a time, i.e. few (<10) measurements per day.

Performing measurements by different measuring chains (i.e. radon detector coupled with closed degassing circuit in case of emanometry), although the test method is exactly the same, should require the development of a specific quality assurance (QA) protocol whose resulting reproducibility needs to be evaluated: it should be investigated the agreement between the results of measurements of the same measurand carried out with different instruments (Joint Committee for Guides in Metrology, 2008).

5.2 Materials and methods

Three measuring systems have been assembled: three pulsed ion chamber detectors (PICs) – the same model from the same manufacturer (AlphaGUARD PQ 2000PRO (Genitron InstrumentGmbH, 2012) by Bertin Instruments) – have been coupled with three degassing circuits (AquaKIT(Saphymo GmbH, 2017) by Bertin Instruments), each equipped with identical active (i.e. volumetric pumps) and passive (i.e. vessels, tubing and filters) components.

The evaluation test has relied on $q = 39$ measurand levels (i.e. different radon concentrations in water), $n = 3$ measurements – one replicate for each measuring system – for every single level, and $p = 1$ laboratory (considering the same indexes used by ISO 5725-2:2019 (International Standard Organization, 1994)). The total number of measurements has been $q \cdot n \cdot p = 117$.

During the measurements, the following conditions have been kept unchanged: *i*) principle of measurement (i.e. radon and its decay products detection in air after radon degassing from water), *ii*) method of detection (i.e. ionization chamber), *iii*) laboratory location, *iv*) condition of use (i.e. environmental parameters and radon in air background), and *v*) team of operators. Besides, although the q measurands have been measured on different days, the n measurements have been performed simultaneously. The only condition changed has been the measuring system, each performing one of the $n = 3$ measurements at each q level.

5.2.1 Emanometry measuring system

The measuring set-up (Figure 5.1), in three replicates, consists of *i*) a degassing vessel, *ii*) a degassing washing vessel of DURAN®, *iii*) a security vessel to collect water drops from the gas flow, *iv*) an active coal filter, frequently unused due to the very low (i.e.≈ 20 Bq m^{-3}) laboratory background, *v*) an Alpha Pump (Bertin Instruments®) and *vi*) six Tygon® connecting tubes ($ID = 5/32$").

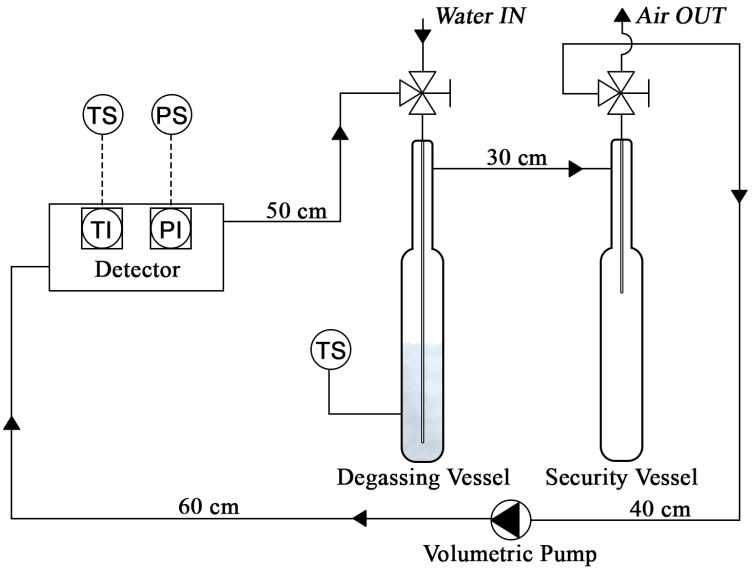

Figure 5.1: Scheme of the experimental setup used to measure radon in water concentration. It shows, other than components and flow direction, locations for temperature and pressure monitoring and connection tubes length.

The radon concentration in water results from the following equation:

$$C_w = \frac{C_{air} \cdot \left(\frac{V_{sys}-V_w}{V_w} + K\right) - C_0 \cdot \left(\frac{V_{sys}-V_w}{V_w}\right)}{1000} \tag{5.1}$$

where:

C_w is the radon concentration in the water sample, Bq L^{-1}

C_{air} is the radon concentration in the air flowing in the measuring system during sample degassing, Bq m^{-3}. It is obtained from detector measurements performed for 22 minutes in 1 min FLOW operation mode.

C_0 is the radon concentration in the air enclosed in the degassing circuit before sample injection and degassing (background radon concentration), Bq m^{-3}

V_{sys} is the total inner volume of the whole measuring system, 1102 mL ± 1% (Saphymo GmbH, 2017)

V_w is the water sample volume, 100 mL

K is the Ostwald coefficient standing for the ratio of radon concentration in water to radon concentration in air, at thermodynamic equilibrium. It has been computed using the following formula (Battino and Clever, 1965;

Weigel, 1978):

$$K = 0.105 + 0.405e^{-0.0502 \cdot T[^{\circ}\mathrm{C}]} \tag{5.2}$$

5.2.2 Water samples

All the waters analysed are spring waters sampled directly at the source.

The 39 different measurand levels have been obtained by considering 20 different sources: 1 from radon-in-water PT and 19 from springs located in central Italy.

As regards to PT water sample, European Commission's Joint Research Centre sent two separate transport containers to the ISS Laboratory of Radioactivity: two subsamples have been so drawn from the same container and the third from the other one. The remaining 19 sources from central Italy have been chosen in the framework of a different survey on not-bottled mineral spring waters[14]. From each source, six separate transport containers have been filled, three following the method suggested by ISO 13164-3 such to avoid degassing during sampling procedure, and three simulating the everyday consumers' habits without any expedients to prevent radon escape. The so obtained 39 levels of radon in water concentration are all above the detection limit and ranged from few $\mathrm{Bq\,L^{-1}}$ to about $300\,\mathrm{Bq\,L^{-1}}$. The average value of DL for the discussed measurements is $1.5\,\mathrm{Bq\,L^{-1}}$.

5.3 Results and discussion

5.3.1 Quality assurance procedures

According to the ISO 13164-3, a quality assurance protocol was developed for the used measuring system. In this section, only some parts of the measurement protocol are addressed, i.e. those mainly affecting the precision (and, in turn, the reproducibility) of the measurements. The adopted procedures, structured as a temporal sequence of actions to do or care to have, rely both on experience gained through years by operators and on an extensive review of literature on emanometry measurements. The three main key-points of these procedures are:

i) How to choose and adequately assemble each component of the three degassing circuits. Paying attention to the connections of lower and upper nozzles of degassing and security vessels to the outlet and inlet of both ionization chamber and volumetric pump (Figure 5.1) helps to prevent water from flowing back to the chamber. The inner volume of the circuit depends on tubes of proper length and diameter, thus reflecting on the accuracy and reproducibility of measurements.

ii) How to minimize the spontaneous degassing of radon during transfer procedure from transport container to degassing circuit. Indeed, while doing so, water gets into contact with the laboratory air. The degassing is minimized by both avoiding turbulence during sub-sampling and reducing the time spent for transfer. The first goal is achieved by adopting an immersion-overflow technique and by training operators to do it. As regards the second goal, to improve the reproducibility of the measuring

system, the steps to be followed by the operators from transport container opening to circuit inlet valve closure need to be listed as well as the time established for each of these. Any deviations from the schedule for both the operations should be reported and all the three measurements repeated.Storing the sample at least two hours before the measurement in a room at controlled temperature – as low as possible but well above 0°C – helps to increase radon solubility, so reducing the spontaneous degassing.

iii) Controlling the influencing quantities other than circuit inner volume (*i*) and turbulence while sampling (*ii*): temperature during measurements, storage, stability and contamination of detection system. Accuracy and reproducibility both strongly depend on temperature, whose value is measured in two different locations (Figure 1) with two distinct sensors using two different physical effects (thermal expansion and Seebeck effect). Detectors are stored, while not used, in the same room – storing them together aims to prevent uneven growth of detectors background – with forced air circulation reflecting typical radon concentration lower than $30\,\mathrm{Bq\,m^{-3}}$. During the storage, detectors are always turned on to self-adjust rising background due to the contamination of the ionization chamber with long-lived radon decay products (mainly 210Pb) (Genitron InstrumentGmbH, 2012). The stability of the detector response is verified by periodical comparison tests (within the laboratory or with other national and international laboratories) with other pulsed ionization chamber detectors used for measuring radon in water, i.e. unlikely to have contamination of detection surface and/or presence of radon isotopes in the detection volume.

According to recommendations by ISO 13164-3 about method verification, the same three measuring systems took part in an intercomparison exercise, the radon-in-water proficiency test (PT) organized by the European Commission's Joint Research Centre on September 2018. The results, in terms of percentage difference from the reference value (i.e. $318\pm16\,\mathrm{Bq\,L^{-1}}$), ranged between 3.1% and 5% (Jobbágy et al., 2020).

5.3.2 Reproducibility analysis

The reproducibility has been evaluated by computing, for each measurand level q^*, the coefficient of variation:

$$CV_{q^*} = \sqrt{\frac{1}{2}\frac{\sum_{i=1}^{3}(C_{i,q^*} - \mu_{q^*})}{\mu_{q^*}^2}} \tag{5.3}$$

whre C_{i,q^*} stands for each measurement of q^* by the measuring system i and μ_{q^*} is the arithmetic mean of $n = 3$ measurements of q^*. Table 5.1 reports the main statistical parameters for this coefficient.

Results are grouped in two, by considering all measurements first and then only those exceeding the Euratom Drinking Water Directive Detection Limit (DWD-DL) equal to $10\,\mathrm{Bq\,L^{-1}}$.

Restricting the analysis to concentrations >DWD-DL, the arithmetic mean of coefficients of variation slightly decreases (passing from 13% to 10%) as well as 3^{rd} quartile (from 16% to 11%) and maximum (from 50% to 19%), the latter

Table 5.1: Statistical parameters for coefficients of variations between results from the three measuring systems.

	All data	$10\,\mathrm{Bq\,L^{-1}}$
N	39	24
AM	13%	10%
Min	1%	1%
1^{st} Quartile	8%	7%
Median	10%	10%
3^{rd} Quartile	16%	11%
Max	50%	19%

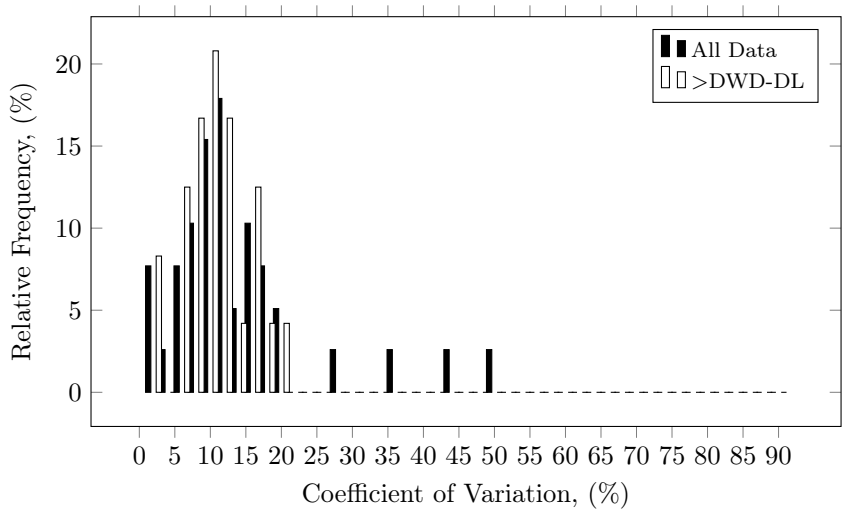

Figure 5.2: Relative frequency distribution of coefficients of variation ($k = 1$) between the results of the three measuring systems for each q level. In white, the distribution of all data, in black that for levels greater than $10\,\mathrm{Bq\,L^{-1}}$ (DWD-DL).

being the most influenced parameter. This is clearly explained by the reduction in the stochastic component of error, which decreases when the observed quantity (i.e. counts from radon and its decay products) rises.

As a general trend (Figure 5.3), the coefficient of variation among the measuring systems increases for very low radon concentration (i.e. $< 10\,\mathrm{Bq\,L^{-1}}$). Instead, it results to be usually lower than 15% even for radon concentration higher than $100\,\mathrm{Bq\,L^{-1}}$. Finally, it is worth noting that this amount of variation is close to the typical uncertainty associated with a single measurement (Jobbágy et al., 2017).

The variability tuned out to be <= 15% for the 84% of q levels in the range 10–$100\,\mathrm{Bq\,L^{-1}}$ and for the 100% of q levels $> 100\,\mathrm{Bq\,L^{-1}}$. These findings support the interchangeable use of the three measuring systems, and consequently allow to increase the number of feasible measurements per day without a performance loss. The periodical check of the reproducibility of the three measuring systems has been introduced in the quality assurance program.

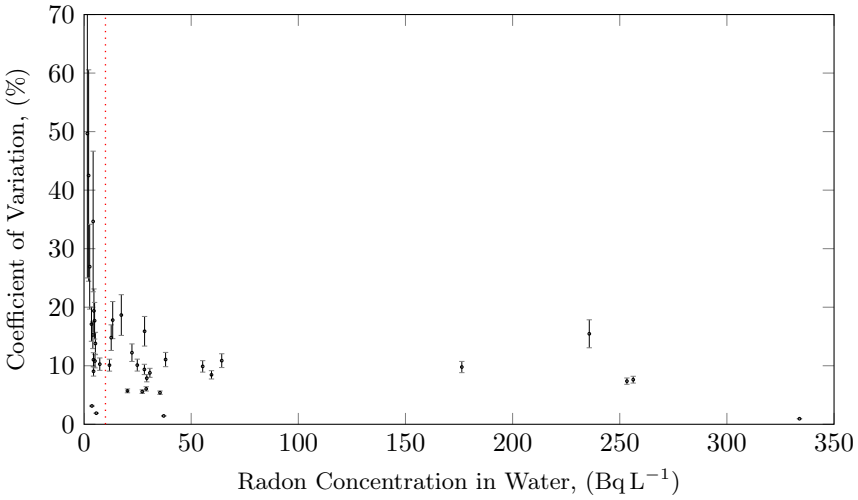

Figure 5.3: Scatter plot of coefficients of variation between results returned by the three measuring systems for each measurand level. Vertical dotted line indicates the DWD-DL.

5.4 A case study: the first survey addressing radon concentration measurements in self-bottled mineral spring waters

Mineral waters are exempted from radioactivity control by the Council Directive 2013/51/Euratom regardless their consumption in different countries. The issue is particularly significant in Italy, the first country in Europe for mineral water consumption, with more than 200 L per person per year (Statista - The Statistics Portal, 2016). This exemption refers both to bottled and not-bottled mineral waters.

As regards to bottled waters, population exposure to radon concentration in such waters is usually low because radon half-life is much shorter than the typical time needed by bottled waters to reach consumers' houses. As a consequence, radon concentration measured in mineral bottled waters is usually lower or much lower than its above-mentioned parametric value (e.g. Kralik et al., 2003).

About non-bottled mineral waters, radon exposure can be not negligible when consumers can fill bottles and containers directly from public fountains or from fountains within mineral spring water plants, thus reducing significantly the time elapsing between mineral water bottling and subsequent consumption. In Italy, few radon concentration measurements were performed in mineral spring waters (Giovani et al., 2000), whereas several surveys were carried out on radon concentration in groundwaters and tap waters since the '90s (see Nuccetelli et al., 2012, and references therein). Therefore, a survey addressing radon concentration in all the 20 natural mineral spring waters of Lazio (a region of Central Italy) was planned and conducted in order to assess if such waters, when self-bottled, may be of concern for public health. This region has been chosen because its soil is largely made of materials of volcanic origin, such as tuff and pozzolana, leading potentially to high levels of radon in waters.

5.4.1 Surveyed mineral spring waters

In Lazio, a total of 33 mineral spring water concession (MSWCs) are present until 2018, according to the number of authorizations granted by the regional authority to public and private subjects (Regione Lazio, 2018). These concessions are distributed in six areas of the region (showed in Figure 5.5). The sampling operations interested only the 18 MSWCs of Lazio whose concession owner allows people to self-bottle directly from municipal public fountains or from fountains within the plants for industrial bottling. However, two of the sampled MSWPs actually manage two different spring waters, so that the total number of different waters included in this survey rises to 20 (Table 5.2).

For some concessions (13), measurements could not be performed due to different reasons. Some plants (6) were closed/inoperative (or actually did not exist) during the survey. One plant was seriously damaged by a recent earthquake. In two plants, two different concessions were managed and it was not possible to distinguish them. For two concessions (both distributed via public fountains), the fountains supplied by the source were not identified. In all other cases (4), the policy adopted by the concession companies does not allow the consumer to fill bottles or containers directly at the source within the plant.

5.4.2 Water sampling procedure

The radon concentration is evaluated at the point where the water is put into containers for two main reasons:

i the radon concentration in samples collected directly at the plant is higher than in any other scenario interesting the same source. Indeed, referring to bottled water, the radon concentration in water stored in containers for transport and subsequent consumption decreases due to the natural radioactive decay of Rn and the leakage through the sealing of the bottles. Besides, the operations of packing and bottling could highly influence the radon concentration in water, reducing it.

ii) sampling the water inside the plant allows to know and minimize the time elapsing between the collection and the first opening of the bottle.

Water was collected in polyethylene terephthalate (PET) bottles. It was observed that polyethylene terephthalate (PET) has generally lower radon loss during storage (Leaney and Herczeg, 2006; Lucchetti et al., 2016) than high density and low-density polyethylene (Jobbágy et al., 2019). The material and the sealing are compliant with ISO 13164-1 and ISO 13164-3 concerning principles to be adopted in water sampling, storage, and transportation. All the containers, having a volume larger than 1 L, were filled to the brim and plugged such to avoid air volumes between the free surface and the cap. Polyethylene terephthalate was chosen in order to have the possibility of squeezing the bottle when capping, such reducing the air gap and radon diffusion towards the gas phase, too.

For each spring, three samplings were carried out in the so-called *preventive way*. Such filling method aims to obtain a near laminar water flux that avoids spontaneous degassing of dissolved gases when filling the bottle. *Preventive way* was obtained by inclining the bottle and reducing the water flow rate at

the minimum value. The remaining three samples were collected in *typical way*, with a medium water flux and by simply placing the bottle in vertical position during filling operation, as a common user would have done. The sealed samples were then transported to the Italian National Institute of Health where the radon concentration measurements were performed. The time delay between the sample collection and measurements was always kept below 24 h in order to increase measurements precision and to reduce radon loss due to diffusion through PET.

5.4.3 Results and discussions

The mean radon concentration in water from each source was estimated as the average of the values returned by the measurements of three samples collected one after the other. As introduced, two sampling method, have been considered for each mineral water in order to investigate the effect of filling method on radon degassing.

The obtained results, expressed in terms of average ± standard error (equal to the ratio of standard deviation of the 3 measurements results to $\sqrt{3}$) of radon concentration, are shown in Table 5.3. The results are grouped in the table according to the region division into six sampling areas.

The measurement identification codes, reported in the third column of Table 5.3, allow associating the proper radon concentration of each source to the corresponding circle of Figure 5.5.

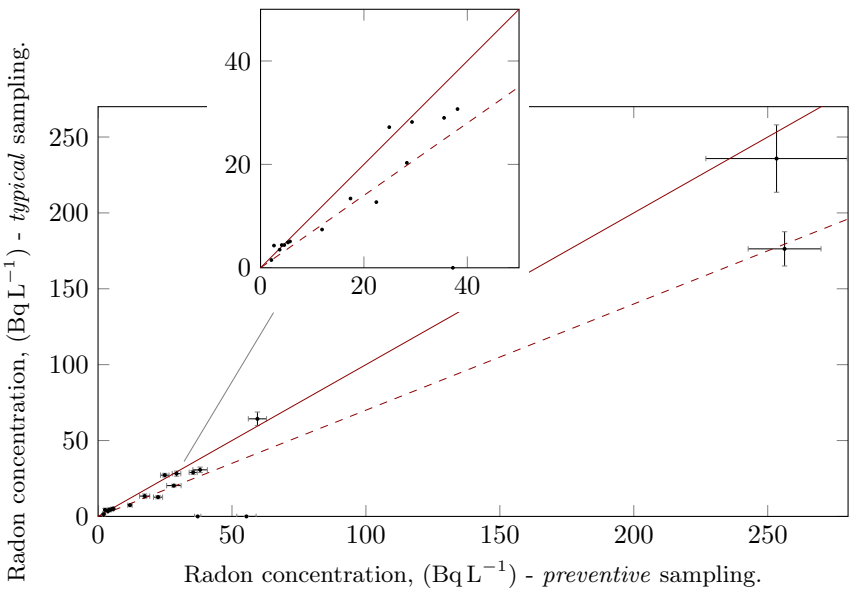

Figure 5.4: Radon in water concentrations obtained through typical versus preventive sampling. The blue solid line denotes the equality of the two variables (i.e.$y = x$). The dashed line denotes a situation where y variable is 30% lower than x variable (i.e. $y = 0.7x$). The uncertainties are expressed with coverage factor (k) equal to 1.

As expected, radon concentration measured from samples obtained in preventive way is generally lower (for about 80% of the cases) than the correspond-

ing values obtained using the typical sampling method. However, considering the uncertainties, the differences between the two approaches are statistically significant only for 3 cases (about 20% of the total) and the relative difference between to two approaches is mostly lower than 30% (see Figure 2), also for radon levels higher than $100\,\mathrm{Bq\,L^{-1}}$.

Hence, the *typical* sampling leads to a radon loss not so large as compared to a more careful sampling procedure. Since *typical* sampling reproduces the typical consumer's handling for the water sampling from the fountains, it can be considered more representative of the actual radon levels than the other sampling approach. Therefore, data analysis and comparison with previous studies will be hereafter carried out using data of radon concentration in water measured with the *typical* sampling approach.

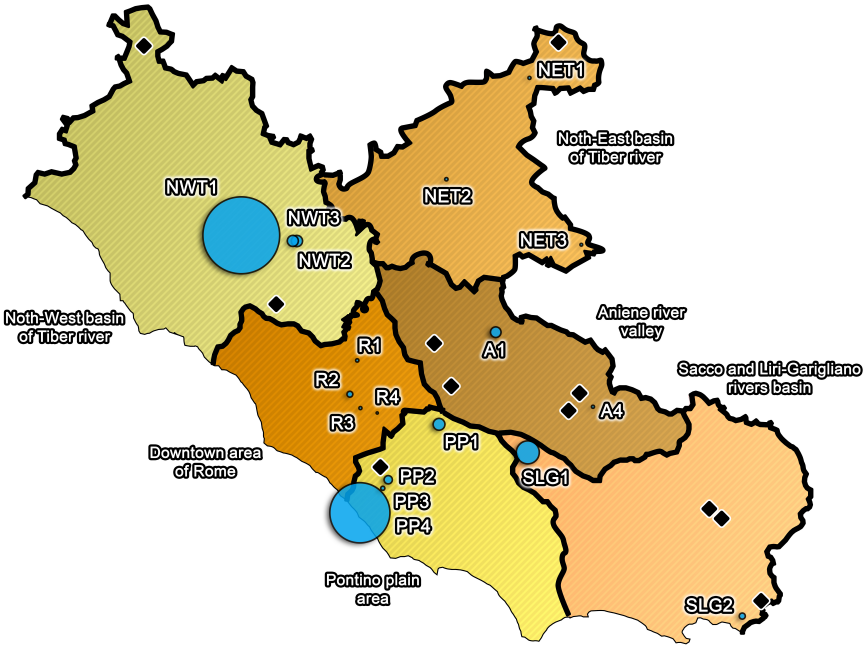

Figure 5.5: Radon concentration distribution in mineral spring waters of Lazio sampled in the so-called "*typical*" way. Each mineral spring water source is associated to a circle of dimension proportional to radon content measured. Thick lines represent the boundaries dividing the territory into the six sampling areas discussed above. The black diamonds identify the position of the mineral spring water plants whose samples could not be collected during the survey. *The image has been created through GIMP 2.10.12 (https://www.gimp.org/).*

Radon concentration levels measured in the surveyed spring waters follow a right-skewed distribution, similarly to the usual log-normal distribution of indoor radon concentration levels. In fact, generally low levels of radon concentration were found: 50% of them has values lower than $13\,\mathrm{Bq\,L^{-1}}$ and 75% of them has values lower than about $30\,\mathrm{Bq\,L^{-1}}$. The variability of radon concentrations in spring waters within the same area is quite high (Table 5.3), mostly higher than 80% if expressed in terms of coefficient of variation of radon levels.

The high data variability within areas and the presence of mostly low radon levels were also found in a previous study on radon concentration in different types of waters conducted in 14 Italian regions (Giovani et al., 2000), including Lazio region, although limited to the Province of Viterbo (VT), approximately in the same North-West Basin of Tiber River area of the present study. In this area, the authors found a high fraction of tap and spring waters having high radon levels: 25% of them higher than $87\,\mathrm{Bq\,L^{-1}}$ with a maximum of $624\,\mathrm{Bq\,L^{-1}}$ (Giovani et al., 2000). These results are similar to those of the present study and can be explained with the fact that soils of Viterbo province are mainly on volcanic origin, with an high concentration of natural radionuclides, including radium which decays into radon(Bochicchio et al., 1999).

The present study shows an exceedance of $100\mathrm{Bq\,L^{-1}}$, the parametric value for radon in water intended for human consumption established by Council Directive 2013/51/Euratom, for two mineral spring waters in two different areas, one in North-West basin of Tiber river and one in Sacco and Liri-Garigliano rivers basin. The presence of waters exceeding the parametric value was previously found in only 5 out of 14 Italian regions, including also spring and tap waters of Lazio (Giovani et al., 2000).

Table 5.2: Summary of mineral spring water concessions (MSWP) involved in the present survey and different waters sampled.

Area of Lazio	Total number of MSWCs	Number of sampled MSWCs	Number of different waters sampled
N-W basin of Tiber river	6	2	3[a]
N-E basin of Tiber river	4	3	3
Downtown are of Rome	4	4	4
Aniene river valley	7	3	4[a]
Sacco and Liri-Garigliano rivers basin	6	2	2
Pontino plain area	6	4	4
Total	33	18	20

[a] Two plants, one in the municipality of Nepi (VT) and one in the municipality of Marano Equo (RM), manage two different waters with specific physical-chemical properties.

Table 5.3: Radon concentration in all the mineral spring waters analysed, expressed in [Bq L^{-1}] and computed as the average of the three samples collected in the so-called "preventive" and "typical" approaches. The uncertainties are expressed with coverage factor (k) equal to 1.

Area denomination	**Municipality**	**Measurement ID**	***"Preventive" Sampling***	***"Typical" Sampling***
			$C_{^{222}\mathrm{Rn}}$ [Bq L^{-1}]	$C_{^{222}\mathrm{Rn}}$ [Bq L^{-1}]
N-W Basin of Tiber river	Capranica (VT)	NWT1	253±13	236±22
	Nepi,*Sulfur* (VT)	NWT2	29±2	28±2
	Nepi (VT)	NWT3	35±2	29±2
N-E Basin of Tiber river	Città Reale (RI)	NET1	4±1	4±1
	Rieti (RI)	NET2	5±1	5±1
	Sant'Anatolia (RI)	NET3	4±1	3±1
Downtown Area of Rome	Rome (RM)	R1	6±1	5±1
	Rome (RM)	R2	22±2	13±1
	Rome (RM)	R3	5±1	4±1
	Rome (RM)	R4	2±1	2±1
Aniene River Valley	Marano Equo (RM)	A1	25±2	27±1
	Marano Equo, *Magnesian* (RM)	A2	55±4	
	Fiuggi (FR)	A3	37±1	
	Guarcino (FR)	A4	3±1	4±1
Pontino Plain Area	Rocca Priora (RM)	PP1	38±3	31±2
	Aprilia (LT)	PP2	28±3	20±1
	Aprilia (LT)	PP3	12±1	7±1
	Aprilia (LT)	PP4	256±14	176±11
Sacco and Liri-Garigliano River Basin	Gavignano (RM)	SLG1	59±3	64±4
	Minturno (LT)	SLG2	17±2	13±1

For mineral spring waters A2 and A3, "typical" results are not available due to the restrictions adopted by the owners about the number of bottles non-residents can fill: in such a condition, the three containers were all filled in the "preventive way".

Bibliography

W. W. Nazaroff and A. V. Nero. *Radon and its Decay Products in Indoor Air*. 1988. ISBN 0-471-62810-7.

M. V.J. Culot, H. G. Olson, and K. J. Schiager. Effective diffusion coefficient of radon in concrete, theory and method for field measurements. *Health Physics*, 30(3):263–270, 1976. ISSN 15385159. doi: 10.1097/00004032-197603000-00002.

G. Prasad, T. Ishikawa, M. Hosoda, A. Sorimachi, M. Janik, S. K. Sahoo, S. Tokonami, and S. Uchida. Estimation of radon diffusion coefficients in soil using an updated experimental system. *Review of Scientific Instruments*, 83 (9):0–6, 2012. ISSN 00346748. doi: 10.1063/1.4752221.

V. C. Rogers and K. K. Nielson. Correlations for predicting air permeabilities and Rn diffusion coefficients of soils. *Health Physics*, 61(2):225–230, 1991. ISSN 15385159. doi: 10.1097/00004032-199108000-00006.

P. Bossew. The radon emanation power of building materials, soils and rocks. *Applied Radiation and Isotopes*, 59(5-6):389–392, 2003. ISSN 09698043. doi: 10.1016/j.apradiso.2003.07.001.

W. Zhang, Y. Zhang, and Q. Sun. Analyses of Influencing Factors for Radon Emanation and Exhalation in Soil. *Water, Air, and Soil Pollution*, 230(1), 2019. ISSN 15732932. doi: 10.1007/s11270-018-4063-z.

W. Zhuo, T. Iida, and M. Furukawa. Modeling radon flux density from the earth's surface. *Journal of Nuclear Science and Technology*, 43(4):479–482, 2006. ISSN 00223131. doi: 10.1080/18811248.2006.9711127.

V. C. Rogers and K. K. Nielson. Data and models for radon transport through concrete. In *The 1992 International Symposium on Radon and Radon Reduction Technology*, pages VI–3, 1992.

P. H. Gleick, Pacific Institute for Studies in Development, Environment and Security, and Stockholm Environment Institute. *Water in crisis: a guide to the world's fresh water resources*. Oxford University Press, 1993. ISBN 9780195076288.

ISTAT. Censimento delle acque per uso civile. Technical report, 2017.

D. N. Winslow. The pore size distribution of Portland cement paste. Technical report, Purdue University Lafayette Indiana, 1968.

G. Keller, B. Hoffmann, and T. Feigenspan. Radon permeability and radon exhalation of building materials. *Science of the Total Environment*, 272(1-3): 85–89, 2001. ISSN 00489697. doi: 10.1016/S0048-9697(01)00669-6.

Sensirion. Humidity and Temperature Sensor Sensirion datasheet SHT75, 2011.

Bosch Sensortec. BMP 085 Digital Pressure Sensor Datasheet, 2009. URL https://www.bosch-sensortec.com/bst/products/all{_}products/bmp280.

United Nations Scientific Committee on the Effects of Atomic Radiation. Sources and Effects of Ionizing Radiation. Technical report, 2000.

C. Nuccetelli, S. Risica, S. Onisei, F. Leonardi, and R. Trevisi. Natural radioactivity in building materials in the Eurpean Union: a database of activity concentrations, radon emanations and radon exhalation rates, Rapporti Istisan. 2018.

C. Nuccetelli, F. Leonardi, and R. Trevisi. Building material radon emanation and exhalation rate: Need of a shared measurement protocol from the european database analysis. *Journal of Environmental Radioactivity*, 225 (September):106438, 2020. ISSN 18791700. doi: 10.1016/j.jenvrad.2020.106438. URL https://doi.org/10.1016/j.jenvrad.2020.106438.

A. K. Narula, R. P. Chauhan, and S. K. Chakarvarti. Testing permeability of building materials for radon diffusion. *Indian Journal of Pure and Applied Physics*, 48(7):505–507, 2010. ISSN 00195596.

UNEP, Global Environment Monitoring System: Monitoring and Assessment Research Centre, D.C.) World Resources Institute (Washington, and United Kingdom Department of the Environment. *Environmental data report, 1989/90*. Basil Blackwell, Oxford, England, 1989. ISBN 0631169873.

United Nations Scientific Committee on the Effects of Atomic Radiation. Sources and Effects of Ionizing Radiation. Technical report, 1993.

Danske Vandværkers Forening and Danmarks Statistik. Communication to European Environment Agency (EEA), 1997.

Statistiska Centralbyrån. Mir rapport 2000:6. Technical report, 2000.

Environment Agency/Ofwat. DETR Indicators for sustainable development D07, 2000.

Statistics Norway. Communication to European Environment Agency (EEA), 1981.

Finnish Environment Institute. Etelämäki 1999. Veden käyttö Suomessa. Suomen ympäristö 305., 1999.

RIVM. Milieucompendium 1999: A6.4 Huishoudelijk waterverbruik per hoofd van de bevolking. Technical report, 1999.

How to make a glass of water | McGinley News | 29th September 2015 | News | McGinley Support Services. URL https://www.mcginley.co.uk/news/how-to-make-a-glass-of-water/bp142/.

European Commission. Council Directive 2013/59/Euratom of 5 December 2013 laying down basic safety standards for protection against the dangers arising from exposure to ionising radiation, and repealing Directives 89/618/Euratom, 90/641/Euratom, 96/29/Euratom, 97/43/Euratom a. *Official Journal of the European Union*, L(13):1–73, 2014. ISSN 0144-557X. doi: 10.3000/19770677.L_2013.124.eng.

United Nations Scientific Committee on the Effects of Atomic Radiation. Sources and Effects of Ionizing Radiation. Technical report, 2008.

United Nations Scientific Committee on the Effects of Atomic Radiation. Ionizing radiation: Sources and Biological Effects. Technical report, 1982.

T. Iida, Y. Ikebe, K. Suzuki, K. Ueno, Z. Wang, and Y. Jin. Continuous measurements of outdoor radon concentrations at various locations in East Asia. *Environment International*, 22:139–147, jan 1996. ISSN 01604120. doi: 10.1016/S0160-4120(96)00102-X.

S. Oikawa, N. Kanno, T. Sanada, N. Ohashi, M. Uesugi, K. Sato, J. Abukawa, and H. Higuchi. A nationwide survey of outdoor radon concentration in Japan. *Journal of Environmental Radioactivity*, 65(2):203–213, jan 2003. ISSN 0265931X. doi: 10.1016/S0265-931X(02)00097-8.

A.V. Nero and W.W. Nazaroff. Characterising the Source of Radon Indoors. *Radiation Protection Dosimetry*, 7(1-4):23–39, jan 1984. ISSN 1742-3406. doi: 10.1093/oxfordjournals.rpd.a082958.

S. Tokonami, M. Furukawa, Y. Shicchi, T. Sanada, and Y. Yamada. Characteristics of radon and its progeny concentrations in air-conditioned office buildings in Tokyo. *Radiation Protection Dosimetry*, 106(1):71–75, 2003. ISSN 01448420. doi: 10.1093/oxfordjournals.rpd.a006338.

T. Iimoto. Time variation of the radon equilibrium factor in a reinforced concrete dwelling. *Radiation Protection Dosimetry*, 92(4):319–321, 2000. ISSN 01448420. doi: 10.1093/oxfordjournals.rpd.a033299.

P. K. Hopke, B. Jensen, C. Li, N. Montassier, P. Wasiolek, A. J. Cavallo, K. Gatsby, R H. Socolow, and A. C. James. Assessment of the Exposure to and Dose from Radon Decay Products in Normally Occupied Homes. *Environmental Science & Technology*, 29(5):1359–1364, may 1995. ISSN 0013-936X. doi: 10.1021/es00005a031.

M. Prasad, M. Rawat, A. Dangwal, T. Kandari, G. S. Gusain, R. Mishra, and R. C. Ramola. Variability of radon and thoron equilibrium factors in indoor environment of Garhwal Himalaya. *Journal of Environmental Radioactivity*, 151:238–243, 2016. ISSN 18791700. doi: 10.1016/j.jenvrad.2015.10.017.

T. V. Ramachandran and M. C. S. Ramu. Variation of equilibrium factor F between radon and its short-lived decay products in an indoor atmosphere. *Nuclear Geophysics*, 8, Oct 1994.

United Nations Scientific Committee on the Effects of Atomic Radiation. Sources, Effects and Risks of Ionizing Radiation, Report to the General Assembly. Technical report, 1988.

United Nations Scientific Committee on the Effects of Atomic Radiation. Effects of Ionizing Radiation. Technical report, apr 2006.

World Health Organization. *WHO Handbook on Indoor Radon: A Public Health Perspective*, volume 67. feb 2010. ISBN 9789241547673.

D. Avramović, I. Čeliković, P. Ujić, I. Vukanac, A. Kandić, A. Jevremović, D. Antonijević, and B. Lončar. Radon exhalation rate of some building materials common in Serbia. In *RAD Conference Proceedings*, volume 3, pages 119–122. RAD Association, feb 2019. doi: 10.21175/RadProc.2018.26.

F. Leonardi, M. Bonczyk, C. Nuccetelli, M. Wysocka, B. Michalik, M. Ampollini, S. Tonnarini, J. Rubin, K. Niedbalska, and R. Trevisi. A study on natural radioactivity and radon exhalation rate in building materials containing norm residues: preliminary results. *Construction and Building Materials*, 173:172–179, 2018. ISSN 09500618. doi: 10.1016/j.conbuildmat.2018.03.254. URL https://doi.org/10.1016/j.conbuildmat.2018.03.254.

B. K. Sahoo, B. K. Sapra, J. J. Gaware, S. D. Kanse, and Y. S. Mayya. A model to predict radon exhalation from walls to indoor air based on the exhalation from building material samples. *Science of the Total Environment*, 409(13): 2635–2641, 2011. ISSN 18791026. doi: 10.1016/j.scitotenv.2011.03.031. URL http://dx.doi.org/10.1016/j.scitotenv.2011.03.031.

T. Feng and X. Lu. Natural radioactivity, radon exhalation rate and radiation dose of fly ash used as building materials in Xiangyang, China. *Indoor and Built Environment*, 25(4):626–634, jul 2016. ISSN 1420-326X. doi: 10.1177/1420326X15573276. URL http://journals.sagepub.com/doi/10.1177/1420326X15573276.

M. Gupta, A. K. Mahur, R. Varshney, R. G. Sonkawade, K. D. Verma, and R. Prasad. Measurement of natural radioactivity and radon exhalation rate in fly ash samples from a thermal power plant and estimation of radiation doses. *Radiation Measurements*, 50:160–165, 2013. ISSN 13504487. doi: 10.1016/j.radmeas.2012.03.015. URL http://dx.doi.org/10.1016/j.radmeas.2012.03.015.

A. K. Mahur, R. Kumar, M. Mishra, D. Sengupta, and R. Prasad. An investigation of radon exhalation rate and estimation of radiation doses in coal and fly ash samples. *Applied Radiation and Isotopes*, 66(3):401–406, mar 2008. ISSN 09698043. doi: 10.1016/j.apradiso.2007.10.006.

P. Ujić, I. Čeliković, A. Kandić, I. Vukanac, M. Durašević, D. Dragosavac, and Z. S. Žunić. Internal exposure from building materials exhaling 222Rn and 220Rn as compared to external exposure due to their natural radioactivity content. *Applied Radiation and Isotopes*, 68(1):201–206, jan 2010. ISSN 09698043. doi: 10.1016/j.apradiso.2009.10.003.

M. Orabi. Estimation of the radon surface exhalation rate from a wall as related to that from its building material sample. *Canadian Journal of Physics*, 96 (3):353–357, 2018. ISSN 00084204. doi: 10.1139/cjp-2017-0629.

N. Jonassen and J.P. McLaughlin. Exhalation of Radon-222 from building materials and walls. In *Natural Radiation Environment III*, pages 1211–1224, 1980. URL https://inis.iaea.org/search/search.aspx?orig{_}q=RN:12619473.

International Organization for Standardization. ISO 11665-7 Measurement of radioactivity in the environment — Air: radon-222 — Part 7: Accumulation method for estimating surface exhalation rate. Technical report, 2012a.

European Commission. Council Directive 2013/51/Euratom of 22 October 2013 laying down requirements for the protection of the health of the general public with regard to radioactive substances in water intended for human consumption. *Official Journal of the European Union*, 296(November 1998):12–21, 2013.

Viktor Jobbágy, Timotheos Altzitzoglou, Petya Malo, Vesa Tanner, and Mikael Hult. A brief overview on radon measurements in drinking water. *Journal of Environmental Radioactivity*, 173:18–24, 2017. ISSN 18791700. doi: 10.1016/j.jenvrad.2016.09.019.

L. Pujol and M. E. Pérez-Zabaleta. Comparison of three methods for measuring 222Rn in drinking water. *Journal of Radioanalytical and Nuclear Chemistry*, 314(2):781–788, nov 2017. ISSN 15882780. doi: 10.1007/s10967-017-5472-y.

International Standard Organization. Water quality — Radon-222 Part 3 : Test method using emanometry. *ISO 13164-3*, 2013.

International Organization for Standardization. Water quality — Radon-222 Part 1 : General principles. *ISO 13164-1*, (January), 2014.

C. Y. H. Chao, T. C. W. Tung, and J. Burnett. Influence of ventilation on indoor radon level. *Building and Environment*, 32(6):527–534, 1997. ISSN 03601323. doi: 10.1016/S0360-1323(97)00017-6.

H. Arvela. *Residential Radon in Finland Sources, Variation, Modelling and Dose Comparisons*. PhD thesis, Helsinki University of Technology, 1995.

T. F. Gesell. Background atmospheric 222Rn concentrations outdoors and indoors: A review. *Health Physics*, 45(2):289–302, 1983. ISSN 15385159. doi: 10.1097/00004032-198308000-00002.

M.H. Wilkening, W.E. Clements, and D. Stanley. Radon 222 flux measurements in widely separated regions, 1972.

Joint Research Center. Radiological Maps - European Commission - Uranium Concentration in Soil, 2017a. URL https://remap.jrc.ec.europa.eu/Atlas.aspx?layerId=11.

Soil Science Glossary Terms Committee. *Glossary of Soil Science Terms 2008*. Madison, 2008. ISBN 978-0-89118-851-4. doi: 10.2135/1992.glossarycropsciterms.frontmatter.

D. L. Sparks. The Chemistry of Saline and Sodic Soils. In *Environmental Soil Chemistry*, pages 285–300. Elsevier, 2003. doi: 10.1016/b978-012656446-4/50010-4.

W. W. Nazaroff. Radon transport from soil to air. *Reviews of Geophysics*, 30 (2):137–160, 1992. ISSN 19449208. doi: 10.1029/92RG00055.

G. Cinelli, T. Tollefsen, P. Bossew, V. Gruber, K. Bogucarskis, L. De Felice, and M. De Cort. Digital version of the European Atlas of natural radiation. *Journal of Environmental Radioactivity*, 196(February 2018):240–252, 2019. ISSN 18791700. doi: 10.1016/j.jenvrad.2018.02.008.

Joint Research Center. Radiological Maps - European Commission - Soil Permeability, 2017b. URL https://remap.jrc.ec.europa.eu/Atlas.aspx?layerId=8.

S. Feng, H. Wang, Y. Cui, Y. Ye, X. Li, D. Xie, Z. He, and R. Yang. Monte Carlo method for determining radon diffusion coefficients in porous media. *Radiation Measurements*, 126:106130, jul 2019. ISSN 13504487. doi: 10.1016/j.radmeas.2019.106130.

N. K. Ryzhakova. A new method for estimating the coefficients of diffusion andemanation of radon in the soil. *Journal of Environmental Radioactivity*, 135:63–66, 2014. ISSN 18791700. doi: 10.1016/j.jenvrad.2014.04.002.

M. Hosoda, S. Tokonami, A. Sorimachi, M. Janik, T. Ishikawa, Y. Yatabe, J. Yamada, and S. Uchida. Experimental system to evaluate the effective diffusion coefficient of radon. *Review of Scientific Instruments*, 80(1), 2009. ISSN 00346748. doi: 10.1063/1.3049379.

W. Hirst and G. E. Harrison. The diffusion of radon gas mixtures. *Proceedings of the Royal Society of London. Series A. Mathematical and Physical Sciences*, 169(939):573–586, mar 1939. ISSN 0080-4630. doi: 10.1098/rspa.1939.0016.

N. Epstein. On tortuosity and the tortuosity factor in flow and diffusion through porous media. *Chemical Engineering Science*, 44(3):777–779, jan 1989. ISSN 00092509. doi: 10.1016/0009-2509(89)85053-5.

V. Chisté and M.M. Bé. LNE - LNHB/CEA - Table de Radionucléides. Technical report, 2007.

J. E. Martin. *Physics for Radiation Protection*. Wiley-VCH Verlag GmbH & Co. KGaA, Boschstr (Germany), third comp edition, 2013. ISBN 978-3-527-41176-4.

A. B. Tanner. Radon migration in the ground: a supplementary review. *Proc. Natural Radiation Environment III*, page 5, 1980.

K. P. Strong and D. M. Levins. Effect of moisture content on radon emanation from uranium ore and tailings. *Health Physics*, 42(1):27–32, 1982. ISSN 15385159. doi: 10.1097/00004032-198201000-00003.

Y. Ishimori, K. Lange, P. Martin, Y. S. Mayya, and M. Phaneuf. Measurement and Calculation of Radon Releases from NORM Residues. Technical Report 474, International Atomic Energy Agency (IAEA), Vienna, 2013.

J. F. Ziegler and J. P. Biersack. The Stopping and Range of Ions in Matter. In *Treatise on Heavy-Ion Science*, pages 93–129. Springer US, 1985. doi: 10.1007/978-1-4615-8103-1_3.

V. Jobbágy, J. Somlai, J. Kovács, G. Szeiler, and T. Kovács. Dependence of radon emanation of red mud bauxite processing wastes on heat treatment. *Journal of Hazardous Materials*, 2009. ISSN 03043894. doi: 10.1016/j.jhazmat.2009.07.131.

C. Carpentieri, C. Di Carlo, G. Venoso, M. Ampollini, S. Bonifazi, V. Dante, E. Petetti, S. Pozzi, S. Valentini, B. Caccia, and F. Bochicchio. Radon mitigation actions in large public buildings: some review and a case study. In *Book of abstracts 9th International Conference on Protection against Radon at Home and at Work 16-20 September 2019, Prague, Czech Republic*, page 78, 2019.

R. Trevisi, F. Leonardi, S. Risica, and C. Nuccetelli. Updated database on natural radioactivity in building materials in Europe. *Journal of Environmental Radioactivity*, 187(February):90–105, 2018. ISSN 18791700. doi: 10.1016/j.jenvrad.2018.01.024. URL https://doi.org/10.1016/j.jenvrad.2018.01.024.

Agenzia Nazionale per la Protezione dell'Ambiente (ANPA). Le discariche di fosfogessi nella laguna di Venezia: valutazioni preliminari dell'impatto radiologico. Technical report, 2000.

E. Garver and M. Baskaran. Effects of heating on the emanation rates of radon-222 from a suite of natural minerals. *Applied Radiation and Isotopes*, 61(6): 1477–1485, dec 2004. ISSN 09698043. doi: 10.1016/j.apradiso.2004.03.107. URL http://www.ncbi.nlm.nih.gov/pubmed/15388150.

D. R. Kalkwarf, P. O. Jackson, and J. C. Kutt. Emanation coefficients for rn in sized coal fly ash. *Health Physics*, 48(4):429–436, apr 1985. ISSN 15385159. doi: 10.1097/00004032-198504000-00005. URL http://www.ncbi.nlm.nih.gov/pubmed/3980228.

A. Sakoda, Y. Ishimori, K. Hanamoto, T. Kataoka, A. Kawabe, and K. Yamaoka. Experimental and modeling studies of grain size and moisture content effects on radon emanation. *Radiation Measurements*, 45(2):204–210, feb 2010a. ISSN 13504487. doi: 10.1016/j.radmeas.2010.01.010.

A. Sakoda, K. Hanamoto, Y. Ishimori, T. Kataoka, A. Kawabe, and K. Yamaoka. First model of the effect of grain size on radon emanation. *Applied Radiation and Isotopes*, 68(6):1169–1172, jun 2010b. ISSN 09698043. doi: 10.1016/j.apradiso.2009.11.070. URL http://www.ncbi.nlm.nih.gov/pubmed/20117006.

T. P. Barton and P. L. Ziemer. The effects of particle size and moisture content on the emanation of Rn from coal ash. *Health Physics*, 50(5):581–588, 1986. ISSN 15385159. doi: 10.1097/00004032-198605000-00001.

K. H. Folkerts, G. Keller, and H. Muth. An Experimental Study on Diffusion and Exhalation of Rn-222 and Rn-220 from Building Materials. *Radiation Protection Dosimetry*, 9(1):27–34, jul 1984. ISSN 1742-3406. doi: 10.1093/oxfordjournals.rpd.a083067. URL https://academic.oup.com/rpd/article-lookup/doi/10.1093/oxfordjournals.rpd.a083067.

L. G. Li, J. J. Feng, J. Zhu, S. H. Chu, and A. K. H. Kwan. Pervious concrete: Effects of porosity on permeability and strength. *Magazine of Concrete Research*, pages 1–35, 2019. ISSN 0024-9831. doi: 10.1680/jmacr.19.00194.

C. Hall and A. Hamilton. Porosity–density relations in stone and brick materials. *Materials and Structures/Materiaux et Constructions*, 48(5):1265–1271, 2015. ISSN 13595997. doi: 10.1617/s11527-013-0231-1.

W. Wedekind, R. López-Doncel, R. Dohrmann, M. Kocher, and S. Siegesmund. Weathering of volcanic tuff rocks caused by moisture expansion. *Environmental Earth Sciences*, 69(4):1203–1224, 2013. ISSN 18666280. doi: 10.1007/s12665-012-2158-1.

M. Raviv, R. Wallach, A. Silber, Sh Medina, and A. Krasnovsky. The effect of hydraulic characteristics of volcanic materials on yield of roses grown in soilless culture. *Journal of the American Society for Horticultural Science*, 124(2):205–209, 1999. ISSN 00031062. doi: 10.21273/jashs.124.2.205.

K. J. Renken and T. Rosenberg. Laboratory measurements of the transport of radon gas through concrete samples. *Health Physics*, 68(6):800–808, 1995. ISSN 15385159. doi: 10.1097/00004032-199506000-00006.

Society of Petroleum Engineers. The SI Metric System of Units and SPE METRIC STANDARD. Technical report, U.S.A., 1984.

R. P. Chauhan and Amit Kumar. A Comparative Study of Indoor Radon Contributed by Diffusive and Advective Transport through Intact Concrete. *Physics Procedia*, 80:109–112, 2015. ISSN 18753892. doi: 10.1016/j.phpro.2015.11.066.

World Health Organization. *Guidelines for Drinking-water Quality. Forth Edition*. 2017. ISBN 9789241549950.

A. Auvinen, L. Salonen, J. Pekkanen, E. Pukkala, T. Ilus, and P. Kurttio. Radon and other natural radionuclides in drinking water and risk of stomach cancer: A case-cohort study in Finland. *International Journal of Cancer*, 114 (1):109–113, 2005. ISSN 00207136. doi: 10.1002/ijc.20680.

W. Ye, T. Sobue, V. S. Lee, H. Tanooka, M. Mifune, A. Suyama, T. Koga, H. Morishima, and S. Kondo. Mortality and cancer incidence in Misasa, Japan, a spa area with elevated radon levels. *Japanese Journal of Cancer Research*, 89(8):789–796, 1998. ISSN 09105050. doi: 10.1111/j.1349-7006.1998.tb00630.x.

UNESCO, WHO, and UNEP. Water Quality Assessments-A Guide to Use of Biota, Sediments and Water in Environmental Monitoring-Second Edition. Technical Report 1996, 1992. URL https://www.who.int/water{_}sanitation{_}health/resourcesquality/wqachapter3.pdf.

P. W Mayer, W. B. Deoreo, E. M. Opitz, J. C. Kiefer, W. Y. Davis, B. Dziegielewski, and J. O. Nelson. *Residential end uses of water*. AWWA Research Foundation and American Water Works Association, 1999.

W. B. DeOreo, P. Mayer, B. Dziegielewski, and J. Kiefer. *Residential End Uses of Water: Version 2*. Water Research Foundation, 2016. ISBN 9781605732367. URL www.waterrf.org/4309.

P. Bendito, S. Mudgal, D. Dias, V. Jean-Baptise, M. Kong, D. Inman, and M. Muro. European Commission (DG ENV) Study on Water Efficiency Standards. Technical Report 0, 2009.

J. Schleich and T. Hillenbrand. Determinants of Residential Water Demand in Germany. Technical report, 2007.

D. A. Costa, E. Jobard, J. Marquay, M. Ollagnon, B. Plat, and S. Radureau. Public Water and Wastewater Services in France Economic, Social and Environmental Data 6th edition October 2015. Technical report.

ARPAE Emilia Romagna. I consumi domestici. URL https://www.arpae.it/pianetaacqua/data/acque{_}potabili/consumi{_}domestici/text1.html.

R. W. Boyle. The solubility of radium emanation. Application of Henry's law at low partial pressures. *The London, Edinburgh, and Dublin Philosophical Magazine and Journal of Science*, 22(132):840–854, 1911. ISSN 1941-5982. doi: 10.1080/14786441208637183.

R. Battino and H. L. Clever. The solubility of gases in liquids. *Chemical Reviews*, 66(4):395–463, 1965.

F. Weigel. Radon. *Chemiker Zeitung*, 102(9):287–299, 1978.

J. E. Partridge, T. R. Horton, and E. L. Sensintaffer. A study of radon-222 released from water during typical household activities. Technical report, U.S. Environmental Protection Agency, Montgomery, AL, 1979.

T. F. Gesell and H. M. Prichard. The contribution of radon in tap water to indoor radon concentrations. In *Conference on Natural Radiation Environment III*, Houston, TX, USA, 1980.

C. T. Hess, C. V. Weiffenbach, and S. A. Norton. Variations of airborne and waterborne Rn-222 in houses in Maine. *Environment International*, 8(1-6): 59–66, 1982. ISSN 01604120. doi: 10.1016/0160-4120(82)90010-1.

H. M. Prichard. The transfer of radon from domestic water to indoor air. *Journal / American Water Works Association*, 79(4):159, 1987. ISSN 0003150X. doi: 10.1002/j.1551-8833.1987.tb02828.x.

N. H. Harley, P. Chittaporn, G. B. Cook, and I. M. Fisenne. Radonwater to air transfer measured in a bathroom in an energy-efficient home with a private well. *Radiation Protection Dosimetry*, 160(1-3):231–234, 2014. ISSN 17423406. doi: 10.1093/rpd/ncu085.

National Research Council. *Risk Assessment of Radon in Drinking Water*. National Academies Press, Washington, D.C., jun 1999. ISBN 978-0-309-06292-3. doi: 10.17226/6287. URL http://www.nap.edu/catalog/6287.

D. S. Vinson, T. R. Campbell, and A. Vengosh. Radon transfer from groundwater used in showers to indoor air. *Applied Geochemistry*, 23(9):2676–2685, 2008. ISSN 08832927. doi: 10.1016/j.apgeochem.2008.05.021.

W. W. Nazaroff, S. M. Doyle, A. V. Nero, and R. G. Sextro. Potable water as a source of airborne 222rn in U.S. Dwellings: A review and assessment. *Health Physics*, 52(3):281–295, 1987. ISSN 15385159. doi: 10.1097/00004032-198703000-00002.

V. Jobbágy, M. Hult, T. Altzitzoglou, V. Tanner, and P. Malo. A brief overview on radon measurements in drinking water. *Journal of Environmental Radioactivity*, 173:18–24, 2016. ISSN 0265931X. doi: 10.1016/j.jenvrad.2016.09.019.

N. Todorovic, J. Nikolov, S. Forkapic, I. Bikit, D. Mrdja, M. Krmar, and M. Veskovic. Public exposure to radon in drinking water in SERBIA. *Applied Radiation and Isotopes*, 70(3):543–549, 2012. ISSN 09698043. doi: 10.1016/j.apradiso.2011.11.045. URL http://dx.doi.org/10.1016/j.apradiso.2011.11.045.

K. Somlai, S. Tokonami, T. Ishikawa, P. Vancsura, M. Gáspár, V. Jobbágy, J. Somlai, and T. Kovács. 222Rn concentrations of water in the Balaton Highland and in the southern part of Hungary, and the assessment of the resulting dose. *Radiation Measurements*, 42(3):491–495, 2007. ISSN 13504487. doi: 10.1016/j.radmeas.2006.11.005.

D. Nikolopoulos and A. Louizi. Study of indoor radon and radon in drinking water in Greece and Cyprus: Implications to exposure and dose. *Radiation Measurements*, 43(7):1305–1314, aug 2008. ISSN 13504487. doi: 10.1016/j.radmeas.2008.03.043.

G. Wallner, R. Wagner, and C. Katzlberger. Natural radionuclides in Austrian mineral water and their sequential measurement by fast methods. *Journal of Environmental Radioactivity*, 99(7):1090–1094, 2008. ISSN 0265931X. doi: 10.1016/j.jenvrad.2007.12.021.

V. Gruber, F. J. Maringer, and C. Landstetter. Radon and other natural radionuclides in drinking water in Austria: Measurement and assessment. *Applied Radiation and Isotopes*, 67(5):913–917, may 2009. ISSN 09698043. doi: 10.1016/j.apradiso.2009.01.056. URL https://www.sciencedirect.com/science/article/pii/S0969804309000645.

M. Beyermann, T. Bünger, K. Schmidt, and D. Obrikat. Occurrence of natural radioactivity in public water supplies in Germany: 238U, 234U, 235U, 228Ra, 226Ra, 222Rn, 210Pb, 210Po and gross α activity concentrations. *Radiation Protection Dosimetry*, 141(1):72–81, sep 2010. ISSN 0144-8420. doi: 10.1093/rpd/ncq139.

I. Lopes, M.J. Madruga, and F.P. Carvalho. Application of liquid scintillation counting techniques to gross alpha, gross beta, radon and radium measurement in portuguese waters. In *Proceedings of an international conference held in Szczyrk, Poland, 17–21 May 2004*, pages 357–367, 2004.

D. L. Henshaw, J. Perryman, P. A. Keitch, J. E. Allen, and G. C. Camplin. Radon in domestic water supplies in the UK. *Radiation Protection Dosimetry*, 46(4):285–289, 1993.

V. Moreno, J. Bach, C. Baixeras, and Ll Font. Radon levels in groundwaters and natural radioactivity in soils of the volcanic region of La Garrotxa, Spain. *Journal of Environmental Radioactivity*, 128:1–8, feb 2014. ISSN 18791700. doi: 10.1016/j.jenvrad.2013.10.021.

T. A. Przylibski, J. Gorecka, A. Kula, L. Fijałkowska-Lichwa, K. Zagożdżon, P. Zagozdzon, W. Miśta, and R. Nowakowski. 222 Rn and 226 Ra activity concentrations in groundwaters of southern Poland: New data and selected genetic relations. *Journal of Radioanalytical and Nuclear Chemistry*, 301(3): 757–764, jun 2014. ISSN 15882780. doi: 10.1007/s10967-014-3215-x.

L. Salonen. Natural radionuclides in groundwaters in Finland. *Radiation Protection Dosimetry*, 24:163–166, 1988.

M. Trautmannsheimer, W. Schindlmeier, and K. Hübel. Radon exposure levels of the staff in the drinking water supply facilities in Bavaria. In *Ger. Int. Congr. Ser. 1225*, pages 81–86, 2002.

A. J.S.C. Pereira, M. D. Pereira, L. J.P.F. Neves, J. M.M. Azevedo, and A. B.A. Campos. Evaluation of groundwater quality based on radiological and hydrochemical data from two uraniferous regions of Western Iberia: Nisa (Portugal) and Ciudad Rodrigo (Spain). *Environmental Earth Sciences*, 73(6): 2717–2731, 2015. ISSN 18666299. doi: 10.1007/s12665-014-3500-6.

D. Gibbons and R. Kalin. A Survey of Radon-222 in Ground Water from the Sherwood Sandstone Aquifer: Belfast and Newtownards, Northern Ireland. *Groundwater Monitoring & Remediation*, 17(2):88–92, may 1997. ISSN 1069-3629. doi: 10.1111/j.1745-6592.1997.tb01281.x.

K. Skeppström and B. Olofsson. A prediction method for radon in groundwater using GIS and multivariate statistics. *Science of the Total Environment*, 367 (2-3):666–680, aug 2006. ISSN 00489697. doi: 10.1016/j.scitotenv.2006.02.044.

R.R. Bourgoignie, P. Lejeine, A. Poffijn, O. Sefaert, and J. Uyttenhove. On the Rn- 222 and Ra-226 concentrations in water from the Pletrou source (Vise). Ann. Belg. Ver. Stralingsbescherm 7, 5e16. In *Ann. Belg. Ver. Stralingsbescherm 7*, pages 5–16, 1982.

A Kasić, A. Kasumović, F. Adrović, and M. Hodžić. Radon measurements in well and spring water of the Tuzla area, Bosnia and Herzegovina. *Arhiv za Higijenu Rada i Toksikologiju*, 67(4):332–339, 2016. ISSN 00041254. doi: 10.1515/aiht-2016-67-2788.

D. Desideri, C. Roselli, A. Rongoni, and D. Saetta. 222Rn determination in drinkable waters of a central eastern Italian area: Comparison between liquid scintillation and gamma-spectrometry. *Journal of Radioanalytical and Nuclear Chemistry*, 266(2):191–197, nov 2005. ISSN 02365731. doi: 10.1007/s10967-005-0891-6. URL http://link.springer.com/10.1007/s10967-005-0891-6.

A. V. Vasilyev, I. V. Yarmoshenko, and M. V. Zhukovsky. Low air exchange rate causes high indoor radon concentration in energy-efficient buildings. *Radiation Protection Dosimetry*, 164(4):601–605, jun 2015. ISSN 0144-8420. doi: 10.1093/rpd/ncv319.

D. Al-Azmi, I. C. Okeyode, O. O. Alatise, and A. O. Mustapha. Setup and procedure for routine measurements of radon exhalation rates of building materials. *Radiation Measurements*, 112:6–10, may 2018. ISSN 13504487. doi: 10.1016/j.radmeas.2018.03.001.

B. G. Jagadeesha and Y. Narayana. Radon exhalation rate measurement in the environment of Hassan district of southern India. *Radiochemistry*, 59(1): 104–108, jan 2017. ISSN 10663622. doi: 10.1134/S1066362217010143.

T. Kovács, A. Shahrokhi, Z. Sas, T. Vigh, and J. Somlai. Radon exhalation study of manganese clay residue and usability in brick production. *Journal of Environmental Radioactivity*, 168:15–20, mar 2017. ISSN 18791700. doi: 10.1016/j.jenvrad.2016.07.014.

M. P. Campos, L. J.P. Costa, M. B. Nisti, and B. P. Mazzilli. Phosphogypsum recycling in the building materials industry: assessment of the radon exhalation rate. *Journal of Environmental Radioactivity*, 172:232–236, jun 2017. ISSN 18791700. doi: 10.1016/j.jenvrad.2017.04.002.

N. Sharma, J. Singh, S. C. Esakki, and R. M. Tripathi. A study of the natural radioactivity and radon exhalation rate in some cements used in India and its radiological significance. *Journal of Radiation Research and Applied Sciences*, 9(1):47–56, 2016. ISSN 1687-8507. doi: 10.1016/j.jrras.2015.09.001. URL http://dx.doi.org/10.1016/j.jrras.2015.09.001.

A. F. Saad, Hend H. Al-Awami, and N. A. Hussein. Radon exhalation from building materials used in Libya. *Radiation Physics and Chemistry*, 101:15–19, 2014. ISSN 18790895. doi: 10.1016/j.radphyschem.2014.03.030. URL http://dx.doi.org/10.1016/j.radphyschem.2014.03.030.

E. Bavarnegin, N. Fathabadi, M. Vahabi Moghaddam, M. Vasheghani Farahani, M. Moradi, and A. Babakhni. Radon exhalation rate and natural radionuclide content in building materials of high background areas of Ramsar, Iran. *Journal of Environmental Radioactivity*, 117:36–40, 2013. ISSN 0265931X. doi: 10.1016/j.jenvrad.2011.12.022. URL http://dx.doi.org/10.1016/j.jenvrad.2011.12.022.

N. M. Hassan, T. Ishikawa, M. Hosoda, K. Iwaoka, A. Sorimachi, S. K. Sahoo, M. Janik, C. Kranrod, H. Yonehara, M. Fukushi, and S. Tokonami. The effect of water content on the radon emanation coefficient for some building materials used in Japan. *Radiation Measurements*, 46(2):232–237, feb 2011. ISSN 13504487. doi: 10.1016/j.radmeas.2010.11.006.

J. Chen, N. M. Rahman, and I. A. Atiya. Radon exhalation from building materials for decorative use. *Journal of Environmental Radioactivity*, 101(4): 317–322, apr 2010. ISSN 0265931X. doi: 10.1016/j.jenvrad.2010.01.005.

R. Shweikani and G. Raja. Radon exhalation from some finishing materials frequently used in Syria. *Radiation Measurements*, 44(9-10):1019–1023, oct 2009. ISSN 13504487. doi: 10.1016/j.radmeas.2009.10.034.

B. K. Sahoo, D. Nathwani, K. P. Eappen, T. V. Ramachandran, J. J. Gaware, and Y. S. Mayya. Estimation of radon emanation factor in Indian building materials. *Radiation Measurements*, 42(8):1422–1425, sep 2007. ISSN 13504487. doi: 10.1016/j.radmeas.2007.04.002.

S. Rahman, N. Mati, Matiullah, and B. Ghauri. Radon exhalation rate from the soil, sand and brick samples collected from NWFP and FATA, Pakistan. *Radiation Protection Dosimetry*, 124(4):392–399, may 2007. ISSN 0144-8420. doi: 10.1093/rpd/ncm226.

S. Righi and L. Bruzzi. Natural radioactivity and radon exhalation in building materials used in Italian dwellings. *Journal of Environmental Radioactivity*, 88(2):158–170, jan 2006. ISSN 0265931X. doi: 10.1016/j.jenvrad.2006.01.009.

A. F. Maged and F. A. Ashraf. Radon exhalation rate of some building materials used in Egypt. *Environmental Geochemistry and Health*, 27(5-6):485–489, oct 2005. ISSN 02694042. doi: 10.1007/s10653-005-5332-5.

S. Stoulos, M. Manolopoulou, and C. Papastefanou. Assessment of natural radiation exposure and radon exhalation from building materials in Greece. *Journal of Environmental Radioactivity*, 69(3):225–240, jan 2003. ISSN 0265931X. doi: 10.1016/S0265-931X(03)00081-X.

N. P. Petropoulos, M. J. Anagnostakis, and S. E. Simopoulos. Building materials radon exhalation rate: ERRICCA intercomparison exercise results. In *Science of the Total Environment*, volume 272, pages 109–118. Elsevier, may 2001. doi: 10.1016/S0048-9697(01)00674-X.

L. Shen and Z. Chen. Critical review of the impact of tortuosity on diffusion. *Chemical Engineering Science*, 62(14):3748–3755, 2007. ISSN 00092509. doi: 10.1016/j.ces.2007.03.041.

F. A. L. Dullien. *Porous Media: Fluid Transport and Fluid Structures*. Academic Press Limited, i edition, jan 1979. ISBN 9780323151351.

J. R. Nimmo. Porosity and Pore-Size Distribution. *Encyclopedia of Soils in the Environment*, 4:295–303, 2004. doi: 10.1016/B0-12-348530-4/00404-5.

W. J. Ullman and R. C. Aller. Diffusion coefficients in nearshore marine sediments, may 1982. ISSN 19395590.

E. Buckingham. Contributions to our knowledge of the aeration of soils, 1904.

M. Matyka, A. Khalili, and Z. Koza. Tortuosity-porosity relation in porous media flow. *Physical Review E - Statistical, Nonlinear, and Soft Matter Physics*, 78(2):1–8, 2008. ISSN 15393755. doi: 10.1103/PhysRevE.78.026306.

J. Porstendörfer. Properties and behaviour of radon and thoron and their decay products in the air. *Journal of Aerosol Science*, 25(2):219–263, 1994. ISSN 00218502. doi: 10.1016/0021-8502(94)90077-9.

I. López-Coto, J. L. Mas, A. Vargas, and J. P. Bolívar. Studying radon exhalation rates variability from phosphogypsum piles in the SW of Spain. *Journal of Hazardous Materials*, 280:464–471, 2014. ISSN 18733336. doi: 10.1016/j.jhazmat.2014.07.025. URL http://dx.doi.org/10.1016/j.jhazmat.2014.07.025.

M. Antonopoulos-Dornis, P. Krifidis, and C. Raptis. Diffusion Model of Radon Exhalation Rates. *Health Physics*, 74(5):574–580, 1998. ISSN 0017-9078. doi: 10.1097/00004032-199805000-00005.

V. C. Rogers, K. K. Nielson, and R. B. Holt. Radon diffusion coefficients for aged residential concretes. *Health Physics*, 68(6):832–834, 1995. ISSN 15385159. doi: 10.1097/00004032-199506000-00011.

M. (Marvin) Wilkening. *Radon in the environment*. Elsevier, 1990. ISBN 0080874991.

Z. Yan, C. Chen, P. Fan, M. Wang, and X. Fang. Pore structure characterization of ten typical rocks in China. *Electronic Journal of Geotechnical Engineering*, 20(2):479–494, 2015. ISSN 10893032.

J. Straube. *Moisture Control and Enclosure Wall Systems*. PhD thesis, 1998.

T. J. Marshall, J. W. Holmes, and C. W. Rose. *Soil physics. Third edition*. Cambridge University Press, 1996. ISBN 0521451515.

S. Ordóñez, R. Fort, and M. A. Garcia del Cura. Pore size distribution and the durability of a porous limestone. *Quarterly Journal of Engineering Geology*, 30:221–230, 1997. doi: 10.1144/GSL.QJEG.1997.030.P3.04.

M. Kashif, Y. Cao, G. Yuan, M. Asif, K. Javed, J. N. Mendez, D. Khan, and L. Miruo. Pore size distribution, their geometry and connectivity in deeply buried Paleogene Es1 sandstone reservoir, Nanpu Sag, East China. *Petroleum Science*, 16(5):981–1000, oct 2019. ISSN 19958226. doi: 10.1007/s12182-019-00375-3.

M. Knudsen. Die Gesetze der Molekularströmung und der inneren Reibungsströmung der Gase durch Röhren. *Annalen der Physik*, 333(1):75–130, 1909. ISSN 15213889. doi: 10.1002/andp.19093330106.

G. R. Youngquist. Symposium on Flow Through Porous Media Diffusion and Flow of Gases in Porous Solids. *Industrial and Engineering Chemistry*, 62(8):52–63, 1970. ISSN 00197866. doi: 10.1021/ie50728a006.

S. Y. Chung, P. Sikora, T. Rucinska, D. Stephan, and M. Abd Elrahman. Comparison of the pore size distributions of concretes with different air-entraining admixture dosages using 2D and 3D imaging approaches. *Materials Characterization*, 162:110182, 2020. ISSN 10445803. doi: 10.1016/j.matchar.2020.110182. URL https://doi.org/10.1016/j.matchar.2020.110182.

P. M. C. Baretto. Radon-222 emanation characteristics of rocks and minerals. In *Radon in Uranium Mining Proceedings of a Panel, Washington, D.C.*, pages 129–150, 1973.

D. Iskandar, H. Yamazawa, and T. Iida. Quantification of the dependency of radon emanation power on soil temperature. *Applied Radiation and Isotopes*, 60(6):971–973, 2004. ISSN 09698043. doi: 10.1016/j.apradiso.2004.02.003.

K. Y. Lee, Y. Y. Yoon, and K. S. Ko. Determination of the emanation coefficient and the Henry's law constant for the groundwater radon. *Journal of Radioanalytical and Nuclear Chemistry*, 286(2):381–385, 2010. ISSN 02365731. doi: 10.1007/s10967-010-0730-2.

P. Sahu, D. C. Panigrahi, and D. P. Mishra. A comprehensive review on sources of radon and factors affecting radon concentration in underground uranium mines. *Environmental Earth Sciences*, 75(7), 2016. ISSN 18666299. doi: 10.1007/s12665-016-5433-8.

S. Whitaker. Flow in porous media I: A theoretical derivation of Darcy's law. *Transport in Porous Media*, 1(1):3–25, mar 1986. ISSN 01693913. doi: 10.1007/BF01036523.

H. Darcy. *The public fountains of the city of Dijon. Experience and application principles to follow and formulas to be used in the question of the distribution of water.* 1856.

J. A. Guin, D. P. Kessler, and R. A. Greenkorn. The permeability tensor for anisotropic nonuniform porous media. *Chemical Engineering Science*, 26(9):1475–1478, 1971. ISSN 00092509. doi: 10.1016/0009-2509(71)80067-2.

P. A. Rice, A. J. Barduhn, D. J. Fontugne, and R. G. Latini. Anisotropic Permeability in Porous Media. *Industrial and Engineering Chemistry*, 62(6):23–31, 1970. ISSN 00197866. doi: 10.1021/ie50726a005.

A. E. Scheidegger. *The Physics of Flow Through Porous Media (3rd Edition)*. University of Toronto Press, 1974. ISBN 9781487582395. URL http://www.jstor.org/stable/10.3138/j.ctvfrxmtw.

L. Wang, Y. Li, G. Zhao, N. Chen, and Y. Xu. Experimental Investigation of Flow Characteristics in Porous Media at Low Reynolds Numbers (Re→0) under Different Constant Hydraulic Heads. *Water*, 11(2317), 2019.

K. Chaudhary, M. B. Cardenas, W. Deng, and P. C. Bennett. The role of eddies inside pores in the transition from Darcy to Forchheimer flows. *Geophysical Research Letters*, 38(24):n/a–n/a, dec 2011. ISSN 00948276. doi: 10.1029/2011GL050214. URL http://doi.wiley.com/10.1029/2011GL050214.

J. Bear. Dynamics of Fluids in Porous Media. *Soil Science*, 120(2):162–163, 1975. ISSN 0038-075X. doi: 10.1097/00010694-197508000-00022.

H. Muskat. *The flow of homogeneous fluids through porous media*. J. W. Edwards, In., 1907.

P. Forchheimer. Wasserbewegung durch Boden Zeit. *Ver. Deut. Ing.*, 45, 1901.

J. Dupuit. *Études théoriques et pratiques sur le mouvement des eaux*. Libraire des corps impériaux des ponts et chaussées et des mines, Paris, 1863.

J. S. Andrade, U. M.S. Costa, M. P. Almeida, H. A. Makse, and H. E. Stanley. Inertial effects on fluid flow through disordered porous media. *Physical Review Letters*, 82(26):5249–5252, jun 1999. ISSN 10797114. doi: 10.1103/PhysRevLett.82.5249.

G. H. Fancher and J. A. Lewis. Flow of Simple Fluids through Porous Materials. *Industrial and Engineering Chemistry*, 25(10):1139–1147, oct 1933. ISSN 00197866. doi: 10.1021/ie50286a020.

N. B. Carrigy, L. M. Pant, S. Mitra, and M. Secanell. Knudsen Diffusivity and Permeability of PEMFC Microporous Coated Gas Diffusion Layers for Different Polytetrafluoroethylene Loadings. *Journal of The Electrochemical Society*, 160(2):F81–F89, dec 2013. ISSN 0013-4651. doi: 10.1149/2.036302jes.

C. N. Hsu, S. C. Tsai, and S. M. Liang. Evaluation of diffusion parameters of radon in porous material by flow-through diffusion experiment. *Applied Radiation and Isotopes*, 45(8):845–850, 1994. ISSN 09698043. doi: 10.1016/0969-8043(94)90215-1.

V. Leivo, M. Kiviste, A. Aaltonen, M. Turunen, and U. Haverinen-Shaughnessy. Air pressure difference between indoor and outdoor or staircase in multifamily buildings with exhaust ventilation system in Finland. *Energy Procedia*, 78:1218–1223, 2015. ISSN 18766102. doi: 10.1016/j.egypro.2015.11.188. URL http://dx.doi.org/10.1016/j.egypro.2015.11.188.

T. Čechák, A. Froňka, and L. Moučka. Indoor Radon Concentration and Outdoor /Indoor Pressure Difference. In *Proceedings of the 4th European conference on protection against radon at home and at work*, page 377, 2004.

R. C. Dorf. *The Engineering Handbook*. CDC Press, 2nd edition edition, 2004. URL https://www.routledge.com/The-Engineering-Handbook/Dorf/p/book/9780849315862.

I. Suaro. *Modelling of radon diffusion trough the soil*. PhD thesis, National Institute of Technology Rourkela, 2014.

N. Chitra, S. Bala Sundar, M. T. Jose, K. Sivasubramanian, and B. Venkatraman. A simple model to simulate the diffusion pattern of radon in different soil media. *Journal of Radioanalytical and Nuclear Chemistry*, 322(2):1151–1158, 2019. ISSN 15882780. doi: 10.1007/s10967-019-06820-2. URL https://doi.org/10.1007/s10967-019-06820-2.

W. J. Speelman, R. Lindsay, R. T. Newman, and A. D. Joseph. Modelling and Measurement of Radon Diffusion Through Soil for Application on Mine Tailings Dams. In *VII Radiation Physics & Protection Conference*, number November, pages 279–287, 2004.

F. S. Abd Ali, K. H. Mahdi, and E. A. Jawad. Humidity effect on diffusion and length coefficient of radon in soil and building materials. In *Technologies and Materials for Renewable Energy, Environment and Sustainability, TMREES18, 19–21 September 2018, Athens, Greece 19–21 September 2018, Athens, Greece Humidity*, volume 157, pages 384–392, 2019. ISBN 0000000000. doi: 10.1016/j.egypro.2018.11.203.

L. Minkin. Is Diffusion, Thermodiffusion, or Advection a Primary Mechanism of Indoor Radon Entry? *Radiation Protection Dosimetry*, 102(2):153–161, 2002. ISSN 0144-8420. doi: 10.1093/oxfordjournals.rpd.a006084.

L. Font and C. Baixeras. The RAGENA dynamic model of radon generation, entry and accumulation indoors. *Science of the Total Environment*, 307(1-3): 55–69, 2003. ISSN 00489697. doi: 10.1016/S0048-9697(02)00462-X.

D. T. Kendrick and G. H. Langner. Direct measurement of radon flux through structure boundaries on differential pressure. In *The 1991 International Symposium on Radon and Radon Reduction Technology*, Philadelphia, Pennsylvania, 1991.

T. Turtiainen. Radon: origin, entry and affecting factors.

J. C. Dixon. *The Shock Absorber Handbook*. Second edi edition, 2007. ISBN 9780470510209. doi: 10.1002/9780470516430.app2.

I. López-Coto, J.L. Mas, and J.P. Bolivar. A 40-year retrospective European radon flux inventory including climatological variability. *Atmospheric Environment*, 73:22–33, jul 2013. ISSN 1352-2310. doi: 10.1016/J.ATMOSENV.2013.02.043. URL https://www.sciencedirect.com/science/article/pii/S1352231013001441.

Sérgio L. R. Seco, F. P. Domingos, A. J. S. C. Pereira, and L. V. Duarte. Estimation of the radon production potential in sedimentary rocks : A case study in the Lower and Middle Jurassic of the Lusitanian Basin (Portugal). 221(October 2019), 2020. doi: 10.1016/j.jenvrad.2020.106272.

G. E. Manger. Geological Survey Bulletin 1144-E: Porosity and Bulk Density of Sedimentary Rocks. Technical report, U.S. Atomic Energy Commission, 1963.

International Organization for Standardization. ISO 11665-9 Measurement of radioactivity in the environment — Air: radon 222 — Part 9: Method for determining exhalation rate of building materials. Technical report, 2012b.

B. K. Sahoo and Y. S. Mayya. Two dimensional diffusion theory of trace gas emission into soil chambers for flux measurements. *Agricultural and Forest Meteorology*, 150(9):1211–1224, 2010. ISSN 01681923. doi: 10.1016/j.agrformet.2010.05.009. URL http://dx.doi.org/10.1016/j.agrformet.2010.05.009.

M. Al-Jarallah. Radon exhalation from granites used in Saudi Arabia. *Journal of Environmental Radioactivity*, 53(1):91–98, 2001. ISSN 0265931X. doi: 10.1016/S0265-931X(00)00110-7.

M. I. Al-Jarallah, F. Abu-Jarad, and F. Fazal-ur Rehman. Determination of radon exhalation rates from tiles using active and passive techniques. *Radiation Measurements*, 34(1-6):491–495, 2001. ISSN 13504487. doi: 10.1016/S1350-4487(01)00213-X.

E. Stranden. Building materials as a source of indoor radon. *Radon and its decay products in indoor air.*, (l):113–130, 1988.

R. M. Amin. A study of radon emitted from building materials using solid state nuclear track detectors. *Journal of Radiation Research and Applied Sciences*, 8(4):516–522, 2015. ISSN 1687-8507. doi: 10.1016/j.jrras.2015.06.001. URL http://dx.doi.org/10.1016/j.jrras.2015.06.001.

A. F. Saad, Y. K. Abdalla, N. A. Hussein, and I. S. Elyaseery. Radon exhalation rate from building materials used on the garyounis university campus, benghazi, libya. *Turkish Journal of Engineering and Environmental Sciences*, 34(1):67–74, 2010. ISSN 13000160. doi: 10.3906/muh-0810-17.

J. Seo, M. M. Nirwono, S. J. Park, and S. H. Lee. Standard Measurement Procedure for Soil Radon Exhalation Rate and Its Uncertainty. *Journal of Radiation Protection and Research*, 43(1):29–38, 2018. ISSN 2508-1888. doi: 10.14407/jrpr.2018.43.1.29.

I. Yarmoshenko, G. Malinovsky, A. Vasilyev, and M. Zhukovsky. Method for measuring radon flux density from soil activated by a pressure gradient. *Radiation Measurements*, 119(July):150–154, 2018. ISSN 13504487. doi: 10.1016/j.radmeas.2018.10.011. URL https://doi.org/10.1016/j.radmeas.2018.10.011.

J. Vaupotiĉ, A. Gregoriĉ, I. Kobal, P. Žvab, K. Kozak, J. Mazur, E. Kochowska, and D. Grzadziel. Radon concentration in soil gas and radon exhalation rate at the Ravne Fault in NW Slovenia. *Natural Hazards and Earth System Science*, 10(4):895–899, 2010. ISSN 16849981. doi: 10.5194/nhess-10-895-2010.

S. D. Schery, S. Whittlestone, K. P. Hart, and S. E. Hill. The flux of radon and thoron from Australian soils. *Journal of Geophysical Research*, 94(D6): 8567–8576, 1989. doi: 10.1029/JD094iD06p08567.

A. Sharma, A. Kumar, M. Sonkawade, and R. Kumar. Radon exhalation in some building construction materials and effect of plastering and paints on the radon exhalation rate using fired bricks. *Advances in Applied Science Research*, 5(2):382–386, 2014.

Y. Tan and D. Xiao. A simple model for automatically measuring radon exhalation rate from medium surface. *Radiation Measurements*, 64:44–47, 2014. ISSN 13504487. doi: 10.1016/j.radmeas.2014.04.006. URL http://dx.doi.org/10.1016/j.radmeas.2014.04.006.

Y. Tan and D. Xiao. Measurement of the radon exhalation rate from the medium surface by tracing the radon concentration. *Journal of Radioanalytical and Nuclear Chemistry*, 295(3):2295–2299, 2013. ISSN 02365731. doi: 10.1007/s10967-012-2294-9.

Y. Tan and D. Xiao. Revision for measuring the radon exhalation rate from the medium surface. *IEEE Transactions on Nuclear Science*, 58(1 PART 2): 209–213, 2011. ISSN 00189499. doi: 10.1109/TNS.2010.2090897.

F. J. Aldenkamp, R. J. de Meijer, L. W. Put, and P. Stoop. An Assessment of In Situ Radon Exhalation Measurements, and the Relation Between Free and Bound Exhalation Rates. *Radiation Protection Dosimetry*, 45(1-4):449–453, dec 1992. ISSN 0144-8420. doi: 10.1093/rpd/45.1-4.449. URL https://academic.oup.com/rpd/article/45/1-4/449/5091741.

A. Noverques, G. Verdú, B. Juste, and M. Sancho. Experimental radon exhalation measurements: Comparison of different techniques. *Radiation Physics and Chemistry*, 155(August 2018):319–322, 2019. ISSN 18790895. doi: 10.1016/j.radphyschem.2018.08.002.

M. Jiránek and J. Hůlka. Applicability of various insulating materials for radon barriers. *Science of the Total Environment*, 272(1-3):79–84, 2001. ISSN 00489697. doi: 10.1016/S0048-9697(01)00668-4.

Genitron InstrumentGmbH. AlphaGUARD Portable Radon Monitor - User Manual, 2012.

G. V. Centomani, R. Remetti, and C. Di Carlo. Messa a punto e collaudo di una camera di taratura per l'analisi della risposta dinamica di rivelatori per radon, 2018.

G.V. Centomani, C. Di Carlo, L. Lepore, and R. Remetti. Design and commissioning of an innovative radon chamber with a single 226Ra source and continuous variation and control of concentration vs. time. *Nuclear Instruments and Methods in Physics Research Section A: Accelerators, Spectrometers, Detectors and Associated Equipment*, 940(June):109–115, 2019. ISSN 01689002. doi: 10.1016/j.nima.2019.05.084. URL https://linkinghub.elsevier.com/retrieve/pii/S016890021930748X.

Zephyr Honeywell. Analog Airflow Sensors: HAF Series High Accuracy, 2012.

T. Ahmed. *Equations of state and PVT analysis*. Gulf, 2013. ISBN 9781933762036. doi: 10.1016/C2013-0-15511-0.

Joint Committee for Guides in Metrology. Evaluation of measurement data — Guide to the expression of uncertainty in measurement. (International Organization for Standardization Geneva), 2008. ISSN 00099147. URL http://www.bipm.org/en/publications/guides/gum.html.

D. Azimi-Garakani. A comparison of different radon chambers. *Nuclear Instruments and Methods in Physics Research Section B: Beam Interactions with Materials and Atoms*, 71(1):99–102, jul 1992. ISSN 0168583X. doi: 10.1016/0168-583X(92)95347-T. URL https://linkinghub.elsevier.com/retrieve/pii/0168583X9295347T.

G. Venoso, M. Pugliese, V. Roca, and C. Sabbarese. A radon facility at Naples University: Features and first tests. *Applied Radiation and Isotopes*, 67(5):863–866, 2009. ISSN 09698043. doi: 10.1016/j.apradiso.2009.01.082.

F. Cardellini, E. Chiaberto, L. Garlati, D. Giuffrida, F. Leonardi, M. Magnoni, G. Minchillo, A. Prandstatter, E. Serena, R. Trevisi, R. Tripodi, and M. Veschetti. Metrological aspects of international intercomparison of passive radon detectors under field conditions in Marie Curie's tunnel in Lurisia. *Nukleonika*, 61(3):251–256, 2016. ISSN 15085791. doi: 10.1515/nuka-2016-0042.

A. Honig, A. Paul, S. Röttger, and U. Keyser. Environmental control of the German radon reference chamber. *Nuclear Instruments and Methods in Physics Research, Section A: Accelerators, Spectrometers, Detectors and Associated Equipment*, 416(2-3):525–530, 1998. ISSN 01689002. doi: 10.1016/S0168-9002(98)00788-8.

International Electrotechnical Commission. IEC 61577-4 Protection instrumentation — Radon and radon decay product. Technical report, 2009.

A. Röttger and A. Honig. Recent developments in radon metrology: New aspects in the calibration of radon, thoron and progeny devices. *Radiation Protection Dosimetry*, 145(2-3):260–266, 2011. ISSN 01448420. doi: 10.1093/rpd/ncr047.

J. M. Lee, K. H. Ahn, H. S. Chai, and T. S. Park. Development of radon calibration chamber at KRISS. *Applied Radiation and Isotopes*, 61(2-3):237–241, 2004. ISSN 09698043. doi: 10.1016/j.apradiso.2004.03.052.

A. Vargas, X. Ortega, and J. L.Martín Matarranz. Traceability of radon-222 activity concentration in the radon chamber at the technical university of Catalonia (Spain). *Nuclear Instruments and Methods in Physics Research, Section A: Accelerators, Spectrometers, Detectors and Associated Equipment*, 526(3):501–509, 2004. ISSN 01689002. doi: 10.1016/j.nima.2004.02.022.

K. Mamont-Cieśla, O. Stawarz, M. Karpińska, J. Kapała, K. Kozak, D. Grzadziel, S. Chałupnik, I. Chmielewska, J. Olszewski, T. A. Przylibski, and A. Zebrowski. Intercomparison of radon CR-39 detector systems conducted in CLOR's calibration chamber. *Nukleonika*, 55(4):589–593, 2010. ISSN 00295922.

W. Arafa. Permeability of radon-222 through some materials. *Radiation Measurements*, 35(3):207–211, 2002. ISSN 13504487. doi: 10.1016/S1350-4487(02)00043-4.

V. Jobbágy, H. Stroh, G. Marissens, P. Malo, M. Hult, R. Van Ammel, V. Gruber, and D. Roth. Technical report on the REM 2018 radon-in-water proficiency test. Technical report, European Commission, Luxembourg, 2020.

Arduino Uno Rev3 | Arduino Official Store, a. URL https://store.arduino.cc/arduino-uno-rev3.

Arduino Wireless SD Shield, b. URL https://store.arduino.cc/arduino-wireless-sd-shield.

D.B. Pelowitz. *MCNPX User's Manual. Version 2.7.0.* LA-CP-11-00438, Los Alamos National Laboratory, 2011. URL https://www.scirp.org/(S(lz5mqp453edsnp55rrgjct55))/reference/ReferencesPapers.aspx?ReferenceID=1950835.

ARDUINO UNO WiFi REV2 | Arduino Official Store, c. URL https://store.arduino.cc/arduino-uno-wifi-rev2.

Dwyer Instruments. Series VF, Visi-Float® Acrylic Flowmeter, a. URL https://www.dwyer-inst.com/Product/Flow/Flowmeters/VariableArea/SeriesVF.

Dwyer Instruments. Series SBSV-B, Brass Solenoid Valves, b. URL https://www.dwyer-inst.com/Product/Valves/Valves/Solenoid/SeriesSBSV-B.

Dwyer Instruments. Series BICV , Brass Inline Check Valve, c. URL https://www.dwyer-inst.com/Product/Valves/Valves/Check/SeriesBICV.

SUNON. SUNON - Fan, motor, cooling module, thermal solution. URL https://www.sunon.com/eu/Support2.aspx.

KNF. NMP09 Series Micro Diaphragm Gas Pumps.

World Health Organization. *Management of radioactivity in drinking-water*. Geneva, 2018. ISBN 9789241513746. URL http://www.who.int/water{_}sanitation{_}health/publications/management-of-radioactivity-in-drinking-water/en/.

G. M. Kendall and T. J. Smith. Doses to organs and tissues from radon and its decay products. *Journal of Radiological Protection*, 22(4):389–406, 2002. ISSN 09524746. doi: 10.1088/0952-4746/22/4/304.

V. Jobbágy, H. Stroh, G. Marissens, and M. Hult. Comprehensive study on the technical aspects of sampling, transporting and measuring radon-in-water. *Journal of Environmental Radioactivity*, 197:30–38, feb 2019. ISSN 18791700. doi: 10.1016/j.jenvrad.2018.11.012. URL https://www.sciencedirect.com/science/article/pii/S0265931X18305976.

Saphymo GmbH. AquaKIT: Accessory for radon in water measurement in combination with the radon monitor AlphaGUARD. 2017.

International Standard Organization. Accuracy (trueness and precision) of measurement methods and results - Part 2: Basic method for the determination of repeatability and reproducibility of a standard measurement method. *ISO 5725-2*, 1994.

Statista - The Statistics Portal. Per capita consumption of bottled water in Europe in 2016, by country, 2016.

C. Kralik, M. Friedrich, and F. Vojir. Natural radionuclides in bottled water in Austria. *Journal of Environmental Radioactivity*, 65(2):233–241, 2003. ISSN 0265931X. doi: 10.1016/S0265-931X(02)00099-1.

C. Giovani, L. Achilli, G. Agnesod, L. Bellino, M. Bonomi, M. Cappai, G. Cherubini, M. Forte, M. Garavaglia, S. Maggiolo, M. Magnoni, L. Minach, S. Risica, A. Sansone Santamaria, and F. Trotti. Natural Radioactivity in Italian Drinking and Mineral Water: Experimental Data and Dose Assesment. In *High levels of natural radiation and radon areas: radiation dose and health effects*, Munich, Germany, 2000.

C. Nuccetelli, R. Rusconi, and M. Forte. Radioactivity in drinking water: Regulations, monitoring results and radiation protection issues. *Annali dell'Istituto Superiore di Sanita*, 48(4):362–363, 2012. ISSN 00212571. doi: 10.4415/ANN-12-04-04.

Regione Lazio. Sviluppo Economico - Elenco Concessioni Acque Minerali, 2018.

Fred W. Leaney and Andrew L. Herczeg. A rapid field extraction method for determination of radon-222 in natural waters by liquid scintillation counting. *Limnology and Oceanography: Methods*, 4(7):254–259, jul 2006. ISSN 15415856. doi: 10.4319/lom.2006.4.254. URL http://doi.wiley.com/10.4319/lom.2006.4.254.

C. Lucchetti, G. De Simone, G. Galli, and P. Tuccimei. Evaluating radon loss from water during storage in standard PET, bio-based PET, and PLA bottles. *Radiation Measurements*, 84:1–8, 2016. ISSN 13504487. doi: 10.1016/j.radmeas.2015.11.001. URL http://dx.doi.org/10.1016/j.radmeas.2015.11.001.

F. Bochicchio, S. Bucci, M. Bonomi, G. Cherubini, C. Giovani, M. Magnoni, L. Minach, and P. Sabatini. Areas with high radon levels in Italy. In *Radon in the Living Environment*, Athens (Greece), 1999.